The University of Sheffield

Control of Asymmetric Permanent Magnet Synchronous Generator Systems

Yashan Hu

A thesis submitted for the degree of Doctor of Philosophy

Department of Electronic and Electrical Engineering

The University of Sheffield

Mapping Building, Sheffield, S1 3JD, UK

November 25, 2015

Abstract

The thesis focuses on the control of asymmetric permanent magnet synchronous generator (PMSG) system, with particular reference to the suppression of its second harmonic (2h) power, DC bus voltage and torque ripples.

The asymmetries include the unbalanced resistances, unbalanced inductances, and unbalanced 3-phase back-electromotive forces (EMFs). The mathematical model of the general asymmetries in the PMSG system is firstly presented. The power ripple and torque ripple due to the asymmetries without/with negative-(*N*-) sequence currents are then analysed in detail. It shows that there are 2h impedances in the synchronous *dq*-axis frame. Consequently, the *N*-sequence currents emerge under the conventional current proportional and integral (PI) control, which will result in undesired 2h power, DC bus voltage and torque ripples.

To suppress the 2h torque resulted from the *N*-sequence currents, three typical methods aiming for balanced currents without *N*-sequence currents are reviewed, evaluated and their relationship is revealed. It shows that all these three methods are capable of suppressing the *N*-sequence currents as verified by experiments. However, the 2h power and DC bus voltage cannot be suppressed.

To suppress the undesired 2h power and DC bus voltage, an improved power control without any sequential component decomposers under general unbalanced conditions is proposed. Its effectiveness is validated by elaborated experiments on a prototype PMSG with inherent asymmetry and deliberately introduced asymmetries. However, the 2h torque is compromised.

To solve the 2h torque, power and DC bus voltage simultaneously, the compensation in parallel with the DC bus is investigated in the PMSG system with asymmetric impedances. The undesired 2h power from the PMSG is compensated by the 2h power from the compensation unit. Two topologies of the compensation unit and corresponding control methods are investigated, while the compensation effectiveness is validated by experiments.

Furthermore, the compensation unit with external circuits in series with the asymmetric PMSG is investigated. By the compensation in series, the original unbalanced system is modified to a balanced system in theory. Therefore, the *N*-

sequence currents, 2h power, DC bus voltage, and torque ripple can be naturally suppressed. The feasibility of this compensation method is verified by experiments at different speeds and load conditions, although the effectiveness may be slightly affected by the non-linearity of the compensation inductors in practice.

Finally, the research of suppressing the 2h DC bus voltage and torque ripple is extended to the dual 3-phase PMSG system with one channel failed. By utilizing the windings, rectifier or inverter in the faulty channel which are still functional, three methods designated as two sets in parallel, two DC buses in parallel and *N*-sequence currents compensation are investigated, which require minimum extra hardware investment compared with the compensation in parallel and in series.

Acknowledgements

First and foremost I offer my sincerest gratitude to my supervisor, Prof Z.Q. Zhu, who supports me throughout my PhD period with his professional technical guidance and help. Without him, this thesis would not have been completed. I simply could not wish for a better supervisor in the whole world.

Profound gratitude goes to my second supervisor Dr Milijana Odavic for her supervision and loads of constructive discussions. I am also hugely appreciative to Dr Zhan-Yuan Wu and Dr Heng Deng for their help in many ways, as well as other staffs in my sponsor company of Sheffield Siemens Wind Power (S^2WP) Research Centre.

I am very grateful to all the PhD students and staff in the Electrical Machines and Drives Group at the University of Sheffield. Without them, my whole PhD life will never be the same.

Finally, I am very grateful to my wife, Xuefei Li, and my son, Yixiao Hu, for their continued love and consistent support, which make me dedicate great efforts on my research. I also would like to thank my parents and sister for their endless care.

CONTENTS

Abstract **I**

Acknowledgements **III**

Contents **IV**

Nomenclature **IX**

Chapter 1 General Introduction **1**

1.1 Introduction 1

1.2 PMSG Direct-drive System 3

1.2.1 Conventional PMSG Drive System 3

1.2.2 Back-to-back PMSG Drive System 4

1.3 Conventional Vector Control 5

1.4 Asymmetric PMSG 10

1.5 Influence of Asymmetries 12

1.6 Control of Asymmetric PMSG 13

1.6.1 Balanced Current Control 13

1.6.2 Second Harmonic Power Suppression 15

1.6.3 Summary 22

1.7 Scope and Contributions of Research 23

1.7.1 Scope 23

1.7.2 Contributions 26

Chapter 2 Influence of the PMSG Asymmetries **28**

2.1 Introduction 28

2.2 Mathematical Modeling of PMSG 28

2.2.1 Voltage and Flux-linkage Equations 28

2.2.2 Mathematical Modeling of Inductances 30

2.2.3 Power and Torque Equations 31

2.3 Modeling of Asymmetries 33

2.3.1 Unbalanced Resistances 33

2.3.2 Unbalanced Inductances 33

2.3.3 Unbalanced Back-EMFs 34

2.4 Influence of Asymmetries without *N*-sequence Currents 34

2.4.1 Unbalanced Resistors 34

2.4.2 Unbalanced Inductances 35

2.4.3 Unbalanced Back-EMFs 40
2.4.4 Summary 41
2.5 Influence of Asymmetries with *N*-sequence Currents 41
2.5.1 Unbalanced Resistors 42
2.5.2 Unbalanced Inductances 43
2.5.3 Unbalanced Back-EMFs 48
2.6 Conclusions 49
Chapter 3 Current Control of Asymmetric PMSG 51
3.1 Introduction 51
3.2 Modeling of Asymmetric PMSG 52
3.2.1 Mathematical Model in *abc*-frame 52
3.2.2 Mathematical Model in *αβ*-frame 53
3.2.3 Mathematical Model in PSRF and NSRF 54
3.3 Evaluation of Current Control of Asymmetric PMSG 60
3.3.1 PR control 61
3.3.2 Dual Current Control 63
3.3.3 PI-R Control in PSRF 65
3.3.4 Summary 66
3.4 Experiments 68
3.4.1 Conventional Current Control 69
3.4.2 PR Control in *αβ*-frame 72
3.4.3 Dual Current Control 74
3.4.4 PI-R Control in PSRF 76
3.4.5 Summary 78
3.5 Conclusions 79
Chapter 4 Instantaneous Power Control of Asymmetric PMSG (without sequential component decomposers) 80
4.1 Introduction 80
4.2 Second Harmonic DC Bus Voltage Introduced by Asymmetries 81
4.3 Review of Instantaneous Power Control 82
4.3.1 Input Power Control 83
4.3.2 Output Power Control 84
4.3.3 Input-output-power Control 85
4.4 Proposed Control Strategy 86

4.4.1 Extraction of the *P*- and *N*-Sequence Output Voltages 86
4.4.2 Control Scheme 88
4.4.3 Summary 90
4.5 Experiments 91
4.5.1 Balanced Current Control 91
4.5.2 Proposed Power Control 93
4.5.3 Extraction of Sequential Output Voltages 96
4.5.4 Different Asymmetries 97
4.6 Conclusion 98
Chapter 5 Control of Asymmetric PMSG with Compensation in Parallel 100
5.1 Introduction 100
5.2 Compensation in Parallel (Topology-*RL*) 102
5.2.1 Introduction 102
5.2.2 Compensation Principle 103
5.2.3 Implementation 104
5.2.4 Experimental Investigation 107
5.2.5 Summary 118
5.3 Compensation in Parallel (Topology-*RLE*) 119
5.3.1 Introduction 119
5.3.2 Compensation Principle 120
5.3.3 Implementation 121
5.3.4 Experiment Investigation 124
5.3.5 Summary 136
5.4 Conclusion 136
Chapter 6 Control of Asymmetric PMSG with Compensation in Series 137
6.1 Introduction 137
6.2 Principle of Compensation 138
6.2.1 Perspective of the Mathematical Model 139
6.2.2 Perspective of the 2h Power 141
6.2.3 Summary 142
6.3 Compensation for the Prototype PMSG 143
6.3.1 Optimized Compensation Inductance 144
6.3.2 Non-linearity of Compensation Inductor 146
6.3.3 Extra Copper Loss 149

6.4 Experiments 150
6.4.1 Influence of Non-linearity of Compensation Inductor 151
6.4.2 Results without/with Compensation 155
6.4.3 Feasibility at Different Speeds and Loads 158
6.5 Conclusion 159
Chapter 7 Control of Asymmetric Dual 3-Phase PMSG System with One Channel Failed 160
7.1 Introduction 160
7.2 Different Scenarios of Faults 162
7.2.1 One Faulty Channel of 3-phase Windings 162
7.2.2 One Faulty Channel of Inverter 163
7.2.3 One Faulty Channel of Rectifier 163
7.3 Proposed Methods 164
7.3.1 Method 1- Two Sets in Parallel 164
7.3.2 Method 2- Two DC Buses in Parallel 165
7.3.3 Method 3- *N*-sequence Currents Compensation 165
7.3.4 Summary 169
7.4 Experiments 169
7.4.1 Method 1- Two Sets in Parallel 171
7.4.2 Method 2- Two DC Buses in Parallel 173
7.4.3 Method 3- *N*-sequence Currents Compensation 176
7.4.4 Comparison 181
7.5 Conclusion 182
Chapter 8 General Conclusions 183
8.1 Introduction 183
8.1.1 Current Control of Asymmetric PMSG 184
8.1.2 Instantaneous Power Control of Asymmetric PMSG 184
8.1.3 Control of Asymmetric PMSG (Compensation in Parallel) 185
8.1.4 Control of Asymmetric PMSG (Compensation in Series) 187
8.1.5 Control of Asymmetric Dual 3-Phase PMSG System with One Channel Failed 188
8.2 Future work 189
Appendix A. Coordinate Transformation for 3-Phase System 190
Appendix B. Description of Test Rig 192
Appendix C. Inherent Asymmetries of the Prototype PMSG 195

C.1 Resistances 195
C.2 Inductances 195
C.3 Back-EMFs 199
Appendix D. Current Control For Dual 3-Phase PM Synchronous Motors Accounting For Current Unbalance and Harmonics 201
D.1 Introduction 201
D.2 Mathematical Model of Dual 3-phase PMSM 205
D.3 Proposed Current Control Scheme 206
A. Current Unbalance Compensation 207
B. Fifth and Seventh Current Harmonics Compensation 210
C. Proposed Current Control Scheme 214
D.4 Experiments 216
A. Fifth and Seventh Current Harmonics Compensation 217
B. Current Unbalance Compensation in Steady State Operation 220
C. Dynamic Performance Comparison 226
D.5 Conclusion 226
Reference 228
Publications 244

Nomenclature

abc-frame	3-phase coordinate system frame
AC	Alternating Current
back-EMF	Back electromotive force
BTB	Back-to-back
DC	Direct Current
DFIG	Doubly fed induction generator
DSOGI	Dual second-order generalized integrator
dq-frame	*dq*-axis synchronous frame
E_{1p}, and E_{1n}	Amplitude of *P*-sequence and *N*-sequence back-EMFs
e_a, e_b, and e_c	3-phase back-EMFs
e_d, and e_q	*d*- and *q*-axis back-EMFs
e_α, and e_β	α- and β-axis back-EMFs
F_d^p and F_q^p	**P*-sequence components in PSRF
F_d^n and F_q^n	**N*-sequence components in NSRF
F_d^+ and F_q^+	*3-phase components in PSRF
F_d^n and F_q^n	*3-phase components in NSRF
IPark	Inverse Park transformation
I_{1p}, and I_{1n}	Amplitude of *P*-sequence and *N*-sequence phase currents
i_a, i_b, and i_c	3-phase currents
i_{an}, i_{bn}, and i_{cn}	*N*-sequence currents
i_{ap}, i_{bp}, and i_{cp}	*P*-sequence currents
i_d, and i_q	*d*- and *q*-axis currents
IGBT	Insulated gate bipolar transistor
i_α, i_β	α- and β-axis currents
K_i	Integral gain
K_p	Proportional gain
L_{AA}, L_{BB}, and L_{CC}	3-phase self-inductances
L_d	*d*-axis inductance in *dq*-frame
L_q	*q*-axis inductance in *dq*-frame
M_{AB}, M_{BC}, and M_{CA}	Mutual inductances

M_{dq}	Mutual inductances between d-axis and q-axis
MPPT	maximum power point tracking
$M_{\alpha\beta}$	Mutual inductances between α-axis and β-axis
NSRF	Negative-sequence reference frame
N-sequence	Negative-sequence
PI	Proportional and integral
PI-R	Proportional and integral plus resonant
PM	permanent magnet
PMSG	Permanent magnet synchronous generator
PMSM	Permanent magnet synchronous machine
PR	Proportional and resonant
PSRF	Positive-sequence reference frame
PWM	Pulse width modulation
P-sequence	Positive-sequence
p	Pole pairs
p_E	Instantaneous power generated by PM
p_L	Instantaneous power in the inductor
p_R	Instantaneous power in the resistor
p_{in}	Instantaneous power generated by the back-EMFs
p_{in_c2}	Coefficient of cosine item in the 2h components in p_{in}
p_{in_s2}	Coefficient of sine item in the 2h components in p_{in}
p_{out}	Instantaneous power generated by the PMSG
p_{out}	Active power generated by PMSG
p_{out_c2}	Coefficient of cosine item in the 2h components in p_{out}
p_{out_s2}	Coefficient of sine item in the 2h components in p_{out}
q_{in}	Reactive power generated by PM
q_{out}	Reactive power generated by PMSG
R_A,R_B, and R_C	3-phase stator resistances
RMS	Root mean square
R_s	Stator resistance
SOGI	Second-order generalized integrator
THD	Total harmonic distortion
T_d	Delay time

T_e	Electromagnetic torque
T_{eL}	Reluctance torque
T_{ePM}	Electromagnetic torque by the permanent magnet
$T_{dq}(\theta)$	Park transformation matrix
$T_{\alpha\beta}$	Clark transformation matrix
$T_{\alpha\beta\_inv}$	Inverse Clark transformation matrix
$\alpha\beta$-frame	$\alpha\beta$-*axis* stationary frame
ΔR_A, ΔR_B, and ΔR_C	Unbalanced resistances
ΔL_{A0}, ΔL_{B0}, and ΔL_{C0}	Unbalanced self-inductances
ΔM_{AB0}, ΔM_{BC0}, and ΔM_{CA0}	Unbalanced mutual-inductances
ψ_a, ψ_b, and ψ_c	3-phase stator flux-linkages
ψ_d, and ψ_q	d- and q-axis stator flux-linkages
ψ_{fa}, ψ_{fb}, and ψ_{fc}	3-phase PM flux-linkages
ψ_{fd}, and ψ_{fq}	d- and q-axis PM flux-linkages
$\psi_{f\alpha}$, and $\psi_{f\beta}$	α- and β-axis PM flux-linkages
ψ_α, and ψ_β	α- and β-axis stator flux-linkages
θ_e	Electrical position of the machine
θ_m	Mechanical position of the machine
$[F_{dq}]$	*Voltage, current, stator flux-linkage in dq-frame = $[F_d\ F_q]^T$
$[F_s]$	*Voltage, current, stator flux in abc-frame=$[F_a\ F_b\ F_c]^T$
$[F_{\alpha\beta}]$	*Voltage, current, stator flux-linkage in $\alpha\beta$-frame = $[F_\alpha\ F_\beta]^T$
$[L_s]$	3-phase inductance matrix in abc-frame
$[L_{dq}]$	Three -phase inductance matrix in dq-frame
$[L_{\alpha\beta}]$	Three -phase inductance matrix in $\alpha\beta$-frame
$[R_s]$	Three -phase resistance matrix in abc-frame
$[R_{dq}]$	Three -phase resistance matrix in dq-frame
$[R_{\alpha\beta}]$	Three -phase resistance matrix in $\alpha\beta$-frame
$[e]$	Back-EMFs matrix in abc-frame
$[e_{dq}]$	Back-EMFs matrix in dq-frame
$[e_{\alpha\beta}]$	Back-EMFs matrix in $\alpha\beta$-frame
$[\psi_f]$	Permanent flux-linkage in abc-frame = $[\psi_{fa}\ \psi_{fb}\ \psi_{fc}]^T$
$[\psi_{fdq}]$	Permanent flux-linkage dq-frame = $[\psi_{fd}\ \psi_{fq}]^T$
$[\psi_{f\alpha\beta}]$	Permanent flux-linkage in $\alpha\beta$-frame = $[\psi_{f\alpha}\ \psi_{f\beta}]^T$

$\left[F_{dq}^{+}\right]$	*Voltage, current, flux in PSRF = $\left[F_d^{+} \quad F_q^{+}\right]^T$
$\left[F_{dq}^{-}\right]$	*Voltage, current, flux in NSRF = $\left[F_d^{-} \quad F_q^{-}\right]^T$
ω_e	Electrical angular speed
ω_0	Resonant frequency in the resonant control
2h	Second harmonic

*: F can be v, i or ψ, which correspond to voltage, current, and stator flux respectively

Chapter 1 General Introduction

1.1 Introduction

Wind power generation technology has been developed since 1970s and developed rapidly from 1990s [1]. Various wind turbine concepts have been developed and different wind turbine generators have been built. According to the speed controllability, power electronics, and generator type, the wind turbine can generally be categorized into different types [1-5], as described as follows.

According to the speed controllability, the wind turbines can be classified into fixed-speed and variable-speed wind turbines [5]. The fixed-speed wind turbines work at fixed speed, which are designed to obtain the maximum efficiency at one wind speed. When the wind speed increases beyond the level at which the rated power is generated, the power will be regulated by pitching the blades. The variable-speed wind turbines are designed to achieve maximum aerodynamic efficiency over a wide range of wind speeds. By adapting the turbine speed to wind speed by tracing the optimum tip-speed ratio, it is possible to obtain maximum power from the incident wind and achieve optimum aerodynamic efficiency when the wind speed is below the level of the rated wind power. In contrast, when the wind speed is above the level of rated wind power, the blades are pitched necessarily to regulate the power. Compared with the fixed-speed wind turbines, the variable-speed wind turbines have many advantages such as increased energy capture and operation at maximum power point below the level of the rated power, improved efficiency, and power quality, etc.[6].

According to the power electronics employed in the wind turbine system, the power converters can be divided as partial-scale power converter and full-scale power converter [7]. The doubly fed induction generator (DFIG)-based wind turbine [6, 8] equipped with partial-scale power converter is the most adopted solution nowadays and has been used extensively since 2000s. The DFIGs are typically used in the applications that require varying speed of the generator in a limited range around the synchronous speed. The stator windings of DFIG are directly connected to the grid, whereas the rotor windings are connected to the grid by a power converter with normally 30% capacity of the wind turbine. The converter controls the rotor's speed within typically ±30% synchronous speed [6]. From the economical point of view, the DFIG-based wind turbine is very competitive because of the smaller converter.

However, its major problem is the use of slip rings, poor controllability and grid support under the grid faults conditions [9].

In the wind turbine system with full-scale power converter, the energy from the generator is rectified to DC bus by rectifier and then transferred to the grid by inverter [10]. The generator can be asynchronous generator, electrically excited synchronous generator, or permanent magnet (PM) excited synchronous generator. The stator windings are connected to the grid through the full-scale power converter, which can perform reactive power compensation and smooth grid connection for the entire speed range. Compared with the DFIG-based partial-scale converter system, the full-scale power converter wind turbine system has higher losses and it is more expensive. However, the elimination of slip rings, simpler control, full power and speed controllability, and better grid support ability are the major advantages. In the near future, the wind turbine with full-scale power converter is expected to take over the DFIG-based wind turbine [10, 11].

According to the generator type, the wind turbine can be classified as DFIG, asynchronous generator, and synchronous generator based wind turbine. The synchronous generator, either externally electrical excited or PM excited, are becoming the preferred generator in the best seller power range [4, 5, 11, 12], especially the PMSG wind turbine system is the most attractive wind turbine systems and is increasingly used due to its high efficiency, low maintenance cost, low noise, maximum wind power capability in wide wind speed range, and good grid support ability, etc [13-16].

One of the problems associated with some wind turbine systems is the presence of the multi-stage or single-stage gearbox coupling the wind turbine to the generator in the geared wind turbine system. This mechanical element suffers from considerable faults and increased maintenance expenses. To improve reliability of the wind turbine and reduce maintenance expenses, the gearbox can be eliminated by using direct-drive multi-poles generator with high torque at low rated speed [1, 17]. The wind turbine without gearbox is namely the direct-drive system.

The system with the multi-pole PMSG and full power back-to-back (BTB) converter without gearbox becomes the most adopted generator system in the near future due to the reduced losses, reduced noise, high drive stiffness and lower weight [10]. However, the increased price of rare-earth magnets might change the philosophy of wind turbine drive trains to avoid high risk in expenses.

1.2 PMSG Direct-drive System

Generally, there are two types of PMSG direct-drive system. The first is the conventional system; the second is the BTB system.

1.2.1 Conventional PMSG Drive System

The power topology of the conventional PMSG drive system is illustrated in Fig.1.1, which is constructed by a PMSG, a passive diode rectifier, a boost converter and a grid side IGBT inverter [7, 18-24]. The boost converter controls the DC-side voltage or DC-side current according to the maximum power point tracking (MPPT) [18, 19, 25, 26]. The control function of the grid-side inverter is to regulate the DC bus voltage by transferring the power from the DC-link capacitor to the grid.

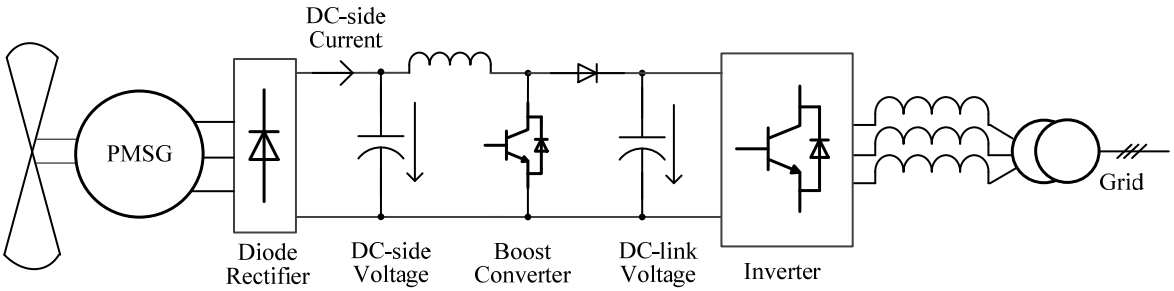

Fig.1.1 Conventional PMSG drive system [20, 21].

The conventional PMSG drive system is widely used in small-scale wind turbine system for its low cost and high reliability. The major disadvantage is that the PMSG current is not controlled by the passive diode rectifier; which results in severe low-order current harmonics. The corresponding large electromagnetic torque ripple may have a detrimental effect on the life of the turbine through fatigue induced by shaft torque ripple [21, 27, 28] and result in noise [29-32]. The problem of wind turbine acoustic noise was addressed in detail in [29, 33, 34], when the wind turbine is sited within residential areas, noise is a primary siting constraint as it causes hearing loss and sleep disturbance [35]. The complaint of wind turbine noise has been reported many times in recent years.

As detailed in [36], the mechanical drive train of wind turbine can be modelled as two masses connected with spring. Therefore, there are resonance frequencies in the system. If the resonance frequencies are in accordance with torque ripple frequencies, severe mechanical vibrations could be induced by even 1.5~2% of torque ripple [37]. Any torque harmonic located near a shaft's natural frequency will create an oscillation with significant magnitude,

potentially leading to accelerated fatigue or severe damage of the system, unless the oscillation is sufficiently damped [27].

Since the reduction of torque ripple can significantly reduce the vibration and acoustic noise [38, 39], it is very important to suppress the torque ripple in the PMSG wind turbine system. It is detailed in [40, 41] that the current harmonics due to the passive diode rectifier can be minimized by making the boost converter work in discontinuous mode, and then the torque ripple can be significantly reduced. However, the current stress of the boost converter switch in discontinuous mode is much higher than that in continuous mode; which makes the conventional PMSG drive system impractical as the system power level increases.

The conventional PMSG drive system without the DC-side capacitor was investigated in [7, 20, 21]. It is detailed in [21] that the torque ripple can be reduced by removing the DC-side capacitor, and it can be further reduced by controlling the DC-side current compared with controlling the DC-side voltage. However, abundant low-order current harmonics and torque ripple are still inevitable.

1.2.2 Back-to-back PMSG Drive System

Since 2000, more and more advanced BTB power converters were introduced to regulate the power from the wind turbines [3, 11, 42, 43]. At first, it was employed mostly in the partial-scale power capacity for the DFIG [6, 44, 45], then in the full-scale power capacity for the asynchronous/synchronous generator [10, 11, 46-50]. By introducing the BTB in the wind turbine system, the extracted power from the wind turbines can be fully controlled. Meanwhile, it enables the whole wind turbine system to act like a completely controllable generation unit which can better integrate the wind power into the grid [4, 10, 12, 51, 52].

The BTB PMSG drive system can be illustrated in Fig.1.2, where a controlled IGBT rectifier is employed for PMSG drive [42] instead of the passive diode bridge rectifier in Fig.1.1. By using the controlled rectifier, the currents of PMSG can be controlled independently by the vector control techniques, and therefore, electromagnetic torque ripple can be minimized and the mechanical stress can be correspondingly reduced [42].

The DC bus voltage can be maintained to a fixed value. Alternatively, it can be regulated to an adaptive value for reduction of losses in the wind turbine converter and higher reliability [53, 54]. There are generally two kinds of control strategies for the wind turbine system according to which side is in charge of controlling the DC bus voltage.

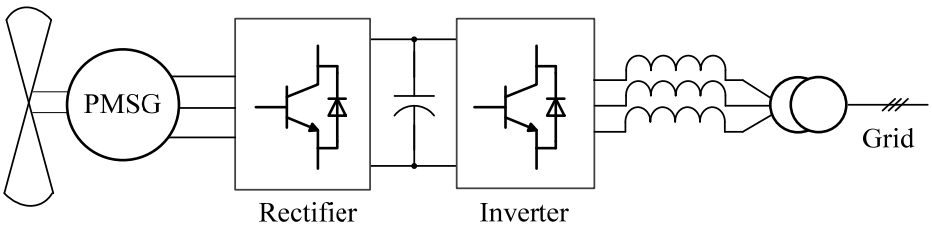

Fig.1.2 BTB system.

In the first control strategy, the speed control plus current/power control are applied to the generator side, while the speed reference is from the MPPT [42]. The generator works in generation mode and transfers the power from the wind turbine to the DC bus. The DC bus voltage control is applied to the grid side, which tries to regulate the DC bus voltage so that it can follow the DC bus voltage reference by transferring the power from the DC bus to grid side so as to avoid the accumulation of power on the DC bus capacitor.

In the second control strategy, the DC bus voltage control is employed in generator side, the power/current control is employed in grid side, while how much power should be extracted from the wind turbine is from an offline lookup table according to the wind speed [55]. The advantage of this control strategy is that it can regulate the DC bus voltage during a supply dip, which could provide better grid support compared with the first control strategy.

1.3 Conventional Vector Control

Nowadays, numerous control strategies such as direct torque control (DTC) [56], model predictive control [57-59] and vector control [42, 60-63] have been developed for 3-phase drive system. The DTC has the advantages of low machine parameter dependence and fast dynamic torque response. However, the drawback of the DTC is represented by the torque and flux ripples [64]. In order to obtain equivalent dynamic torque response as DTC, a preferred alternative is the model predictive control. The main objective of the model predictive control is to control instantaneous stator currents with high accuracy in a transient interval that is as short as possible [65]. It can provide high dynamic performance and low current harmonic to ensure the quality of the torque and speed controls [66]. However, its applicability is hindered due to parameters sensitivity and high cost in computation. The vector control [42, 60-63] control is for its simplicity and low torque ripple. It controls the torque related *q*-axis current and air gap flux-linkage related *d*-axis current in *dq*-frame individually. The torque ripples can be reduced by controlling the stator currents [67]. Consequently, the vector control is widely adopted in industrial applications.

The typical PMSG drive system can be illustrated in Fig.1.3, which is mainly constructed by the controller and power driver. The controller acquires the necessary information such as the current, speed, and rotor position, etc., and then the stator voltage that should be applied to the machine can be obtained according to the control object. The controller outputs corresponding PWM signals to the power system and then the power system converts the PWM signal to PWM output voltages, which are equivalent to the stator voltage that should be applied to the machine.

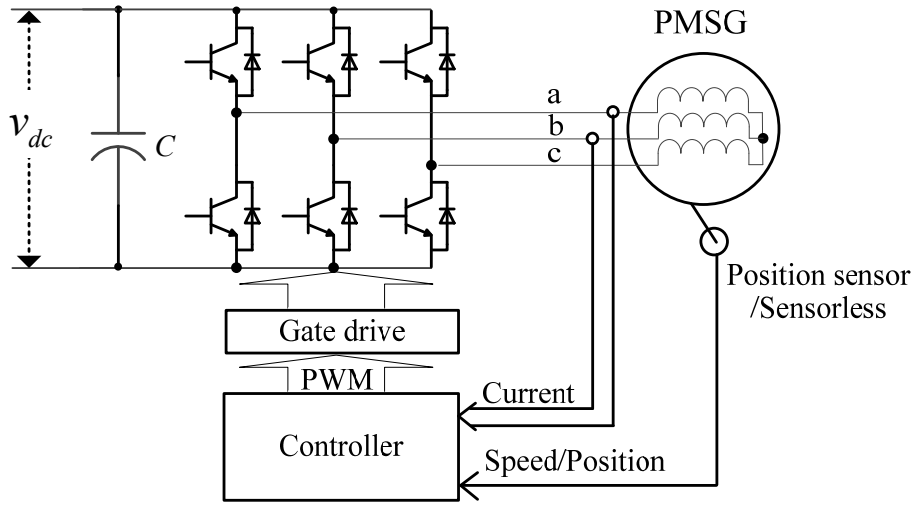

Fig.1.3 Typical PMSG drive system.

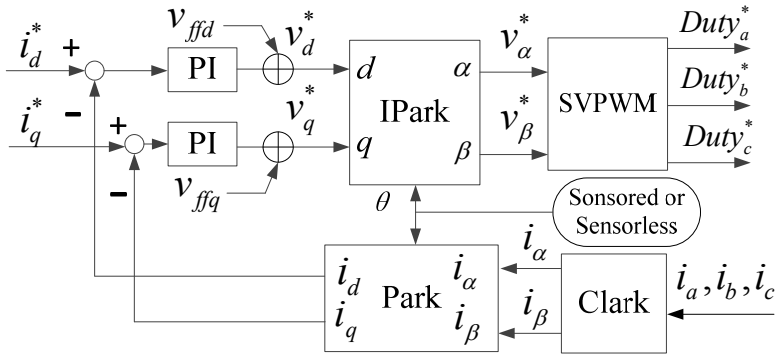

Fig.1.4 Vector control of 3-phase system.

The flowchart of conventional vector control is shown in Fig.1.4. The PI controllers in *dq*-frame can be expressed as

$$\begin{bmatrix} v_d^* \\ v_q^* \end{bmatrix} = \begin{bmatrix} K_p + \dfrac{K_i}{s} & \\ & K_p + \dfrac{K_i}{s} \end{bmatrix} \begin{bmatrix} \Delta i_d \\ \Delta i_q \end{bmatrix} \tag{1.1}$$

where

$$\begin{bmatrix} \Delta i_d \\ \Delta i_q \end{bmatrix} = \begin{bmatrix} i_d^* - i_d \\ i_q^* - i_q \end{bmatrix} \tag{1.2}$$

Assuming that the induced 3-phase back-EMFs are sinusoidal and balanced, eddy current and hysteresis losses, mutual leakage inductance, and saturation are neglected, the voltage equation for the ideal 3-phase PMSG without asymmetries in *dq*-frame can be expressed as (1.3)-(1.4) respectively [60, 61, 68, 69].

$$\begin{bmatrix} v_d \\ v_q \end{bmatrix} = \begin{bmatrix} \left(R_s + sL_d\right) i_d \\ \left(R_s + sL_q\right) i_q \end{bmatrix} + \begin{bmatrix} v_{ffd\_d} \\ v_{ffd\_q} \end{bmatrix} \tag{1.3}$$

where

$$\begin{bmatrix} v_{ffd\_d} \\ v_{ffd\_q} \end{bmatrix} = \omega_e \begin{bmatrix} -L_q i_q \\ L_d i_d \end{bmatrix} + \begin{bmatrix} e_d \\ e_q \end{bmatrix} = \omega_e \begin{bmatrix} -L_q i_q \\ L_d i_d \end{bmatrix} + \omega_e \begin{bmatrix} 0 \\ \psi_f \end{bmatrix} \tag{1.4}$$

where s is differential operator, R_s is the stator winding resistance. L_d and L_q are the *dq*-axis inductances respectively. ψ_f is PM flux. The ω_e is the electrical angular speed. i_d, v_d, i_q, v_q, e_d and e_q are the *dq*-axis currents, voltages and back-EMFs respectively. v_{ffd_d} and v_{ffd_q} are decoupling voltages in *dq*-frame.

The electromagnetic torque can be expressed as

$$T_e = \frac{3}{2} p\left(\psi_d i_q - \psi_q i_d\right) = \frac{3}{2} p\left(\psi_f i_q + \left(L_d - L_q\right) i_d i_q\right) \tag{1.5}$$

where p is the number of pole-pairs. The equivalent circuits for (1.3)-(1.4) can be illustrated in Fig.1.5. It can be seen from Fig.1.5 that the equivalent circuits in *dq*-frame are decomposed completely, which are similar to the equivalent circuit of DC machine. Therefore, the PMSG can be controlled like a separately excited DC machine and has the equivalent fast transient response while does not have the drawbacks of mechanical commutation in the DC machine [69].

Therefore, the conventional current control with cross-coupling feed-forward control for PMSG can be illustrated in Fig.1.6. The output of PI controllers can be expressed as

$$v_d^* = \left(K_p + \frac{K_i}{s}\right)\left(i_d^* - i_d\right) + e_d - \omega_e L_q i_q \tag{1.6}$$

$$v_q^* = \left(K_p + \frac{K_i}{s}\right)\left(i_q^* - i_q\right) + e_q + \omega_e L_d i_d \tag{1.7}$$

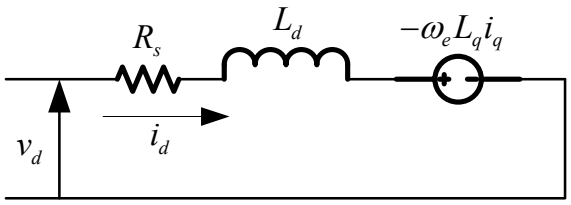

(a)

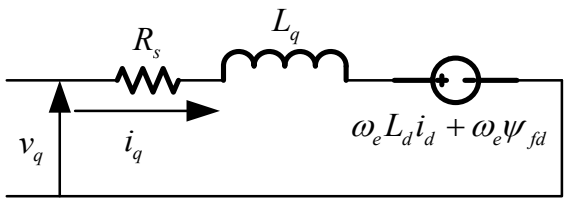

(b)

Fig.1.5 Equivalent circuits of 3-phase PMSG in *dq*-frame. (a) *d*-axis equivalent circuit. (b) *q*-axis equivalent circuit.

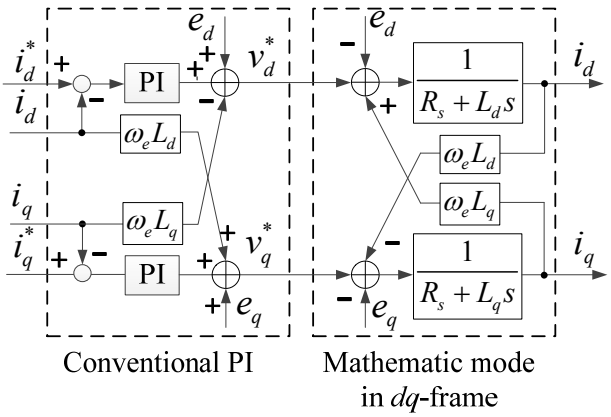

Fig.1.6 Conventional current control in *dq*-frame with cross-coupling feed-forward control.

When voltage (1.6) and (1.7) are applied to the PMSG, according to the voltage equations in (1.3), the current responses can be expressed as

$$\left(K_p + \frac{K_i}{s}\right)\left(i_d^* - i_d\right) = \left(R_s + sL_d\right) i_d \tag{1.8}$$

$$\left(K_p + \frac{K_i}{s}\right)\left(i_q^* - i_q\right) = \left(R_s + sL_q\right) i_q \tag{1.9}$$

As can be seen from (1.8) and (1.9), after the cross-coupling feed-forward compensation, the mathematical model in *dq*-frame can be simplified as a resistance and inductance (*RL*) load [63]. Considering the time delay in the current control loop, the current control in *dq*-frame can be illustrated in Fig.1.7, where T_d is the total delay time in the close loop, including

current sampling delay, PWM voltage output delay, etc. L is L_d in i_d current controller and it is L_q in i_q current controller.

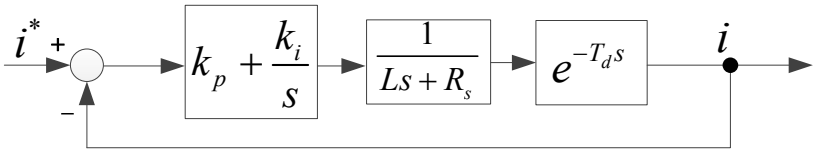

Fig.1.7 Current control after cross-coupling feed-forward compensation.

To simplify the design of PI gains, the delay function $e^{-T_d s}$ is usually simplified as a low-pass filter [70], which can be expressed as $1/(1+sT_d)$. If the dominant pole of $-R/L$ is canceled by the zero point of PI controller, the open loop of whole system can be simplified as typical first order system in control theory [70]; then K_p and K_i equation can be optimally designed as

$$K_p = \frac{L}{4\xi^2 T_d} \tag{1.10}$$

$$K_i = \frac{R_s}{4\xi^2 T_d} \tag{1.11}$$

where ξ is damping factor. The ξ is equal to 0.707 for optimized design in the typical first order system, which can achieve good rising time and overshot simultaneously. However, if the inductance and resistance vary with temperature, the dominant pole and zero in the close current control loop are not well matched; therefore, the dynamic performance will be affected. In some cases, the K_p and K_i gains need to be reduced to guarantee the system stability in the whole working range. Or alternatively, if the inductances and resistances can be identified from online tuning, the K_p and K_i gains can be always optimized according to (1.10) and (1.11).

The current control structure can be illustrated in Fig.1.8. Since the gains of PI controller are chosen to cancel the dominant pole related to inductance and resistance, the dynamic performance is only related to the total time delay.

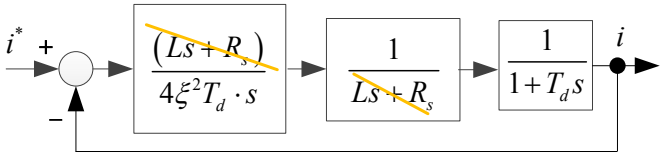

Fig.1.8 Current control with major pole point cancellation.

The close loop transfer function can be expressed as

$$\frac{i(s)}{i^*(s)} = \frac{1}{4T_d^2\xi^2 s^2 + 4T_d\xi^2 s + 1} \tag{1.12}$$

Usually, the coefficient of the s^2 term is much smaller than the coefficient of s term. Therefore, (1.12) can be rewritten as (1.13), which is a typical low-pass filter.

$$\frac{i(s)}{i^*(s)} = \frac{1}{4T_d^2\xi^2 s^2 + 4T_d\xi^2 s + 1} \approx \frac{1}{4T_d\xi^2 s + 1} \tag{1.13}$$

As the cut-off frequency of the low-pass filter in (1.13) is related with T_d, the bandwidth of PI controller is directly related with T_d. When T_d is smaller, the bandwidth is higher, vice versa, when T_d is larger, the bandwidth is lower [70]. As presented in [32], the bandwidth can expanded by using double current sampling and PWM duty cycle double update to reduce the time delay T_d.

It is worth noting that, the cross coupling feed-forward voltages in (1.4) are not always accurate due to the parameters variation in practice, which may be resulted from temperature variation, saturation, etc. In this case, the mismatched crossing-coupling compensation voltages will be compensated by the PI controllers. This increases the burden of PI controllers. Therefore, the cross coupling feed-forward voltage compensation should be as accurate as possible.

1.4 Asymmetric PMSG

In practice, the perfectly symmetrical machine is impossible. Generally, the asymmetries of PMSG include the unbalanced resistances, unbalanced inductances and unbalanced 3-phase back-EMFs, which may be resulted from the poor connections [71-74], winding asymmetries [75-81], rotor eccentricities [82], manufacturing tolerances, or faulty conditions [83, 84], etc.

The stator resistances may be unbalanced due to the poor connection resulted from the combination of poor workmanship, thermal cycling, vibration, or damage of the contact surfaces due to pitting, corrosion, or contamination [72-74]. In [74], an online detection of the high-resistance of the induction machine was developed based on monitoring the asymmetry in the voltage and current measurements. In [85], the analytical model of 3-phase induction machine with unbalanced 3-phase resistances was developed in terms of voltage and current space vectors. In [72], the detection of stator resistance asymmetry in multi-phase induction machine was investigated, it showed that the *P*-sequence and *N*-sequence current components appeared in the harmonic sub-planes, which are normally absent in balanced operating conditions. In [86], the current control for six-phase induction machine was investigated in

the scenarios with introduced asymmetries by connecting extra resistor in series with phase windings. In all these researches, the stator resistances were assumed not equal to each other and the unbalanced resistances were modelled as extra resistance connected in series with the original balanced system [72, 74, 85].

The unbalanced inductances may be resulted from the winding asymmetries. In [75], the winding asymmetries in small synchronous generators was studied, it was found that the synchronous machines are slightly asymmetric with unbalanced slot leakage inductances and unbalanced 3-phase back-EMFs due to the winding asymmetries. An extreme example of the winding asymmetries is the linear machine, e.g. as presented in [78], the average self-inductances are unbalanced in the PM linear synchronous machine. Another example of the winding asymmetries is the multi-unit 3-phase machine in the event of fault. When all units work normally, there is no difference between the multi-unit machine and the single 3-phase machine with all units in parallel. However, in this case of failure of one unit, only the healthy units are supplied, the remaining healthy windings may work under unbalanced conditions. In [79], various winding configurations of the dual 3-phase 12-slot, 10-pole (12s/10p) PM machine were investigated. In the first winding topology of double-layer windings and single-layer windings in [79], the remaining phase windings are asymmetric after removing one set of the dual 3-phase windings, which will result in unbalanced magnetic flux paths, unbalanced radial force and unbalanced inductances. Although doubling the slots and poles (24s/20p) can reduce unbalanced radial force [80], however, the magnetic flux paths are still unbalanced, which will result in unbalanced inductances. In [76] and [81], the average mutual inductances in the same unit of the multi-unit 3-phase machine are unbalanced, and the 2h mutual inductances may be different as well with different winding connections. As also shown in Fig.C.1(a), the measured mutual-inductances of the prototype PMSG employed in the thesis are unbalanced.

In [82], the back-EMFs of the PM brushless machine due to eccentricity was investigated. It shows that the eccentricity does not affect the back-EMFs and electromagnetic torque of rotational symmetrical machines whose configuration repeats every certain amount of angle, but the back-EMFs waveforms of rotational asymmetric machines are distorted significantly. Further, the static eccentricity does not change the harmonic contents of back-EMFs, but results in unbalanced 3-phase back-EMFs.

1.5 Influence of Asymmetries

The performance of the PMSG drive system may be affected by the potential asymmetries. When the 3-phase system is asymmetric, the unbalanced phase currents are produced [87-90] under conventional current control due to the limited bandwidth of the PI controller. Based on the symmetrical-component theory [91], the unbalanced currents in 3-phase system can be decomposed as positive-(*P*-) and negative-(*N*-)sequence currents. The *N*-sequence currents will interact with the back-EMFs and result in the torque ripple at the twice fundamental frequency and 2h power which will flow towards DC bus capacitors.

In the wind turbine system, the speed of generator depends on the aerodynamic torque T_w and the electromagnetic torque T_e. The aerodynamic torque oscillations are resulted from random wind fluctuation, tower shadow or wind shear [92]. On the other hand, electromagnetic torque ripple is mainly resulted from the generator-side harmonic current. Both these torque ripples are a source of mechanical stress on the drive train and may have a detrimental effect on turbine lifetime.

The aerodynamic torque T_w ripple caused by wind fluctuation and shear is hard to be avoided because of environmental factors. However, the electromagnetic torque T_e ripple can be suppressed since it is related to generator current and therefore can be controlled. If there are *N*-sequence currents in the stator currents, the *N*-sequence currents will interact with the back-EMFs and the 2h torque component will be produced. As mentioned in [37], severe vibrations, corresponding acoustic noise, and fatigue could happen due to mechanical resonance[27, 28], which is not allowed in the wind turbine system.

The undesired 2h power flowing through the DC bus capacitors will result in the 2h current and 2h DC bus voltage. Since the equivalent series resistance of capacitors increases at low frequencies, the low-order current harmonics contribute disproportionately to the capacitor power losses and temperature rise, resulting in reduced lifetime [93, 94]. Nowadays, the DC bus capacitors are very fragile components in the power system [88, 93, 95], especially the cost reduction pressure from global competition indicates minimum design margin of capacitors, which increases the risk of failure of DC bus capacitors. Meanwhile, as the inverter of grid side in Fig.1.2 is trying to maintain the DC bus voltage, the undesired 2h power will be transferred to the grid side and results in higher current THD of grid side.

1.6 Control of Asymmetric PMSG

1.6.1 Balanced Current Control

To suppress the 2h torque due to the *N*-sequence currents, the effective way is to suppress the *N*-sequence currents if the 3-phase back-EMFs are balanced. In the unbalanced 3-phase system, the balanced current control, which tries to suppress the *N*-sequence currents in the 3-phase currents, is intensively investigated. Generally, there are three typical current control methods which are applicable for supressing the *N*-sequence currents. The first is the proportional and resonant (PR) control in *αβ*-frame, the second is the dual current control, and the third is the proportional and integral plus resonant (PI-R) control in *P*-sequence reference frame (PSRF).

1.6.1.1 PR Control in *αβ*-frame

In general, the conventional PI regulators in *αβ*-frame are regarded as unsatisfactory for ac current regulation since the conventional PI regulator in this reference frame suffers from significant steady-state amplitude and phase errors. In [96, 97], the PR control in *αβ*-frame was proposed to trace the fundamental currents without tracing error due to the infinite selection characteristic at the centre frequency in the resonant control. The PR control has been widely employed in the industry applications. For example, the resonant control was employed to compensate selected current harmonics in active power filter system in [98, 99]. The resonant control at the centre frequency of fundamental was employed to regulate the *P*-sequence and *N*-sequence currents in the grid application under generalized unbalanced operation conditions in [100, 101].

Since the PR control can trace the fundamental currents without tracing error in *αβ*-frame, if the current references in *αβ*-frame are fundamental, sinusoidal and have the same amplitude but 90° displacement, which means the reference currents are balanced, then the phase currents will be balanced. Compared with the conventional current control in synchronous *dq*-frame which could not achieve balanced currents in asymmetric system, this method can achieve balanced currents without requiring Park and inverse Park transformations [97], and it also does not require decomposing the sequential current components.

1.6.1.2 Dual Current Control

Since the *P*-sequence currents in PSRF and the *N*-sequence currents in *N*-sequence reference frame (NSRF) are DC components, if the DC components in NSRF can be

suppressed successfully, then the *N*-sequence currents can be suppressed and the balanced currents can be achieved.

The dual current control was proposed in [102] for grid application with unbalanced supply voltages, where two PI controllers in PSRF and NSRF were employed to regulate the *P*-sequence currents in PSRF and *N*-sequence currents in NSRF respectively. The notch filters were employed to extract *P*- and *N*-sequence currents as current feedback in the current controllers [102]. The dual current control was applied to PM synchronous machine with asymmetric phases in [87], where the sequence separation delaying method [103] was employed to extract *P*- and *N*-sequence currents. In [84], the dual current control was applied in the surface-mounted PM synchronous machine with internal turn short fault to suppress the *N*-sequence currents so as to suppress the torque ripple, where the notch filters were employed in each synchronous frame (PSRF and NSRF) to extract *P*- or *N*-sequence components.

In the applications in [84, 87, 102], the dynamic performance may be compromised due to the use of the notch filter or delaying method. In [104, 105], the dual current control without notch filter was investigated for general unbalanced electrical systems, which can regulate the *P*-sequence and *N*-sequence current effectively. As there are DC and 2h currents in the current feedback in each frame, there are tracing errors in each set of the dual PI controllers. In [106], the dual current control with two PI plus resonant control (PI-R) in PSRF and NSRF respectively without notch filter was employed in grid applications. Although this method is also effective in terms of regulating the *P*-sequence and *N*-sequence currents, the dual current control of PI-R control is actually redundant. In fact, only the PI-R control in PSRF or NSRF will be sufficient in term of regulating the *P*-sequence and *N*-sequence currents.

It is generally assumed that the cross coupling can be applied to decouple the cross coupling between *d*-axis and *q*-axis in *dq*-frame in the conventional current control. However, as detailed in [107] where the cross-coupling decoupling in the dual current control was evaluated, it is found that this technique does not produce noticeable improvement in the dual current control.

Although the dual current control can be employed to suppress the *N*-sequence currents and achieve balanced 3-phase currents, it requires twice of the current controllers as that in conventional current control, which is the major disadvantage.

1.6.1.3 PI-R Control in PSRF

When the unbalanced currents in *abc*-frame are mapped to synchronous *dq*-frame, the *N*-sequence currents will be converted to 2h components in the *dq*-frame. If the 2h components in *dq*-frame are suppressed, then the *N*-sequence currents can be suppressed.

In [108-110], the PI-R control with the resonant controller at the centre frequency of twice fundamental frequency in PSRF, was employed to suppress the 2h components in *dq*-frame so as to suppress the *N*-sequence currents. In [109], the currents in both DFIG and grid side are controlled in PSRF without decomposing sequential currents in the DFIG system with unbalanced network. In [108], the same control strategy was employed in a stand-alone DFIG system with unbalanced and nonlinear loads. In [111], the PI-R control in *dq*-frame in dual 3-phase PMSM system was employed to eliminate the current unbalance between two sets and between phases in each set.

This method has only one set of current controllers in PSRF, which is different from the dual current control with two sets of current controllers in PSRF and NSRF respectively.

1.6.2 Second Harmonic Power Suppression

When the currents are unbalanced in the asymmetric 3-phase system, the 2h power can be produced [112], which flows through the DC bus capacitors and results in the 2h DC bus voltage [113, 114]. Therefore, to suppress the 2h DC bus voltage, the 2h power flowing through the DC bus capacitors should be suppressed.

1.6.2.1 Instantaneous Power Control

Since the 2h DC bus voltage is related to the 2h power flowing through the DC bus capacitors [115, 116] and the 2h power is from the asymmetric PMSG, the effective way to suppress the 2h DC bus voltage is to suppress the 2h power from the PMSG, which can be achieved by the instantaneous power control [100, 102, 114, 117, 118]. The instantaneous power control has been widely employed in a weak grid-connected PWM rectifier system [100, 102, 114, 117, 118], where the grid voltages are unbalanced. By injecting the *N*-sequence currents into the system in the instantaneous power control, the 2h power generated by the *P*-sequence currents and *N*-sequence voltages can be compensated by the 2h power generated by the *N*-sequence currents and *P*-sequence voltages.

To illustrate the instantaneous power control principle, the block diagram of BTB system is shown in Fig.1.9, where the definition of current direction is based on motor mode rather than

generate mode. It is worth noting that the powers p_{in} and p_{out} are negative when the PMSG is in generation mode. In Fig.1.9, e_a, e_b, and e_c denote back EMFs. The power generated by e_a, e_b, and e_c is designated as p_{in}, the power of the resistor and inductor are P_R and P_L respectively, the output power from the inverter is designated as p_{out}, which is the sum of p_{in}, P_R and P_L.

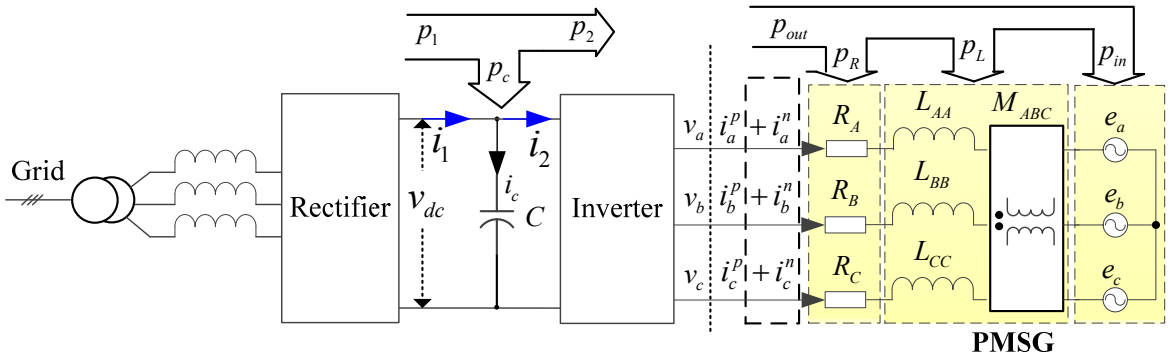

Fig.1.9 Illustration of power flow in BTB system.

Generally, there are three kinds of instantaneous power control. The first is the instantaneous input power control [102, 117, 119], the second is the input-output-power control [100, 118], and the third is the output power control [114].

The first method is the instantaneous input power control [117], where the negative (*N*-) sequence currents were introduced aiming for no 2h power in the input active power p_{in} and zero average input reactive power. The average input power, zero 2h power in p_{in} and zero average reactive power from e_a, e_b, and e_c were employed as constraints to calculate the *P*- and *N*-sequence current references. However, the *dq*-axis currents were regulated by proportional-integral **(**PI) controllers in *dq*-frame [117], which would cause tracing errors due to the limited bandwidth of the PI controllers. To solve this problem, the dual current control scheme was proposed in [102], where the *P*- and *N*-sequence currents were regulated in the positive synchronous reference frame (PSRF) and negative synchronous frame (NSRF) respectively. By using a notch filter in each synchronous reference frame (SRF), the *P*- and *N*-sequence currents could be extracted so that they can be regulated. However, this method neglects the pulsating power in the impedances (P_R+P_L). Actually, the DC bus voltage essentially depends on the instantaneous output power p_{out} rather than the input power p_{in}. The power in the impedances fluctuates when the impedances or currents are unbalanced. Therefore, p_{out} fluctuates even when p_{in} is constant, and then it will still result in DC bus voltage ripple. In [119], the PR control in $\alpha\beta$-frame was employed to regulate the *P*-sequence and *N*-sequence currents without the sequential current components. However, to obtain the

current reference, the sequential components decomposer for supply voltage was necessary. Meanwhile, as the input power control cannot eliminate the 2h DC bus voltage, the DC bus voltage PI-R control with resonant control at the center frequency of twice fundament was employed, which resulted in third phase current harmonics.

The second method is the input-output-power control [100, 118]. Since the 2h DC bus voltage depends on the 2h power in p_{out} rather than p_{in}, the average input active power p_{in}, 2h power in p_{out} and zero input reactive power from e_a, e_b, and e_c were employed as constraints to calculate the *P*- and *N*-sequence current references. Since the 2h power in p_{out} is considered, this method is capable of suppressing the 2h power even under generalized unbalanced operation conditions. Therefore, there is no 2h DC bus voltage ripple. To avoid tracing errors in the current regulators [117] and to avoid notch filters to extract *P*- and *N*-sequence currents [102] which may reduce overall bandwidth of the current regulators, the resonant control was employed in [100, 101, 109, 118]. For example, the dual current regulators with PI-R control in the PSRF and NSRF respectively were employed in [118], the PR control in $\alpha\beta$-frame was employed in [100, 101], and the PI-R control in PSRF was employed in [109]. However, to calculate the current references, the sequential component decomposers were still required to extract *P*- and *N*-sequence supply voltages and output voltages, e.g. the notch filter was employed in [100, 109, 118] and the dual second-order generalized integrator(DSOGI) method [120] was employed in [101].

The third method is the output power control [114], where the average power in p_{out}, the 2h power in p_{out} and zero average output reactive power were employed as constraints to calculate the *P*- and *N*-sequence current references. Similar to the second method, this method is also robust to the generalized asymmetries due to the consideration of the 2h power in p_{out}. Furthermore, it does not need extract the *P*- and *N*-sequence components of e_a, e_b and e_c in Fig.1.9. However, the sequential output voltages are still essential for the calculation of the *P*- and *N*-sequence current references. To avoid the extraction of the sequential output voltages, the sum of supply voltages and inductor voltages were used to estimate the sequential output voltages in [114, 121, 122], which means the impedance asymmetries were not considered and the sequential component decomposers for the currents and supply voltage were inevitable in [114]. More specifically, the sequence separation delaying method [103] was employed to extract *P*- and *N*-sequence supply voltages and the notch filter method [102] was employed to extract *P*- and *N*-sequence currents in [114].

From the aforementioned introduction, the second and third methods can essentially deal with the 2h DC bus voltage regardless of the asymmetries including the unbalanced impedances. However, some sequential component decomposers were required in the previous works. The comparison of various methods can be summarized in TABLE 1.1.

1.6.2.2 Power Feed-forward Control

To suppress the undesired 2h power flowing through the DC bus capacitors in the asymmetric PMSG drive system, the undesired 2h power from the asymmetric PMSG can be transferred to grid network by the instantaneous power feed forward control [123-125]. As shown in Fig.1.9, if all the power from p_2 including the 2h power are transferred to the grid side, i.e. the 2h power in p_2 is compensated by the 2h power in p_1, there will be no 2h power flowing through the DC bus capacitors. Therefore, the 2h DC bus voltage can be suppressed.

Although this approach can suppress the 2h DC bus voltage, the current of gird side will be distorted because the undesired 2h power is transferred to the grid side and results in some undesired grid current harmonics. Therefore, the THD of the grid currents will be increased. As the grid penetration and power level of the wind turbines increase steadily, the wind power starts to have significant impacts to the power grid system [3]. Therefore, the quality of power generated by the PMSG is crucial [126]. The limits on the amount of harmonic currents and voltages have been established in the IEEE standards 519 [127], IEEE standards 1547 [128], and in the IEC-61000-3 standard [129]. For example, the total harmonic current distortion should be less than 5% [128]. Therefore, this approach may not meet the required power quality and should be avoided.

1.6.2.3 Power Compensation

To avoid the undesired 2h power flowing towards the grid side and DC bus capacitors, the fluctuated power in the DC bus can be diverted to an energy storage device shown in Fig.1.10 [3, 130-132]. The energy storage device is connected in parallel with the DC bus. In [132], the inverter in the grid side and the DC/DC converter with energy storage device connected collaborated to regulate the DC bus voltage considering the pulsating power from incident wind. The current reference from the DC bus voltage PI controller was distributed between the grid side and the energy storage system so that the power generated by the PMSG was distributed between them. The high frequency power from PMSG was diverted to the energy storage system, while the low frequency power from PMSG was transferred to the grid side.

Therefore, the high frequency power flowing through the DC bus capacitors can be suppressed.

TABLE 1.1
EVALUATION OF DIFFERENT POWER CONTROL

Methods	Input power control [102, 117]	Input power control [119]	Input-output-power control [100, 101, 109, 118]	Output power control method [114]
Power condition equations	$\begin{cases} p_{in0} = p^* \\ p_{in\_c2} = 0 \\ p_{in\_s2} = 0 \\ q_{in0} = 0 \end{cases}$	$\begin{cases} p_{in0} = p^* \\ p_{in\_c2} = 0 \\ p_{in\_s2} = 0 \\ q_{in0} = 0 \end{cases}$	$\begin{cases} p_{in0} = p^* \\ p_{out\_c2} = 0 \\ p_{out\_s2} = 0 \\ q_{in0} = 0 \end{cases}$	$\begin{cases} p_{out0} = p^* \\ p_{out\_c2} = 0 \\ p_{out\_s2} = 0 \\ q_{in0} = 0 \end{cases}$
DC bus control	PI	PI-R($2\omega_e$)	PI	PI
Current control	[117]:PI control in PSRF [102]:Dual current control in PSRF and NSRF	PR(ω_e) control in $\alpha\beta$-frame	[118]:Dual current PI-R control in PSRF and NSRF [100, 101]: PR control in $\alpha\beta$-frame [109]: PI-R control in PSRF	Dual current control in PSRF and NSRF
Unit input power factor	✓	✓	✓	×
Unity output power factor	×	×	×	✓
2nd harmonic DC voltage	High	Low	Low	Low
3rd current harmonics	High	High	Low	Low
Current reference calculation in dq-frame/ $\alpha\beta$-frame	dq-frame	dq-frame	[100, 109, 118]: dq-frame [101]: $\alpha\beta$-frame	dq-frame
Current reference calculation	Simple	Simple	Complicated	Simple
Sequential components decomposer for supply voltage/back-EMFs	Yes/Notch filter	Yes/Notch filter	[100, 109, 118]: Yes/Notch filter [101]: Yes/DSOGI	Yes/Sequence separation delaying method [103]
Sequential components decomposer for currents	Yes/Notch filter	No	No	Yes/Notch filter [102]
Sequential components decomposer for output voltages	No	No	[100, 109, 118]: Yes/Notch filter [101]: Yes/DSOGI	No/Estimation assuming balanced inductances

Note: p_{in_c2}, p_{in_s2}: coefficient of cosine/sine items in the 2h input power. p_{out_c2}, p_{out_s2}: coefficient of cosine/sine items in the 2h input power.
p_{in0}, q_{in0}: average active and reactive input power. p_{out0}, q_{out0}: average active and reactive output power.

This approach did not require the information of generator output power and it can be classified as the post-treatment because it dealt with the fluctuated power that was there already. However, some software modification was required to distribute the power. According to this approach's compensation principle, it can also be employed to suppress the 2h DC bus voltage in theory when the PMSG is asymmetric. However, to suppress the high frequency DC bus pulsation effectively, the bandwidth of DC bus voltage PI control has to be very high, which may result in potential instability.

In [133], a compensation device in parallel with the DC bus was employed to compensate the 2h power due to the grid supply voltage asymmetries in the solar power system, which can illustrated in Fig.1.11. This approach requires the 2h power information from the unbalanced 3-phase system, and then the 2h power is compensated by the devices of energy conversion and energy storage. This compensation principle can be employed to suppress the 2h power due to the asymmetries of the PMSG. By this method, the 2h power flowing through the DC bus capacitors can be suppressed without involvement of the control of grid side in the wind turbine system. However, the 2h power pulsation due to the asymmetric impedances in [133] was not considered, which means it essentially cannot eliminate the 2h power in the DC bus.

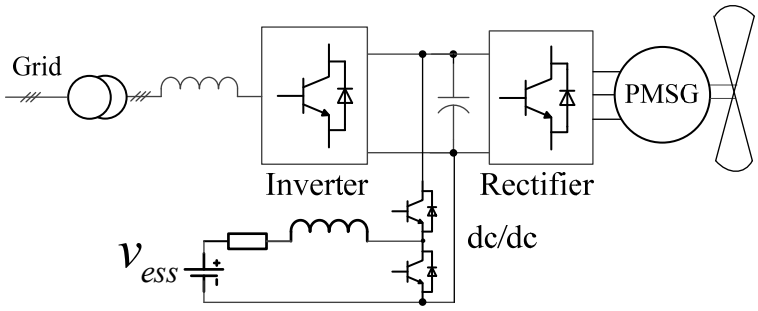

Fig.1.10 Coordinated DC bus voltage control [132].

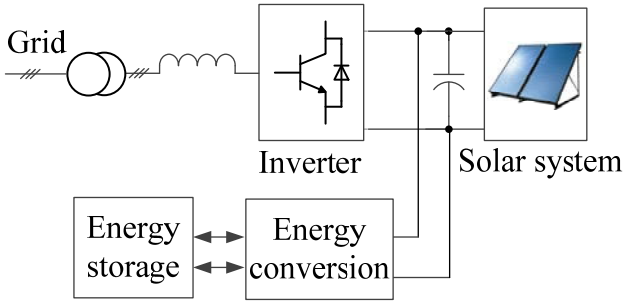

Fig.1.11 Second harmonic power compensation [133].

1.6.3 Summary

According to the aforementioned introduction, to suppress the 2h torque of PMSG with asymmetric impedances, the *N*-sequence currents should be suppressed. However, with only the *P*-sequence currents injection, the undesired 2h power due to the asymmetries will be produced and then results in 2h DC bus voltage. As shown in Fig.1.12, the undesired 2h power can flow through DC bus capacitors, or be transferred to the grid side by power feed forward control, or be diverted to the compensation unit in parallel with the DC bus, or be compensated by the PMSG itself with *N*-sequence currents injection in the instantaneous power control.

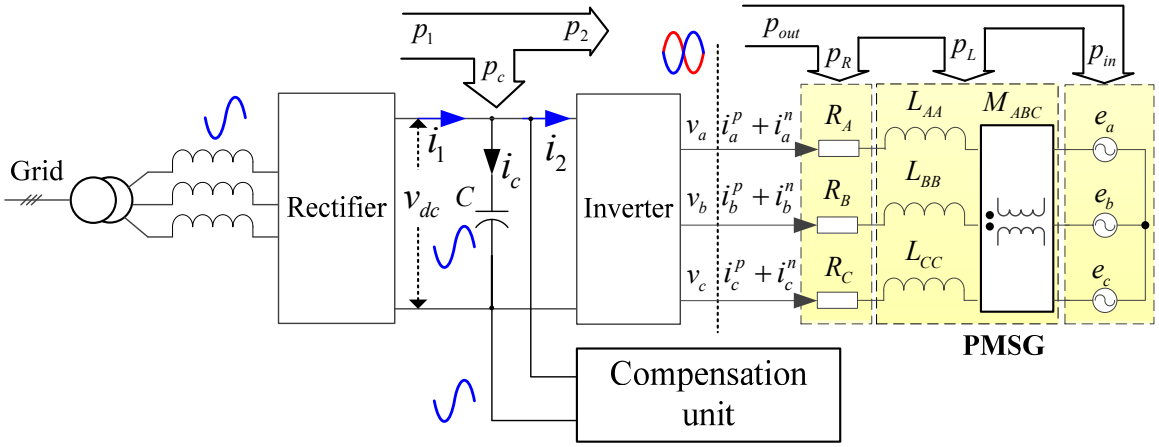

Fig.1.12 Illustration of power flow in BTB system.

TABLE 1.2

SUMMARY OF CONTROL OF ASYMMETRIC PMSG DRIVE SYSTEM

Methods	Balanced current control	Power control	Power feed forward	Compensation in parallel
N-sequence currents	N	Y	N	N
2h power by PMSG	Y	N	Y	Y
2h power to DC bus capacitor	Y	N	N	N
2h DC bus voltage	Y	N	N	N
2h torque	N	Y	N	N
Increased grid current THD	Y	N	Y	N
Increased cost	N	N	N	Y

The balanced current control can suppress the 2h torque if the back-EMFs are balanced. However, it cannot suppress the 2h power and DC bus voltage. In contrast, the instantaneous

power control can suppress the 2h power and DC bus voltage. However, it cannot solve the problem of 2h torque. Although the power feed-forward control can transfer the undesired 2h power to grid side to avoid the 2h power flowing through the DC bus capacitors, the current THD of grid side will be deteriorated. To suppress the 2h DC bus voltage and 2h torque simultaneously without deterioration of current THD of grid side, the 2h power can be transferred to a compensation unit in parallel with the DC bus. However, extra hardware and software modification is required, which increases the system cost. Overall, all the aforementioned methods can be summarized as TABLE 1.2.

1.7 Scope and Contributions of Research

1.7.1 Scope

This thesis is aiming for suppressing the 2h DC bus voltage and 2h torque when the PMSG has asymmetric impedances. The influence of PMSG asymmetries is described and analysed in Chapter 2. From Chapter 3 to Chapter 6, the research is focused on the single 3-phase asymmetric PMSG, while the research is extended to dual 3-phase PMSG system when one channel fails in Chapter 7. To verify the research, the test rig is based on a dual 3-phase PMSG which has apparent inherent asymmetries in single 3-phase mode while is balanced in dual 3-phase mode. The test rig is shown in Appendix B while the inherent asymmetries are detailed in Appendix C. The whole research structure can be illustrated in Fig.1.13.

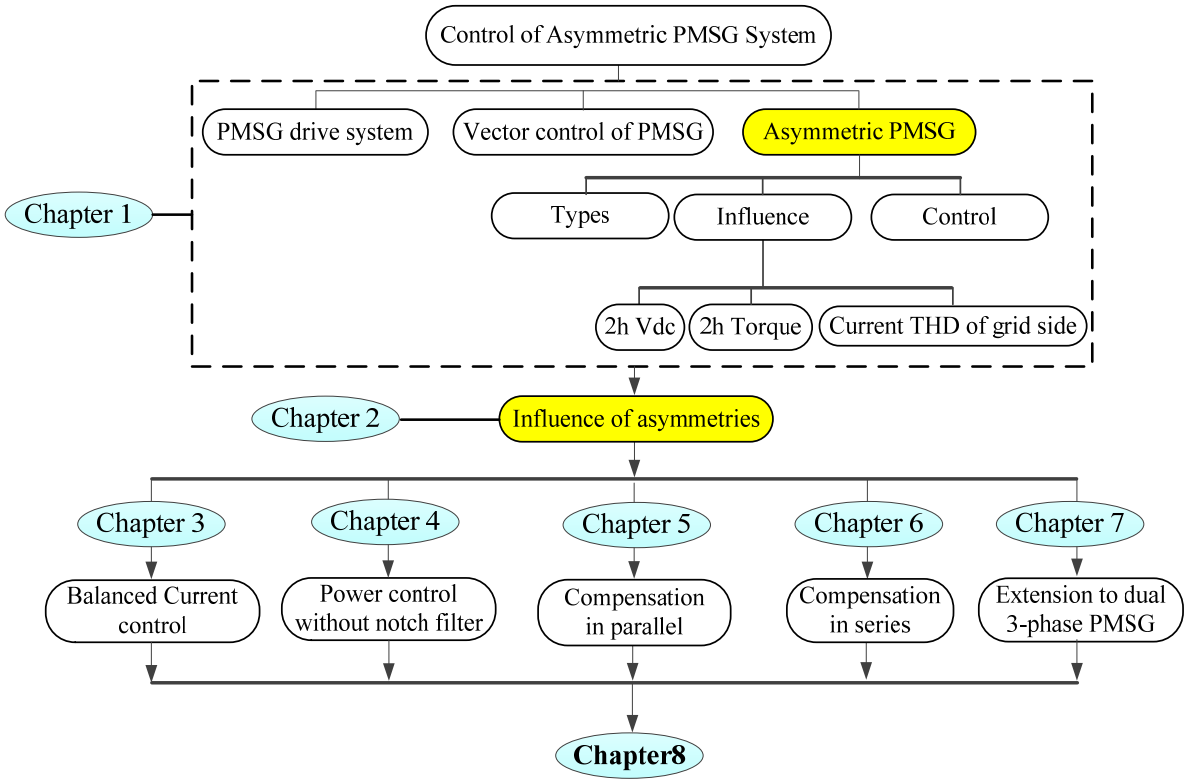

Fig.1.13 Research structure.

The thesis is organized as follows:

Chapter 2 Influence of the PMSG Asymmetries

In this chapter, the power ripple and torque ripple without/with *N*-sequence currents are analysed in detail when the resistances, self-inductances, mutual inductances or 3-phase back-EMFs are unbalanced.

Chapter 3 Current Control of Asymmetric PMSG

This chapter introduces the mathematical modeling of asymmetric PMSG, which considers the unbalanced resistances, unbalanced self-inductances, unbalanced mutual inductances and unbalanced 3-phase back-EMFs. The current control of asymmetric PMSG is reviewed and evaluated. Three typical balanced current control methods, including the PR control in $\alpha\beta$-frame, dual current control in PSRF and NSRF respectively, and PI-R control in PSRF, are investigated and the relationship between these methods will be revealed for the first time. Elaborate experiments of the convention current control and balanced current control of asymmetric PMSG will be conducted and experimental results will be compared in depth.

Chapter 4 Instantaneous Power Control of Asymmetric PMSG (without sequential component decomposers)

This chapter proposes an improved power control of suppressing the 2h DC bus voltage in asymmetric PMSG system under generalized unbalanced conditions. The proposed power control does not require any sequential component decomposers. Usually, the sequential components are essential for the current reference calculation in the power control. How to extract the necessary sequential components and why they can be extracted without sequential component decomposers will be demonstrated. Finally, the effectiveness of the proposed power control is verified on an asymmetric 3-phase PMSG prototype with inherent asymmetry and deliberately introduced asymmetries.

Chapter 5 Control of Asymmetric PMSG with Compensation in Parallel

This chapter proposes an effective method for suppressing the 2h DC bus voltage pulsation accounting for the 2h torque ripple in the PMSG system with asymmetric impedances. A compensation unit with Topology-*RL* in parallel with the DC bus and corresponding control method are introduced to suppress the 2h DC bus voltage. Elaborate experiments will be conducted to verify the effectiveness of the proposed method under generalized unbalanced conditions with asymmetric impedances and at different speeds.

In addition, a compensation unit with Topology-*RLE* in parallel with DC bus is proposed to suppress the 2h DC bus voltage in PMSG system with asymmetric impedances. The corresponding control method will be introduced and the compensation with Topology-*RLE* will be compared with Topology-*RL* in depth. Finally, elaborate experiments will be conducted to verify the effectiveness of the proposed method under generalized unbalanced conditions of asymmetric impedances and at different speeds.

Chapter 6 Control of Asymmetric PMSG with Compensation in Series

In this chapter, how to compensate the unbalanced impedances of the asymmetric PMSG by external circuits in series is investigated. How to determinate the parameters of the compensation unit in series will be introduced when the resistances, self-inductances and even when mutual inductances are unbalanced. After the compensation, the original unbalanced 3-phase system is modified to a balanced 3-phase system. The comparative experiments on the original asymmetric system and the system after compensation will be conducted. It shows that the proposed method is effective at different speeds under different load conditions.

Chapter 7 Control of Asymmetric Dual 3-Phase PMSG System

In this chapter, the suppression of the 2h DC bus voltage and torque ripple is extended to dual 3-phase PMSG drive system when one channel fails. In the previous research on single 3-phase asymmetric PMSG, the 2h power was suppressed by compensation in parallel or in series with some hardware investment and reconfiguration. In this chapter, by utilizing the inverter, rectifier or the second set of 3-phase windings in the fault channel which are still functional, the 2h DC bus voltage can be suppressed with minimum cost or without any hardware investment.

Chapter 8 General Conclusions

This chapter summarizes this research work and gives some discussions on future work.

1.7.2 Contributions

- Modeling of the asymmetries and their influence on power ripple and torque ripple without/with negative sequence currents has been investigated systematically;
- Mathematical modeling of asymmetric PMSG and comparison of conventional current control and three typical balanced current control methods, and the relationship between them is revealed for the first time, while their relationship was not addressed in the literature before;
- Improved instantaneous power control without any sequential component decomposers despites of the type of asymmetries, while the sequential component decomposer was inevitable in the previous research;
- Proposed an effective method for suppressing the 2h DC bus voltage pulsation accounting for 2h torque ripple in PMSG system with asymmetric impedances (Compensation in parallel with Topology-*RL*);
- Proposed an improved method of suppressing the 2h DC bus voltage in asymmetric PMSG system (Compensation in parallel with Topology-*RLE*); compared with the compensation in parallel with Topology-*RL*, it has smaller compensation current and its implementation is easier;
- Proposed a passive method of suppressing the 2h DC bus voltage in asymmetric PMSG system; the unbalanced impedances of the asymmetric 3-phase PMSG is compensated by external circuits in series. Without any active control, the unbalanced 3-phaes system is modified to a balanced system and the 2h DC bus voltage is naturally suppressed.

- Proposed three methods of suppressing the 2h DC bus voltage and torque ripple in dual 3-phase PMSG drive system with minimum cost or without any hardware investment when one channel fails.

Chapter 2 Influence of the PMSG Asymmetries

2.1 Introduction

In [134], the torque ripple of the PM machine due to unbalanced back-EMFs was investigated, which showed that the 2h torque ripple was generated in the current-fed, voltage-fed or vector control mode. However, a comprehensive analysis of the torque ripple due to the unbalanced impedances was not given, the power ripple due to unbalanced 3-phase back-EMFs and impedances were not investigated, and their analytical expressions were not given.

As introduced in Chapter 1, the *N*-sequence currents emerge under the conventional current control and instantaneous power control in the unbalanced 3-phase system, while the *N*-sequence currents can be suppressed by balanced current control. Up to now, the torque ripple and power ripple due to asymmetries without/with *N*-sequence currents are not investigated systematically.

In this chapter, the power ripple and torque ripple in the asymmetric PMSG system will be systematically investigated. Firstly, the mathematical modeling of the PMSG will be reviewed, and then the modeling of PMSG asymmetries will be introduced. Subsequently, the power ripple and torque ripple resulted from asymmetries without and with *N*-sequence currents will be analyzed in detail.

2.2 Mathematical Modeling of PMSG

2.2.1 Voltage and Flux-linkage Equations

The 3-phase PMSG with Y connected windings can be illustrated in Fig.2.1. R_A, R_B and R_C are the resistances of each phase winding respectively. L_{AA}, L_{BB}, and L_{CC} are the self-inductances of each phase respectively. M_{AB}, M_{BC} and M_{CA} are the mutual inductances between phase *A* and *B*, between phase *B* and *C*, and between phase *C* and *A* respectively. e_a, e_b, and e_c are the back-EMFs of each phase respectively. v_a, v_b and v_c are the terminal voltages of each phase respectively and i_a, i_b, and i_c are the phase currents of each phase respectively.

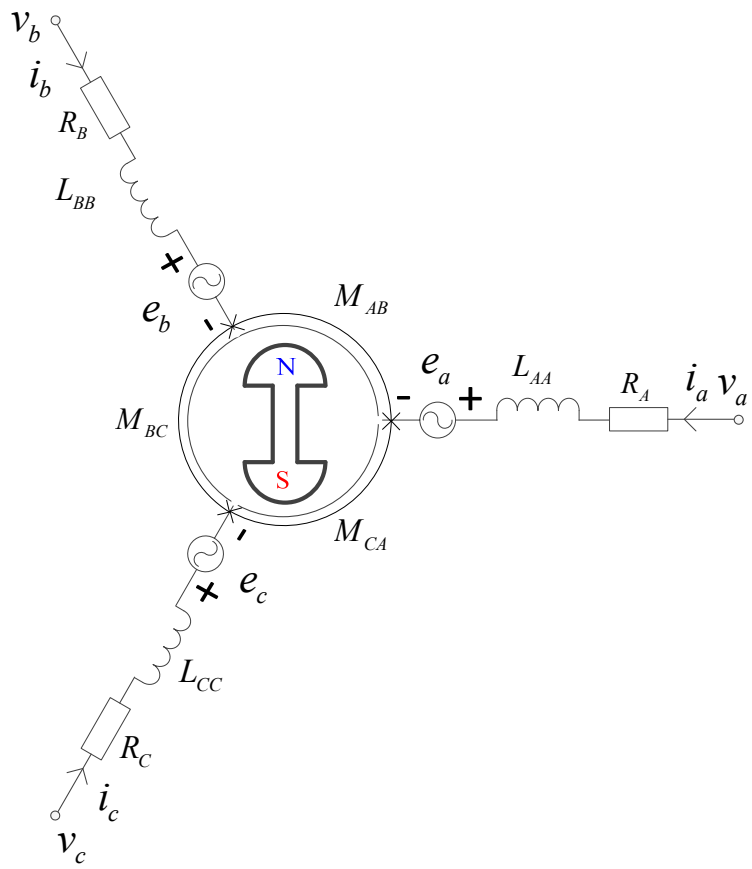

Fig.2.1 Three-phase PMSG with Y connection.

The flux-linkage equation of the 3-phase PMSG in *abc*-frame can be expressed as

$$[\psi_s] = [L_s][i_s] + [\psi_f] \tag{2.1}$$

where $[\psi_s]$ is the stator flux-linkage, $[\psi_f]$ is the PM flux-linkage, $[L_s]$ is the inductance matrix, $[i_s]$ is the stator current. They can be expressed as (2.2), (2.3), (2.4) and (2.5) respectively.

$$[\psi_s] = [\psi_a \quad \psi_b \quad \psi_c]^T \tag{2.2}$$

$$[\psi_f] = [\psi_{fa} \quad \psi_{fb} \quad \psi_{fc}]^T \tag{2.3}$$

$$[L_s] = \begin{bmatrix} L_{AA} & M_{AB} & M_{AC} \\ M_{BA} & L_{BB} & M_{BC} \\ M_{CA} & M_{CB} & L_{CC} \end{bmatrix} \tag{2.4}$$

$$[i_s] = [i_a \quad i_b \quad i_c] \tag{2.5}$$

The back-EMFs are denoted as $[e] = [e_a\ e_b\ e_c]^T$, which are equal to the differential values of PM flux-linkages and can be expressed as

$$[e]=\frac{d}{dt}[\psi_f] \tag{2.6}$$

The voltage equation of 3-phase PMSG can be expressed as

$$[v_s]=[R_s][i_s]+\frac{d}{dt}[\psi_s]=[R_s][i_s]+\frac{d}{dt}([L_s][i_s])+[e] \tag{2.7}$$

where $[v_s]$ is the stator voltage, which can be expressed as

$$[v_s]=[v_a \quad v_b \quad v_c]^T \tag{2.8}$$

$[R_s]$ is the stator resistance matrix, which can be expressed as

$$[R_s]=\begin{bmatrix} R_A & & \\ & R_B & \\ & & R_C \end{bmatrix} \tag{2.9}$$

2.2.2 Mathematical Modeling of Inductances

The self-inductances and mutual inductances in functions of rotor position θ_e can be generally expressed by Fourier expansions. Considering the higher order harmonics, the self-inductances can be expressed as [135-137]

$$L_{PP}=L_{P0}+\sum_{n=1}^{\infty}L_{P2n}\cos\left(2n\cdot\Delta\theta_p+\varphi_{P2n}\right) \tag{2.10}$$

The mutual inductances between two phases can be expressed as

$$M_{PQ}=M_{PQ0}\cos\left(\Delta\theta_p-\Delta\theta_Q\right)+\sum_{n=1}^{\infty}M_{PQ2n}\cos\left(\Delta\theta_p+\Delta\theta_Q+\varphi_{PQ2n}\right) \tag{2.11}$$

where P stands for phase A, B, or C, while Q stands for the other phase that is different with phase P. $\Delta\theta_P$ and $\Delta\theta_Q$ are the electrical angle of the axis of phase P winding and phase Q shifted from d-axis of PM machine, which can be illustrated in Fig.2.2, which can be expressed as

$$\Delta\theta_P=\theta_P-\theta_e, \quad \Delta\theta_Q=\theta_Q-\theta_e \tag{2.12}$$

where θ_A, θ_B, θ_C can be expressed as (2.13) and $\theta_s=\pi/6$.

$$\theta_A=0, \quad \theta_B=4\theta_s, \quad \theta_C=8\theta_s \tag{2.13}$$

L_{P0} is average value of self-inductance, L_{P2n} is the coefficient of inductance harmonics (second, 4th, 6th…), and φ_{P2n} is the displacement angle of the corresponding harmonic components in the self-inductance.

M_{PQ0} is coefficient of the average mutual inductance between phase P and Q, M_{PQ2n} is the coefficient of inductance harmonics (2nd, 4th, 6th…) in the mutual inductance, and the φ_{PQ2n} is the displacement angle of corresponding harmonic components in the mutual inductance.

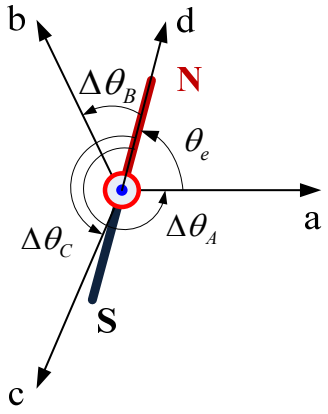

Fig.2.2 Illustration of winding position.

Neglecting the higher order (>2nd) harmonic inductances, (2.10) and (2.11) can be simplified as

$$L_{PP} = L_{P0} + L_{P2}\cos\left(2\Delta\theta_p + \varphi_{P2}\right) \tag{2.14}$$

$$M_{PQ} = M_{PQ0}\cos\left(\Delta\theta_p - \Delta\theta_Q\right) + M_{PQ2}\cos\left(\Delta\theta_p + \Delta\theta_Q + \varphi_{PQ2}\right) \tag{2.15}$$

where

$$M_{PQ} = M_{QP};\quad M_{PQ0} = M_{QP0};\quad M_{PQ2} = M_{QP2}; \tag{2.16}$$

Usually, φ_{P2} and φ_{PQ2} are zero in PMSG. Therefore, the inductance matrix (2.4) can be rewritten as

$$\begin{aligned}\left[L_s\right] = &\begin{bmatrix} L_{A0} & -\frac{1}{2}M_{AB0} & -\frac{1}{2}M_{AC0} \\ -\frac{1}{2}M_{BA0} & L_{B0} & -\frac{1}{2}M_{BC0} \\ -\frac{1}{2}M_{CA0} & -\frac{1}{2}M_{CB0} & L_{C0} \end{bmatrix} \\ &+ \begin{bmatrix} L_{A2}\cos(2\theta_e) & M_{AB2}\cos(2\theta_e - 4\theta_s) & M_{AC2}\cos(2\theta_e - 8\theta_s) \\ M_{BA2}\cos(2\theta_e - 4\theta_s) & L_{B2}\cos(2\theta_e - 8\theta_s) & M_{BC2}\cos(2\theta_e) \\ M_{CA2}\cos(2\theta_e - 8\theta_s) & M_{CB2}\cos(2\theta_e) & L_{C2}\cos(2\theta_e - 4\theta_s) \end{bmatrix}\end{aligned} \tag{2.17}$$

2.2.3 Power and Torque Equations

The power flowing in the PMSG drive system can be demonstrated in Fig.2.3, where the direction of the positive current is defined as the direction from the inverter to the PMSG.

The power generated by the resistances, inductances and back-EMFs are designated as p_R, p_L and p_E respectively. When the PMSG works in generation mode, p_E is negative. In contrast, when the PMSG works in motor mode, p_E is positive.

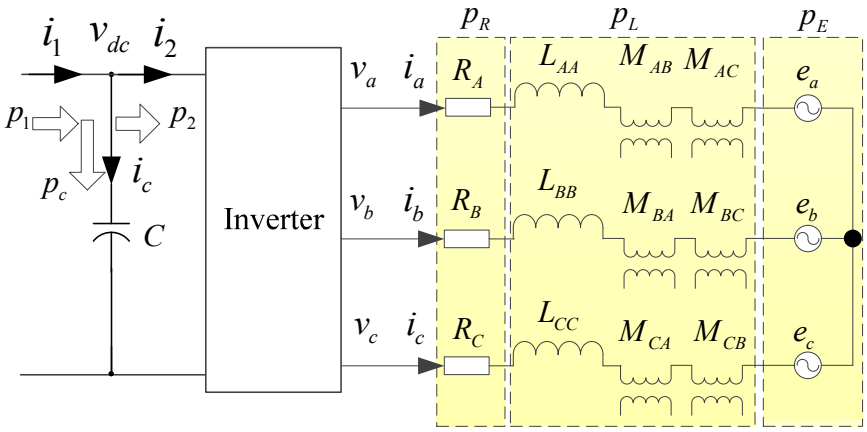

Fig.2.3 Power flowing in the PMSG drive system.

Assuming the inverter is zero-loss system, the power p_2 flowing into the inverter will be equal to the power flowing out of the inverter, which is the sum of p_R, p_L and p_E. Therefore, the power p_2 can be expressed as

$$\begin{aligned} p_2 = \begin{bmatrix} i_a & i_b & i_c \end{bmatrix} \begin{bmatrix} v_a \\ v_b \\ v_c \end{bmatrix} = \underbrace{\begin{bmatrix} i_a & i_b & i_c \end{bmatrix} \begin{bmatrix} R_A & & \\ & R_B & \\ & & R_C \end{bmatrix} \begin{bmatrix} i_a \\ i_b \\ i_c \end{bmatrix}}_{p_R} \\ + \underbrace{\begin{bmatrix} i_a & i_b & i_c \end{bmatrix} \frac{d}{dt} \left(\begin{bmatrix} L_{AA} & M_{AB} & M_{AC} \\ M_{BA} & L_{BB} & M_{BC} \\ M_{CA} & M_{CB} & L_{CC} \end{bmatrix} \begin{bmatrix} i_a \\ i_b \\ i_c \end{bmatrix} \right)}_{p_L} + \underbrace{\begin{bmatrix} i_a & i_b & i_c \end{bmatrix} \begin{bmatrix} e_a \\ e_b \\ e_c \end{bmatrix}}_{p_E} \end{aligned} \tag{2.18}$$

The torque can be calculated as the derivative of the stored magnetic co-energy W_c with respect to a small displacement [138]. Therefore, the torque generated by 3-phase PMSG can be expressed as (2.19).

$$T_e = \frac{\partial W_c}{\partial \theta_m} = p \frac{\partial W_c}{\partial \theta_e} = \underbrace{\frac{p}{2} \begin{bmatrix} i_s \end{bmatrix}^T \frac{\partial [L_s]}{\partial \theta_e} \begin{bmatrix} i_s \end{bmatrix}}_{T_{eL}} + \underbrace{p \begin{bmatrix} i_s \end{bmatrix}^T \frac{\partial [\psi_f]}{\partial \theta_e}}_{T_{ePM}} \tag{2.19}$$

where p is the number of pole pairs, θ_m and θ_e are the mechanical position and electrical position respectively. The first part in (2.19) is reluctance torque, which is designated as T_{eL}; the second part of (2.19) is torque generated by PM, which is designated as T_{ePM}.

2.3 Modeling of Asymmetries

In the asymmetric 3-phase PMSG system, the asymmetries may be resulted from the unbalanced resistances, unbalance inductances or unbalance back-EMFs.

2.3.1 Unbalanced Resistances

In (2.20), the maximum value of R_A, R_B and R_C is defined as R_0. If the resistances are not balanced, i.e. R_A, R_B and R_C are not equal to each other, the asymmetries due to unbalanced resistances can be indicated by ΔR_A, ΔR_B and ΔR_C, which can be expressed as (2.21), (2.22) and (2.23) respectively.

$$R_0 = \max\left(R_A, R_B, R_C\right) \tag{2.20}$$

$$\Delta R_A = R_0 - R_A \geq 0 \tag{2.21}$$

$$\Delta R_B = R_0 - R_B \geq 0 \tag{2.22}$$

$$\Delta R_C = R_0 - R_C \geq 0 \tag{2.23}$$

Since R_0 is the maximum value of R_A, R_B and R_C, at least one of them is zero and only two of them are not zero in the worst case.

2.3.2 Unbalanced Inductances

If the average self-inductances are not balanced, the average value of L_{AA}, L_{BB} and L_{CC} are not equal to each other. If L_0 is defined as the maximum average value of L_{AA}, L_{BB} and L_{CC}, i.e.

$$L_0 = \max\left(L_{A0}, L_{B0}, L_{C0}\right) \tag{2.24}$$

where L_{A0}, L_{B0} and L_{c0} are the average self-inductances of phase *A, B* and *C* respectively, then the asymmetries due to the unbalanced average self-inductances L_{AA}, L_{BB} and L_{CC} can be indicated as (2.25),(2.26) and (2.27) respectively.

$$\Delta L_{A0} = L_0 - L_{A0} \tag{2.25}$$

$$\Delta L_{B0} = L_0 - L_{B0} \tag{2.26}$$

$$\Delta L_{C0} = L_0 - L_{C0} \tag{2.27}$$

If M_0 is chosen as the minimum average value of M_{AB0}, M_{BC0}, and M_{CA0}, i.e.

$$M_0 = \min\left(M_{AB0}, M_{BC0}, M_{CA0}\right) \tag{2.28}$$

where M_{AB0}, M_{BC0} and M_{CA0} are the average values of M_{AB}, M_{BC}, and M_{CA} respectively, then the asymmetries due to the unbalanced average mutual inductances M_{AB}, M_{BC}, and M_{CA} can be indicated as (2.29), (2.30) and (2.31) respectively.

$$\Delta M_{AB0} = M_{AB0} - M_0 \tag{2.29}$$

$$\Delta M_{BC0} = M_{BC0} - M_0 \tag{2.30}$$

$$\Delta M_{CA0} = M_{CA0} - M_0 \tag{2.31}$$

2.3.3 Unbalanced Back-EMFs

If the 3-phase back-EMFs are unbalanced, based on the symmetrical-component theory [91], the unbalanced back-EMFs can be decomposed as *P*-sequence back-EMFs and *N*-sequence back-EMFs in the unbalanced 3-phase system without access of neutral point. If the rotor position is chosen as the zero crossing point of *P*-sequence back-EMFs of phase *A* from positive to negative, the 3-phase back-EMFs can be expressed as (2.32)

$$\begin{bmatrix} e_a \\ e_b \\ e_c \end{bmatrix} = \underbrace{E_{1p}\begin{bmatrix} \cos(\theta_e + \pi/2) \\ \cos(\theta_e - 4\theta_s + \pi/2) \\ \cos(\theta_e - 8\theta_s + \pi/2) \end{bmatrix}}_{P-sequence} + \underbrace{E_{1n}\begin{bmatrix} \cos(\theta_e + \pi/2 + \varphi_{en}) \\ \cos(\theta_e - 8\theta_s + \pi/2 + \varphi_{en}) \\ \cos(\theta_e - 4\theta_s + \pi/2 + \varphi_{en}) \end{bmatrix}}_{N-sequence} \tag{2.32}$$

where θ_e is the electrical rotor position, E_{1p} and E_{1n} are the amplitude of *P*-sequence and *N*-sequence back-EMFs respectively, the φ_{1n} is the displacement angle of the *N*-sequence components.

2.4 Influence of Asymmetries without *N*-sequence Currents

The power ripple and torque ripple due to the unbalanced resistances, unbalanced inductances or unbalanced 3-phase back-EMFs with only *P*-sequence currents injection will be discussed in this section. Assuming the phase currents are balanced, which have only *P*-sequence currents, the phase currents can be expressed as

$$\begin{bmatrix} i_a \\ i_b \\ i_c \end{bmatrix} = I_{1p}\begin{bmatrix} \cos(\theta_e - 0\theta_s + \pi/2) \\ \cos(\theta_e - 4\theta_s + \pi/2) \\ \cos(\theta_e - 8\theta_s + \pi/2) \end{bmatrix} \tag{2.33}$$

where I_{1p} is the amplitude of *P*-sequence currents, $\theta_s = \pi/6$.

2.4.1 Unbalanced Resistors

According to (2.18), p_R can be expressed as

$$p_R = i_a^2 R_A + i_b^2 R_B + i_c^2 R_C = {I_{1p}}^2 \begin{pmatrix} R_A \cos^2\left(\theta_e - 0\theta_s + \pi/2\right) \\ +R_B \cos^2\left(\theta_e - 4\theta_s + \pi/2\right) \\ +R_C \cos^2\left(\theta_e - 8\theta_s + \pi/2\right) \end{pmatrix} \tag{2.34}$$

If the resistances are balanced, i.e. $R_A=R_B=R_C=R_0$, (2.34) can be rewritten as

$$p_R = I_{1p}^2 R_0 \left(\cos^2\left(\theta_e + \pi/2\right) + \cos^2\left(\theta_e - 4\theta_s + \pi/2\right) + \cos^2\left(\theta_e - 8\theta_s + \pi/2\right)\right) \tag{2.35}$$

(2.35) can be simplified as

$$p_R = \frac{3}{2} I_{1p}^2 R_0 \tag{2.36}$$

From (2.36), it can be seen that the p_R is a constant value if the resistances are balanced. However, if the resistances are unbalanced, i.e. ΔR_A, ΔR_B and ΔR_C are not zero in the modeling (2.20)~(2.23), the (2.34) can be rewritten as

$$\begin{aligned} p_R &= \frac{3}{2} I_{1p}^2 R_0 - \frac{1}{2} I_{1p}^2 \begin{pmatrix} \Delta R_A \cos^2\left(\theta_e - 0\theta_s + \pi/2\right) \\ +\Delta R_B \cos^2\left(\theta_e - 4\theta_s + \pi/2\right) \\ +\Delta R_C \cos^2\left(\theta_e - 8\theta_s + \pi/2\right) \end{pmatrix} \\ &= \frac{3}{2} I_{1p}^2 R_0 - \frac{1}{2} I_{1p}^2 \left(\Delta R_A + \Delta R_B + \Delta R_C\right) + \frac{1}{2} I_{1p}^2 \begin{pmatrix} \Delta R_A \cos\left(2\theta_e + 0\theta_s\right) \\ +\Delta R_B \cos\left(2\theta_e + 4\theta_s\right) \\ +\Delta R_C \cos\left(2\theta_e + 8\theta_s\right) \end{pmatrix} \end{aligned} \tag{2.37}$$

As can be seen from (2.37), there will be 2h power in p_R if the resistances are unbalanced.

It is worth noting the unbalanced resistances do not affect the torque ripple at all according to (2.19).

2.4.2 Unbalanced Inductances

2.4.2.1 Power Ripple

The self-inductances and mutual inductances of the machine can be expressed as (2.14) and (2.15) respectively if the higher order (>2nd) harmonic inductances are neglected. If the inductances are balanced, i.e. (2.38) and (2.39)

$$L_{P0} = L_0,\ L_{P2} = L_2,\ \varphi_{P2} = \varphi_{L2} \tag{2.38}$$

$$M_{PQ0} = M_0,\ \ M_{PQ2} = M_2,\ \ \varphi_{PQ2} = \varphi_{M2} \tag{2.39}$$

According to (2.18), the power of inductances with balanced currents (2.33) injection can be expressed as

$$p_L = \begin{bmatrix} i_a & i_b & i_c \end{bmatrix} \frac{d}{dt} \left(\begin{bmatrix} L_{AA} & M_{AB} & M_{AC} \\ M_{BA} & L_{BB} & M_{BC} \\ M_{CA} & M_{CB} & L_{CC} \end{bmatrix} \begin{bmatrix} i_a \\ i_b \\ i_c \end{bmatrix} \right) \tag{2.40}$$
$$= \frac{3}{4} \omega_e I_{1p}^2 \left(L_2 \sin\left(\varphi_{L2}\right) + 2M_2 \sin\left(\varphi_{M2}\right) \right)$$

where ω_e is the electrical frequency. From (2.40), it can be seen that p_L is a constant value without ripple. Usually, φ_{L2} and φ_{M2} are zero. Therefore, the instantaneous power of the balanced 3-phase inductances is zero. However, if the inductances are unbalanced, the power p_L will not be a constant value anymore.

According to modeling of unbalanced self-inductance (2.25), the 2h power due to ΔL_{A0} will be

$$\Delta p_{L\_A} = \begin{bmatrix} i_a & i_b & i_c \end{bmatrix} \frac{d}{dt} \left(\begin{bmatrix} -\Delta L_{A0} & 0 & 0 \\ 0 & 0 & 0 \\ 0 & 0 & 0 \end{bmatrix} \begin{bmatrix} i_a \\ i_b \\ i_c \end{bmatrix} \right) = \frac{1}{2} \omega_e \Delta L_{A0} I_{1p}^2 \cdot \cos\left(2\theta_e + 3\theta_s\right) \tag{2.41}$$

In the same way, according to modeling of unbalanced self-inductances (2.26) and (2.27), the 2h power due to ΔL_{B0} and ΔL_{C0} will be (2.42) and (2.43) respectively.

$$\Delta p_{L\_B} = \begin{bmatrix} i_a & i_b & i_c \end{bmatrix} \frac{d}{dt} \left(\begin{bmatrix} 0 & 0 & 0 \\ 0 & -\Delta L_{B0} & 0 \\ 0 & 0 & 0 \end{bmatrix} \begin{bmatrix} i_a \\ i_b \\ i_c \end{bmatrix} \right) = \frac{1}{2} \omega_e \Delta L_{B0} I_{1p}^2 \cos\left(2\theta_e - 5\theta_s\right) \tag{2.42}$$

$$\Delta p_{L\_C} = \begin{bmatrix} i_a & i_b & i_c \end{bmatrix} \frac{d}{dt} \left(\begin{bmatrix} 0 & 0 & 0 \\ 0 & 0 & 0 \\ 0 & 0 & -\Delta L_{C0} \end{bmatrix} \begin{bmatrix} i_a \\ i_b \\ i_c \end{bmatrix} \right) = \frac{1}{2} \omega_e \Delta L_{C0} I_{1p}^2 \cos\left(2\theta_e - 1\theta_s\right) \tag{2.43}$$

According to modeling of unbalanced mutual inductance (2.29), the 2h power due to the unbalanced mutual average inductances between phase *A* and *B* can be expressed as (2.44).

In the same way, according to modeling of unbalanced mutual inductance (2.30) and (2.31), the 2h power due to the unbalanced mutual average inductances between phase *B* and *C*, between phase *A* and *C* can be expressed as (2.45) and (2.46) respectively.

$$\Delta p_{M\_AB} = \begin{bmatrix} i_a & i_b & i_c \end{bmatrix} \frac{d}{dt} \left(\begin{bmatrix} 0 & -\frac{1}{2}\Delta M_{AB0} & 0 \\ -\frac{1}{2}\Delta M_{AB0} & 0 & 0 \\ 0 & 0 & 0 \end{bmatrix} \begin{bmatrix} i_a \\ i_b \\ i_c \end{bmatrix} \right) \tag{2.44}$$

$$= \frac{1}{2}\omega_e \Delta M_{AB0} I_{1p}^2 \cdot \cos\left(2\theta_e - 1\theta_s\right)$$

$$\Delta p_{M\_BC} = \begin{bmatrix} i_a & i_b & i_c \end{bmatrix} \frac{d}{dt} \left(\begin{bmatrix} 0 & 0 & 0 \\ 0 & 0 & -\frac{1}{2}\Delta M_{BC0} \\ 0 & -\frac{1}{2}\Delta M_{BC0} & 0 \end{bmatrix} \begin{bmatrix} i_a \\ i_b \\ i_c \end{bmatrix} \right) \tag{2.45}$$

$$= \frac{1}{2}\omega_e \Delta M_{BC0} I_{1p}^2 \cdot \cos\left(2\theta_e + 3\theta_s\right)$$

$$\Delta p_{M\_AC} = \begin{bmatrix} i_a & i_b & i_c \end{bmatrix} \frac{d}{dt} \left(\begin{bmatrix} 0 & 0 & -\frac{1}{2}\Delta M_{CA0} \\ 0 & 0 & 0 \\ -\frac{1}{2}\Delta M_{CA0} & 0 & 0 \end{bmatrix} \begin{bmatrix} i_a \\ i_b \\ i_c \end{bmatrix} \right) \tag{2.46}$$

$$= \frac{1}{2}\omega_e \Delta M_{CA0} I_{1p}^2 \cos\left(2\theta_e - 5\theta_s\right)$$

If the amplitudes of the 2h inductances are unbalanced, e.g. $L_{A2} = L_2 + \Delta L_2$, where L_2 is the average 2h self-inductances in L_{A2}, L_{B2} and L_{C2}, the power ripple due to ΔL_2 can be expressed as

$$\Delta p_{L\_A2} = \begin{bmatrix} i_a & i_b & i_c \end{bmatrix} \frac{d}{dt} \left(\begin{bmatrix} \Delta L_2 \cos\left(2\Delta\theta_A + \varphi_{L2}\right) & 0 & 0 \\ 0 & 0 & 0 \\ 0 & 0 & 0 \end{bmatrix} \begin{bmatrix} i_a \\ i_b \\ i_c \end{bmatrix} \right) \tag{2.47}$$

$$= \frac{1}{4}\omega_e \Delta L_2 I_{1p}^2 \left(3\sin\left(4\theta_e + \varphi_{L2}\right) - 4\sin\left(2\theta_e + \varphi_{L2}\right) + \sin\left(\varphi_{L2}\right)\right)$$

In the same way, if $M_{AB2} = M_2 + \Delta M_2$, where M_2 is the average 2h mutual inductance in M_{AB2}, M_{BC2} and M_{CA2}, the power ripple due to ΔM_2 can be expressed as (2.48).

If other 2h self-inductances L_{B2}, L_{C2}, or other 2h mutual inductances M_{BC2}, M_{CA2} are unbalanced, the power ripple due to these asymmetries have similar expressions as (2.47) and (2.48) respectively.

$$\begin{aligned}\Delta p_{M\_AB2} &= \begin{bmatrix} i_a \\ i_b \\ i_c \end{bmatrix}^T \frac{d}{dt}\left(\begin{bmatrix} 0 & \Delta M_2\cos\left(\Delta\theta_A+\Delta\theta_B+\varphi_{M2}\right) & 0 \\ \Delta M_2\cos\left(\Delta\theta_A+\Delta\theta_B+\varphi_{M2}\right) & 0 & 0 \\ 0 & 0 & 0 \end{bmatrix}\right) \\ &= -\frac{1}{2}\omega_e\Delta M_2 I_{1p}^2\begin{pmatrix} 3\sin\left(4\theta_e+\varphi_{M2}-2\theta_s\right) \\ +2\sin\left(2\theta_e+\varphi_{M2}-8\theta_s\right)+2\sin\left(2\theta_e+\varphi_{M2}\right) \\ -\sin\left(\varphi_{M2}\right) \end{pmatrix}\end{aligned} \tag{2.48}$$

Overall, the power ripple due to unbalanced inductances without *N*-sequence currents can be summarized as follows:

1) There will be 2h power ripple if the average self-inductances or average mutual inductances are unbalanced according to (2.41)~(2.46);

2) There will be second and 4th harmonic power ripple if the 2h self-inductances or 2h mutual inductances are unbalanced according to (2.47) and (2.48);

2.4.2.2 Torque Ripple

When the self-inductances and mutual inductances are balanced as shown in (2.38) and (2.39) respectively, the reluctance torque T_{eL} can be simplified as

$$T_{eL} = \frac{p}{2}\left[i_s\right]^T\frac{\partial\left[L_s\right]}{\partial\theta_e}\left[i_s\right] = \frac{3}{4}p\left(L_2\sin(\varphi_{L2})+2M_2\sin(\varphi_{M2})\right)I_{1p}^2 \tag{2.49}$$

As can be seen from (2.49), there is no torque ripple if the inductances are balanced. However, if the average self-inductances are unbalanced as the modeling as (2.25)-(2.27), the torque ripple in the reluctance torque due to ΔL_{A0}, ΔL_{B0} and ΔL_{C0} can be expressed as (2.50), (2.51) and (2.52) respectively.

$$\Delta T_{eL\_A} = \frac{p}{2}\begin{bmatrix} i_a & i_b & i_c \end{bmatrix}\frac{\partial}{\partial\theta_e}\left(\begin{bmatrix} -\Delta L_{A0} & 0 & 0 \\ 0 & 0 & 0 \\ 0 & 0 & 0 \end{bmatrix}\right)\begin{bmatrix} i_a \\ i_b \\ i_c \end{bmatrix} = 0 \tag{2.50}$$

$$\Delta T_{eL\_B} = \frac{p}{2}\begin{bmatrix} i_a & i_b & i_c \end{bmatrix}\frac{\partial}{\partial\theta_e}\left(\begin{bmatrix} 0 & 0 & 0 \\ 0 & -\Delta L_{B0} & 0 \\ 0 & 0 & 0 \end{bmatrix}\right)\begin{bmatrix} i_a \\ i_b \\ i_c \end{bmatrix} = 0 \tag{2.51}$$

$$\Delta T_{eL\_C} = \frac{p}{2}\cdot\begin{bmatrix} i_a & i_b & i_c \end{bmatrix}\frac{\partial}{\partial\theta_e}\left(\begin{bmatrix} 0 & 0 & 0 \\ 0 & 0 & 0 \\ 0 & 0 & -\Delta L_{C0} \end{bmatrix}\right)\begin{bmatrix} i_a \\ i_b \\ i_c \end{bmatrix} = 0 \tag{2.52}$$

If the average mutual inductances are unbalanced and modeled as (2.29)-(2.31), the torque ripple in the reluctance torque due to ΔM_{AB0}, ΔM_{BC0} and ΔM_{CA0} can be expressed as (2.53), (2.54) and (2.55) respectively.

$$\Delta T_{eL\_MAB} = \frac{p}{2}\begin{bmatrix} i_a & i_b & i_c \end{bmatrix}\frac{\partial}{\partial \theta_e}\left(\begin{bmatrix} 0 & -\frac{1}{2}\Delta M_{AB0} & 0 \\ -\frac{1}{2}\Delta M_{AB0} & 0 & 0 \\ 0 & 0 & 0 \end{bmatrix}\right)\begin{bmatrix} i_a \\ i_b \\ i_c \end{bmatrix} = 0 \tag{2.53}$$

$$\Delta T_{eL\_MBC} = \frac{p}{2}\cdot\begin{bmatrix} i_a & i_b & i_c \end{bmatrix}\frac{\partial}{\partial \theta_e}\left(\begin{bmatrix} 0 & 0 & 0 \\ 0 & 0 & -\frac{1}{2}\Delta M_{BC0} \\ 0 & -\frac{1}{2}\Delta M_{BC0} & 0 \end{bmatrix}\right)\begin{bmatrix} i_a \\ i_b \\ i_c \end{bmatrix} = 0 \tag{2.54}$$

$$\Delta T_{eL\_MBC} = \frac{p}{2}\cdot\begin{bmatrix} i_a & i_b & i_c \end{bmatrix}\frac{\partial}{\partial \theta_e}\left(\begin{bmatrix} 0 & 0 & -\frac{1}{2}\Delta M_{CA0} \\ 0 & 0 & 0 \\ -\frac{1}{2}\Delta M_{CA0} & 0 & 0 \end{bmatrix}\right)\begin{bmatrix} i_a \\ i_b \\ i_c \end{bmatrix} = 0 \tag{2.55}$$

If the 2h self-inductances are unbalanced, e.g. if $L_{A2} = L_2+\Delta L_2$, the torque ripple of reluctance torque due to the unbalanced 2h self-inductance ΔL_2 can be expressed as

$$\begin{aligned}\Delta T_{eL\_A2} &= \frac{p}{2}\begin{bmatrix} i_a & i_b & i_c \end{bmatrix}\frac{\partial}{\partial \theta_e}\left(\begin{bmatrix} \Delta L_2\cos\left(2\Delta\theta_A+\varphi_{L2}\right) & 0 & 0 \\ 0 & 0 & 0 \\ 0 & 0 & 0 \end{bmatrix}\right)\begin{bmatrix} i_a \\ i_b \\ i_c \end{bmatrix} \\ &= \frac{p}{4}\Delta L_2 I_{1p}^2\left(\sin\left(4\theta_e+\varphi_{L2}\right)-2\sin\left(2\theta_e+\varphi_{L2}\right)+\sin\left(\varphi_{L2}\right)\right)\end{aligned} \tag{2.56}$$

If the 2h mutual inductances are unbalanced, e.g. if $M_{AB2} = M_2+\Delta M_2$, the torque ripple of reluctance torque due to the unbalanced 2h mutual inductance ΔM_2 can be expressed as

$$\begin{aligned}&\Delta T_{eL\_AB2} \\ &= \begin{bmatrix} i_a \\ i_b \\ i_c \end{bmatrix}^T \frac{\partial}{\partial \theta_e}\left(\begin{bmatrix} 0 & \Delta M_2\cos\left(\Delta\theta_A+\Delta\theta_B+\varphi_{M2}\right) & 0 \\ \Delta M_2\cos\left(\Delta\theta_A+\Delta\theta_B+\varphi_{M2}\right) & 0 & 0 \\ 0 & 0 & 0 \end{bmatrix}\right)\begin{bmatrix} i_a \\ i_b \\ i_c \end{bmatrix} \\ &= -\frac{p}{2}\Delta M_2 I_{1p}^2\left(-\cos\left(4\theta_e+\varphi_{M2}+\theta_s\right)+\cos\left(2\theta_e+\varphi_{M2}+\theta_s\right)+\sin\left(2\theta_e+\varphi_{M2}\right)-\sin\left(\varphi_{M2}\right)\right)\end{aligned} \tag{2.57}$$

If other 2h self-inductances L_{B2}, L_{C2}, or other 2h mutual inductances M_{BC2}, M_{CA2} are unbalanced, the torque ripple due to those asymmetries have similar expressions as (2.56) and (2.57) respectively.

Overall, the torque ripple due to asymmetric inductances without *N*-sequence currents can be summarized as below

1) There is no 2h torque ripple if the average self-inductances are unbalanced or the average mutual inductances are unbalanced according to (2.50)~(2.55);

2) There will be 2h and 4th harmonic torque ripple if the second self-inductances or mutual inductances are unbalanced according to (2.56) and (2.57);

2.4.3 Unbalanced Back-EMFs

2.4.3.1 Power Ripple

Assuming the 3-phase back-EMFs are balanced with only *P*-sequence components and can be expressed as (2.58)

$$\begin{bmatrix} e_a \\ e_b \\ e_c \end{bmatrix} = \underbrace{E_{1p}\begin{bmatrix} \cos\left(\theta_e + \pi/2\right) \\ \cos\left(\theta_e - 4\theta_s + \pi/2\right) \\ \cos\left(\theta_e - 8\theta_s + \pi/2\right) \end{bmatrix}}_{P-sequence} \tag{2.58}$$

where E_{1p} is the amplitude of the back-EMFs, then the power p_E generated by the PM can be expressed as

$$p_E = \begin{bmatrix} i_a & i_b & i_c \end{bmatrix}\begin{bmatrix} e_a \\ e_b \\ e_c \end{bmatrix} = \frac{3}{2}E_{1p}I_{1p} \tag{2.59}$$

As can be seen from (2.59), there is no 2h power. However, if the 3-phase back-EMFs are unbalanced as (2.32), the p_E can be expressed as (2.60) which consists of 2h power.

$$p_E = \frac{3}{2}E_{1p}I_{1p} - \frac{3}{2}E_{1n}I_{1p}\cos\left(2\theta_e + \varphi_{en}\right) \tag{2.60}$$

2.4.3.2 Torque Ripple

According to (2.19), the torque T_{ePM} resulted from the PM can be expressed as

$$T_{ePM} = p\left[i_s\right]^T\frac{\partial[\psi_f]}{\partial\theta_e} = p\left[i_s\right]^T\frac{\partial[\psi_f]}{\partial t}\frac{\partial t}{\partial\theta_e} = p\frac{p_E}{\omega_e} \tag{2.61}$$

Combining the (2.60) and (2.61) together, T_{ePM} can be rewritten as

$$T_{ePM} = p\frac{p_E}{\omega_e} = \frac{3p}{2\omega_e}\left(E_{1p}I_{1p} - E_{1n}I_{1p}\cdot\cos\left(2\theta_e + \varphi_{en}\right)\right) \tag{2.62}$$

As can be seen from (2.62), there is 2h torque when the 3-phase back-EMFs are unbalanced.

2.4.4 Summary

The power ripple and torque ripple due to the unbalanced impedances and unbalanced 3-phase back-EMFs can be summarized as below.

TABLE 2.1

POWER AND TORQUE VARIATION WITH BALANCED CURRENTS INJECTION

Items	Description
p_R	1. Second harmonic power ripple if resistances are unbalanced;
p_L	1. Second harmonic power ripple if average self- or mutual inductances are unbalanced; 2. Second and fourth harmonic power ripples if the second self- or mutual inductances are unbalanced.
p_E	1. Second harmonic power ripple if the 3-phase back-EMFs are unbalanced;.
T_{eL}	1. No torque ripple if the average self- or mutual inductances are unbalanced; 2. Second and fourth torque ripples if the second self- or mutual inductances are unbalanced.
T_{ePM}	1. Second harmonic torque ripple if the 3-phase back-EMFs are unbalanced;

2.5 Influence of Asymmetries with *N*-sequence Currents

The power ripple and torque ripple due to the unbalanced resistances, unbalanced inductances and unbalanced 3-phase back-EMFs with *N*-sequence currents injection will be discussed in this section.

Assuming the 3-phase currents are unbalanced, which include *P*-sequence and *N*-sequence currents, the 3-phase currents can be expressed as (2.63).

$$\begin{bmatrix} i_a \\ i_b \\ i_c \end{bmatrix} = \underbrace{\begin{bmatrix} i_{ap} \\ i_{bp} \\ i_{cp} \end{bmatrix}}_{P-sequence} + \underbrace{\begin{bmatrix} i_{an} \\ i_{bn} \\ i_{cn} \end{bmatrix}}_{N-sequence} \tag{2.63}$$

where the *P*-sequence and *N*-sequence currents can be expressed as (2.64) and (2.65) respectively.

$$\begin{bmatrix} i_{ap} \\ i_{bp} \\ i_{cp} \end{bmatrix} = I_{1p} \begin{bmatrix} \cos\left(\theta_e - 0\theta_s + \pi/2 + \varphi_{ip}\right) \\ \cos\left(\theta_e - 4\theta_s + \pi/2 + \varphi_{ip}\right) \\ \cos\left(\theta_e - 8\theta_s + \pi/2 + \varphi_{ip}\right) \end{bmatrix} \tag{2.64}$$

$$\begin{bmatrix} i_{an} \\ i_{bn} \\ i_{cn} \end{bmatrix} = I_{1n} \begin{bmatrix} \cos\left(\theta_e - 0\theta_s + \pi/2 + \varphi_{in}\right) \\ \cos\left(\theta_e - 8\theta_s + \pi/2 + \varphi_{in}\right) \\ \cos\left(\theta_e - 4\theta_s + \pi/2 + \varphi_{in}\right) \end{bmatrix} \tag{2.65}$$

where I_{1P} and I_{1N} are the amplitude of *P*-sequence and *N*-sequence currents respectively. The φ_{ip} and φ_{in} are the displacement angle of *P*-sequence and *N*-sequence currents respectively.

2.5.1 Unbalanced Resistors

According to (2.18), with the unbalanced currents (2.63) injection into stator currents, the p_R can be expressed as

$$\begin{aligned} p_R &= \begin{bmatrix} i_a & i_b & i_c \end{bmatrix} \begin{bmatrix} R_A & & \\ & R_B & \\ & & R_C \end{bmatrix} \begin{bmatrix} i_a \\ i_b \\ i_c \end{bmatrix} \\ &= \begin{bmatrix} i_{ap}+i_{an} & i_{bp}+i_{bn} & i_{cp}+i_{cn} \end{bmatrix} \begin{bmatrix} R_A & & \\ & R_B & \\ & & R_C \end{bmatrix} \begin{bmatrix} i_{ap}+i_{an} \\ i_{bp}+i_{bn} \\ i_{cp}+i_{cn} \end{bmatrix} \end{aligned} \tag{2.66}$$

If the resistances are balanced, i.e. $R_A=R_B=R_C=R_0$, then (2.66) can be simplified as

$$p_R = \frac{3}{2} R_0^{\,2} \left(I_{1p}^2 + I_{1p}^2 - 2I_{1p}I_{1p} \cos\left(2\theta + \varphi_{ip} + \varphi_{in}\right) \right) \tag{2.67}$$

From (2.67), it can be seen that there is 2h component in p_R even the resistances are balanced. When the resistances are unbalanced, i.e. ΔR_A, ΔR_B and ΔR_C are not zero in the modeling (2.20)~(2.23), (2.66) can be rewritten as (2.68).

Compared with (2.67), it can be seen from (2.68), there are more items of 2h power if the resistances are unbalanced.

$$
\begin{aligned}
p_R = & \frac{3}{2}R_0{}^2\left(I_{1p}^2+I_{1n}^2-2I_{1p}I_{1n}\cos\left(2\theta_e+\varphi_{ip}+\varphi_{in}\right)\right)\\
& -\frac{1}{2}I_{1p}^2\cdot\left(\Delta R_A+\Delta R_B+\Delta R_C\right)+\frac{1}{2}I_{1p}^2\begin{pmatrix}\Delta R_A\cdot\cos\left(2\theta_e\right)\\ +\Delta R_B\cdot\cos\left(2\theta_e+4\theta_s\right)\\ +\Delta R_C\cdot\cos\left(2\theta_e-4\theta_s\right)\end{pmatrix}\\
& -\frac{1}{2}I_{1n}^2\cdot\left(\Delta R_A+\Delta R_B+\Delta R_C\right)+\frac{1}{2}I_{1n}^2\begin{pmatrix}\Delta R_A\cdot\cos\left(2\theta_e\right)\\ +\Delta R_B\cdot\cos\left(2\theta_e-4\theta_s\right)\\ +\Delta R_C\cdot\cos\left(2\theta_e+4\theta_s\right)\end{pmatrix}\\
& +I_{1p}I_{1n}\begin{pmatrix}\cos\left(2\theta_e+\varphi_{ip}+\varphi_{in}\right)\left(\Delta R_A+\Delta R_B+\Delta R_C\right)-\\ \left(\Delta R_A\cdot\cos\left(\varphi_{ip}-\varphi_{in}\right)+\Delta R_B\cdot\cos\left(\varphi_{ip}-\varphi_{in}+4\theta_s\right)+\Delta R_C\cdot\cos\left(\varphi_{ip}-\varphi_{in}-4\theta_s\right)\right)\end{pmatrix}
\end{aligned}
\tag{2.68}
$$

2.5.2 Unbalanced Inductances

2.5.2.1 Power Ripple

According to (2.18), the power of inductances with unbalanced currents (2.33) injection can be expressed as

$$
p_L=\begin{bmatrix}i_{ap}+i_{an} & i_{bp}+i_{bn} & i_{cp}+i_{cn}\end{bmatrix}\frac{d}{dt}\left(\begin{bmatrix}L_{AA} & M_{AB} & M_{AC}\\ M_{BA} & L_{BB} & M_{BC}\\ M_{CA} & M_{CB} & L_{CC}\end{bmatrix}\begin{bmatrix}i_{ap}+i_{an}\\ i_{bp}+i_{bn}\\ i_{cp}+i_{cn}\end{bmatrix}\right) \tag{2.69}
$$

If the self-inductances (2.14) and mutual inductances (2.15) are balanced and modeled as (2.38) and (2.39), then the (2.69) can be deduced as

$$
\begin{aligned}
p_L = & \frac{3}{2}\omega_e I_{1p}I_{1n}\left(2L_0+M_0\right)\sin\left(2\theta_e+\varphi_{ip}+\varphi_{in}\right)\\
& -\frac{3}{4}\omega_e I_{1p}^2\left(L_2\sin\left(2\varphi_{ip}-\varphi_{L2}\right)+2M_2\sin\left(2\varphi_{ip}-\varphi_{M2}\right)\right)\\
& +\frac{9}{4}\omega_e I_{1n}^2\left(L_2\sin\left(4\theta_e+2\varphi_{in}+\varphi_{L2}\right)+2M_2\sin\left(4\theta_e+2\varphi_{in}+\varphi_{M2}\right)\right)\\
& -3\omega_e I_{1p}I_{1n}\left(L_2\sin\left(2\theta_e-\varphi_{ip}+\varphi_{in}+\varphi_{L2}\right)+2M_2\sin\left(2\theta_e-\varphi_{ip}+\varphi_{in}+\varphi_{M2}\right)\right)
\end{aligned}
\tag{2.70}
$$

As can be seen from (2.70) that there are second and fourth harmonic components in p_L even when the inductances are balanced, and the fourth harmonic power depends on the *N*-sequence currents and the 2h inductances.

When the average self-inductances are unbalanced, i.e. ΔL_{A0}, ΔL_{B0} or ΔL_{C0} are not zero in the modeling (2.25)~(2.27), the power ripple due to ΔL_{A0}, ΔL_{B0} and ΔL_{C0} can be expressed as (2.71), (2.72) and (2.73) respectively.

$$\Delta p_{L\_A} = \begin{bmatrix} i_a & i_b & i_c \end{bmatrix} \frac{d}{dt} \left(\begin{bmatrix} -\Delta L_{A0} & 0 & 0 \\ 0 & 0 & 0 \\ 0 & 0 & 0 \end{bmatrix} \begin{bmatrix} i_a \\ i_b \\ i_c \end{bmatrix} \right)$$
$$= \frac{1}{2} \omega_e \Delta L_{A0} \begin{pmatrix} I_{1p}^2 \cos\left(2\theta_e + 2\varphi_{ip} + 3\theta_s\right) \\ +I_{1n}^2 \cos\left(2\theta_e + 2\varphi_{in} + 3\theta_s\right) \\ +2I_{1p} I_{1n} \cos\left(2\theta_e + \varphi_{ip} + \varphi_{in} + 3\theta_s\right) \end{pmatrix} \tag{2.71}$$

$$\Delta p_{L\_B} = \begin{bmatrix} i_a & i_b & i_c \end{bmatrix} \frac{d}{dt} \left(\begin{bmatrix} 0 & 0 & 0 \\ 0 & -\Delta L_{B0} & 0 \\ 0 & 0 & 0 \end{bmatrix} \begin{bmatrix} i_a \\ i_b \\ i_c \end{bmatrix} \right)$$
$$= \frac{1}{2} \omega_e \Delta L_{B0} \begin{pmatrix} I_{1p}^2 \cos\left(2\theta_e + 2\varphi_{ip} - 5\theta_s\right) \\ +I_{1n}^2 \cos\left(2\theta_e + 2\varphi_{in} - 1\theta_s\right) \\ +2I_{1p} I_{1n} \cos\left(2\theta_e + \varphi_{ip} + \varphi_{in} + 3\theta_s\right) \end{pmatrix} \tag{2.72}$$

$$\Delta p_{L\_C} = \begin{bmatrix} i_a & i_b & i_c \end{bmatrix} \frac{d}{dt} \left(\begin{bmatrix} 0 & 0 & 0 \\ 0 & 0 & 0 \\ 0 & 0 & -\Delta L_{B0} \end{bmatrix} \begin{bmatrix} i_a \\ i_b \\ i_c \end{bmatrix} \right)$$
$$= \frac{1}{2} \omega_e \Delta L_{C0} \begin{pmatrix} I_{1p}^2 \cos\left(2\theta_e + 2\varphi_{ip} - 1\theta_s\right) \\ +I_{1n}^2 \cos\left(2\theta_e + 2\varphi_{in} - 5\theta_s\right) \\ +2I_{1p} I_{1n} \cos\left(2\theta_e + \varphi_{ip} + \varphi_{in} + 3\theta_s\right) \end{pmatrix} \tag{2.73}$$

When the average mutual-inductances are unbalanced, i.e. ΔM_{AB0}, ΔM_{BC0} or ΔM_{CA0} are not zero in the modeling (2.29) ~ (2.31), the power ripple due to ΔM_{AB0} can be expressed as

$$\Delta p_{M\_AB} = \begin{bmatrix} i_a & i_b & i_c \end{bmatrix} \frac{d}{dt} \left(\begin{bmatrix} 0 & -\frac{1}{2}\Delta M_{AB0} & 0 \\ -\frac{1}{2}\Delta M_{AB0} & 0 & 0 \\ 0 & 0 & 0 \end{bmatrix} \begin{bmatrix} i_a \\ i_b \\ i_c \end{bmatrix} \right)$$
$$= \frac{1}{2} \omega_e \Delta M_{AB0} \begin{pmatrix} I_{1p}^2 \cos\left(2\theta_e + 2\varphi_{ip} - 1\theta_s\right) \\ +I_{1n}^2 \cos\left(2\theta_e + 2\varphi_{in} - 5\theta_s\right) \\ -I_{1p} I_{1n} \cos\left(2\theta_e + \varphi_{ip} + \varphi_{in} + 3\theta_s\right) \end{pmatrix} \tag{2.74}$$

In the same way, the power ripple due to the ΔM_{BC0} and ΔM_{CA0} will be (2.75) and (2.76) respectively.

$$\Delta p_{M\_BC} = \begin{bmatrix} i_a & i_b & i_c \end{bmatrix} \frac{d}{dt} \left(\begin{bmatrix} 0 & 0 & 0 \\ 0 & 0 & -\frac{1}{2}\Delta M_{BC0} \\ 0 & -\frac{1}{2}\Delta M_{BC0} & 0 \end{bmatrix} \begin{bmatrix} i_a \\ i_b \\ i_c \end{bmatrix} \right)$$
$$= \frac{1}{2}\omega_e \Delta M_{BC0} \begin{pmatrix} I_{1p}^2 \cos\left(2\theta_e + 2\varphi_{ip} + 3\theta_s\right) \\ +I_{1n}^2 \cos\left(2\theta_e + 2\varphi_{in} + 3\theta_s\right) \\ -I_{1p} I_{1n} \cos\left(2\theta_e + \varphi_{ip} + \varphi_{in} + 3\theta_s\right) \end{pmatrix} \tag{2.75}$$

$$\Delta p_{M\_AC} = \begin{bmatrix} i_a & i_b & i_c \end{bmatrix} \frac{d}{dt} \left(\begin{bmatrix} 0 & 0 & -\frac{1}{2}\Delta M_{CA0} \\ 0 & 0 & 0 \\ -\frac{1}{2}\Delta M_{CA0} & 0 & 0 \end{bmatrix} \begin{bmatrix} i_a \\ i_b \\ i_c \end{bmatrix} \right)$$
$$= \frac{1}{2}\omega_e \Delta M_{CA0} \begin{pmatrix} I_{1p}^2 \cos\left(2\theta_e + 2\varphi_{ip} - 5\theta_s\right) \\ +I_{1n}^2 \cos\left(2\theta_e + 2\varphi_{in} - 1\theta_s\right) \\ -I_{1p} I_{1n} \cos\left(2\theta_e + \varphi_{ip} + \varphi_{in} + 3\theta_s\right) \end{pmatrix} \tag{2.76}$$

If the amplitude of the 2h self-inductances are unbalanced, e.g. $L_{A2} = L_2 + \Delta L_2$, where L_2 is the average 2h self-inductances of L_{A2}, L_{B2} and L_{C2}, the power ripple due to unbalanced self-inductances ΔL_2 can be expressed as

$$\Delta p_{L\_A2} = \begin{bmatrix} i_a & i_b & i_c \end{bmatrix} \frac{d}{dt} \left(\begin{bmatrix} \Delta L_2 \cos\left(2\Delta\theta_A + \varphi_{L2}\right) & 0 & 0 \\ 0 & 0 & 0 \\ 0 & 0 & 0 \end{bmatrix} \begin{bmatrix} i_a \\ i_b \\ i_c \end{bmatrix} \right)$$
$$= \frac{1}{4}\omega_e \Delta L_2 I_{1p}^2 \left(3\sin\left(4\theta_e + 2\varphi_{ip} + \varphi_{L2}\right) - 4\sin\left(2\theta_e + \varphi_{L2}\right) + \sin\left(\varphi_{L2} - 2\varphi_{ip}\right)\right)$$
$$+ \frac{1}{4}\omega_e \Delta L_2 I_{1n}^2 \cdot \left(3\sin\left(4\theta_e + 2\varphi_{in} + \varphi_{L2}\right) - 4\sin\left(2\theta_e + \varphi_{L2}\right) + \sin\left(\varphi_{L2} - 2\varphi_{in}\right)\right) \tag{2.77}$$
$$+ \frac{1}{2}\omega_e \Delta L_2 I_{1p} I_{1n} \begin{pmatrix} 3\sin\left(4\theta_e + \varphi_{ip} + \varphi_{in} + \varphi_{L2}\right) \\ -2\sin\left(2\theta_e + \varphi_{ip} - \varphi_{in} + \varphi_{L2}\right) - 2\sin\left(2\theta_e - \varphi_{ip} + \varphi_{in} + \varphi_{L2}\right) \\ +\sin\left(\varphi_{L2} - \varphi_{ip} - \varphi_{in}\right) \end{pmatrix}$$

In the same way, if $M_{AB2} = M_2 + \Delta M_2$, where M_2 is the average 2h mutual inductance of M_{AB2}, M_{BC2} and M_{CA2}, the power ripple due to unbalanced mutual inductances ΔL_2 can be expressed as

$$
\begin{aligned}
\Delta p_{M\_AB2} &= \begin{bmatrix} i_a \\ i_b \\ i_c \end{bmatrix}^T \frac{d}{dt}\left(\begin{bmatrix} 0 & \Delta M_2 \cos\left(\Delta\theta_A + \Delta\theta_B + \varphi_{M2}\right) & 0 \\ \Delta M_2 \cos\left(\Delta\theta_A + \Delta\theta_B + \varphi_{M2}\right) & 0 & 0 \\ 0 & 0 & 0 \end{bmatrix} \begin{bmatrix} i_a \\ i_b \\ i_c \end{bmatrix} \right) \\
&= -\frac{1}{2}\omega_e \Delta M_2 I_{1p}^2 \begin{pmatrix} 3\sin\left(4\theta_e + 2\varphi_{ip} + \varphi_{M2} - 2\theta_s\right) \\ +2\sin\left(2\theta_e + \varphi_{M2} + 4\theta_s\right) + 2\sin\left(2\theta_e + \varphi_{M2}\right) \\ -\sin\left(\varphi_{M2} - 2\varphi_{ip}\right) \end{pmatrix} \\
&\quad -\frac{1}{2}\omega_e \Delta M_2 I_{1n}^2 \begin{pmatrix} 3\sin\left(4\theta_e + 2\varphi_{in} + \varphi_{M2} + 6\theta_s\right) \\ +2\sin\left(2\theta_e + \varphi_{M2} + 4\theta_s\right) + 2\sin\left(2\theta_e + \varphi_{M2}\right) \\ -\sin\left(\varphi_{M2} - 2\varphi_{ip} + 4\theta_s\right) \end{pmatrix} \\
&\quad -\frac{1}{2}\omega_e \Delta M_2 I_{1p} I_{1n} \begin{pmatrix} 3\sin\left(4\theta_e + \varphi_{ip} + \varphi_{in} + \varphi_{M2} - 4\theta_s\right) \\ +4\sin\left(2\theta_e - \varphi_{ip} + \varphi_{in} + \varphi_{M2}\right) + 4\sin\left(2\theta_e + \varphi_{ip} - \varphi_{in} + \varphi_{M2} + 4\theta_s\right) \\ -\sin\left(\varphi_{M2} - \varphi_{ip} - \varphi_{in} + 2\theta_s\right) \end{pmatrix}
\end{aligned}
\tag{2.78}
$$

If other 2h self-inductances L_{B2}, L_{C2}, or other 2h mutual inductances M_{BC2}, M_{CA2} are unbalanced, the power ripple due to those asymmetries have similar expressions as (2.77) and (2.78) respectively.

Overall, the power ripple with *N*-sequence currents can be summarized as below

1) According to (2.70), there will be 2h power ripple even when the average self-inductances and mutual inductances are balanced. Furthermore, there will be fourth harmonic power ripple if there are 2h inductances;

2) According to (2.71)~(2.76), there will be 2h power ripple due to the unbalanced average self-inductance and mutual inductances;

3) According to (2.77) and (2.78), there will be second and 4th harmonic power ripple due to the unbalanced 2h self-inductances or 2h mutual inductances.

2.5.2.2 Torque Ripple

According to (2.19), the reluctance torque T_{eL} with *N*-sequence currents injection can be rewritten as

$$
T_{eL} = \frac{p}{2}\left[i_s\right]^T \frac{\partial[L_s]}{\partial\theta_e}\left[i_s\right] = \frac{p}{2}\begin{bmatrix} i_{ap} + i_{an} & i_{bp} + i_{bn} & i_{cp} + i_{cn} \end{bmatrix} \frac{\partial[L_s]}{\partial\theta_e} \begin{bmatrix} i_{ap} + i_{an} \\ i_{bp} + i_{bn} \\ i_{cp} + i_{cn} \end{bmatrix} \tag{2.79}
$$

If the self-inductances (2.14) and mutual inductances (2.15) are balanced and modeled as (2.38) and (2.39) respectively, the (2.79) can be deduced as

$$\begin{aligned} T_{eL} = & -\frac{3p}{4} I_{1p}^2 \left(L_2 \sin\left(2\varphi_{ip} - \varphi_{L2}\right) + 2M_2 \sin\left(2\varphi_{ip} - \varphi_{M2}\right)\right) \\ & + \frac{3p}{4} I_{1n}^2 \left(L_2 \sin\left(4\theta_e + 2\varphi_{in} + \varphi_{L2}\right) + 2M_2 \sin\left(4\theta_e + 2\varphi_{in} + \varphi_{M2}\right)\right) \\ & - \frac{3p}{2} I_{1p} I_{1n} \left(L_2 \sin\left(2\theta_e - \varphi_{ip} + \varphi_{in} + \varphi_{L2}\right) + 2M_2 \sin\left(2\theta_e - \varphi_{ip} + \varphi_{in} + \varphi_{M2}\right)\right) \end{aligned} \tag{2.80}$$

As can be seen from (2.80) that there are 2h and fourth harmonic components in T_{eL} no matter the inductances are balanced, and the second and fourth torque harmonics depend on the *N*-sequence currents and the 2h inductances.

When the average self-inductances are unbalanced, e.g. ΔL_{A0}, ΔL_{B0} and ΔL_{C0} are not zero in (2.25)~(2.27), or when the average mutual-inductances are unbalanced, e.g. ΔM_{AB0}, ΔM_{BC0} and ΔM_{CA0} are not zero in (2.29)~(2.31), similar to (2.50)~(2.55), the torque will be not affected by the unbalanced average inductances.

If the amplitudes of the 2h inductances are unbalanced, e.g. $L_{A2} = L_2 + \Delta L_2$, where L_2 is the average 2h self-inductances of L_{A2}, L_{B2} and L_{C2}, the torque ripple due to ΔL_2 can be expressed as

$$\begin{aligned} T_{eL\_A2} &= \begin{bmatrix} i_a & i_b & i_c \end{bmatrix} \left(\frac{\partial}{\partial \theta_e} \begin{bmatrix} \Delta L_2 \cos\left(2\Delta\theta_A + \varphi_{L2}\right) & 0 & 0 \\ 0 & 0 & 0 \\ 0 & 0 & 0 \end{bmatrix} \right) \begin{bmatrix} i_a \\ i_b \\ i_c \end{bmatrix} \\ &= -p\Delta L_2 \sin\left(2\theta_e + \varphi_{L2}\right) \left(I_{1p} \sin\left(\theta_e + \varphi_{ip}\right) + I_{1n} \sin\left(\theta_e + \varphi_{in}\right)\right)^2 \\ &= \frac{p}{4} \Delta L_2 \left\{ \begin{array}{l} I_{1p}^2 \left(\sin\left(4\theta_e + 2\varphi_{ip} + \varphi_{L2}\right) - 2\sin\left(2\theta_e + \varphi_{L2}\right) - \sin\left(2\varphi_{ip} - \varphi_{L2}\right)\right) \\ + I_{1n}^2 \left(\sin\left(4\theta_e + 2\varphi_{in} + \varphi_{L2}\right) - 2\sin\left(2\theta_e + \varphi_{L2}\right) - \sin\left(2\varphi_{in} - \varphi_{L2}\right)\right) \\ + 2I_{1p} I_{1n} \left(\begin{array}{l} -\sin\left(4\theta_e + \varphi_{ip} + \varphi_{in} + \varphi_{L2}\right) + \sin\left(2\theta_e + \varphi_{ip} - \varphi_{in} + \varphi_{L2}\right) \\ + \sin\left(2\theta_e - \varphi_{ip} + \varphi_{in} + \varphi_{L2}\right) - \sin\left(\varphi_{L2} - \varphi_{ip} - \varphi_{in}\right) \end{array} \right) \end{array} \right\} \end{aligned} \tag{2.81}$$

In the same way, if $M_{AB2} = M_2 + \Delta M_2$, where M_2 is the average 2h mutual inductance of M_{AB2}, M_{BC2} and M_{CA2}, the torque ripple due to ΔM_2 can be expressed as (2.82).

If other 2h self-inductances L_{B2}, L_{C2}, or other 2h mutual inductances M_{BC2}, M_{CA2} are unbalanced, the torque ripples due to those asymmetries have similar expressions as (2.81) and (2.82) respectively.

$$
\begin{aligned}
&T_{eL\_MAB2} \\
&= \begin{bmatrix} i_a \\ i_b \\ i_c \end{bmatrix}^T \left(\frac{\partial}{\partial \theta_e} \begin{bmatrix} 0 & \Delta M_2 \cos\left(\Delta\theta_A + \Delta\theta_B + \varphi_{M2}\right) & 0 \\ \Delta M_2 \cos\left(\Delta\theta_A + \Delta\theta_B + \varphi_{M2}\right) & 0 & 0 \\ 0 & 0 & 0 \end{bmatrix} \right) \begin{bmatrix} i_a \\ i_b \\ i_c \end{bmatrix} \\
&= \frac{p}{2}\Delta M_2 \left\{ \begin{array}{l} -I_{1p}^2 \begin{pmatrix} \sin\left(4\theta_e + 2\varphi_{ip} + \varphi_{M2} - 2\theta_s\right) \\ -\sin\left(2\theta_e + \varphi_{M2} - 2\theta_s\right) + \sin\left(2\theta_e + \varphi_{M2}\right) \\ +\sin\left(2\varphi_{ip} - \varphi_{M2}\right) \end{pmatrix} \\ +I_{1n}^2 \begin{pmatrix} \sin\left(4\theta_e + 2\varphi_{in} + \varphi_{M2}\right) \\ +\sin\left(2\theta_e + \varphi_{M2} - 2\theta_s\right) - 2\sin\left(2\theta_e + \varphi_{M2}\right) \\ +\sin\left(-2\varphi_{in} + \varphi_{M2} + 4\theta_s\right) \end{pmatrix} \\ +I_{1p}I_{1n} \begin{pmatrix} \sin\left(4\theta_e + \varphi_{ip} + \varphi_{in} + \varphi_{M2}\right) - \sin\left(4\theta_e + \varphi_{ip} + \varphi_{in} + \varphi_{M2} - 2\theta_s\right) \\ +2\sin\left(2\theta_e + \varphi_{ip} - \varphi_{in} + \varphi_{M2} - 2\theta_s\right) - \sin\left(2\theta_e - \varphi_{ip} + \varphi_{in} + \varphi_{M2}\right) \\ +\sin\left(\varphi_{ip} + \varphi_{in} - \varphi_{M2} + 2\theta_s\right) - \sin\left(\varphi_{ip} + \varphi_{in} - \varphi_{M2}\right) \end{pmatrix} \end{array} \right\}
\end{aligned}
\tag{2.82}
$$

Overall, the torque ripple with *N*-sequence currents can be summarized as below:

1) According to (2.80), there will be second and fourth harmonic torque ripples even when the self-inductances and mutual inductances are balanced. Furthermore, there will be fourth harmonic power ripple if there are the 2h inductances, and the fourth harmonic torque depends on the *N*-sequence currents and the 2h inductances;

2) According to (2.81) and (2.82), there will be second and 4th harmonic power ripples due to the unbalanced 2h self-inductances or mutual inductances;

3) There will be no 2h torque ripple if the average self-inductance and mutual inductances are unbalanced;

4) There will be 2h and fourth harmonic torque ripple due to the unbalanced 2h self-inductance or 2h mutual inductances.

2.5.3 Unbalanced Back-EMFs

2.5.3.1 Power Ripple

According to (2.18), the power p_E resulted from the unbalanced currents (2.33) and unbalanced 3-phase back-EMFs (2.32) can be expressed as

$$p_E = \begin{bmatrix} i_a & i_b & i_c \end{bmatrix} \begin{bmatrix} e_a \\ e_b \\ e_c \end{bmatrix} = \frac{3}{2} \begin{pmatrix} E_{1p} I_{1p} \cos\left(\varphi_{ip}\right) + E_{1n} I_{1n} \cos\left(\varphi_{en} - \varphi_{in}\right) \\ -E_{1p} I_{1n} \cos\left(2\theta_e + \varphi_{in}\right) - E_{1n} I_{1p} \cos\left(2\theta_e + \varphi_{ip} + \varphi_{en}\right) \end{pmatrix} \tag{2.83}$$

As can be seen from (2.83), the 2h power ripple is produced by the interaction of *P*-sequence back-EMFs and *N*-sequence currents and by the interaction of *N*-sequence back-EMFs and *P*-sequence currents.

2.5.3.2 Torque Ripple

According to (2.61), the torque resulted from the unbalanced currents (2.33) and unbalanced back-EMFs (2.32) can be expressed as

$$T_{ePM} = p \frac{p_E}{\omega_e} = \frac{3p}{2\omega_e} \begin{pmatrix} E_{1p} I_{1p} \cos\left(\varphi_{ip}\right) + E_{1n} I_{1n} \cos\left(\varphi_{en} - \varphi_{in}\right) \\ -E_{1p} I_{1n} \cos\left(2\theta_e + \varphi_{in}\right) - E_{1n} I_{1p} \cos\left(2\theta_e + \varphi_{ip} + \varphi_{en}\right) \end{pmatrix} \tag{2.84}$$

As can be seen from (2.84), the 2h torque ripple is produced by the interaction of *P*-sequence back-EMFs and *N*-sequence currents and by the interaction of *N*-sequence back-EMFs and *P*-sequence currents.

2.6 Conclusions

In this chapter, the power ripple and torque ripple due to the generic asymmetries in the PMSG without/with *N*-sequence currents are exclusively investigated, which can be summarized in TABLE 2.2.

With balanced currents injection, there will be 2h power if the resistances, average self-inductances, average mutual inductances and back-EMFs are unbalanced. Furthermore, if the 2h self-inductances and 2h mutual inductances are unbalanced, the fourth harmonic power will be generated. In terms of torque ripple, there is no torque ripple if the system is balanced or when the resistances or average inductances are unbalanced. There will be 2h torque if the back-EMFs are unbalanced. Furthermore, the 4th harmonic torque appears if 2h self-inductances and 2h mutual inductances in the system are unbalanced.

With *N*-sequence currents injection, 2h power will be produced by resistances, inductances, and back-EMFs, no matter whether the system is balanced or not. Furthermore, the 4th harmonic power appears if there are 2h self-inductances or 2h mutual inductances in the system no matter whether they are balanced or not. In terms of torque ripple, the torque ripple with *N*-sequence currents injection is even worse compared with that without *N*-sequence currents injection. There will be 2h torque even the back-EMFs and inductances are balanced.

TABLE 2.2

POWER AND TORQUE RIPPLE WITH UNBALANCED CURRENTS INJECTION

Scenarios	Balanced currents (Without *N*-sequence currents)		Unbalanced currents (With *N*-sequence currents)	
	Power ripple	Torque ripple	Power ripple	Torque ripple
Balanced resistances	/	/	2h	/
Unbalanced resistances	2h	/	2h	/
Balanced inductances	/	/	2h+4h*[1]	2h+4h*[1]
Due to unbalanced average self-inductances	2h	/	2h	/
Due to unbalanced average mutual inductances	2h	/	2h	/
Due to unbalanced 2h self-inductances	2h+4h	2h+4h	2h+4h	2h+4h
Due to unbalanced 2h mutual inductances	2h+4h	2h+4h	2h+4h	2h+4h
Balanced back-EMFs	/	/	2h	2h
Unbalanced back-EMFs	2h	2h	2h	2h

*[1]:2h and 4h components due to 2h inductances

Chapter 3 Current Control of Asymmetric PMSG

3.1 Introduction

In Chapter 2, the power ripple and torque ripple in the unbalanced system without/with *N*-sequence currents are analysed systematically. As shown in TABLE 2.2, there are 2h torque ripple if there are *N*-sequence currents in 3-phase system even when the impedances and 3-phase back-EMFs are balanced. The 2h torque ripple could be reduced by suppressing the *N*-sequence currents if the back-EMFs are balanced. Therefore, it is essential to investigate the current control of asymmetric PMSG aiming for balanced currents.

The conventional current control of 3-phase system is the proportional and integral (PI) current control in the synchronous *dq*-frame, which has become the standard current regulator for 3-phase machine due to its capability of regulating ac currents over a wide frequency range [63, 139]. The mathematical modeling of the ideal 3-phase machine in *dq*-frame can be modeled as a linear resistance and inductance (*RL*) load after the cross-coupling compensation [140]. However, in the unbalanced 3-phase system with unbalanced impedances, there are 2h resistances and inductances in *dq*-frame [100, 104]. When the conventional PI control is applied to the unbalanced system, the 2h impedances will result in unbalanced phase currents due to the limited bandwidth of the PI controller.

To suppress the *N*-sequence currents, the balanced current control aiming for suppressing the *N*-sequence currents has been exclusively investigated [84, 87, 99-102, 104, 108-110, 118, 141, 142]. There are three typical balanced current control methods which can suppress the *N*-sequence currents effectively in unbalanced system, which have been briefly introduced in Section 1.6.1. Although these methods have been employed widely in the unbalanced system, the relationship between these methods has not been evaluated and discussed yet.

In [100], the modelling of grid-connected voltage-sourced rectifier with unbalanced resistances, self-inductances and grid supply voltage was introduced. Although the modelling method can be applied to the unbalanced 3-phase PMSG system, the 2h inductances and the unbalanced mutual inductances were not considered.

In this chapter, the mathematical modelling of asymmetric 3-phase PMSG will be introduced first. The unbalanced resistances, self-inductances, mutual inductances and back-EMFs will be accounted. Then, the conventional current control and three typical balanced

current control methods will be reviewed and evaluated, and the relationship between these methods will be revealed for the first time. Finally, the elaborate experiments of the conventional current control and three typical balanced current control methods will be conducted; the experimental results show that the balanced current control is capable of suppressing the *N*-sequence currents.

3.2 Modeling of Asymmetric PMSG

3.2.1 Mathematical Model in *abc*-frame

The flux linkage equation and voltage equation of 3-phase PMSG in *abc*-frame can be expressed as (2.1) and (2.7) respectively. For the convenience of discussion, they are repeated in this chapter as (3.1) and (3.2) respectively.

$$[\psi_s] = [L_s][i_s] + [\psi_f] \tag{3.1}$$

$$[v_s] = [R_s][i_s] + \frac{d}{dt}[\psi_s] = [R_s][i_s] + \frac{d}{dt}([L_s][i_s]) + [e] \tag{3.2}$$

If the resistances are unbalanced and modeled as (2.20)~(2.23), the resistance matrix (2.9) can be rewritten as

$$[R_s] = \begin{bmatrix} R_A & & \\ & R_B & \\ & & R_C \end{bmatrix} = R_0 I_3 + \begin{bmatrix} -\Delta R_A & & \\ & -\Delta R_B & \\ & & -\Delta R_C \end{bmatrix} \tag{3.3}$$

where I_3 is the unit matrix and is equal to diag(1,1,1), which can be expressed as

$$I_3 = diag(1,1,1) = \begin{bmatrix} 1 & & \\ & 1 & \\ & & 1 \end{bmatrix} \tag{3.4}$$

If the 3-phase back-EMFs are unbalanced, the back-EMFs can be expressed as (2.32). For convenience, it is repeated as follows.

$$[e] = \begin{bmatrix} e_a \\ e_b \\ e_c \end{bmatrix} = \underbrace{E_{1p}\begin{bmatrix} \cos(\theta_e + \pi/2) \\ \cos(\theta_e - 4\theta_s + \pi/2) \\ \cos(\theta_e - 8\theta_s + \pi/2) \end{bmatrix}}_{P-sequence} + \underbrace{E_{1n}\begin{bmatrix} \cos(\theta_e + \pi/2 + \varphi_{en}) \\ \cos(\theta_e - 8\theta_s + \pi/2 + \varphi_{en}) \\ \cos(\theta_e - 4\theta_s + \pi/2 + \varphi_{en}) \end{bmatrix}}_{N-sequence} \tag{3.5}$$

If the average self-inductances and average mutual inductances are unbalanced and modeled as (2.24)~(2.31) while the 2h inductances are balanced, (2.17) can be rewritten as (3.6).

$$[L]=\underbrace{\begin{bmatrix} L_0 & -\frac{M_0}{2} & -\frac{M_0}{2} \\ -\frac{M_0}{2} & L_0 & -\frac{M_0}{2} \\ -\frac{M_0}{2} & -\frac{M_0}{2} & L_0 \end{bmatrix}+\begin{bmatrix} L_2\cos(2\theta_e) & M_2\cos(2\theta_e-4\theta_s) & M_2\cos(2\theta_e-8\theta_s) \\ M_2\cos(2\theta_e-4\theta_s) & L_2\cos(2\theta_e-8\theta_s) & M_2\cos(2\theta_e) \\ M_2\cos(2\theta_e-8\theta_s) & M_2\cos(2\theta_e) & L_2\cos(2\theta_e-4\theta_s) \end{bmatrix}}_{Balanced}+\underbrace{\begin{bmatrix} -\Delta L_{A0} & -\frac{1}{2}\Delta M_{AB0} & -\frac{1}{2}\Delta M_{AC0} \\ -\frac{1}{2}\Delta M_{AB0} & -\Delta L_{B0} & -\frac{1}{2}\Delta M_{BC0} \\ -\frac{1}{2}\Delta M_{AC0} & -\frac{1}{2}\Delta M_{BC0} & -\Delta L_{C0} \end{bmatrix}}_{unbalanced} \tag{3.6}$$

3.2.2 Mathematical Model in *αβ*-frame

Applying the Clark transformation (A.2) and inverse Clark transformation (A.4) to (3.1) and (3.2), the flux-linkage and voltage equation in *αβ*-frame can be expressed as

$$\left[\psi_{\alpha\beta}\right]=\left[L_{\alpha\beta}\right]\left[i_{\alpha\beta}\right]+\left[\psi_{f\alpha\beta}\right] \tag{3.7}$$

$$\left[v_{\alpha\beta}\right]=\left[R_{\alpha\beta}\right]\left[i_{\alpha\beta}\right]+\frac{d}{dt}\left[\psi_{\alpha\beta}\right] \tag{3.8}$$

where $[v_{\alpha\beta}]$ is equal to $T_{\alpha\beta*}[v_s]$; $[i_{\alpha\beta}]$ is equal to $T_{\alpha\beta*}[i_s]$; $[\psi_{\alpha\beta}]$ is equal to $T_{\alpha\beta*}[\psi_s]$; $[\psi_{f\alpha\beta}]$ is equal to $T_{\alpha\beta*}[\psi_f]$; $[R_{\alpha\beta}]$ and is $[L_{\alpha\beta}]$ can be expressed as (3.9) and (3.10) respectively.

$$\left[R_{\alpha\beta}\right]=T_{\alpha\beta}\left[R_s\right]T_{\alpha\beta\_inv} \tag{3.9}$$

$$\left[L_{\alpha\beta}\right]=T_{\alpha\beta}\left[L_s\right]T_{\alpha\beta\_inv} \tag{3.10}$$

$[R_{\alpha\beta}]$ can be deduced as

$$\begin{aligned}\left[R_{\alpha\beta}\right]=T_{\alpha\beta}\left[R_s\right]T_{\alpha\beta\_inv}&=\left(R_0-\left(1/3\right)\left(\Delta R_A+\Delta R_B+\Delta R_C\right)\right)I_2 \\ &+\frac{\Delta R_A}{3}M_1\left(0\theta_s\right)+\frac{\Delta R_B}{3}M_1\left(4\theta_s\right)+\frac{\Delta R_C}{3}M_1\left(8\theta_s\right)\end{aligned} \tag{3.11}$$

where

$$M_1\left(\theta\right)=\begin{bmatrix}-\cos\left(\theta\right) & \sin(\theta) \\ \sin(\theta) & \cos\left(\theta\right)\end{bmatrix} \tag{3.12}$$

$$I_2 = \begin{bmatrix} 1 & \\ & 1 \end{bmatrix} \tag{3.13}$$

$[L_{\alpha\beta}]$ can be deduced as

$$\begin{aligned}
[L_{\alpha\beta}] = & \left(L_0 + \frac{M_0}{2} \right) I_2 + \left(\frac{L_2}{2} + M_2 \right) \begin{bmatrix} \cos(2\theta_e) & \sin(2\theta_e) \\ \sin(2\theta_e) & -\cos(2\theta_e) \end{bmatrix} \\
& - \left(\frac{1}{3} \left(\Delta L_{A0} + \Delta L_{B0} + \Delta L_{C0} \right) I_2 \right) + \left(\frac{1}{6} \left(\Delta M_{AB0} + \Delta M_{BC0} + \Delta M_{AC0} \right) I_2 \right) \\
& + \left(\frac{1}{3} \Delta L_{A0} + \frac{1}{3} \Delta M_{BC0} \right) M_1 (0\theta_s) \\
& + \left(\frac{1}{3} \Delta L_{B0} + \frac{1}{3} \Delta M_{AC0} \right) M_1 (4\theta_s) \\
& + \left(\frac{1}{3} \Delta L_{C0} + \frac{1}{3} \Delta M_{AB0} \right) M_1 (8\theta_s)
\end{aligned} \tag{3.14}$$

The back-EMFs in $\alpha\beta$-frame can be expressed as

$$\left[e_{\alpha\beta} \right] = \frac{d}{dt} \left[\psi_{f\alpha\beta} \right] = \frac{d}{dt} \left(T_{\alpha\beta} \left[\psi_f \right] \right) = T_{\alpha\beta} \frac{d}{dt} \left(\left[\psi_f \right] \right) = T_{\alpha\beta} \left[e \right] \tag{3.15}$$

Substitute (3.5) into (3.15), the back-EMFs in $\alpha\beta$-frame can be rewritten as

$$\left[e_{\alpha\beta} \right] = T_{\alpha\beta} \left[e \right] = E_{1p} \begin{bmatrix} -\sin(\theta_e) \\ \cos(\theta_e) \end{bmatrix} + E_{1n} \begin{bmatrix} -\sin(\theta_e + \theta_{en}) \\ -\cos(\theta_e + \theta_{en}) \end{bmatrix} \tag{3.16}$$

3.2.3 Mathematical Model in PSRF and NSRF

In this section, the *P*-sequence reference frame (PSRF) and *N*-sequence reference frame (NSRF) will be introduced first, and then the mathematical modelling in PSRF and NSRF will be presented.

3.2.3.1 Relationship between PSRF and NSRF

According to the symmetrical-component theory [91], the 3-phase voltages, currents and flux-linkages can be decomposed as *P*- and *N*-sequence components in the 3-phase system without access of neutral point. The general *P*- and *N*-sequence components can be expressed as

$$\begin{bmatrix} F_a \\ F_b \\ F_c \end{bmatrix} = \underbrace{\begin{bmatrix} F_p \cos(\theta - 0\theta_s + \theta_p) \\ F_p \cos(\theta - 4\theta_s + \theta_p) \\ F_p \cos(\theta - 8\theta_s + \theta_p) \end{bmatrix}}_{P-sequence} + \underbrace{\begin{bmatrix} F_n \cos(\theta - 0\theta_s + \theta_n) \\ F_n \cos(\theta - 8\theta_s + \theta_n) \\ F_n \cos(\theta - 4\theta_s + \theta_n) \end{bmatrix}}_{N-sequence} \tag{3.17}$$

where F_p and F_n are the amplitude of *P*-sequence and *N*-sequence components respectively; θ_p and θ_n are the displacement angle of *P*-sequence and *N*-sequence components respectively. By Clark transformation(A.2), the *P*-sequence and *N*-sequence components in *αβ*-frame can be expressed as (3.18) and (3.19) respectively. As the θ increases, the trajectory of (3.18) will rotate in positive direction, while the trajectory of (3.19) will rotate in opposite direction.

$$F_{\alpha\beta}^{p} = F_p e^{j(\theta+\theta_p)} \tag{3.18}$$

$$F_{\alpha\beta}^{n} = F_n e^{-j(\theta+\theta_n)} \tag{3.19}$$

Applying the Park transformation (A.6) to (3.18) and (3.19) respectively, the *P*-sequence components and *N*-sequence components in *dq*-frame can be expressed as (3.20) and (3.21) respectively.

$$F_{dq}^{p} = F_p e^{j\theta_p} = F_p \cos(\theta_p) + jF_p \sin(\theta_p) \tag{3.20}$$

$$F_{dq}^{n} = F_n e^{-j(2\theta+\theta_n)} = F_n \cos(2\theta+\theta_n) - jF_n \sin(2\theta+\theta_n) \tag{3.21}$$

Therefore, the *P*-sequence components will be converted to DC components in *dq*-frame, while the *N*-sequence components will be converted to 2h components in *dq*-frame.

In the unbalanced system, the positive sequence reference frame (PSRF) and negative sequence frame (NSRF) are usually employed for analysis. The relationship between the *αβ*-frame and PSRF is shown in Fig.3.1. It shows that the PSRF is actually the same as the synchronous *dq*-frame. Therefore, the projection of vector $F_{\alpha\beta}$ on *d*-axis and *q*-axis of the PSRF can be obtained by

$$\begin{bmatrix} F_d^+ \\ F_d^+ \end{bmatrix} = T_{dq}(\theta) \begin{bmatrix} F_\alpha \\ F_\beta \end{bmatrix} \tag{3.22}$$

(3.23) can be rewritten as (3.23) in the form of vector.

$$F_{dq}^{+} = e^{-j\theta} F_{\alpha\beta} \tag{3.23}$$

where

$$F_{dq}^{+} = F_d^{+} + jF_q^{+} \tag{3.24}$$

where F_d^+ and F_q^+ are the projection of $F_{\alpha\beta}$ on the *d*-axis and *q*-axis of PSRF respectively.

The relationship between the *αβ*-frame and NSRF is shown in Fig.3.2, where the *d*-axis of NSRF rotates in the opposite direction of the rotor position. Therefore, the projection of vector $F_{\alpha\beta}$ on *d*-axis and *q*-axis of the NSRF can be obtained by

$$\begin{bmatrix} F_d^- \\ F_d^- \end{bmatrix} = T_{dq}(-\theta) \begin{bmatrix} F_\alpha \\ F_\beta \end{bmatrix} \tag{3.25}$$

(3.25) can also be rewritten as (3.26) in the form of vector.

$$F_{dq}^- = e^{j\theta} F_{\alpha\beta} \tag{3.26}$$

where

$$F_{dq}^- = F_d^- + jF_q^- \tag{3.27}$$

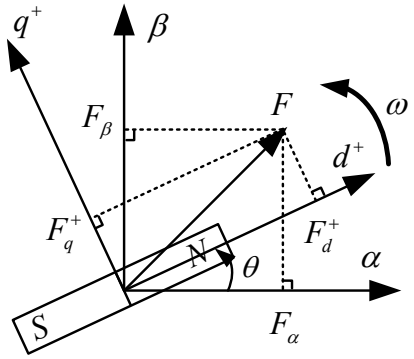

Fig.3.1 Relationship between $\alpha\beta$-frame and PSRF.

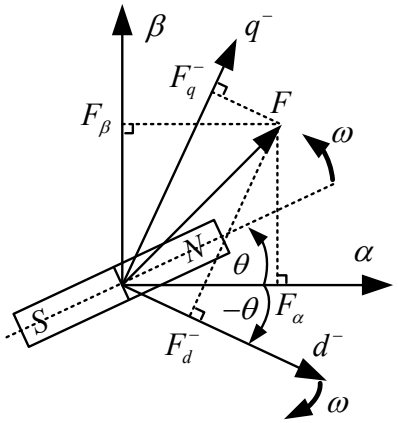

Fig.3.2 Relationship between $\alpha\beta$-frame and NSRF.

Therefore, the *P*-sequence components in NSRF can be expressed as

$$F_{dq}^{p-} = e^{j\theta} F_{\alpha\beta}^{p} = e^{j\theta} F_p e^{j(\theta+\theta_p)} = F_p e^{j(2\theta+\theta_p)} \tag{3.28}$$

While the *N*-sequence components in NSRF can be expressed as

$$F_{dq}^{n-} = e^{j\theta} F_{\alpha\beta}^{n} = e^{j\theta} F_n e^{-j(\theta+\theta_n)} = F_n e^{-j\theta_n} \tag{3.29}$$

As can be seen from (3.28) and (3.29), the *P*-sequence and *N*-sequence components in NSRF are converted to 2h components and DC value respectively.

Overall, the unbalanced components in *abc*-frame, *αβ*-frame and synchronous frame can be summarized as TABLE 3.1.

TABLE 3.1
UNBALANCED COMPONENTS IN DIFFERENT FRAMES

abc-frame	$\begin{bmatrix} F_a \\ F_b \\ F_c \end{bmatrix} = \underbrace{\begin{bmatrix} F_p \cos(\theta - 0\theta_s + \theta_p) \\ F_p \cos(\theta - 4\theta_s + \theta_p) \\ F_p \cos(\theta - 8\theta_s + \theta_p) \end{bmatrix}}_{P-sequence} + \underbrace{\begin{bmatrix} F_n \cos(\theta - 0\theta_s + \theta_n) \\ F_n \cos(\theta - 8\theta_s + \theta_n) \\ F_n \cos(\theta - 4\theta_s + \theta_n) \end{bmatrix}}_{N-sequence}$
αβ-frame	$F_{\alpha\beta} = \underbrace{F^p_{\alpha\beta}}_{P-sequence} + \underbrace{F^n_{\alpha\beta}}_{N-Sequence} = \frac{2}{3}\left(F_a + F_b e^{j2\pi/3} + F_b e^{j4\pi/3}\right)$ where $F^p_{\alpha\beta} = F_p e^{j(\theta+\theta_p)}$, $F^n_{\alpha\beta} = F_n e^{-j(\theta+\theta_n)}$
PSRF (Conventional synchronous *dq*-frame)	$F^+_{dq} = e^{-j\theta} F_{\alpha\beta} = \underbrace{F_p e^{j\theta_p}}_{P-sequence} + \underbrace{F_n e^{-j(2\theta+\theta_n)}}_{N-sequence}$
NSRF	$F^-_{dq} = e^{j\theta} F_{\alpha\beta} = \underbrace{F_p e^{j(2\theta+\theta_p)}}_{P-sequence} + \underbrace{F_n e^{-j\theta_n}}_{N-sequence}$

3.2.3.2 Mathematical modeling in PSRF

By applying the Park transformation (3.22) to the flux-linkage equation (3.7) and voltage equation (3.8) in *αβ*-frame respectively, the flux-linkage and voltage equation in PSRF can be expressed as

$$\left[\psi^+_{dq}\right] = \left[L^+_{dq}\right]\left[i^+_{dq}\right] + \left[\psi^+_{fdq}\right] \tag{3.30}$$

$$\left[v^+_{dq}\right] = \left[R^+_{dq}\right]\left[i^+_{dq}\right] + \frac{d}{dt}\left[\psi^+_{dq}\right] + \omega_e \begin{bmatrix} -\psi^+_q \\ \psi^+_d \end{bmatrix} \tag{3.31}$$

where the superscript "+" means the variables are in PSRF, the voltage, current, flux-linkage, and impedance in PSRF can be expressed as

$$\begin{aligned} &\left[v^+_{dq}\right] = T_{dq}(\theta_e)\left[v_{s\alpha\beta}\right], \quad \left[i^+_{dq}\right] = T_{dq}(\theta_e)\left[i_{\alpha\beta}\right] \\ &\left[\psi^+_{dq}\right] = T_{dq}(\theta_e)\left[\psi_{s\alpha\beta}\right], \quad \left[\psi^+_{fdq}\right] = T_{dq}(\theta_e)\left[\psi_{f\alpha\beta}\right] \end{aligned} \tag{3.32}$$

$$\left[R^+_{dq}\right] = T_{dq}(\theta_e)\left[R_{\alpha\beta}\right]T_{dq}(\theta_e)^{-1} \tag{3.33}$$

$$\left[L^+_{dq}\right] = T_{dq}(\theta_e)\left[L_{\alpha\beta}\right]T_{dq}(\theta_e)^{-1} \tag{3.34}$$

and the back-EMFs in PSRF can be expressed as

$$\left[e_{dq}^{+}\right]=\frac{d}{dt}\left[\psi_{fdq}^{+}\right]+\omega_e\begin{bmatrix}-\psi_{fq}^{+}\\ \psi_{fd}^{+}\end{bmatrix} \tag{3.35}$$

It can be deduced that

$$\left[e_{dq}^{+}\right]=T_{dq}\left(\theta_e\right)\left[e_{\alpha\beta}\right] \tag{3.36}$$

Then the resistance matrix in PSRF can be deduced as

$$\begin{aligned}\left[R_{dq}^{+}\right]=&\left(R_0-\left(1/3\right)\left(\Delta R_A+\Delta R_B+\Delta R_C\right)\right)I_2\\&+\frac{\Delta R_A}{3}M_1\left(2\theta_e+0\theta_s\right)+\frac{\Delta R_B}{3}M_1\left(2\theta_e+4\theta_s\right)+\frac{\Delta R_C}{3}M_1\left(2\theta_e+8\theta_s\right)\end{aligned} \tag{3.37}$$

The inductance matrix in PSRF can be expressed as

$$\begin{aligned}\left[L_{dq}^{+}\right]=&\left(L_0+\frac{1}{2}M_0\right)I_2+\left(\frac{1}{2}L_2+M_2\right)J_2\\&-\left(\frac{1}{3}\left(\Delta L_{A0}+\Delta L_{B0}+\Delta L_{C0}\right)I_2\right)+\left(\frac{1}{6}\left(\Delta M_{AB0}+\Delta M_{BC0}+\Delta M_{AC0}\right)I_2\right)\\&+\left(\frac{1}{3}\Delta L_{A0}+\frac{1}{3}\Delta M_{BC0}\right)M_1\left(2\theta_e+0\theta_s\right)\\&+\left(\frac{1}{3}\Delta L_{B0}+\frac{1}{3}\Delta M_{AC0}\right)M_1\left(2\theta_e+4\theta_s\right)\\&+\left(\frac{1}{3}\Delta L_{C0}+\frac{1}{3}\Delta M_{AB0}\right)M_1\left(2\theta_e+8\theta_s\right)\end{aligned} \tag{3.38}$$

where

$$J_2=\begin{bmatrix}1 & \\ & -1\end{bmatrix} \tag{3.39}$$

As can be seen from (3.37) and (3.38), when the impedances are unbalanced, there will be 2h impedances in the PSRF.

Substitute (3.16) into (3.36), the back-EMFs in PSRF can be rewritten as

$$\left[e_{dq}^{+}\right]=\left[e_{dq}^{+}\right]=T_{dq}\left(\theta_e\right)\left[e_{\alpha\beta}\right]=E_{1p}\begin{bmatrix}0\\1\end{bmatrix}+E_{1n}\begin{bmatrix}-\sin\left(2\theta_e+\theta_{en}\right)\\-\cos\left(2\theta_e+\theta_{en}\right)\end{bmatrix} \tag{3.40}$$

As can be seen from (3.40), the *P*- and *N*-sequence back-EMFs are converted to DC components and 2h components in PSRF respectively.

3.2.3.3 Mathematical Modelling in NSRF

By applying (3.25) to the flux-linkage equation (3.7) and voltage equation (3.8) in $\alpha\beta$-frame respectively, the flux-linkage and voltage equations in NSRF can be expressed as

$$\left[\psi_{dq}^{-}\right]=\left[L_{dq}^{-}\right]\left[i_{dq}^{-}\right]+\left[\psi_{fdq}^{-}\right] \tag{3.41}$$

$$\left[v_{dq}^{-}\right]=\left[R_{dq}^{-}\right]\left[i_{dq}^{-}\right]+\frac{d}{dt}\left[\psi_{dq}^{-}\right]+\omega_e\begin{bmatrix}-\psi_q^{-}\\ \psi_d^{-}\end{bmatrix} \tag{3.42}$$

where the superscript "$^-$" means the variables are in NSRF, and the voltage, current, flux-linkage, and impedance in NSRF can be expressed as

$$\begin{aligned}&\left[v_{dq}^{-}\right]=T_{dq}\left(-\theta_e\right)\left[v_{s\alpha\beta}\right],\quad \left[i_{dq}^{-}\right]=T_{dq}\left(-\theta_e\right)\left[i_{\alpha\beta}\right]\\ &\left[\psi_{dq}^{-}\right]=T_{dq}\left(-\theta_e\right)\left[\psi_{s\alpha\beta}\right],\ \left[\psi_{fdq}^{-}\right]=T_{dq}\left(-\theta_e\right)\left[\psi_{f\alpha\beta}\right]\end{aligned} \tag{3.43}$$

$$\left[R_{dq}^{-}\right]=T_{dq}\left(-\theta_e\right)\left[R_{\alpha\beta}\right]T_{dq}\left(-\theta_e\right)^{-1} \tag{3.44}$$

$$\left[L_{dq}^{-}\right]=T_{dq}\left(-\theta_e\right)\left[L_{\alpha\beta}\right]T_{dq}\left(-\theta_e\right)^{-1} \tag{3.45}$$

The back-EMFs in NSRF can be expressed as

$$\left[e_{dq}^{-}\right]=\frac{d}{dt}\left[\psi_{fdq}^{-}\right]+\omega_e\begin{bmatrix}-\psi_{fq}^{-}\\ \psi_{fd}^{-}\end{bmatrix} \tag{3.46}$$

Substitute (3.16) into (3.46), the back-EMFs in NSRF can be rewritten as

$$\left[e_{dq}^{-}\right]=\left[e_{dq}^{-}\right]=T_{dq}\left(-\theta_e\right)\left[e_{\alpha\beta}\right]=E_{1p}\begin{bmatrix}-\sin\left(2\theta_e\right)\\ \cos\left(2\theta_e\right)\end{bmatrix}+E_{1n}\begin{bmatrix}-\sin\left(\theta_{en}\right)\\ -\cos\left(\theta_{en}\right)\end{bmatrix} \tag{3.47}$$

As can be seen from (3.47), the *P*- and *N*-sequence back-EMFs are converted to 2h components and DC components in NSRF respectively.

According to (3.44), the resistance matrix in NSRF can be deduced as

$$\begin{aligned}\left[R_{dq}^{-}\right]=&\left(R_0-\left(1/3\right)\left(\Delta R_A+\Delta R_B+\Delta R_C\right)\right)I_2\\ &+\frac{\Delta R_A}{3}M_1\left(-2\theta_e+0\theta_s\right)\\ &+\frac{\Delta R_B}{3}M_1\left(-2\theta_e+4\theta_s\right)\\ &+\frac{\Delta R_C}{3}M_1\left(-2\theta_e+8\theta_s\right)\end{aligned} \tag{3.48}$$

According to (3.45), the inductance matrix in NSRF can be deduced as

$$
\begin{aligned}
\left[L_{dq}^{-}\right] = & \left(L_0 + \frac{M_0}{2}\right) I_2 + \left(\frac{L_2}{2} + M_2\right) \begin{bmatrix} \cos(4\theta_e) & \sin(4\theta_e) \\ \sin(4\theta_e) & -\cos(4\theta_e) \end{bmatrix} \\
& - \left(\frac{1}{3}\left(\Delta L_{A0} + \Delta L_{B0} + \Delta L_{C0}\right) I_2\right) + \left(\frac{1}{6}\left(\Delta M_{AB0} + \Delta M_{BC0} + \Delta M_{AC0}\right) I_2\right) \\
& + \left(\frac{1}{3}\Delta L_{A0} + \frac{1}{3}\Delta M_{BC0}\right) M_1\left(-2\theta_e + 0\theta_s\right) \\
& + \left(\frac{1}{3}\Delta L_{B0} + \frac{1}{3}\Delta M_{AC0}\right) M_1\left(-2\theta_e + 4\theta_s\right) \\
& + \left(\frac{1}{3}\Delta L_{C0} + \frac{1}{3}\Delta M_{AB0}\right) M_1\left(-2\theta_e + 8\theta_s\right)
\end{aligned}
\tag{3.49}
$$

As can be seen from (3.48) and (3.49), when the impedances are unbalanced, there are 2h impedances in the NSRF. It is worth noting that there are fourth harmonic inductances in the NSRF if there are 2h self-inductances or mutual inductances.

As listed in Table 3.1 in Section 3.2.3.1, the *N*-sequence currents will be converted to DC currents in NSRF. As there are 2h and fourth harmonic inductances in (3.49), there will be fourth harmonic voltages in NSRF. Therefore, the interaction of DC currents and fourth harmonic voltages in NSRF will result in fourth harmonic power, which is in accordance with the power ripple analysis in Table 2.2.

3.3 Evaluation of Current Control of Asymmetric PMSG

As shown in (3.37) and (3.38), when the impedances of PMSG are unbalanced, there are 2h resistances and 2h inductances in the synchronous *dq*-frame (PSRF). Meanwhile, there are also mutual 2h impedances between *d*-axis and *q*-axis. Since the conventional current control can only trace DC currents in *dq*-frame without tracing error in the linear system. Therefore, it is not applicable to eliminate the *N*-sequence currents in an unbalanced system.

In this section, the PR control in *αβ*-frame, dual current control, and PI-R control in PSRF will be reviewed and evaluated. The brief introduction of these three methods has been presented in Section 1.6.1. It is well known that these methods are all capable of suppressing the 2h current and have been employed widely in various applications. However, the relationship between these methods has not been investigated. In this chapter, the relationship between those current control methods will be revealed for the first time.

3.3.1 PR control

The PR control in $\alpha\beta$-frame can be illustrated in Fig.3.3, where the currents in α-axis and β-axis are regulated by PR control respectively with the resonant control at the centre frequency of fundamental.

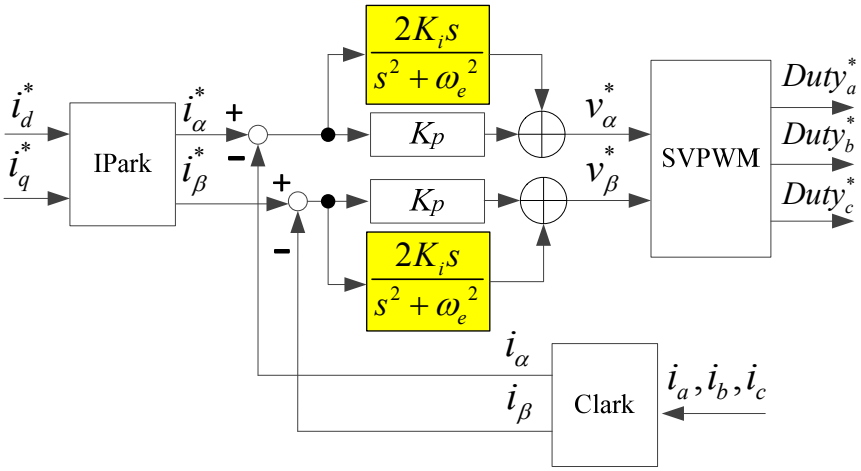

Fig.3.3 PR control in $\alpha\beta$-frame [99-101].

As illustrated in Fig.3.3, the PR controllers in $\alpha\beta$-frame can be expressed as

$$\begin{bmatrix} v_\alpha^* \\ v_\beta^* \end{bmatrix} = \begin{bmatrix} K_p + \dfrac{2K_i s}{s^2+\omega_e^2} & \\ & K_p + \dfrac{2K_i s}{s^2+\omega_e^2} \end{bmatrix} \begin{bmatrix} \Delta i_\alpha \\ \Delta i_\beta \end{bmatrix} \tag{3.50}$$

where

$$\begin{bmatrix} \Delta i_\alpha \\ \Delta i_\beta \end{bmatrix} = \begin{bmatrix} i_\alpha^* - i_\alpha \\ i_\beta^* - i_\beta \end{bmatrix} \tag{3.51}$$

Defining

$$\begin{bmatrix} x_\alpha \\ x_\beta \end{bmatrix} = \begin{bmatrix} \dfrac{2K_i s}{s^2+\omega_e^2} & \\ & \dfrac{2K_i s}{s^2+\omega_e^2} \end{bmatrix} \begin{bmatrix} \Delta i_\alpha \\ \Delta i_\beta \end{bmatrix} \tag{3.52}$$

then (3.50) can be rewritten as

$$\begin{bmatrix} v_\alpha^* \\ v_\beta^* \end{bmatrix} = K_p \begin{bmatrix} \Delta i_\alpha \\ \Delta i_\beta \end{bmatrix} + \begin{bmatrix} x_\alpha \\ x_\beta \end{bmatrix} \tag{3.53}$$

Since

$$\begin{bmatrix} v_d^* \\ v_q^* \end{bmatrix} = T_{dq}(\theta)\begin{bmatrix} v_\alpha^* \\ v_\beta^* \end{bmatrix}, \begin{bmatrix} \Delta i_d \\ \Delta i_q \end{bmatrix} = T_{dq}(\theta)\begin{bmatrix} \Delta i_\alpha \\ \Delta i_\beta \end{bmatrix}, \begin{bmatrix} x_d \\ x_q \end{bmatrix} = T_{dq}(\theta)\begin{bmatrix} x_\alpha \\ x_\beta \end{bmatrix} \tag{3.54}$$

where

$$\begin{bmatrix} \Delta i_d \\ \Delta i_q \end{bmatrix} = \begin{bmatrix} i_d^* - i_d \\ i_q^* - i_q \end{bmatrix} \tag{3.55}$$

Applying the Park transformation to (3.53), (3.56) can be obtained.

$$\begin{bmatrix} v_d^* \\ v_q^* \end{bmatrix} = K_p \begin{bmatrix} \Delta i_d \\ \Delta i_q \end{bmatrix} + \begin{bmatrix} x_d \\ x_q \end{bmatrix} \tag{3.56}$$

The time-domain form of (3.52) in the $\alpha\beta$-frame can be expressed as

$$\frac{d^2 y}{dt^2}\begin{bmatrix} x_\alpha \\ x_\beta \end{bmatrix} + \omega_e^2 \begin{bmatrix} x_\alpha \\ x_\beta \end{bmatrix} = 2K_i \frac{d}{dt}\left(\begin{bmatrix} \Delta i_\alpha \\ \Delta i_\beta \end{bmatrix}\right) \tag{3.57}$$

Substituting (3.54) into (3.57), it can be obtained that

$$\frac{d^2 y}{dt^2}\left(T_{dq}(\theta)^{-1}\begin{bmatrix} x_d \\ x_q \end{bmatrix}\right) + \omega_e^2 T_{dq}(\theta)^{-1}\begin{bmatrix} x_d \\ x_q \end{bmatrix} = 2K_i \frac{d}{dt}\left(T_{dq}(\theta)^{-1}\begin{bmatrix} \Delta i_d \\ \Delta i_q \end{bmatrix}\right) \tag{3.58}$$

The frequency-domain of (3.58) in dq-frame can be expressed as

$$\begin{bmatrix} s^2 & -2\omega_e s \\ 2\omega_e s & s^2 \end{bmatrix}\begin{bmatrix} x_d \\ x_q \end{bmatrix} = 2K_i \begin{bmatrix} s & -\omega_e \\ \omega_e & s \end{bmatrix}\begin{bmatrix} \Delta i_d \\ \Delta i_q \end{bmatrix} \tag{3.59}$$

Solving (3.59), $[x_d\, x_q]^{\mathrm{T}}$ can be expressed as

$$\begin{bmatrix} x_d \\ x_q \end{bmatrix} = \begin{bmatrix} \dfrac{K_i}{s} + \dfrac{K_i s}{s^2 + (2\omega_e)^2} & \dfrac{2K_i\omega_e}{s^2 + (2\omega_e)^2} \\ -\dfrac{2K_i\omega_e}{s^2 + (2\omega_e)^2} & \dfrac{K_i}{s} + \dfrac{K_i s}{s^2 + (2\omega_e)^2} \end{bmatrix}\begin{bmatrix} \Delta i_d \\ \Delta i_q \end{bmatrix} \tag{3.60}$$

Substituting (3.60) into (3.56), the current regulators in dq-frame can be obtained and expressed as

$$\begin{bmatrix} v_d^* \\ v_q^* \end{bmatrix} = \begin{bmatrix} K_p + \dfrac{K_i}{s} + \dfrac{K_i s}{s^2 + (2\omega_e)^2} & \dfrac{2K_i\omega_e}{s^2 + (2\omega_e)^2} \\ -\dfrac{2K_i\omega_e}{s^2 + (2\omega_e)^2} & K_p + \dfrac{K_i}{s} + \dfrac{K_i s}{s^2 + (2\omega_e)^2} \end{bmatrix}\begin{bmatrix} \Delta i_d \\ \Delta i_q \end{bmatrix} \tag{3.61}$$

Therefore, the PR control in $\alpha\beta$-frame is equivalent to (3.61) in synchronous dq-frame, which is consistent with the conclusions in [97].

It is worth noting that the resonant control in (3.50) cannot be realized in a physical filter network since it is lossless [97], an alternative method is approximating an ideal integral using a high-gain low-pass filter $1/(s+\omega_c)$. Therefore, the resonant control in (3.50) can be rewritten as [97]

$$R(\omega_0)=\frac{2K_i\omega_c(s+\omega_c)}{s^2+2\omega_c s+\omega_0^2+\omega_c^2} \tag{3.62}$$

where ω_c is the cut-off frequency of low-pass filter, ω_0 is the resonant frequency, which is equal to ω_e in this case. Assuming $\omega_c << \omega_0$, (3.62) can be further simplified as

$$R(\omega_0)=\frac{2K_i\omega_c s}{s^2+2\omega_c s+\omega_0^2} \tag{3.63}$$

3.3.2 Dual Current Control

The flowchart of dual current control with notch filter [102] is shown in Fig.3.4, where the *P*-sequence currents are regulated in PSRF and *N*-sequence currents are regulated in NSRF respectively. The sequential current components need to be extracted as current feedback. Therefore, the notch filters are employed to extract the *P*-sequence currents and *N*-sequence currents. Although the sequential current components can be regulated effectively, the dynamic performance may be compromised due to the notch filter.

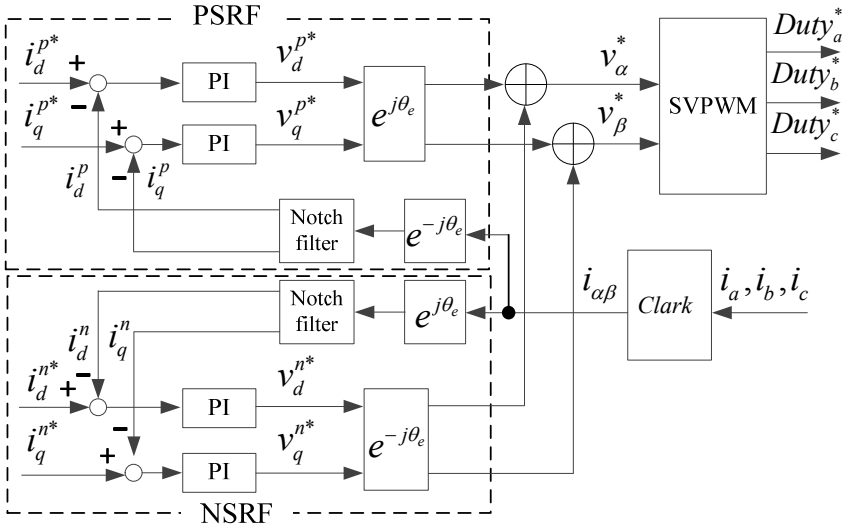

Fig.3.4 Dual current control with notch filter [102].

To improve the dynamic performance, the dual current control without notch filter was investigated in [104] and can be illustrated in Fig.3.5. By regulation of the currents (including the *P*-sequence and *N*-sequence currents) in PSRF and NSRF respectively, the DC components of currents in PSRF and NSRF can be regulated, which means the *P*-sequence

currents in PSRF and *N*-sequence currents in NSRF can be regulated effectively. If the current references in NSRF are zero, the balanced currents can be achieved.

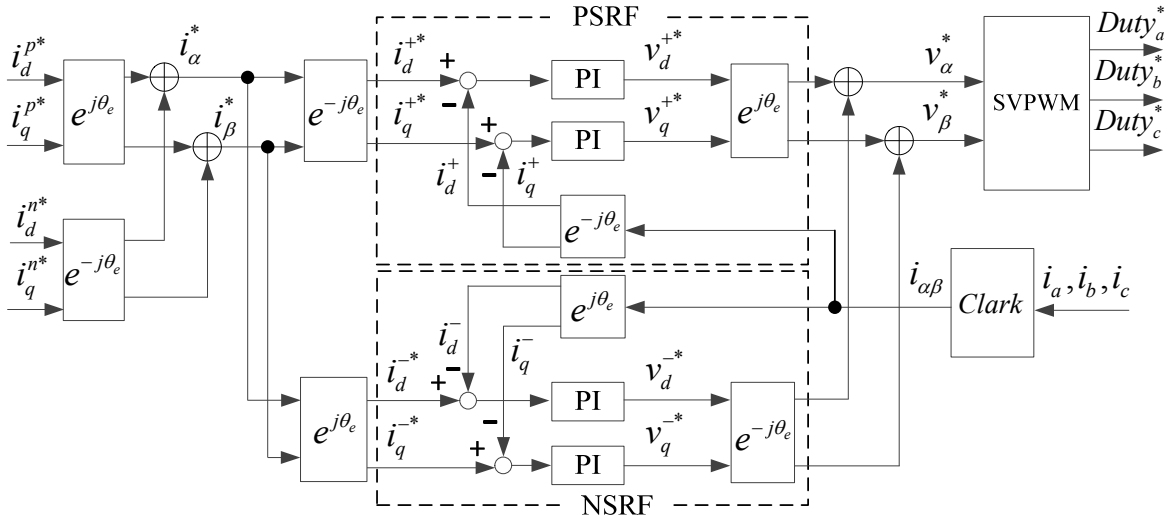

Fig.3.5 Dual current control without notch filter [104].

Assuming the proportional gain in dual current control in Fig.3.5 is half of the proportional gain in the PR control in *αβ*-frame, as illustrated in Fig.3.5, the current control in PSRF can be expressed as

$$\begin{bmatrix} v_d^{+*} \\ v_q^{+*} \end{bmatrix} = \begin{bmatrix} \frac{1}{2}K_p + \frac{K_i}{s} & \\ & \frac{1}{2}K_p + \frac{K_i}{s} \end{bmatrix} \begin{bmatrix} \Delta i_d^{+} \\ \Delta i_q^{+} \end{bmatrix} \tag{3.64}$$

where

$$\begin{bmatrix} \Delta i_d^{+} \\ \Delta i_q^{+} \end{bmatrix} = \begin{bmatrix} i_d^{+*} - i_d^{+} \\ i_q^{+*} - i_q^{+} \end{bmatrix} \tag{3.65}$$

The current control in NSRF in dual current control can be expressed as

$$\begin{bmatrix} v_d^{-*} \\ v_q^{-*} \end{bmatrix} = \begin{bmatrix} \frac{1}{2}K_p + \frac{K_i}{s} & \\ & \frac{1}{2}K_p + \frac{K_i}{s} \end{bmatrix} \begin{bmatrix} \Delta i_d^{-} \\ \Delta i_q^{-} \end{bmatrix} \tag{3.66}$$

where

$$\begin{bmatrix} \Delta i_d^{-} \\ \Delta i_q^{-} \end{bmatrix} = \begin{bmatrix} i_d^{-*} - i_d^{-} \\ i_q^{-*} - i_q^{-} \end{bmatrix} \tag{3.67}$$

Similar to the derivation of the equivalent current control in *dq*-frame for the PR control in *αβ*-frame, according to the relationship between PSRF and NSRF in Section 3.2.3.1, the current control in PSRF which is equivalent to the PI control in NSRF (3.66) can be deduced and expressed as (3.68).

$$\begin{bmatrix} v_d^{+*} \\ v_q^{+*} \end{bmatrix} = \begin{bmatrix} \frac{1}{2}K_p + \frac{K_i s}{s^2+(2\omega_e)^2} & \frac{2K_i\omega_e}{s^2+(2\omega_e)^2} \\ -\frac{2K_i\omega_e}{s^2+(2\omega_e)^2} & \frac{1}{2}K_p + \frac{K_i s}{s^2+(2\omega_e)^2} \end{bmatrix} \begin{bmatrix} \Delta i_d^+ \\ \Delta i_q^+ \end{bmatrix} \tag{3.68}$$

Therefore, combining (3.64) and (3.68), the current control in *dq*-frame which is equivalent to the dual current control can be expressed as

$$\begin{bmatrix} v_d^* \\ v_q^* \end{bmatrix} = \begin{bmatrix} K_p + \frac{K_i}{s} + \frac{K_i s}{s^2+(2\omega_e)^2} & \frac{2K_i\omega_e}{s^2+(2\omega_e)^2} \\ -\frac{2K_i\omega_e}{s^2+(2\omega_e)^2} & K_p + \frac{K_i}{s} + \frac{K_i s}{s^2+(2\omega_e)^2} \end{bmatrix} \begin{bmatrix} \Delta i_d \\ \Delta i_q \end{bmatrix} \tag{3.69}$$

As can be seen that, (3.69) is exactly the same as (3.61). Therefore, the dual current control is equivalent to the PR control in *αβ*-frame in theory.

3.3.3 PI-R Control in PSRF

The PI-R control in PSRF with resonant control at the frequency of twice fundamental frequency is shown in Fig.3.6, where the PI-R control is applied for regulation of *d*-axis and *q*-axis currents respectively. Therefore, the 2h currents in PSRF can be suppressed by the resonant control. As the *N*-sequence currents are converted to 2h components in PSRF, the suppression of 2h components in PSRF means that the *N*-sequence currents can be correspondingly suppressed.

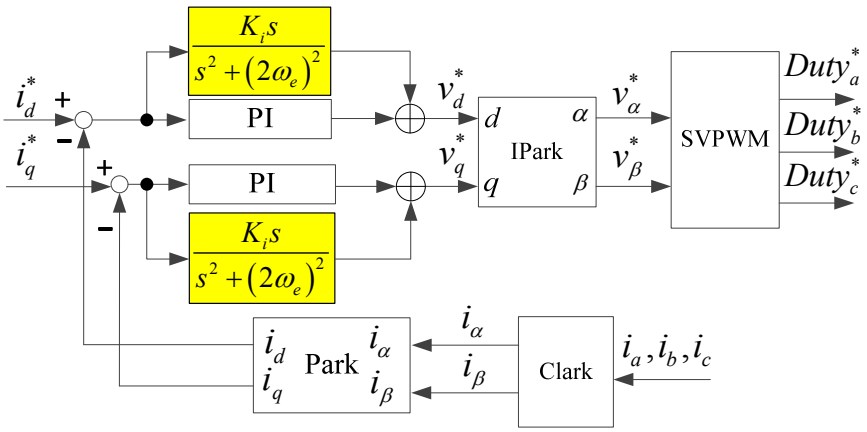

Fig.3.6 PI-R control in PSRF [108-110].

As illustrated in Fig.3.6, the PI-R current control in PSRF (*dq*-frame) can be expressed as

$$\begin{bmatrix} v_d^* \\ v_q^* \end{bmatrix} = \begin{bmatrix} K_p + \dfrac{K_i}{s} + \dfrac{K_i s}{s^2 + (2\omega_e)^2} & \\ & K_p + \dfrac{K_i}{s} + \dfrac{K_i s}{s^2 + (2\omega_e)^2} \end{bmatrix} \begin{bmatrix} \Delta i_d \\ \Delta i_q \end{bmatrix} \tag{3.70}$$

3.3.4 Summary

The conventional current control, PI-R control and the equivalent current control in *dq*-frame for the PR control and dual current control are listed in TABLE 3.2, which reveals their relationship clearly. As can be seen from (3.61), (3.69) and (3.70) there are resonant controllers at the centre frequency of twice fundament frequency in the equivalent control in the *dq*-frame for the PR control in *αβ*-frame, dual current control, and PI-R in PSRF. Therefore, these methods are all capable of suppressing 2h currents in *dq*-frame, which means the *N*-sequence currents can be suppressed. Since the conventional current control does not have the corresponding resonant control in *dq*-frame, it is incapable of eliminating the 2h current. It is also interesting to find that the PR control in *αβ*-frame is actually equivalent to the dual current control in theory.

TABLE 3.2
COMPARISONS OF DIFFERENT CURRENT CONTROL STRATEGIES

Methods	Implementations	Equivalent current control in *dq*-frame
Conventional current control in *dq*-frame	$\begin{bmatrix} v_d^* \\ v_q^* \end{bmatrix} = \begin{bmatrix} K_p + \frac{K_i}{s} & \\ & K_p + \frac{K_i}{s} \end{bmatrix} \begin{bmatrix} \Delta i_d \\ \Delta i_q \end{bmatrix}$	$\begin{bmatrix} v_d^* \\ v_q^* \end{bmatrix} = \begin{bmatrix} K_p + \frac{K_i}{s} & \\ & K_p + \frac{K_i}{s} \end{bmatrix} \begin{bmatrix} \Delta i_d \\ \Delta i_q \end{bmatrix}$
PR control in $\alpha\beta$-frame	$\begin{bmatrix} v_\alpha^* \\ v_\beta^* \end{bmatrix} = \begin{bmatrix} K_p + \frac{2K_i s}{s^2+\omega_e^2} & \\ & K_p + \frac{2K_i s}{s^2+\omega_e^2} \end{bmatrix} \begin{bmatrix} \Delta i_\alpha \\ \Delta i_\beta \end{bmatrix}$	$\begin{bmatrix} v_d^* \\ v_q^* \end{bmatrix} = \begin{bmatrix} K_p + \frac{K_i}{s} + \frac{K_i s}{s^2+(2\omega_e)^2} & \frac{2K_i\omega_e}{s^2+(2\omega_e)^2} \\ -\frac{2K_i\omega_e}{s^2+(2\omega_e)^2} & K_p + \frac{K_i}{s} + \frac{K_i s}{s^2+(2\omega_e)^2} \end{bmatrix} \begin{bmatrix} \Delta i_d \\ \Delta i_q \end{bmatrix}$
Dual current control	$\begin{bmatrix} v_d^{\pm *} \\ v_q^{\pm *} \end{bmatrix} = \begin{bmatrix} \frac{1}{2}K_p + \frac{K_i}{s} & \\ & \frac{1}{2}K_p + \frac{K_i}{s} \end{bmatrix} \begin{bmatrix} \Delta i_d^{\pm} \\ \Delta i_q^{\pm} \end{bmatrix}$	$\begin{bmatrix} v_d^* \\ v_q^* \end{bmatrix} = \begin{bmatrix} K_p + \frac{K_i}{s} + \frac{K_i s}{s^2+(2\omega_e)^2} & \frac{2K_i\omega_e}{s^2+(2\omega_e)^2} \\ -\frac{2K_i\omega_e}{s^2+(2\omega_e)^2} & K_p + \frac{K_i}{s} + \frac{K_i s}{s^2+(2\omega_e)^2} \end{bmatrix} \begin{bmatrix} \Delta i_d \\ \Delta i_q \end{bmatrix}$
PI-R($2\omega_e$) in PSRF	$\begin{bmatrix} v_d^* \\ v_q^* \end{bmatrix} = \begin{bmatrix} \left(K_p + \frac{K_i}{s} + \frac{K_i s}{s^2+(2\omega_e)^2}\right) & \\ & \left(K_p + \frac{K_i}{s} + \frac{K_i s}{s^2+(2\omega_e)^2}\right) \end{bmatrix} \begin{bmatrix} \Delta i_d \\ \Delta i_q \end{bmatrix}$	$\begin{bmatrix} v_d^* \\ v_q^* \end{bmatrix} = \begin{bmatrix} K_p + \frac{K_i}{s} + \frac{K_i s}{s^2+(2\omega_e)^2} & \\ & K_p + \frac{K_i}{s} + \frac{K_i s}{s^2+(2\omega_e)^2} \end{bmatrix} \begin{bmatrix} \Delta i_d \\ \Delta i_q \end{bmatrix}$

3.4 Experiments

The experiments of the conventional current control, PR control in $\alpha\beta$-frame, dual current control, and PI-R in PSRF will be conducted and corresponding experimental results will be analyzed in detail.

The test rig is illustrated in Fig.3.7, where the prototype PMSG is coupled with a servo machine. The servo machine is driven by the Siemens servo drive S120, which is used to simulate the wind turbine. A power resistor R_L (100Ω) is connected in parallel with the DC bus to consume the power generated by the generator. The equivalent capacitance of DC bus capacitors is 3000μF.

The design parameters of the PMSG are shown in TABLE B. 1 and the test rig prototype is shown in Fig.B.2 in Appendix B. The prototype machine is actually a dual 3-phase PMSG. To demonstrate the current control of asymmetric PMSG, only one set of the dual 3-phase windings is deliberately employed as an asymmetric single 3-phase PMSG, whose mutual inductances are unbalanced, Fig.C.1(a) in Appendix C.

The experiments are conducted based on dSPACE DS1006, which is detailed in Appendix B. The calculation rate of the current loop is configured to be 5 kHz, which is the same as the PWM frequency. The overall time delay T_d including the PWM output delay, current sampling delay and processing delay is approximately 1.5 times of PWM period. The design principle of PI parameters in [70] is that the dominant pole of $-R/L$ is canceled by the zero point of PI controller in dq-frame, the open loop of whole system can be simplified as typical first order system in control theory [70]. Then the proportional gain K_p and integral gain K_i can be optimally designed as

$$K_p = \frac{L}{4\xi^2 T_d}; K_i = \frac{R_s}{4\xi^2 T_d} \tag{3.71}$$

However, in the case study of unbalanced system, the inductances vary with the rotor position. For simplicity, the inductance L for designing K_p is simply chosen as the minimum value of L_d and L_q in Fig.C.1(d), which is approximately 17mH. Thus, the optimized PI parameters can be derived by setting the damping factor ξ to 0.707 with the inductance L=17mH and resistance R = 3.76Ω, the coefficients of the current controllers are listed in TABLE 3.3.

It is worth noting that the resonant controller (3.50) is usually implemented by replacing the ideal integral $1/s$ with an approximated low-pass filter transfer function $1/(s+\omega_c)$ in

practice [96, 97], where ω_c is the cut-off frequency of low-pass filter and it is far smaller than the resonant frequency. The cut-off frequency of low-pass filter are very important considering the stability [96]. For simplicity, the cut-off frequency is chosen as 1/1000 times of resonant frequency, and the integral gain of resonant control is set to be the same as the integral gain of PI control [86].

It is also worth noting that the number of pole pairs of the prototype PMSG is 16. Therefore, the 32nd harmonic in the following harmonic analyses based on the mechanical frequency indicates the 2h component in electrical frequency.

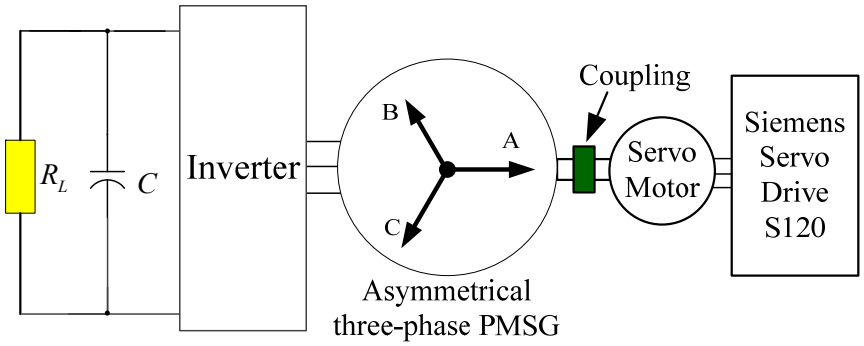

Fig.3.7 Illustration of the test rig.

TABLE 3.3 PARAMETERS OF CURRENT REGULATORS

Parameters	Value
Estimated total time delay	300μs
Proportional gain K_p ($=L/(2T_d)$)	28.33
Integral gain of integral K_i ($=R/(2T_d)$)	6266
Integral gain of resonant control	6266

3.4.1 Conventional Current Control

In this experiment, the conventional current PI control illustrated in Fig.1.4 is employed. The speed is regulated to 60rpm by the servo motor. The *d*-axis and *q*-axis current references in Fig.1.4 are assigned to 0A and -4A respectively. The experimental results are shown in Fig.3.8. As can be seen from the phase currents, Fig.3.8(a), the currents are slightly unbalanced.

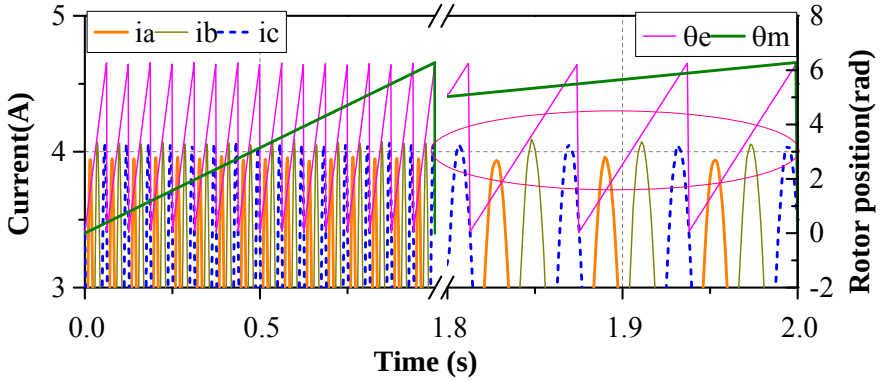
ia
ib
ic
θe
θm
Current(A)
Rotor position(rad)
Time (s)

(a)

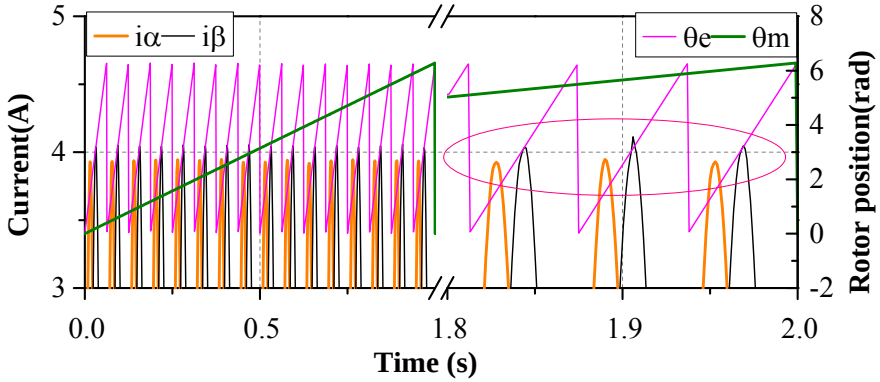
iα
iβ
θe
θm
Current(A)
Rotor position(rad)
Time (s)

(b)

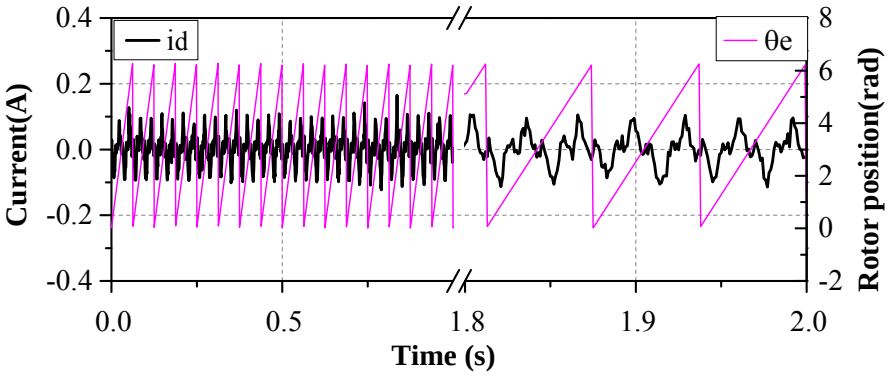
id
θe
Current(A)
Rotor position(rad)
Time (s)

(c)

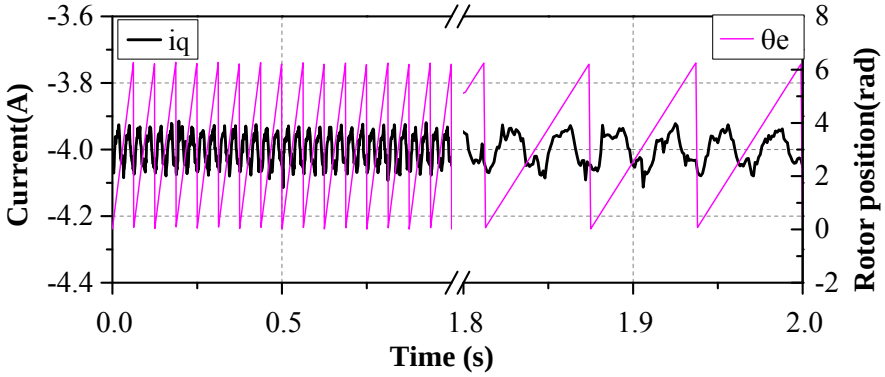
iq
θe
Current(A)
Rotor position(rad)
Time (s)

(d)

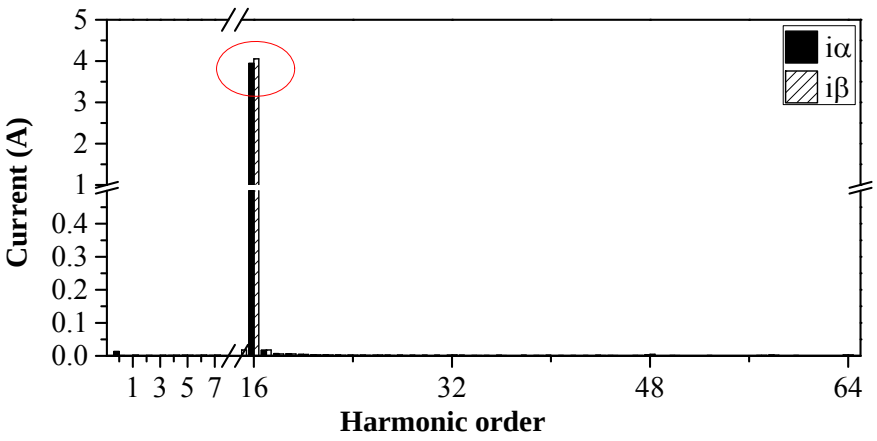

(e)

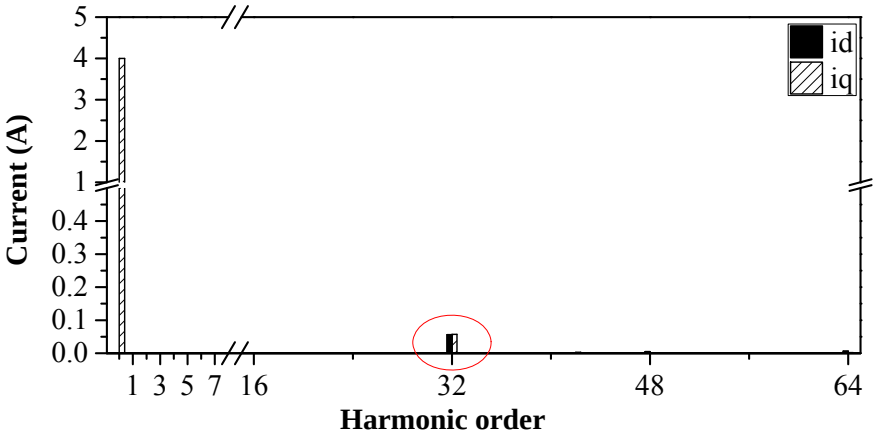

(f)

Fig.3.8 Experimental results of conventional PI control (a) Phase currents. (b) Currents in *αβ*-frame. (c) *d*-axis currents. (d) *q*-axis currents. (e) Harmonic analysis of currents in *αβ*-frame. (f) Harmonic analysis of current in *dq*-frame.

When the unbalanced phase currents are mapped to *αβ*-frame, Fig.3.8(b), it can be seen that the amplitudes of i_α and i_β are slightly different while the corresponding harmonic analysis, Fig.3.8(e), clearly shows that the amplitude of i_α and i_β are different. When the phase currents are converted to *dq*-frame, the 2h currents can be observed apparently from the *d*-axis current, Fig.3.8(c) and *q*-axis current, Fig.3.8(d) and their corresponding harmonic analysis Fig.3.8(f).

It is worth noting that the severity of the unbalanced currents depends on how severe the unbalance is, and it also depends on the bandwidth of the PI controller. If the bandwidth of PI controller is fast enough, the unbalanced currents can also be suppressed to the acceptable level to some extent. However, in reality, the bandwidth of PI controller is usually limited for a given platform. In some applications, the system performance may be very sensitive to the

torque ripple resulted from the unbalanced currents. In this case, the conventional current control may not be applicable.

3.4.2 PR Control in *αβ*-frame

In this experiment, the PR control in Fig.3.3 with resonant control at the center frequency of fundamental frequency is applied in the stationary *αβ*-frame. The speed is regulated to 60rpm by the servo motor and the *d*-axis and *q*-axis current references in Fig.3.3 are assigned to 0A and -4A respectively.

The experimental results are shown in Fig.3.9. As can be seen from the phase currents Fig.3.9(a), the amplitudes of all phase currents are almost the same, which means the 3-phase currents are more balanced than those in Fig.3.8(a). The currents in *αβ*-frame and corresponding harmonic analysis are shown in Fig.3.9(b) and Fig.3.9(e) respectively. It can be seen that the amplitudes of i_α and i_β are the same, which indicates the currents are balanced. Consequently, no 2h currents can be observed from the *d*-axis currents in Fig.3.9(c), *q*-axis currents in Fig.3.9(d) and the corresponding harmonic analysis in Fig.3.9(f).

It is worth noting that the average *q*-axis current in Fig.3.9(d) is slightly deviated from the current reference value -4A. The deviation is about 0.02A, which is 0.5% of the current reference. Although the resonant control has infinite selection characteristic at the centre frequency and the PR control can track fundamental current without tracing error in theory [96-98], in reality, the ideal integral in the resonant control is usually replaced by an approximated low-pass filter transfer function [96]. Therefore, the tracing capability is slightly compromised. Nevertheless, the currents are more balanced than the currents under conventional current control.

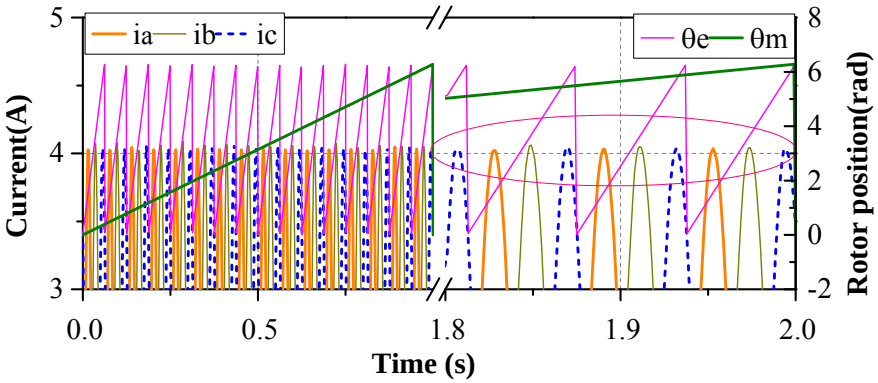

(a)

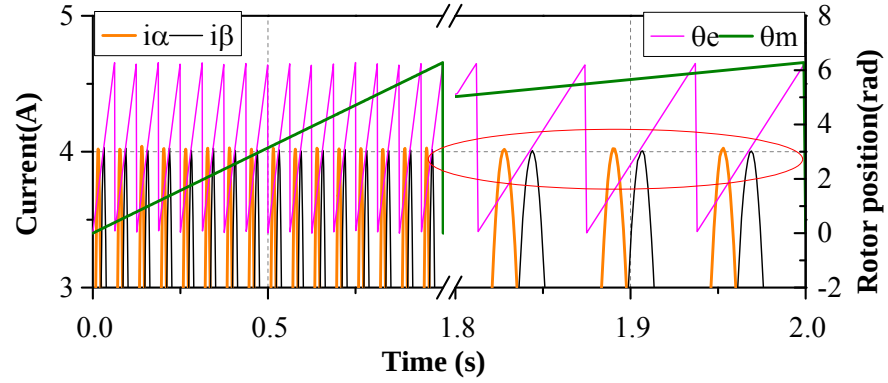
iα
iβ
θe
θm
Current(A)
Rotor position(rad)
Time (s)

(b)

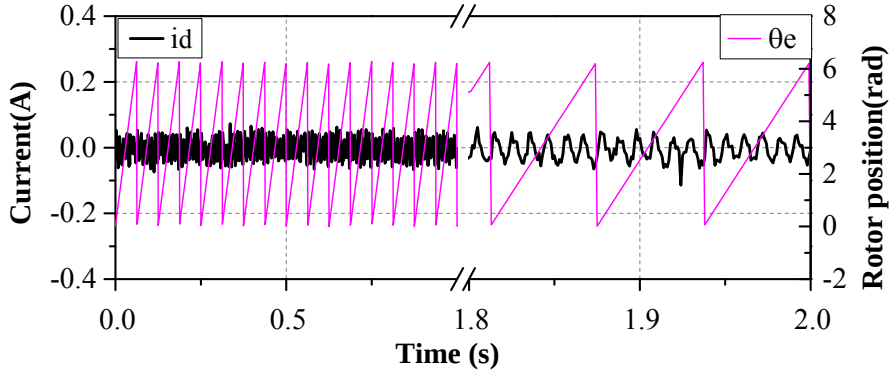
id
θe
Current(A)
Rotor position(rad)
Time (s)

(c)

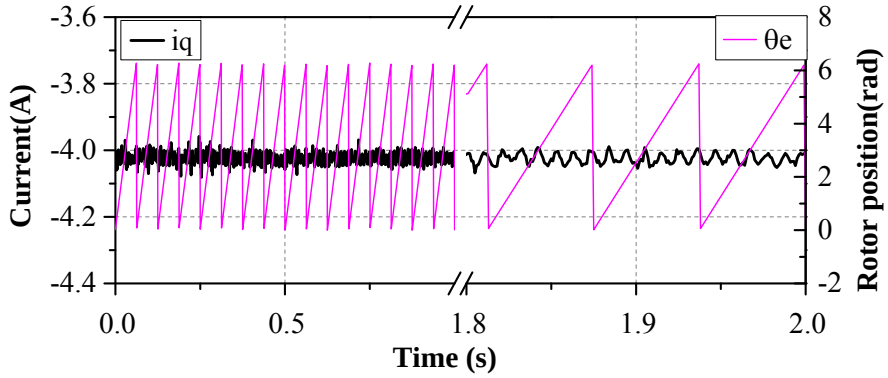
iq
θe
Current(A)
Rotor position(rad)
Time (s)

(d)

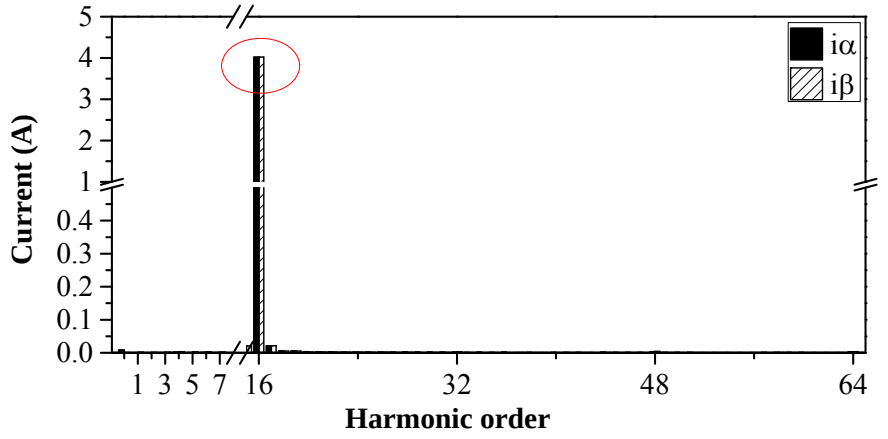
iα
iβ
Current (A)
Harmonic order

(e)

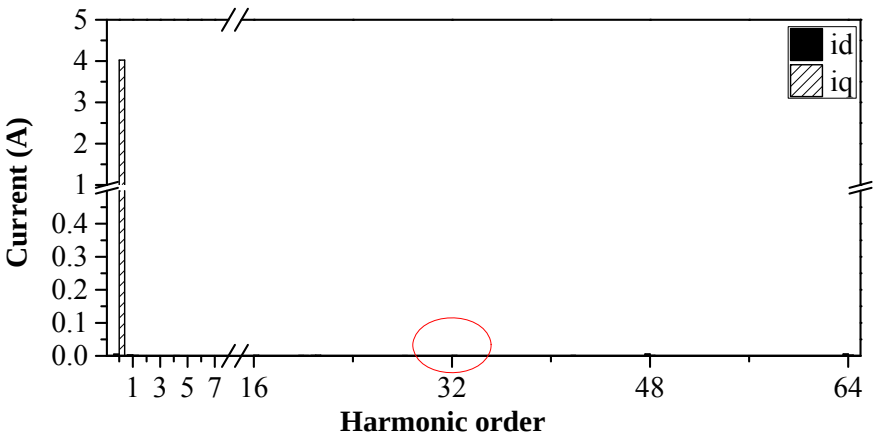

(f)

Fig.3.9 Experimental results of PR control in $\alpha\beta$-frame. (a) Phase currents. (b) Currents in $\alpha\beta$-frame. (c) d-axis currents. (d) q-axis currents. (e) Harmonic analysis of currents in $\alpha\beta$-frame. (f) Harmonic analysis of currents in dq-frame.

3.4.3 Dual Current Control

In this experiment, the dual current control without notch filters in Fig.3.5 is employed. The speed is regulated to 60rpm by the servo motor. The d-axis and q-axis current references in PSRF are assigned to 0A and -4A respectively, while the d-axis and q-axis current references in NSRF are 0A aiming for suppression of the N-sequence currents.

The phase currents are shown in Fig.3.10(a), which shows that the currents under the dual current control are more balanced than those in Fig.3.8(a) under conventional current control. The currents in $\alpha\beta$-frame and corresponding harmonic analysis are shown in Fig.3.10(b) and Fig.3.10(e) respectively. It can be seen that the amplitudes of i_α and i_β are the same, which indicates the currents are balanced. Consequently, no 2h currents can be observed from the dq-axis in Fig.3.10(c), Fig.3.10(d), and the corresponding harmonic analysis in Fig.3.10(f).

Compared with the experimental results in Fig.3.9 and Fig.3.10, it can be concluded that the dual current control has the similar capability of suppressing the N-sequence currents as the PR control in $\alpha\beta$-frame. Furthermore, it can trace the q-axis current reference fairly well, Fig.3.10(d), without tracing error, while there is trivial tracing error under PR control in $\alpha\beta$-frame in reality, Fig.3.9(d).

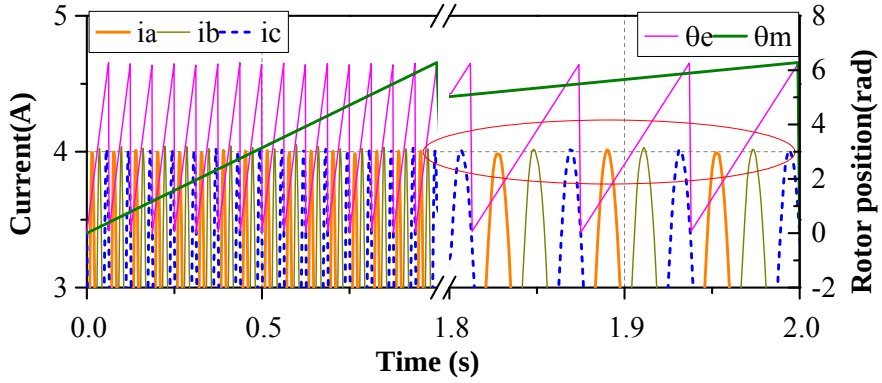
ia
ib
ic
θe
θm
Current(A)
Rotor position(rad)
Time (s)

(a)

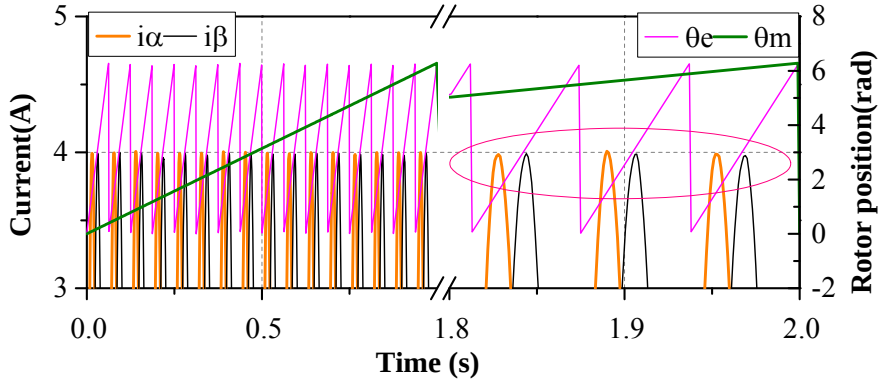
iα
iβ
θe
θm
Current(A)
Rotor position(rad)
Time (s)

(b)

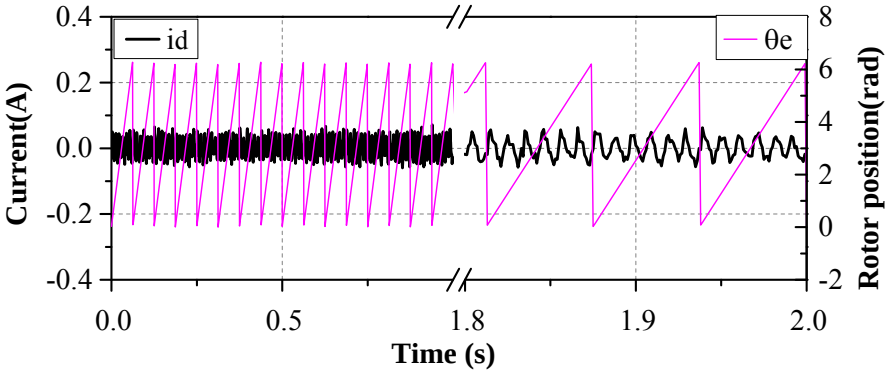
id
θe
Current(A)
Rotor position(rad)
Time (s)

(c)

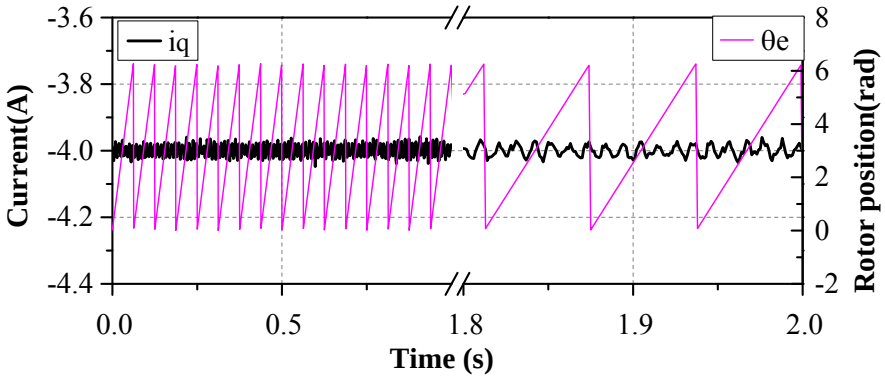
iq
θe
Current(A)
Rotor position(rad)
Time (s)

(d)

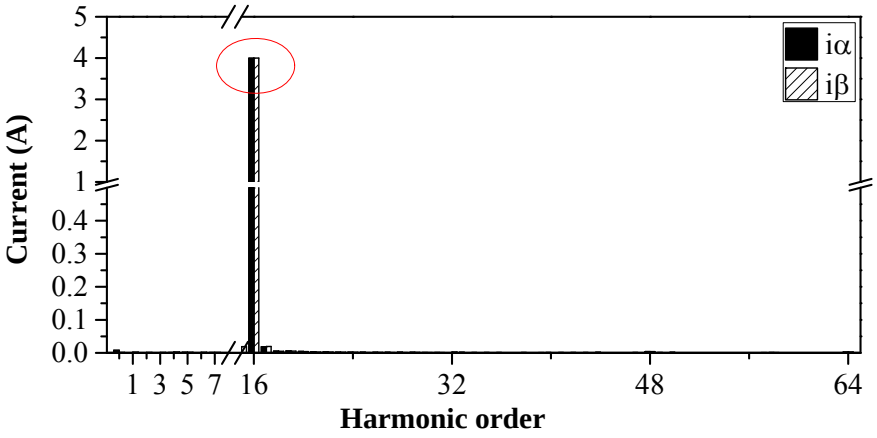

(e)

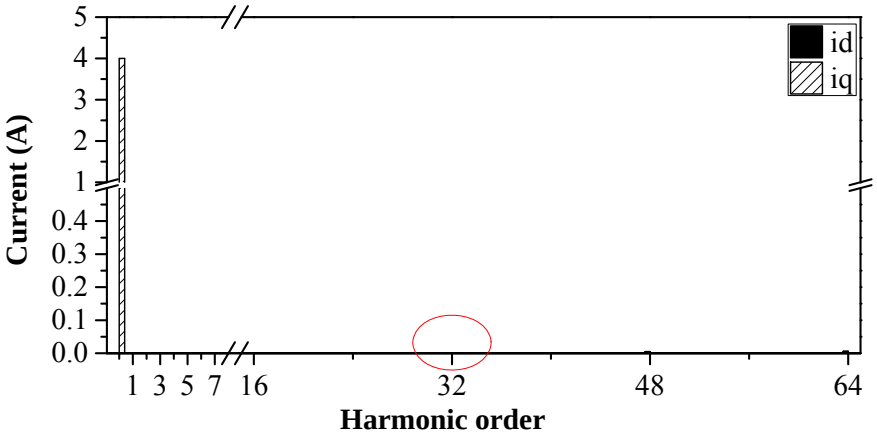

(f)

Fig.3.10 Experimental results of dual current control. (a) Phase currents. (b) Currents in *αβ*-frame. (c) *d*-axis currents. (d) *q*-axis currents. (e) Harmonic analysis of currents in *αβ*-frame. (f) Harmonic analysis of current in *dq*-frame.

3.4.4 PI-R Control in PSRF

In this experiment, the PI-R control in PSRF with resonant control at the center frequency of twice fundamental frequency, Fig.3.6, is employed. The speed is regulated to 60rpm by the servo motor. The *d*-axis and *q*-axis current references in Fig.3.6 are assigned to 0A and -4A respectively. The experimental results are shown in Fig.3.11, it can be seen that the PI-R control has almost the same performance of suppressing the *N*-sequence currents as the dual current control and does not have the trivial tracing error as the PR control in *αβ*-frame. For simplicity, the analyses of the experimental results under the PI-R control in PSRF will not be repeated here anymore.

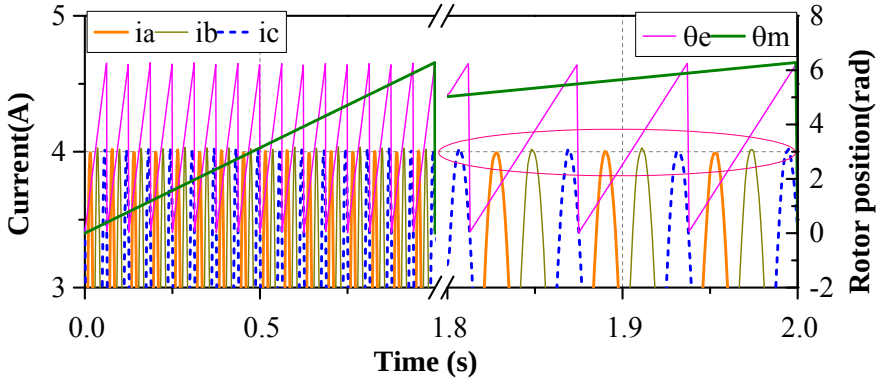
ia
ib
ic
θe
θm
Current(A)
Rotor position(rad)
Time (s)

(a)

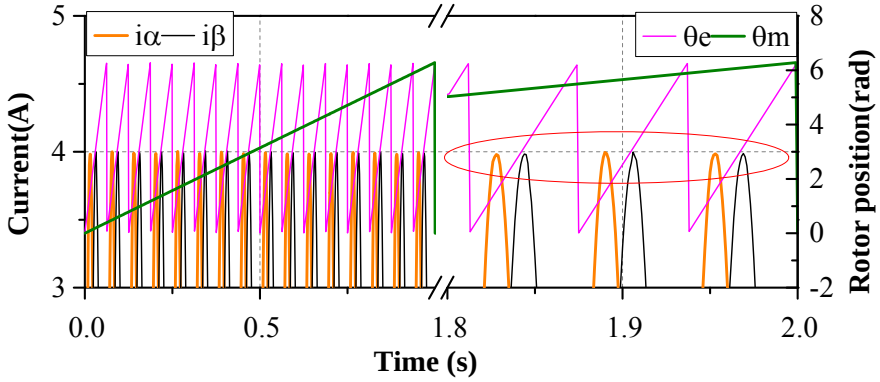
iα
iβ
θe
θm
Current(A)
Rotor position(rad)
Time (s)

(b)

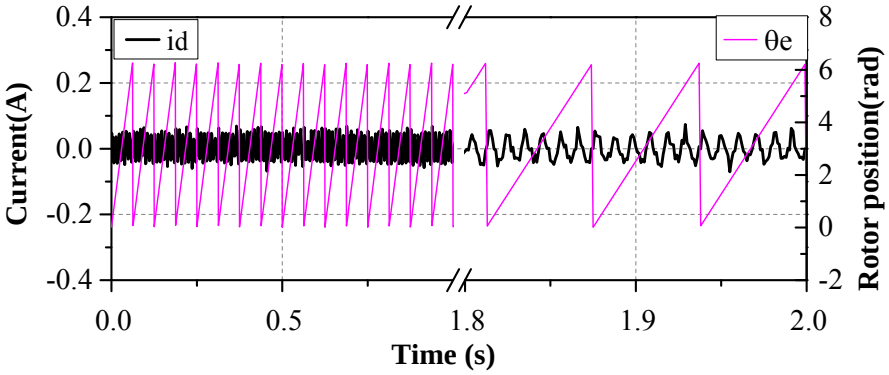
id
θe
Current(A)
Rotor position(rad)
Time (s)

(c)

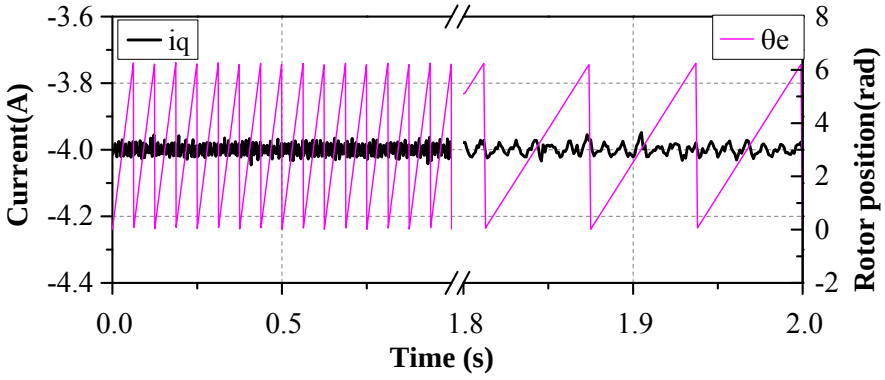
iq
θe
Current(A)
Rotor position(rad)
Time (s)

(d)

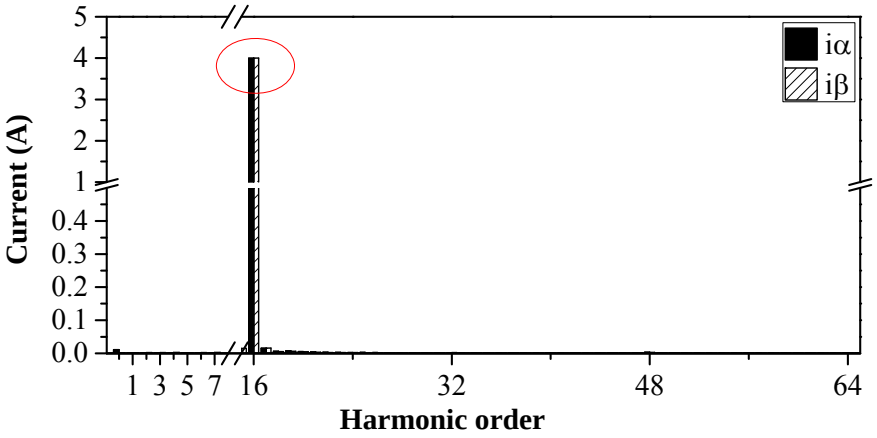

(e)

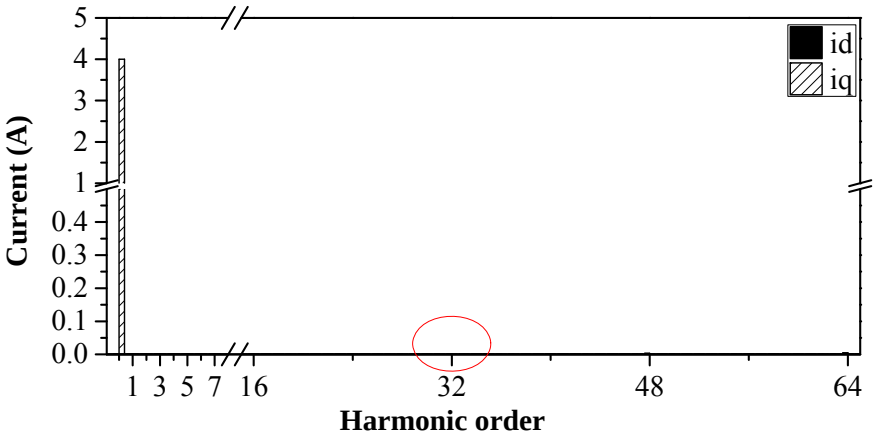

(f)

Fig.3.11 Experimental results of PI-R($2\omega_e$) in PSRF. (a) Phase currents. (b) Currents in $\alpha\beta$-frame. (c) *d*-axis currents. (d) *q*-axis currents. (e) Harmonic analysis of currents in $\alpha\beta$-frame. (f) Harmonic analysis of current in *dq*-frame.

3.4.5 Summary

Through the comparative experimental results, it can be concluded that the conventional current control cannot suppress the *N*-sequence currents properly, while the PR control in $\alpha\beta$-frame, the dual current control, and the PI-R control in PSRF can suppress the *N*-sequence currents effectively. It is worth noting that the PR control in $\alpha\beta$-frame, the dual current control, and the PI-R control in PSRF do not require any information of asymmetries. Therefore, they are robust to any asymmetries although the experiments are only conducted on the asymmetric PMSG with inherent unbalanced mutual inductances.

The PR control in $\alpha\beta$-frame is equivalent to the dual current control in theory. However, the current tracing performance is slightly compromised due to the implement of resonant control with the integral approximately replaced by an approximate low pass filter in reality.

The PI-R control in PSRF has the equivalent performance to the dual current control without average tracing error and it does not require two sets of PI controllers. However, the implementation of PI-R control increases the complexity compared with the implementation of PI control.

The dual current control requires two sets of current controllers, whose control complexity is increased compared with the conventional PI control. It is worth noting that the proportional gain of each set of PI controller should be only half of the proportional gain in other control strategies, otherwise, the system may be unstable due to the relatively high proportional gain.

3.5 Conclusions

In this chapter, the mathematical modelling of generic asymmetric PMSG is presented, which considers the unbalanced resistances, unbalanced average self-inductances, mutual inductances and unbalanced back-EMFs. Four current control methods including the conventional current control, PR control in $\alpha\beta$-frame, dual current control and PI-R control in PSRF are reviewed and evaluated. The relationship between these methods is revealed for the first time. Comparative experiments show that there are unbalanced currents in the asymmetric PMSG under conventional current control, while the PR control in $\alpha\beta$-frame, dual current control and PI-R control in PSRF are all capable of suppressing the N-sequence effectively.

Chapter 4 Instantaneous Power Control of Asymmetric PMSG (without sequential component decomposers)

4.1 Introduction

The PMSG direct-drive system is very attractive in the wind turbine drive system for its highest energy production, high efficiency, high reliability, low maintenance cost, low noise, etc [13]. However, when the PMSG is asymmetric, the undesired 2h power will be produced [112] and results in the 2h DC bus voltage [113, 114, 143]. As the DC bus voltage fluctuates, it results in the current harmonics flowing through the DC bus electrolytic capacitors. Since the equivalent series resistance of capacitors increases at low frequencies, the low-order current harmonics contribute disproportionately to the capacitor power losses and temperature rise, resulting in reduced lifetime [93].

In Chapter 3, the current control of asymmetric PMSG is investigated. Although the *N*-sequence currents can be suppressed effectively by the balanced current control, as shown in TABLE 2.2, there will be 2h power in the asymmetric PMSG. With the 2h power flowing towards the DC bus capacitors, it suffers the 2h DC bus voltage pulsation. Since the 2h DC bus voltage is related to the 2h power flowing through the DC bus capacitors [115, 116], the effective way to suppress the 2h DC bus voltage is to suppress the 2h power, which can be achieved by the instantaneous power control.

The instantaneous power control has been widely employed in the weak grid-connected PWM rectifier system [100, 102, 114, 117, 118]. As introduced in Section 1.6.2.1, the instantaneous power control can be classified as instantaneous input power control [102, 117], the input-output-power control [100, 118], and the output power control [114]. By introducing the *N*-sequence currents, the 2h power generated by the *P*-sequence currents could be compensated by the 2h power generated by the *N*-sequence currents. However, as listed in TABLE 1.1, all the power control methods require sequential component decomposers to extract sequential currents, back-EMFs or output voltages, such as the sequence separation delaying method [103], the notch filter method [102], or the dual second-order generalized integrator(DSOGI) method [120], which increase the system complexity.

In this chapter, an improved power control aiming for suppressing the 2h DC bus voltage accounting for generalized asymmetries without sequential component decomposer will be proposed and verified by elaborated experiments. The proposed method is based on the output power control. With the aid of the current PI-R control in PSRF to regulate the *P*-sequence and *N*-sequence currents, no sequential current decomposers for current controllers are required. The sequential output voltages, which are essential for current reference calculation, are simply obtained from the output voltages of current PI controllers and resonant controllers respectively, which will be detailed in the Section 4.4.1. Since the sequential output voltages in the proposed method are from current controllers rather than from the estimation in [114], the proposed method are robust to generalized asymmetries even when the impedances are unbalanced. Therefore, the proposed power control can be implemented without any sequential decomposers under generalized unbalanced conditions. Finally, the proposed method will be verified on an asymmetric 3-phase PMSG prototype with inherent asymmetry and deliberately introduced asymmetries.

4.2 Second Harmonic DC Bus Voltage Introduced by Asymmetries

From Fig.4.1, it can be deduced that [144, 145]

$$i_c = C\frac{dv_{dc}}{dt} = \frac{p_1 - p_2}{v_{dc}} \tag{4.1}$$

where p_1 is the instantaneous power from external, p_2 is the instantaneous power from the inverter, and p_c is the instantaneous power flowing through the DC bus capacitors. (4.1) indicates that there will be 2h voltage in v_{dc} when there is 2h power in p_1 or p_2 [113, 114, 143]. If the inverter in Fig.4.1is a lossless system, the 2h DC bus voltage will be affected directly by the 2h power in p_{out}.

The 2h power in unbalanced system can be expressed as [146]

$$p_2^{2nd} = P_2^{2nd}\cos\left(2\theta_e + \theta_2\right) \tag{4.2}$$

where θ_e is the electrical rotor position, P_2^{2nd} is the amplitude of the 2h power, θ_2 is the displacement angle.

Usually, v_{dc} is regulated to trace the reference value v_{dc}* by the DC bus voltage PI controller in the grid side inverter. Therefore, assuming the DC bus voltage can be expressed as

$$v_{dc} = v_{dc}^* + V_{dc}^{2nd}\cos(2\theta_e + \theta_{2v}) + \ldots \tag{4.3}$$

where V_{dc}^{2nd} and θ_{2v} are the amplitude and offset angle of the 2h DC bus voltage respectively.

With consideration of DC and 2h components from the inverter side, the power p_2 can be expressed as

$$p_2 = p_2^{dc} + P_2^{2nd}\cos\left(2\theta_e + \theta_{2p}\right) + \ldots \tag{4.4}$$

where p_2^{dc} is the average power; P_2^{2nd} and θ_{2p} are the amplitude and offset angle of the 2h power. Assuming only the average DC power without 2h power in (4.4) is transferred to the left side of the DC bus capacitors, then

$$p_1 = p_2^{dc} \tag{4.5}$$

Substitute (4.3)-(4.5) into (4.1), the amplitude of the 2h DC bus voltage can be deduced as

$$V_{dc}^{2nd} = \frac{P_2^{2nd} R_L}{2v_{dc}^{*}\sqrt{1+\left(\omega_e C R_L\right)^2}} \tag{4.6}$$

where the equivalent R_L [147] can be deduced as

$$R_L = \left(v_{dc}^{*}\right)^2 \Big/ \left(-p_2^{dc}\right) \tag{4.7}$$

4.3 Review of Instantaneous Power Control

As detailed in [102], the unbalanced 3-phase components without zero sequence components can be expressed as the sum of orthogonal *P*- and *N*-sequence components, i.e.

$$F_{\alpha\beta} = e^{j\theta_e} F_{dq}^{p} + e^{-j\theta_e} F_{dq}^{n} \tag{4.8}$$

where F can be voltage v, current i, back-EMFs e in PMSG application or grid voltage in grid applications. θ_e is the rotor electrical position in generator applications or grid angle in grid applications, and $F_{\alpha\beta}$ can be expressed as

$$F_{\alpha\beta} = F_\alpha + jF_\beta = \frac{2}{3}\left(F_a + F_b e^{j2\pi/3} + F_c e^{j4\pi/3}\right) \tag{4.9}$$

In (4.8), $e^{j\theta_e} F_{dq}^{p}$ and $e^{-j\theta_e} F_{dq}^{n}$ are the *P*- and *N*-sequence components in $\alpha\beta$-frame respectively. F_{dq}^{p} are the *P*-sequence components in PSRF, F_{dq}^{n} are *N*-sequence components in the NSRF, and they can be expressed as

$$F_{dq}^{p} = F_d^{p} + jF_q^{p} \tag{4.10}$$

$$F_{dq}^{n} = F_d^{n} + jF_q^{n} \tag{4.11}$$

where subscripts *d, q* mean *d*-axis and *q*-axis respectively, the superscripts *p, n* mean *P*- and *N*-sequence components respectively.

To discuss the principle of the power control, the block diagram of a PWM inverter/rectifier is repeated in Fig.4.1 for convenience.

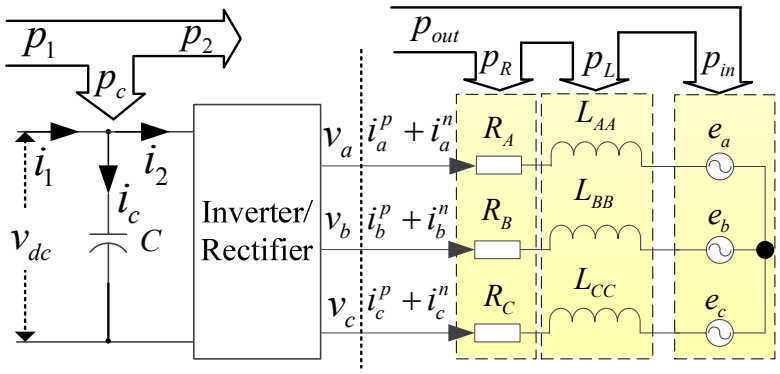

Fig.4.1 Conventional PWM inverter/rectifier.

4.3.1 Input Power Control

In the input power control, the 2h power in the input power in Fig.4.1 is supposed to be suppressed. The instantaneous active and reactive input powers can be expressed as [148]

$$p_{in} = \frac{3}{2}\left(e_\alpha i_\alpha + e_\beta i_\beta\right) \tag{4.12}$$

$$q_{in} = \frac{3}{2}\left(e_\alpha i_\beta - e_\beta i_\alpha\right) \tag{4.13}$$

where e_α, e_β, i_α and i_β are back-EMFs and currents in $\alpha\beta$-frame. By substituting e_α, e_β, i_α and i_β from (4.8) into (4.12) and (4.13) respectively, the instantaneous active and reactive input powers can be deduced as [102, 114]

$$p_{in} = p_{in0} + p_{in\_c2}\cos(2\theta_e) + p_{in\_s2}\sin(2\theta_e) \tag{4.14}$$

$$q_{in} = q_{in0} + q_{in\_c2}\cos(2\theta_e) + q_{in\_s2}\sin(2\theta_e) \tag{4.15}$$

where p_{in0}, q_{in0} are the average active and reactive input powers respectively, p_{in_c2}, p_{in_s2}, q_{in_c2} and q_{in_s2} are the coefficients of 2h active and reactive input powers respectively, which have the following relationship

$$\frac{2}{3}\begin{bmatrix} p_{in0} \\ q_{in0} \\ p_{in\_c2} \\ p_{in\_s2} \end{bmatrix} = \begin{bmatrix} e_d^p & e_q^p & e_d^n & e_q^n \\ -e_q^p & e_d^p & -e_q^n & e_d^n \\ e_d^n & e_q^n & e_d^p & e_q^p \\ e_q^n & -e_d^n & -e_q^p & e_d^p \end{bmatrix} \begin{bmatrix} i_d^p \\ i_q^p \\ i_d^n \\ i_q^n \end{bmatrix} \tag{4.16}$$

If p_{in_c2} and p_{in_s2} in (4.14) are zero aiming for suppressing the 2h input power, and p_{in0} in (4.14) and q_{in0} in (4.15) are the reference average active and reactive input power p_{in0}* and q_{in0}* respectively, by solving (4.16), the *P*- and *N*-sequence current references can be obtained and expressed as

$$\begin{bmatrix} i_d^{p*} \\ i_q^{p*} \\ i_d^{n*} \\ i_q^{n*} \end{bmatrix} = \frac{2p_{in0}^*}{3D_1}\begin{bmatrix} e_d^p \\ e_q^p \\ -e_d^n \\ -e_q^n \end{bmatrix} + \frac{2q_{in0}^*}{3D_2}\begin{bmatrix} -e_q^p \\ e_d^p \\ -e_q^n \\ e_d^n \end{bmatrix} \tag{4.17}$$

where superscript * means reference value and the D_1 and D_2 can be expressed as

$$D_1 = \left(e_d^p\right)^2 + \left(e_q^p\right)^2 - \left(e_d^n\right)^2 - \left(e_q^n\right)^2 \tag{4.18}$$

$$D_2 = \left(e_d^p\right)^2 + \left(e_q^p\right)^2 + \left(e_d^n\right)^2 + \left(e_q^n\right)^2 \tag{4.19}$$

If the current controllers could trace the current references (4.17) without tracing errors, p_{in_c2} and p_{in_s2} will be zero. Consequently, the 2h active input power in (4.14) can be suppressed.

4.3.2 Output Power Control

In the output power control, the 2h power in instantaneous active output power in Fig.4.1 is supposed to be suppressed. The instantaneous active and reactive output powers at the poles of inverter can be expressed as [148]

$$p_{out} = \frac{3}{2}\left(v_\alpha i_\alpha + v_\beta i_\beta\right) \tag{4.20}$$

$$q_{out} = \frac{3}{2}\left(v_\alpha i_\beta - v_\beta i_\alpha\right) \tag{4.21}$$

By substituting v_α, v_β, i_α and i_β from (4.8) into (4.20) and (4.21) respectively, the instantaneous active and reactive output powers can be deduced as [102, 114]

$$p_{out} = p_{out0} + p_{out\_c2}\cos(2\theta) + p_{out\_s2}\sin(2\theta) \tag{4.22}$$

$$q_{out} = q_{out0} + q_{out\_c2}\cos(2\theta) + q_{out\_s2}\sin(2\theta) \tag{4.23}$$

where p_{out0}, q_{out0} are the average active and reactive output powers respectively, p_{out_c2}, p_{out_s2}, q_{out_c2} and q_{out_s2} are the coefficients of 2h active and reactive output powers respectively, which have the following relationship

$$\frac{2}{3}\begin{bmatrix} p_{out0} \\ q_{out0} \\ p_{out\_c2} \\ p_{out\_s2} \end{bmatrix} = \begin{bmatrix} v_d^p & v_q^p & v_d^n & v_q^n \\ -v_q^p & v_d^p & -v_q^n & v_d^n \\ v_d^n & v_q^n & v_d^p & v_q^p \\ v_q^n & -v_d^n & -v_q^p & v_d^p \end{bmatrix} \begin{bmatrix} i_d^p \\ i_q^p \\ i_d^n \\ i_q^n \end{bmatrix} \tag{4.24}$$

If p_{out_c2} and p_{out_s2} in (4.22) are zero aiming for suppressing the 2h output power, and p_{out0} in (4.22) and q_{out0} in (4.23) are the reference average active and reactive output power p_{out0}* and q_{out0}* respectively, by solving (4.24), the *P*- and *N*-sequence current references can be obtained and expressed as

$$\begin{bmatrix} i_d^{p*} \\ i_q^{p*} \\ i_d^{n*} \\ i_q^{n*} \end{bmatrix} = \frac{2p_{out0}^*}{3D_1}\begin{bmatrix} v_d^p \\ v_q^p \\ -v_d^n \\ -v_q^n \end{bmatrix} + \frac{2q_{out0}^*}{3D_2}\begin{bmatrix} -v_q^p \\ v_d^p \\ -v_q^n \\ v_d^n \end{bmatrix} \tag{4.25}$$

where superscript "*" means reference value and D_1 and D_2 can be expressed as

$$D_1 = \left(v_d^p\right)^2 + \left(v_q^p\right)^2 - \left(v_d^n\right)^2 - \left(v_q^n\right)^2 \tag{4.26}$$

$$D_2 = \left(v_d^p\right)^2 + \left(v_q^p\right)^2 + \left(v_d^n\right)^2 + \left(v_q^n\right)^2 \tag{4.27}$$

If the current controllers could trace the current references (4.25) without tracing errors, p_{out_c2} and p_{out_s2} will be zero. Consequently, the 2h active output power in (4.22) will be zero. Therefore, according to (4.1), the 2h DC bus voltage can be suppressed.

4.3.3 Input-output-power Control

In the input-output-power control, the 2h power of instantaneous active output power is supposed to be suppressed to suppress the 2h DC bus voltage, while the average active input power and average reactive input power are regulated for controlling the average input power and the average unity input power factor. The four constraints for current reference calculations in input-output-power control can be expressed as

$$\frac{2}{3}\begin{bmatrix} p_{in0} \\ q_{in0} \\ p_{out\_c2} \\ p_{out\_s2} \end{bmatrix} = \begin{bmatrix} e_d^p & e_q^p & e_d^n & e_q^n \\ -e_q^p & e_d^p & -e_q^n & e_d^n \\ v_d^n & v_q^n & v_d^p & v_q^p \\ v_q^n & -v_d^n & -v_q^p & v_d^p \end{bmatrix} \begin{bmatrix} i_d^p \\ i_q^p \\ i_d^n \\ i_q^n \end{bmatrix} \tag{4.28}$$

If p_{in0} in (4.14) and q_{in0} in (4.15) are the reference average active and reactive input power p_{in0}* and q_{in0}* respectively, p_{out_c2} and p_{out_s2} in (4.22) are zero aiming for suppressing the 2h output power, by solving (4.28), the *P*- and *N*-sequence current references can be obtained and expressed as

$$\begin{bmatrix} i_d^{p*} \\ i_q^{p*} \\ i_d^{n*} \\ i_q^{n*} \end{bmatrix} = \left(\frac{2p_{in0}^*}{3D} \begin{bmatrix} -e_{dp} & 0 & -e_{qn} & -e_{dn} \\ -e_{qp} & 0 & -e_{dn} & e_{qn} \\ 0 & e_{dn} & e_{qp} & e_{dp} \\ 0 & e_{qn} & e_{dp} & -e_{qp} \end{bmatrix} + \frac{2q_{in0}^*}{3D} \begin{bmatrix} -e_{qp} & 0 & e_{dn} & -e_{qn} \\ e_{dp} & 0 & -e_{qn} & -e_{dn} \\ 0 & e_{qn} & -e_{dp} & e_{qp} \\ 0 & -e_{dn} & e_{qp} & e_{dp} \end{bmatrix} \right) \begin{bmatrix} v_{dp}^2 + v_{qp}^2 \\ v_{dn}^2 + v_{qn}^2 \\ v_{dn}v_{qp} + v_{dp}v_{qn} \\ v_{dn}v_{dp} - v_{qn}v_{qp} \end{bmatrix} \tag{4.29}$$

where

$$D = \left\| \begin{bmatrix} e_d^p & e_q^p & e_d^n & e_q^n \\ -e_q^p & e_d^p & -e_q^n & e_d^n \\ v_d^n & v_q^n & v_d^p & v_q^p \\ v_q^n & -v_d^n & -v_q^p & v_d^p \end{bmatrix} \right\| \tag{4.30}$$

Compared with the current reference calculation (4.17) for input power control and (4.25) for output power control, the current reference calculation (4.29) for input-output-power control is more complicated.

4.4 Proposed Control Strategy

As the 2h DC bus voltage essentially depends on the 2h component in the output power p_{out} rather than input power p_{in}, the proposed control is based on output power control which is robust to the generalized asymmetries including the asymmetric impedances. As shown in (4.25), the *P*- and *N*-sequence output voltages are essential for the calculation of *P*- and *N*-sequence current references in the output power control. In this section, the principle of the extraction of *P*- and *N*-sequence output voltages with the aid of *PI-R* controller in PSRF will be introduced first, and then the proposed power control without any sequential component decomposers will be presented.

4.4.1 Extraction of the *P*- and *N*-Sequence Output Voltages

The mathematical modeling of the asymmetric PMSG in *dq*-frame can be linearized as a linear model with disturbance [104, 149]. The linear model can be expressed as a resistance-

inductance (*RL*) with a low-pass filter having the time constant T_d, where T_d is the total time delay including current sampling delay, calculation delay, PWM output delay, and etc. The PI-R control in PSRF is employed to regulate the currents in *dq*-frame. The control flowchart can be illustrated in Fig.4.2(a), where *x* and x_{out} are the current reference and feedback in *dq*-frame respectively, *y* is the output voltage, *d* is disturbance including the 2h voltage.

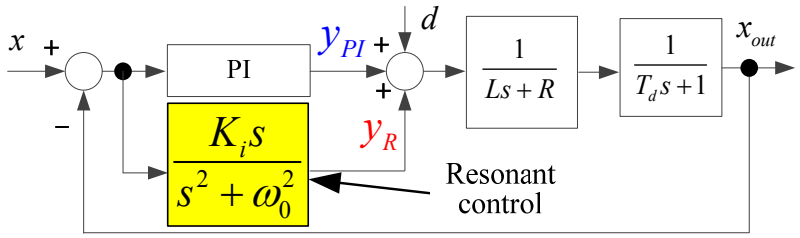

(a)

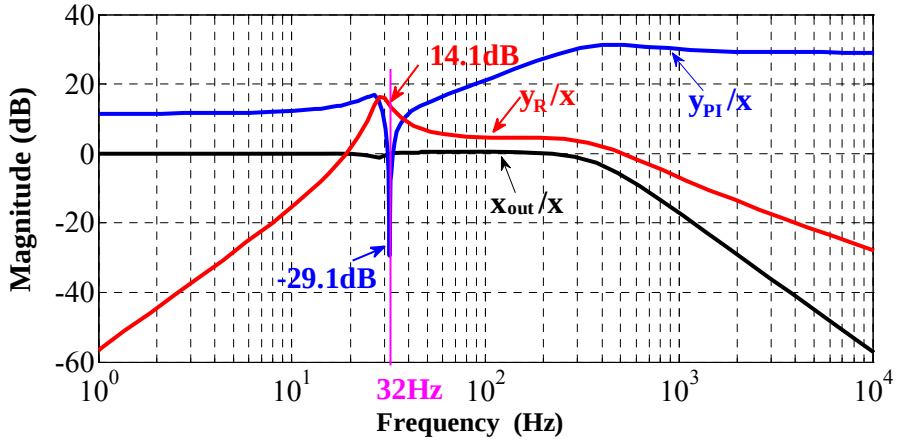

(b)

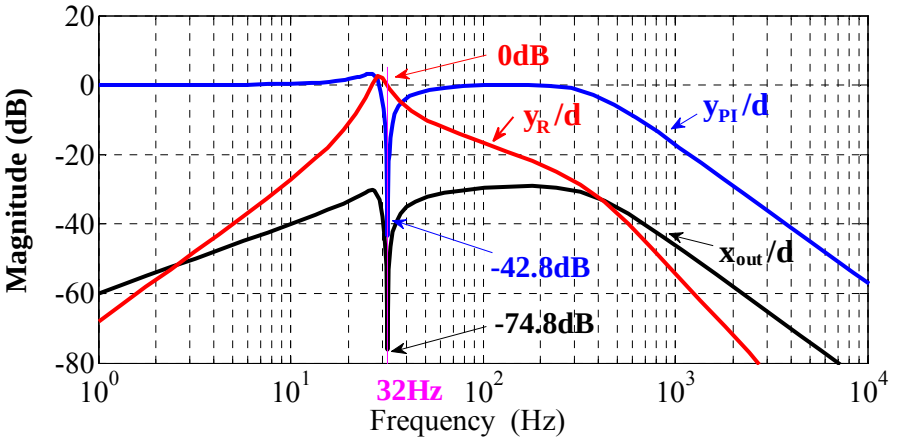

(c)

Fig.4.2 Proposed output voltages extraction of *P*- and *N*-sequence components. (a) Equivalent transfer function. (b) Bode magnitude (input). (c) Bode magnitude (disturbance).

In reality, an approximated low-pass filter transfer function $1/(s+\omega_c)$ is employed to replace the ideal integral $1/s$ in resonant controller in Fig.4.2(a) [96, 97], where ω_c is the cut-off frequency of low-pass filter and ω_c is far smaller than the resonant frequency. The resonant control is usually implemented by (3.63). In this case study, a low-pass filter with cut-off frequency $\omega_c=\omega_0/1000$ is employed and the integral gain of resonant control is set to be the same as the integral gain of PI controller.

Assuming the fundamental frequency is 16Hz, the centre frequency in the resonant control will be 32Hz aiming for suppressing the 2h currents. R, L and T_d in Fig.4.2(a) are 3.76Ω, 17mH and 300μs respectively. The bode magnitude of x_{out}/x, y_{PI}/x and y_R/x can be shown in Fig.4.2 (b), which show that the 2h voltage (32Hz) in y_R is dominant while that in y_{PI} is negligible if there is 2h component in the current reference x. Meanwhile, the DC output voltage in y_{PI} is dominant while that in y_R is negligible.

The bode magnitude of x_{out}/d, y_{PI}/d and y_R/d are shown in Fig.4.2 (c). If there is 2h component in d, it can be seen that the 2h current in x_{out} is suppressed effectively. Meanwhile, the 2h voltage in y_R is almost equal to d, which is dominant while that in y_{PI} is negligible. If there is DC value in the disturbance d, the DC output in y_{PI} will be equal to d as the magnitude of y_{PI}/d at the zero frequency is 0dB, while the DC output in y_R is negligible.

Overall, the DC and the 2h output voltages can be separated by the *PI* controller and resonant controller effectively. The output of the PI controller and resonant controller can be employed to represent the DC voltage and 2h voltage respectively.

4.4.2 Control Scheme

The detailed control block diagram of the proposed method is shown in Fig.4.3. The current references generation is shown in Fig.4.3(a), which are obtained according to (4.25). The average output reactive power reference is assigned to zero for the unity average output power factor in this case study. $T_{dq}(\theta)$ is the standard Park transformation (A.7). By the matrix conversion $T_{dq}(2\theta_e)$, the N-sequence current references in the NSRF (DC value) are converted to AC values ($2\omega_e$) in PSRF. Therefore, there are DC value and AC value with $2\omega_e$ frequency in the current references in PSRF.

The current control scheme is shown in Fig.4.3(b). By *PI-R* control with the resonant control at the center frequency of $2\omega_e$ in the PSRF [109], the currents can be controlled effectively without tracing error. In the previous works, the sequence separation delaying method [103], notch filter method [102], or dual second-order generalized integrator (DSOGI)

method [120] were employed to extract *P*- and *N*-sequence components [100, 101, 109, 114, 118, 119, 121]. In the proposed method shown in Fig.4.3(b), the *P*-sequence voltages in PSRF are directly from the output of the PI controllers, while the *N*-sequence voltages in the PSRF are directly from the output of resonant controllers in the PSRF due to its infinite gain at the center frequency of $2\omega_e$. By matrix conversion $T_{dq}(-2\theta_e)$, the *N*-sequence voltages (2ω) in the PSRF are converted to DC signals in the NSRF. Therefore, the *N*-sequence output voltages in the NSRF can be obtained easily. Since the *P*- and *N*-sequence output voltages are from PI-R controllers, they are robust to generalized unbalance.

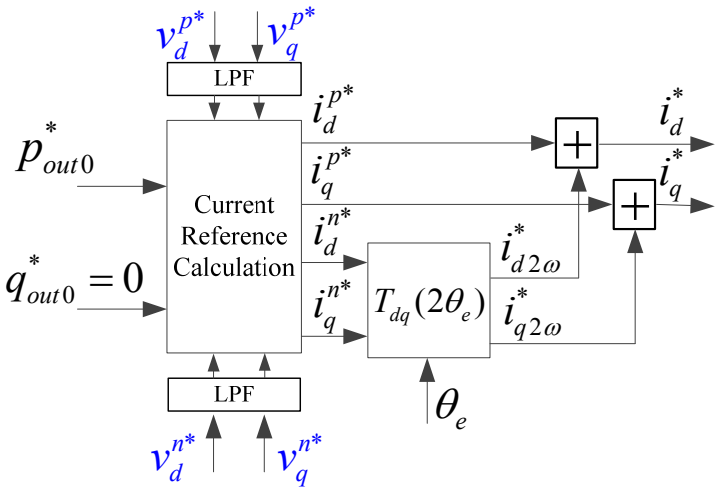

(a)

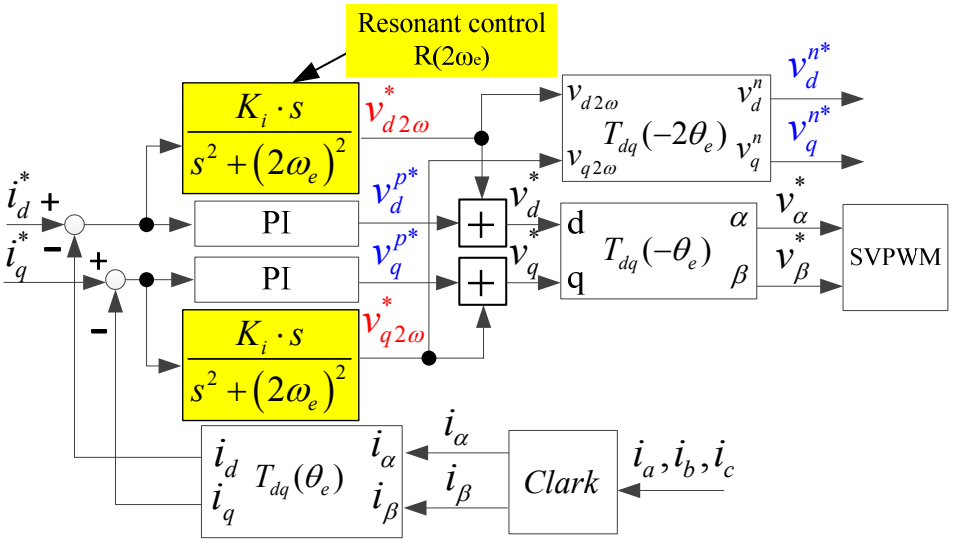

(b)

Fig.4.3 Proposed power control method of suppressing the 2h DC bus voltage. (a) Current reference generation. (b) Current control scheme.

4.4.3 Summary

The proposed method can be summarized as TABLE 4.1. Compared with the power control listed in TABLE 1.1, the proposed power control can be implemented by the proposed method, which does not require any sequential component decomposers for currents, supply voltage/back-EMFs, and especially for output voltages.

As the 2h power and DC bus voltage can be effectively suppressed by the proposed method, the PI-R control employed in the DC bus voltage control aiming for suppressing the 2h DC bus voltage in [119] is not necessary and the PI control is enough for regulation of the DC bus voltage control. Thus, the 2h currents in *dq*-frame can be avoided; correspondingly, the third current harmonics can be avoided.

Since the proposed method is based on the output power control, the output power factor rather than the input power factor can be controlled.

TABLE 4.1

SUMMARY OF THE PROPOSED POWER CONTROL

Items	Proposed method
Power condition equations	$\begin{cases} p_{out0} = p^* \\ p_{out\_c2} = 0 \\ p_{out\_s2} = 0 \\ q_{in0} = 0 \end{cases}$
DC bus voltage control	PI
Current control	PI-R($2\omega_e$) control in PSRF
Unit input power factor	×
Unity output power factor	✓
2nd harmonic DC voltage	Low
3rd current harmonics	Low
Current reference calculation in *dq*-frame/ *αβ*-frame	*dq*-frame
Current reference calculation	Simple
Sequential components decomposer for supply voltage/Back-EMFs	No
Sequential components decomposer for currents	No
Sequential components decomposer for output voltages	No

4.5 Experiments

The test rig is the same as that illustrated in Fig.3.7. A small-scaled asymmetric 3-phase prototype PMSG is employed to verify the proposed method. The PMSG has asymmetric winding topology that results in the inherent unbalance. The inductances measured by HIOKI LCR meter IM3533-01 at the frequency of 120Hz are shown in Fig.C.1(a) and the corresponding harmonic analysis is shown in Fig.C.1(b). It is apparent that the average mutual inductance M_{AB} is quite different with the other mutual inductances M_{CA} and M_{BC}, which indicates the PMSG is unbalanced.

The integral gain of resonant controller is chosen to be equal to the integral gain of PI controller. The overall time delay, including the PWM output delay, current sampling delay and processing delay, is approximately 1.5 times of PWM period. Therefore, the optimized current PI parameters can be derived by setting the damping factor to 0.707 [70].

In this section, the experimental results of balanced current control will be firstly introduced. As expected, the 2h power and DC bus voltage will be produced. Then the proposed power control will be investigated. It will be seen that the 2h power and DC bus voltage can be suppressed effectively. Hereafter, the extraction of the sequential output voltages will be analyzed in detail. Finally, it will be verified that the proposed method is applicable under different asymmetries.

4.5.1 Balanced Current Control

In this experiment, the *d*-axis and *q*-axis current references in the PSRF in Fig.4.3(a) are assigned to zero and -4A respectively, while *N*-sequence current references in the NSRF are assigned to be zero. The speed is regulated to be 60rpm by the servo motor.

The experimental results are shown in Fig.4.4. As can be seen from the phase currents in Fig.4.4(a), they are very balanced. However, due to the unbalanced impedances in the PMSG, the instantaneous output active power p_2 (equal to p_{out} if the inverter loss is neglected) has apparent oscillation, Fig.4.4(b). From the harmonic analysis based on the mechanical frequency, Fig.4.4(b), it can be found that the 2h power (32nd mechanical frequency due to number of the pole pairs is 16) is apparent. Therefore, the DC bus voltage ripple of the second electrical frequency, Fig.4.4(c), is obvious.

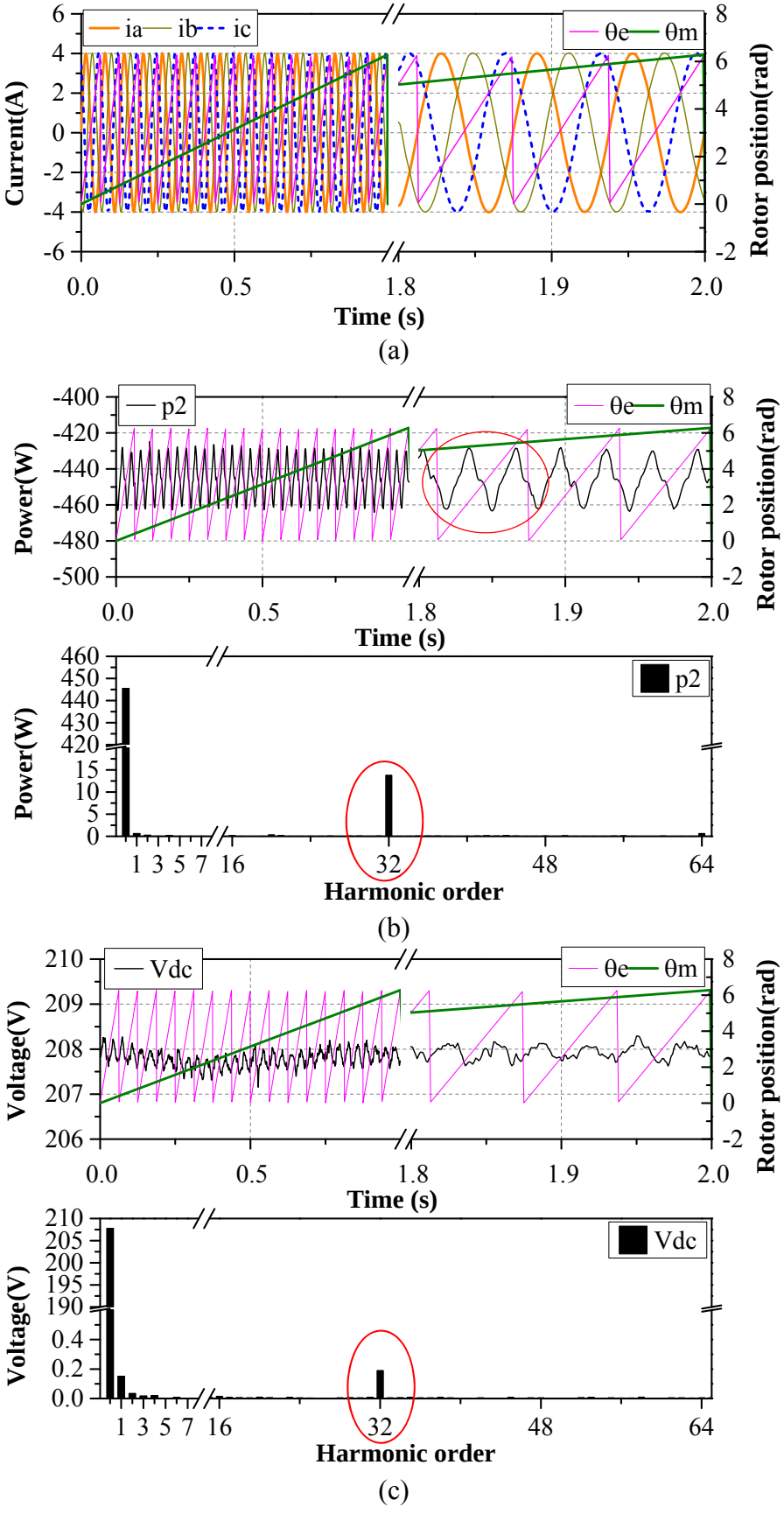

Fig.4.4 Balanced current control, harmonic analysis based on mechanical frequency. (a) Phase currents. (b) Active power. (c) DC bus voltage.

4.5.2 Proposed Power Control

The experimental results of the proposed power control are shown in Fig.4.5 and Fig.4.6. In this experiment, the speed is regulated to be 60rpm by the servo motor, and the average active and reactive power reference in Fig.4.3(a) are assigned to -400W and 0W respectively.

From the active power and the corresponding harmonic analysis, Fig.4.5(b), it can be seen the average active power is -400W, which means the active power is fairly regulated. The phase currents are shown in Fig.4.5(a), which are slightly more unbalanced than those in Fig.4.4(a). This is because the *N*-sequence currents are injected into the stator currents to suppress the 2h active power. As can be seen from Fig.4.5(b), the 2h active power is much smaller than that in Fig.4.4(b). Consequently, the 2h DC bus voltage in Fig.4.5(c) is much smaller than that in Fig.4.4(c).

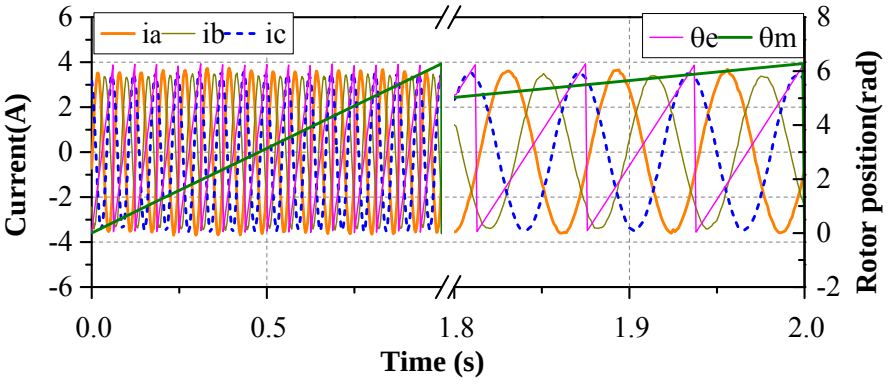

(a)

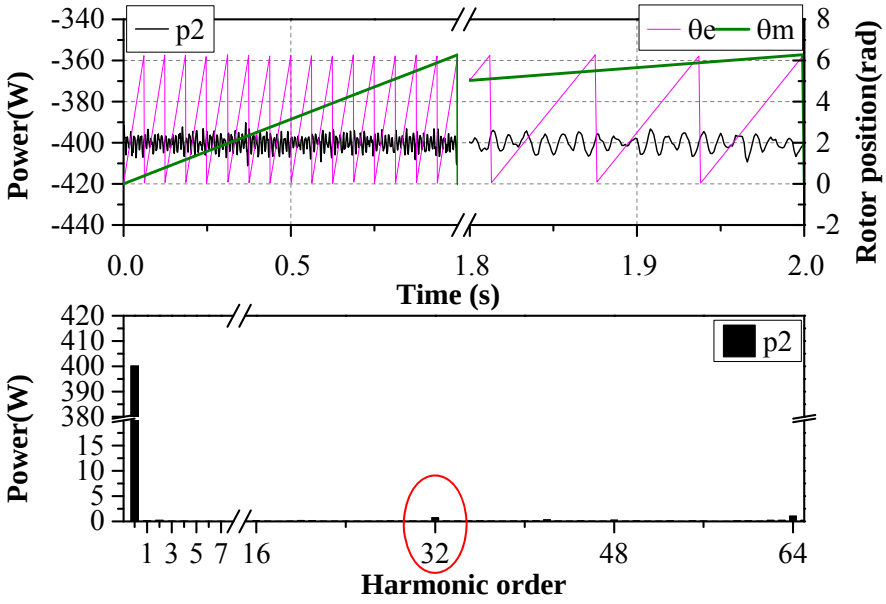

(b)

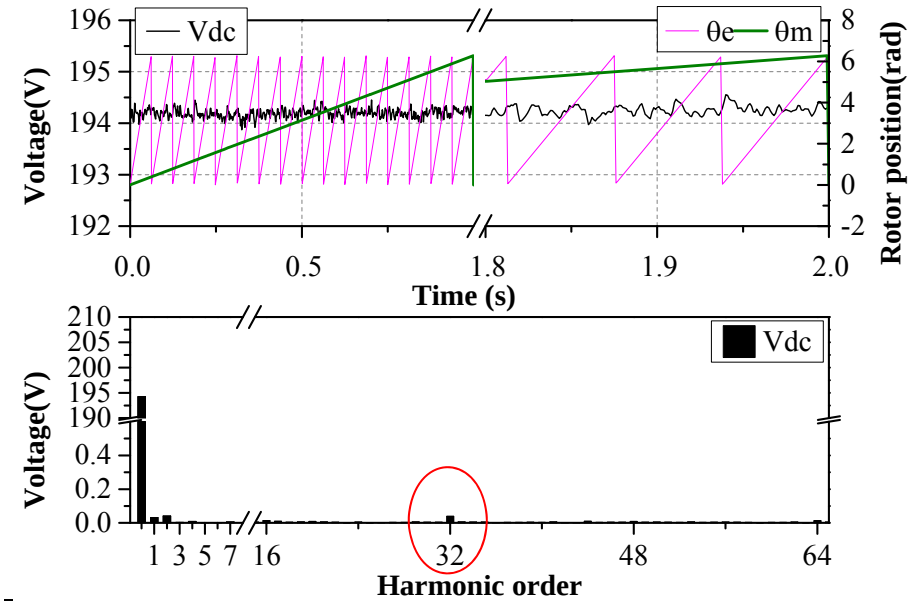

(c)

Fig.4.5 Experimental results-1 of proposed power control, harmonic analysis based on mechanical frequency. (a) Phase currents. (b) Active power and harmonic analysis. (c) DC bus voltage and harmonic analysis.

The *P*-sequence current references in the PSRF and *N*-sequence current references in the NSRF are shown in Fig.4.6(a). It can be seen that they are DC signals. The *P*-sequence output voltages in the PSRF and *N*-sequence output voltages in the NSRF are shown in Fig.4.6(d), where the DC signals are dominant. Since the *N*-sequence currents in NSRF are not zero, there are apparent 2h currents in the *dq*-axis currents in the PSRF, Fig.4.6(b). Due to the unbalanced currents and unbalanced impedances, the output voltages will be unbalanced as well. As shown in Fig.4.6(c), the amplitude of phase voltages are different. Consequently, there are apparent 2h voltages in the *dq*-axis voltages in PSRF, Fig.4.6(e).

It's worth noting that although the average reactive power is zero, Fig.4.6(f), there is evident 2h power since the coefficients of 2h reactive power in (4.23) are not involved for current references generation (4.25).

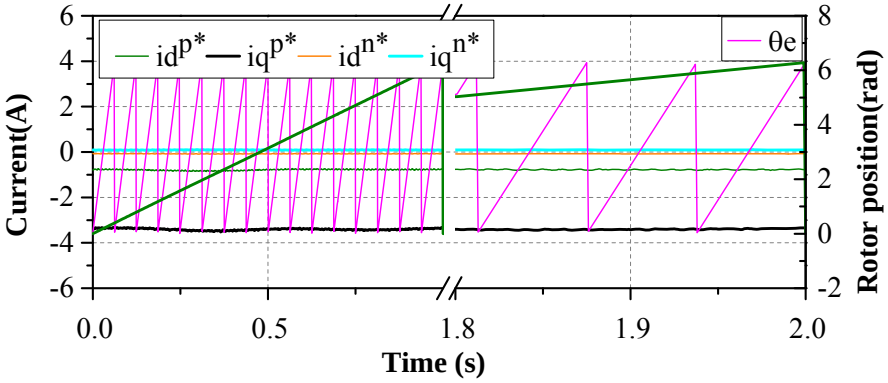
id^p*
iq^p*
id^n*
iq^n*
θe
Current(A)
Rotor position(rad)
Time (s)

(a)

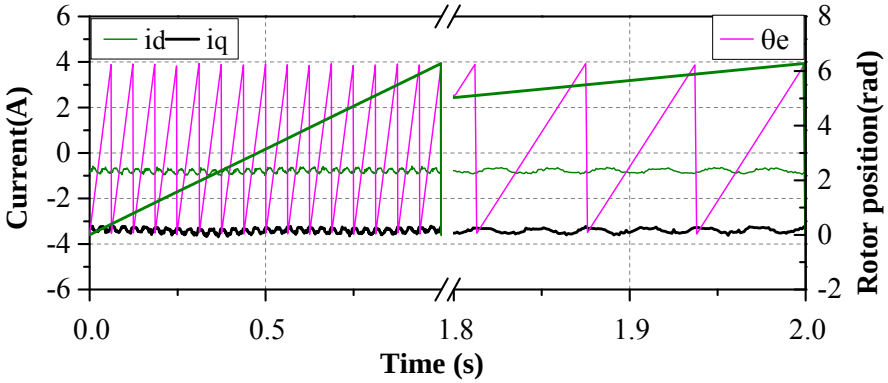
id
iq
θe
Current(A)
Rotor position(rad)
Time (s)

(b)

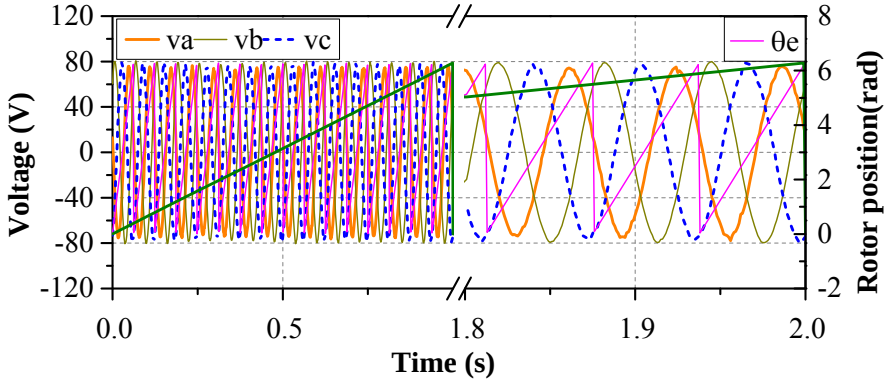
va
vb
vc
θe
Voltage (V)
Rotor position(rad)
Time (s)

(c)

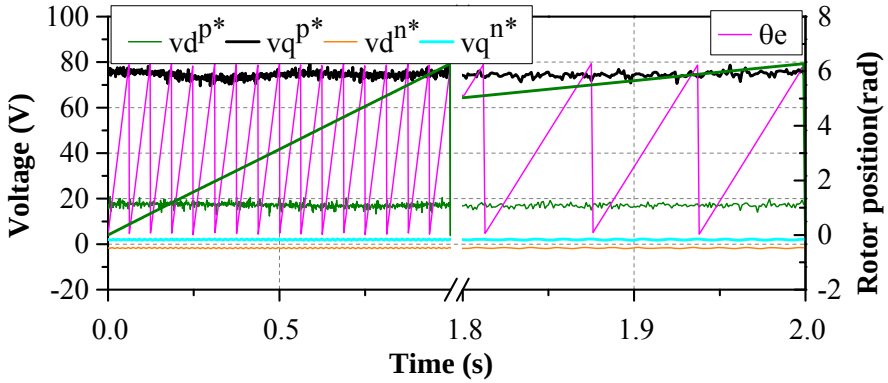
vd^p*
vq^p*
vd^n*
vq^n*
θe
Voltage (V)
Rotor position(rad)
Time (s)

(d)

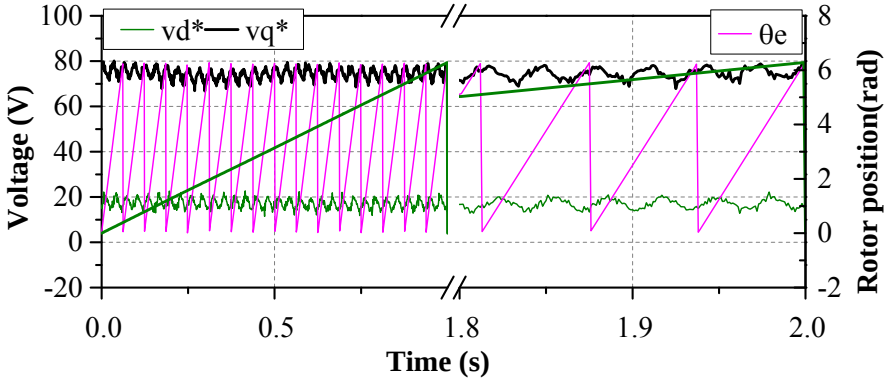

(e)

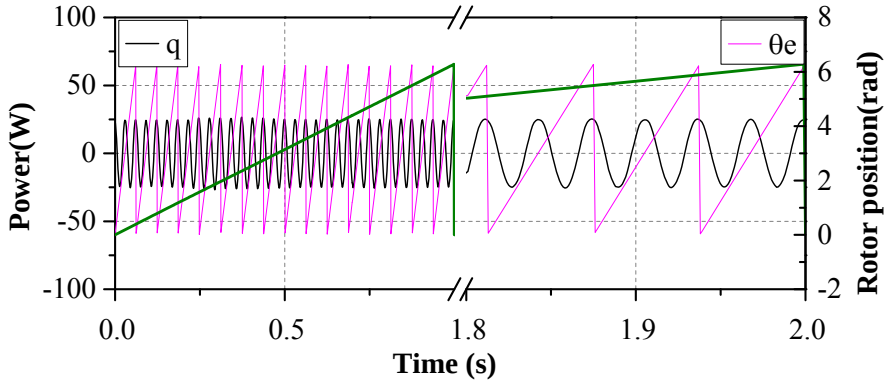

(f)

Fig.4.6 Experimental results-2 of proposed power control, harmonic analysis based on mechanical frequency.. (a) *P*- and *N*-sequence current references in PSRF and NSRF respectively. (b) *dq*-axis currents. (c) Phase ABC output voltages. (d) *P*- and *N*-sequence voltages in PSRF and NSRF respectively. (e) *dq*-axis voltages. (f) Reactive power.

4.5.3 Extraction of Sequential Output Voltages

The extracted sequential output voltages are shown in Fig.4.7. It can be seen from Fig.4.7(a) that the dominant DC values are in V_{dp}* and V_{qp}* rather than in $V_{d2\omega}$* and $V_{q2\omega}$*, which means nearly almost all the *P*-sequence voltages are mapped to V_{dp}* and V_{qp}*. It can also be seen from Fig.4.7(b) that the dominant 2h output voltages are in $V_{d2\omega}$* and $V_{q2\omega}$* rather than in V_{dp}* and V_{qp}*, which means the nearly all the 2h output voltages are mapped to $V_{d2\omega}$* and $V_{q2\omega}$*. Therefore, the *P*- and *N*-sequence voltages can be separated effectively by the proposed method.

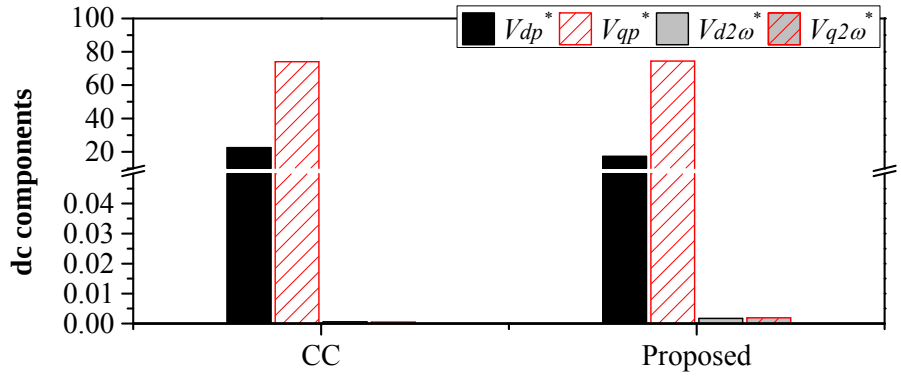

(a)

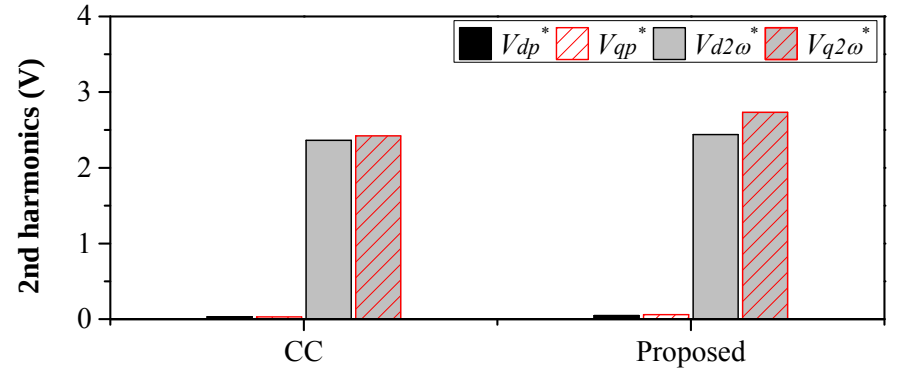

(b)

Fig.4.7 Extraction of the sequential voltages (CC: balanced current control). (a) DC components. (b) Second harmonics.

4.5.4 Different Asymmetries

In the following experiments, an external inductor is deliberately connected in series with phase *A*, *B*, and *C* respectively. The equivalent inductance and resistance in the inductor are 5.63mH and 1.15Ω respectively. The inherent asymmetry, the extra asymmetries can be summarized in TABLE 4.2 when the phase A, B, or C is connected with the extra inductor respectively.

The experimental results of different DC bus capacitors (3000μF or 1500μF) and different asymmetries are shown in Fig.4.8, where "inherent" denotes the inherent asymmetry, "phase A", "phase B", and "phase C" mean the corresponding phase is connected deliberately with the introduced inductor in series, the "CC" means balanced current control, the "Proposed" means the proposed power control. The capacitance in Fig.4.8 means the DC bus capacitance is 3000μF or 1500μF when the experiments are conducted.

The experimental results show that the proposed method can suppress the 2h power and DC bus voltage effectively under the conditions of different asymmetries and different DC bus capacitors.

TABLE 4.2

ASYMMETRIES IN DIFFERENT CASES

Cases	Asymmetries
Case 1	Inherent asymmetry
Case 2	Extra asymmetry when phase *A* with external inductor in series
Case 3	Extra asymmetry when phase *B* with external inductor in series
Case 4	Extra asymmetry when phase *C* with external inductor in series

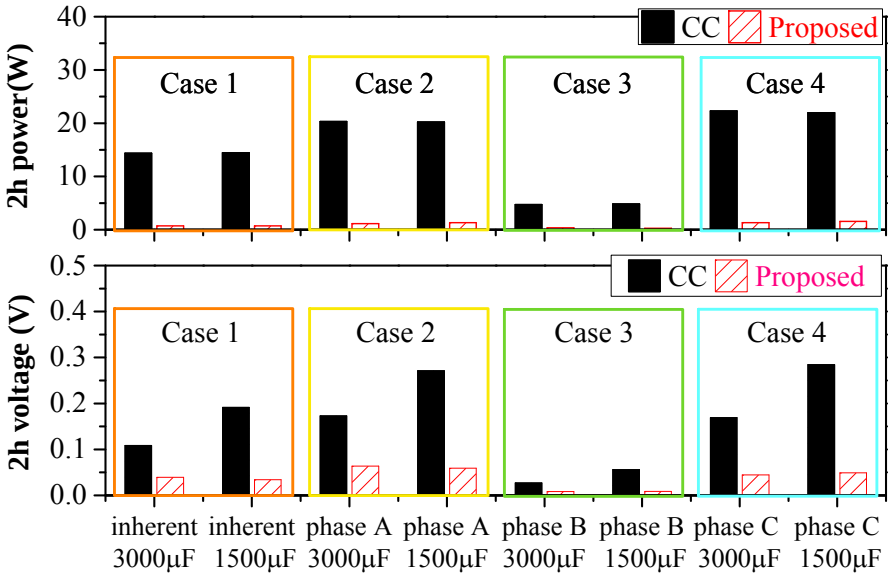

Fig.4.8 Comparison of the 2h power and DC bus voltage under the conditions of different asymmetries and DC bus capacitors (CC: balanced current control, Proposed: Proposed power control).

4.6 Conclusion

An improved power control of suppressing the 2h DC bus voltage under generalized unbalanced conditions without sequential component decomposers has been investigated. No special sequential decomposers, such as time delaying method, notch filter method, or dual second-order generalized integrator (DSOGI) method are required for the extraction of *P*- and *N*-sequence currents and output voltages. Since the proposed method does not require any

information of the PMSG's parameters, it is robust to different types of asymmetries. The effectiveness has been verified on a small-scaled 3-phase prototype PMSG with considerable inherent asymmetry and deliberately introduced asymmetries. The elaborate experimental results show that the proposed method can suppress the 2h DC bus voltage effectively.

Chapter 5 Control of Asymmetric PMSG with Compensation in Parallel

5.1 Introduction

As introduced in Chapter 3, the *N*-sequence currents in the unbalanced system can be suppressed by the balanced current control, e.g. the PR control in $\alpha\beta$-frame [99-101], the dual current control [87, 102, 142], or the PI-R control in PSRF [108-110]. Therefore, the 2h torque can be reduced if the 3-phase back-EMFs are balanced. However, the 2h power due to the system asymmetries will be introduced [112], which flows through the DC bus capacitors and results in 2h DC bus voltage [113, 114], capacitor power losses, temperature rise, and reduced lifetime [93].

In Chapter 4, the 2h power and DC bus voltage suppressed by an improved instantaneous power control is investigated. The principle of instantaneous power control is that the 2h power generated by the *P*-sequence currents is compensated by the 2h power generated by the *N*-sequence currents. Therefore, the *N*-sequence currents are inevitable in order to suppress the 2h power in the unbalanced system. As shown in TABLE 2.2, the *N*-sequence currents will interact with back-EMFs and result in 2h torque and corresponding mechanical vibration. As presented in [37], severe vibrations, corresponding acoustic noise, and fatigue [27] could happen due to mechanical resonance, which is not allowed in the wind turbine system.

Overall, none of the conventional current control, the balanced current control in Chapter 3 or the instantaneous power control in Chapter 4 can suppress the 2h power and the 2h torque of the asymmetric PMSG simultaneously. To solve the 2h torque ripple and DC bus voltage ripple, with only *P*-sequence currents injection to avoid 2h torque ripple, the undesired 2h power can be transferred to the grid network by the instantaneous power feed-forward control [123-125]. However, this approach increases the THD of the grid currents and it should be avoided in most applications. The undesired 2h power generated by the asymmetric PMSG has to be transferred to somewhere else.

An alternative way is to transfer the fluctuated power to an energy storage device [130-132]. In [132], the DC bus voltage ripple was suppressed by coordinated DC bus voltage

control, where the current reference from the DC bus voltage PI controller was distributed between the grid side and energy storage system. To suppress the DC bus voltage pulsation without the information of power pulsation from PMSG, high bandwidth of DC bus voltage PI control is required, which may result in potential instability. This approach can be classified as the post-treatment because it dealt with the fluctuated power that was there already.

In [133], a compensation device in parallel with the DC bus was employed to suppress the 2h DC bus voltage due to the grid supply voltage asymmetries. The 2h power generated by the asymmetric system is compensated by the power generated by the compensation device. Different with the method in [132], this approach requires the information of the 2h power generated by the asymmetric system. When this approach is applied to the asymmetric PMSG wind turbine system, as the 2h power generated by the PMSG have been suppressed before flowing towards the DC bus capacitors, this approach can be classified as pre-treatment, which is especially suitable in distributed DC power systems [150]. However, the problem of the approach in [133] is that the power pulsation due to the asymmetric impedances was not considered.

The comparison of the aforementioned methods is shown in TABLE 5.1. As can be seen from TABLE 5.1, the method of transferring the 2h power to energy storage device is the best solution for suppressing the DC bus voltage ripple and torque ripple without deterioration of current THD of grid side.

TABLE 5.1

COMPARISON OF DIFFERENT METHODS

Methods	Generator side	DC bus capacitors	Grid side
Balanced current control	✓	2h DC bus voltage ripple	Increased current THD
instantaneous power control	Torque ripple	✓	✓
Power feed-forward control	✓	✓	Increased current THD
Transfer the 2nd power to energy storage device	✓	✓	✓

Based on the same principle of transferring the fluctuated power to a compensation unit, [132, 133], an effective pre-treatment method accounting for the asymmetric impedances is investigated in this chapter, which considers the current THD of grid side, the 2h DC bus voltage, and the 2h torque of PMSG. The instantaneous average power control without *N*-sequence currents is employed to avoid the 2h torque, while the 2h power caused by PMSG impedance asymmetries will be directly transferred to the active compensation unit without involvement of the grid side, and consequently, the DC bus voltage ripple can be suppressed. In this chapter, two power topologies of the compensation unit, which are designated as Topology-*RL* and Topology-*RLE*, will be investigated and their corresponding control method will be presented.

5.2 Compensation in Parallel (Topology-*RL*)

5.2.1 Introduction

In this section, the compensation unit with topology-*RL* shown in Fig.5.1 will be investigated. It is constructed by H-bridge power switches and a compensation inductor. Since the compensation inductor (L) with inherent resistance (R) is employed as storage device to exchange the 2h power with the DC bus, the topology of this compensation unit is designated as Topology-*RL*. The proposed control strategy will be introduced in Section 5.2.2 and the corresponding implementation will be introduced in Section 5.2.3, and then elaborated experiments with deliberately introduced asymmetries will be conducted in Section 5.2.4 to validate the effectiveness of the proposed method.

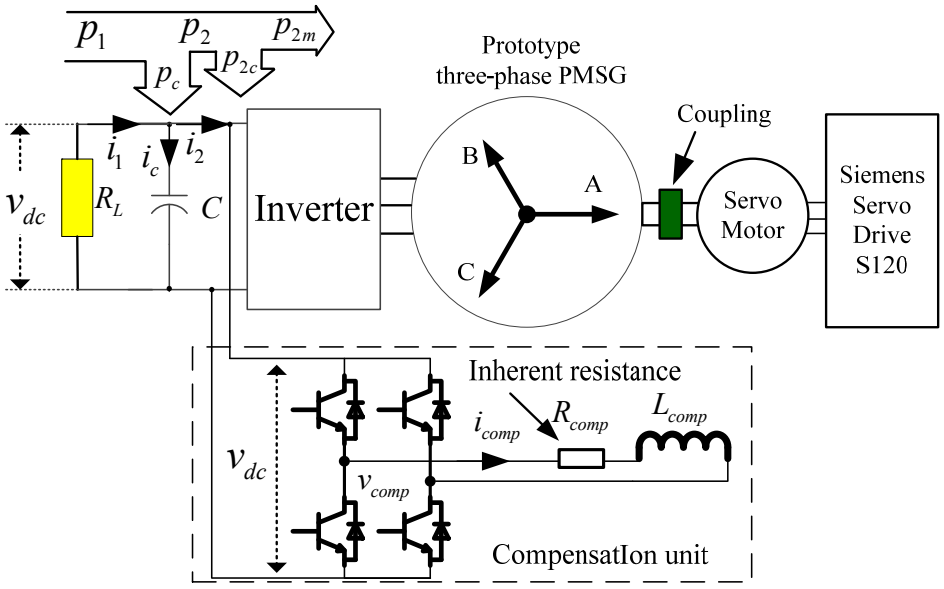

Fig.5.1 Topology of the proposed compensation in parallel (Topology-*RL*).

5.2.2 Compensation Principle

As described in the Appendix C, the mutual inductances of the dual 3-phase PMSG in single 3-phase mode are asymmetric, while the resistances and back-EMFs are balanced although the proposed method will be generally applicable to PMSG having any impedance asymmetries.

If the 2h torque is to be avoided, the *N*-sequence currents cannot be injected into the stator currents, and the 2h power resulted from the inherent asymmetry will flow into the DC bus. If the 2h power is not transferred to the grid side or it does not flow through the DC bus capacitors, another flowing path for the 2h power has to be provided. In this section, an active compensation unit is proposed to absorb the 2h power before it flows towards the DC bus capacitors, as shown in Fig.5.1. If the 2h power in the power p_{2m} from the PMSG and the 2h power in the power p_{2c} from the compensation unit can be cancelled, the 2h power flowing into the DC bus capacitors will be suppressed.

To compensate the 2h power (4.2)，the frequency of the compensation current should be the same as the fundamental frequency. Assuming the compensation current i_{comp} in Fig.5.1 can be expressed as

$$i_{comp} = I_{comp}\cos\left(\theta_e + \theta_{comp}\right) \tag{5.1}$$

where I_{comp} and θ_{comp} are the amplitude and offset angle of the compensation current respectively, the compensation voltage v_{comp} in Fig.5.1 under steady-state operation will be

$$\begin{aligned} v_{comp} &= i_{comp}R_{comp} + L_{comp}\left(di_{comp}/dt\right) \\ &= I_{comp}Z_{comp}\cos\left(\theta_e + \theta_{comp} + \Delta\theta\right) \end{aligned} \tag{5.2}$$

where

$$Z_{comp} = \sqrt{R_{comp}^2 + \left(\omega_e L_{comp}\right)^2} \tag{5.3}$$

$$\Delta\theta = \arctan\left(\omega_e L_{comp} / R_{comp}\right) \tag{5.4}$$

where L_{comp} is the compensation inductance, R_{comp} is the inherent resistance of the inductor.

Therefore, the power from the compensation unit will be

$$p_{2c} = v_{comp}i_{comp} = P_{2c\_2h}\left(\cos\left(\Delta\theta\right) + \cos\left(2\theta_e + 2\theta_{comp} + \Delta\theta\right)\right) \tag{5.5}$$

where

$$P_{2c\_2h} = 0.5 I_{comp}^2 Z_{comp} \tag{5.6}$$

From (5.5), it can be seen that there are DC and 2h components in p_{2c}. The amplitude of p_{2c} is proportional to the square of the I_{comp}. Therefore, by adjusting the amplitude I_{comp} and initial offset angle θ_{comp}, a specific 2h power could be generated to compensate the 2h power resulted from PMSG asymmetries.

As can be seen from (5.5) and (5.6), to compensate the 2h power for given asymmetries, the compensation inductance is inversely proportional to the square of the compensation current. Generally, the inductor size is proportional to the energy stored in the inductor. Therefore, under the constraint of the same inductor size, the compensation inductance can be designed relatively high so that the compensation current can be reduced, which will be beneficial to the power switches of the compensation unit.

5.2.3 Implementation

To avoid the 2h torque resulted from the *N*-sequence currents; the instantaneous average power control without *N*-sequence currents is employed, which is illustrated in Fig.5.3(a). As detailed in [102, 114], the instantaneous active power p_{out} in the unbalanced system can be expressed as

$$p_{out} = p_{out0} + p_{out\_c2}\cos(2\theta_e) + p_{out\_s2}\sin(2\theta_e) \tag{5.7}$$

where p_{out_c2} and p_{out_s2} are the 2h coefficients of active output power, p_{out0} is the average output power which can be expressed as

$$p_{out0} = 1.5\left(v_d^p i_d^p + v_q^p i_q^p + v_d^n i_d^n + v_q^n i_q^n\right) \tag{5.8}$$

where subscripts *d, q* means *d*-axis and *q*-axis respectively, the superscripts *p, n* mean *P*- and *N*-sequence components respectively.

Due to the infinite selection characteristic at the center frequency in the resonant control [96-98], the *N*-sequence output voltages are dominant in the output of the resonant controller. Thus, the output voltages from the PI controller are mainly *P*-sequence voltages. As no zero sequence currents are involved and i_d*=0 control is employed in Fig.5.3(a), the *q*-axis current reference i_q* can be derived directly from the power reference and can be expressed as

$$i_q^* = i_q^{p*} = p_{out0}^* / \left(1.5 v_q^{p*}\right) \tag{5.9}$$

Followed by i_q* calculation, the PI-R control in the PSRF [108] is employed to regulate the current. Since only the *P*-sequence currents are injected into the stator currents, there is no 2h torque with balanced back-EMFs. However, there is 2h power due to asymmetric impedances.

To determine the exact 2h power that should be transferred to the compensation unit, the 2h power in the power p_{2m} from the PMSG should be extracted first. In reality, the internal resistance in the compensation inductor, Fig.5.1, may not be neglected. In this case, there is average DC power and 2h power in the power p_{2c} from the compensation unit. Therefore, the 2h power in p_{2c} also needs to be extracted.

As introduced in [151], the second-order generalized integrator (SOGI) [151] can be employed to extract the 2h power. The transfer function in the SOGI can be expressed as

$$G_\alpha(s) = \frac{x_\alpha}{x_{in}} = \frac{k\omega_0 s}{s^2 + k\omega_0 s + \omega_0^2} \tag{5.10}$$

$$G_\beta(s) = \frac{x_\beta}{x_{in}} = \frac{k\omega_0^2}{s^2 + k\omega_0 s + \omega_0^2} \tag{5.11}$$

where k is the damping factor, ω_0 is the center frequency. By the SOGI filter, the 2h power can be obtained as x_α, while the 2h power delayed by 90° can be obtained as x_β.

As detailed in [151], $G_\alpha(s)$ has better filter performance below ω_0 than $G_\beta(s)$. When there is DC signal in the original input signal x_{in}, there will be considerable DC signal in x_β. Therefore, the cascade-SOGI [152], Fig.5.2, can be employed to extract the 2h power without DC component.

Therefore, according to (5.5), $p_{2c\_2h\_\alpha}$ and $p_{2c\_2h\_\beta}$ in Fig.5.2(b) can be expressed as

$$p_{2c\_2h\_\alpha\beta} = p_{2c\_2h\_\alpha} + jp_{2c\_2h\_\beta} = P_{2c\_2h} e^{j\left(2\theta_e + 2\theta_{comp} + \Delta\theta\right)} \tag{5.12}$$

where P_{2c_2h} is the amplitude of $p_{2c\_2h\_\alpha\beta}$.

Assuming the 2h power in p_{2m} from PMSG is $p_{2m\_2h\_\alpha}$, the signal lags $p_{2m\_2h\_\alpha}$ 90º is $p_{2m\_2h\_\beta}$, and then the vector $p_{2m\_2h\_\alpha\beta}$ can be expressed as

$$p_{2m\_2h\_\alpha\beta} = p_{2m\_2h\_\alpha} + jp_{2m\_2h\_\beta} \tag{5.13}$$

To compensate the 2h power $p_{2m\_2h\_\alpha}$, the 2h power reference $p_{2c\_2h\_\alpha}^*$ and $p_{2c\_2h\_\beta}^*$ for the compensation unit should be

$$p_{2c\_2h\_\alpha\beta}^* = p_{2c\_2h\_\alpha}^* + jp_{2c\_2h\_\beta}^* = -p_{2m\_2h\_\alpha\beta} \tag{5.14}$$

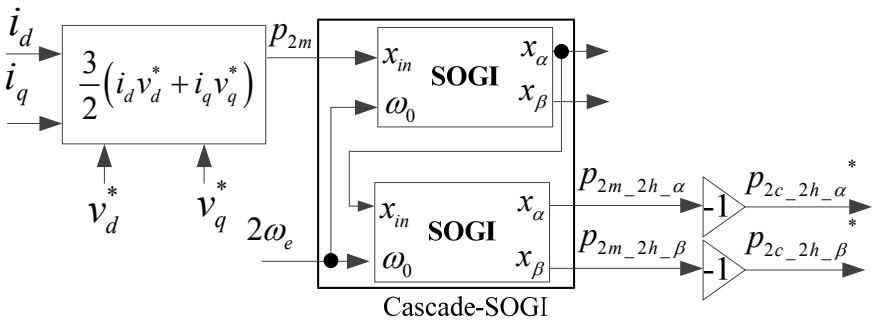

(a)

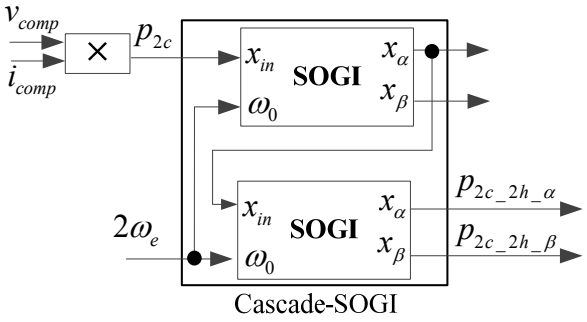

(b)

Fig.5.2 Extraction of 2h power. (a) Extraction of the 2h power reference. (b) Extraction of the 2h power in the compensation unit.

Assuming $p_{2c\_2h\_\alpha\beta}^*$ can be expressed as

$$p_{2c\_2h\_\alpha\beta}^* = P_{2m\_2h} e^{j(2\theta+\theta_{2m})} \tag{5.15}$$

where P_{2m_2h} is the amplitude of $-p_{2m\_2h\_\alpha\beta}$, then the error between the amplitudes of the reference and the feedback 2h powers can be represented as

$$\left|p_{2c\_2h\_\alpha\beta}^*\right|^2 - \left|p_{2c\_2h\_\alpha\beta}\right|^2 = P_{2m\_2h}^2 - P_{2c\_2h}^2 \tag{5.16}$$

The phase error between the reference and the feedback 2h powers can be represented by the cross product of (5.12) and (5.15), which can be expressed as

$$p_{2c\_2h\_\alpha\beta} \times p_{2c\_2h\_\alpha\beta}^* = P_{2m\_2h} P_{2c\_2h} \sin\left(\theta_{2m} - 2\theta_{comp} - \Delta\theta\right) \tag{5.17}$$

The dot product of (5.12) and (5.15) can be expressed as (5.18). To guarantee the phase error between the reference and the feedback 2h powers to be 0° rather than 180°, (5.18) should be bigger than zero.

$$p_{2c\_2h\_\alpha\beta} \cdot p_{2c\_2h\_\alpha\beta}^* = P_{2m\_2h} P_{2c\_2h} \cos\left(\theta_{2m} - 2\theta_{comp} - \Delta\theta\right) \tag{5.18}$$

To compensate the 2h power, (5.16) and (5.17) should be zero. Therefore, (5.16) can be employed to regulate the amplitude of current reference of i^*_{comp}, and (5.17) can be employed to regulate the initial angle of i^*_{comp}, while (5.18) is employed to make sure (θ_{2m} -$2\theta_{comp}$-$\Delta\theta$) is 0° rather than 180°. Therefore, the control block diagram of 2h power compensation can be illustrated in Fig.5.3(b).

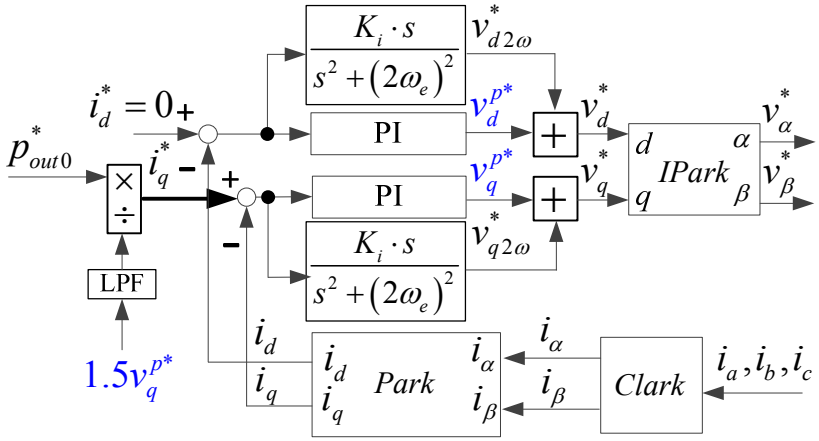

(a)

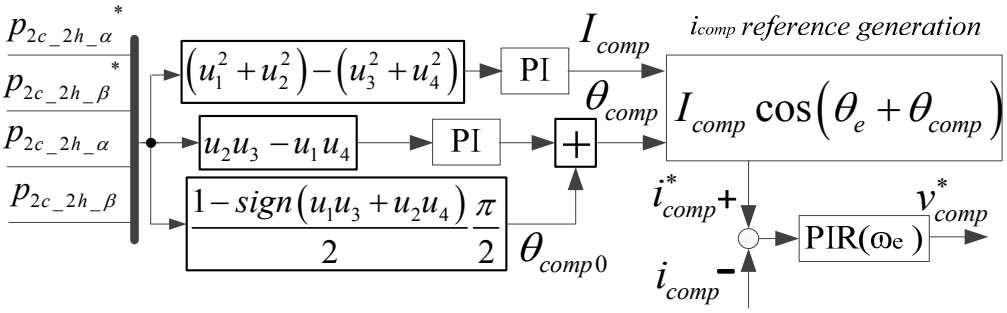

(b)

Fig.5.3 Control scheme of the proposed method. (a) Instantaneous average power control of PMSG. (b) Compensation current regulation.

5.2.4 Experimental Investigation

The test rig is demonstrated in Fig.5.1 and the test rig prototype is shown in Fig.B.2. The prototype PMSG is coupled with a servo machine, which is used to simulate the wind turbine. A power resistor R_L (100 Ω) is parallel with the DC bus to consume the power generated by the PMSG. The prototype machine is actually a dual 3-phase PMSG, which is detailed in Appendix B. To investigate the compensation effect on the asymmetric 3-phase PMSG, the second set of 3-phase windings of the dual 3-phase PMSG is disconnected deliberately. The

inherent asymmetries of the dual 3-phase PMSG are detailed in Appendix C, where it is demonstrated that there is apparent asymmetry in the single set of 3-phase windings.

The compensation inductor is shown in Fig.5.4, which is constructed by 12 cells connected in series and its size is about 0.86% of the prototype PMSG. The inherent resistance and inductance of the inductor are 1Ω and 8.67mH, respectively. The measured parameters of total compensation inductor by HIOKI LCR meter IM3533-01 are listed as TABLE 5.2.

TABLE 5.2
PARAMETERS OF COMPENSATION CIRCUIT

Parameters	Value
L_{comp} (mH)	8.67 (39% of L_0)
R_{comp} (Ω)	1
RMS current *(A)*	10
Dimensions(each cell)	**Configurations and Dimensions** 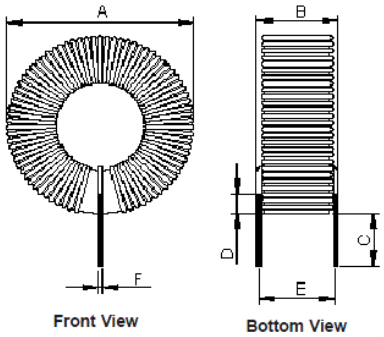 A 43 mm (Max.) B 16 mm C 12.5 ±1 mm - D 1 mm (Min.) E 13.5 ±1 mm - F 1 ±0.1 mm - http://www.farnell.com/datasheets/1323796.pdf

Fig.5.4 Compensation inductor.

In this section, the power and torque ripple in the balanced current control, instantaneous power control and proposed method will be investigated and compared.

It is worth noting that the number of pole pairs of the prototype machine is 16. Therefore, the 32nd harmonic in the following harmonic analyses based on the mechanical frequency indicates the 2h component in electrical frequency.

5.2.4.1 Inherent Asymmetry Without/With Compensation

5.2.4.1.1 Balanced Current Control without Compensation

In this experiment, the PI-R control in PSRF in Fig.3.6, which is capable to suppress the N-sequence currents in the asymmetric system, is employed. The speed is 60rpm, which is regulated by the servo machine. The *d*-axis and *q*-axis current references are 0*A* and -4*A* respectively. The experiment results without compensation have been presented in Fig.4.4 in Section 4.5.1. For the convenience of comparison with the proposed compensation, the phase currents, power, and DC bus voltage without compensation are repeated in Fig.5.5(a), (b) and (c) respectively. Meanwhile, the measured torque is shown in Fig.5.5(d). As can be seen from Fig.5.5(a), the phase currents are quite balanced. However, due to the unbalance introduced in Appendix C, there is considerable 2h power in the instantaneous power of p_2, Fig.5.5(b). Therefore, there is also apparent 2h DC bus voltage in Fig.5.5(c). However, since the currents and back-EMFs of the prototype machine are quite balanced, the 2h torque in Fig.5.5(d) is negligible.

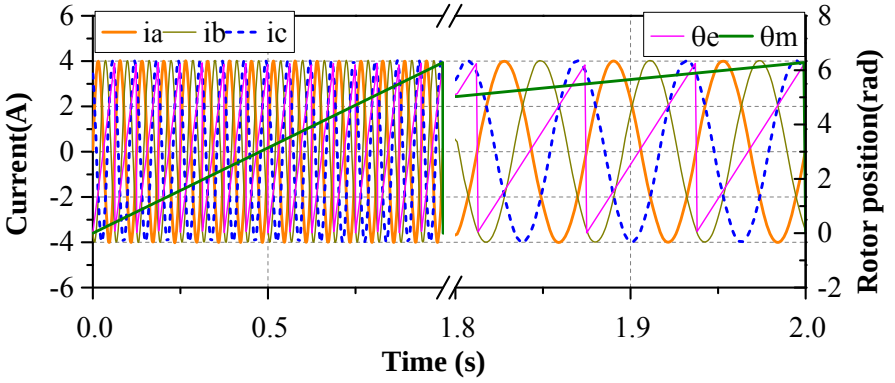
ia
ib
ic
θe
θm
Current(A)
Rotor position(rad)
Time (s)

(a)

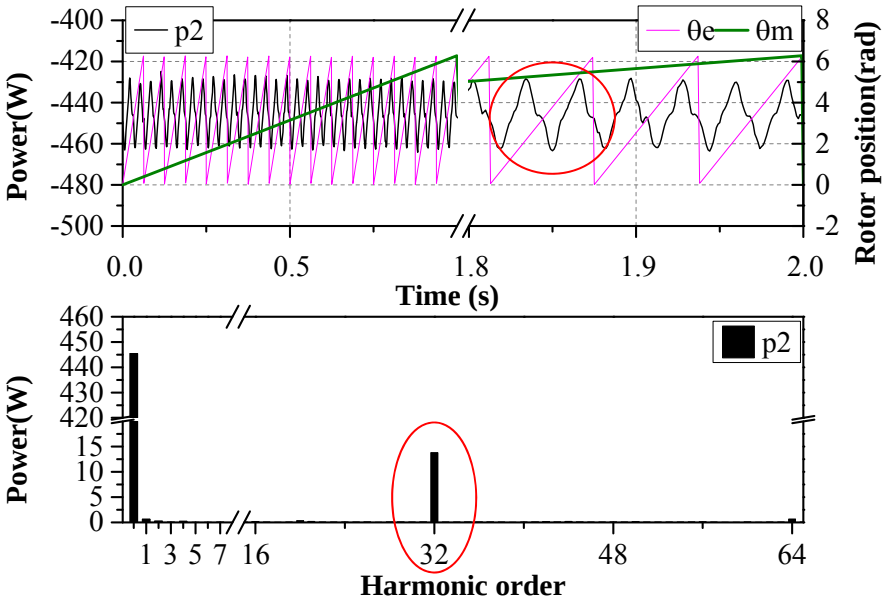
p2
θe
θm
Power(W)
Rotor position(rad)
Time (s)
p2
Power(W)
Harmonic order

(b)

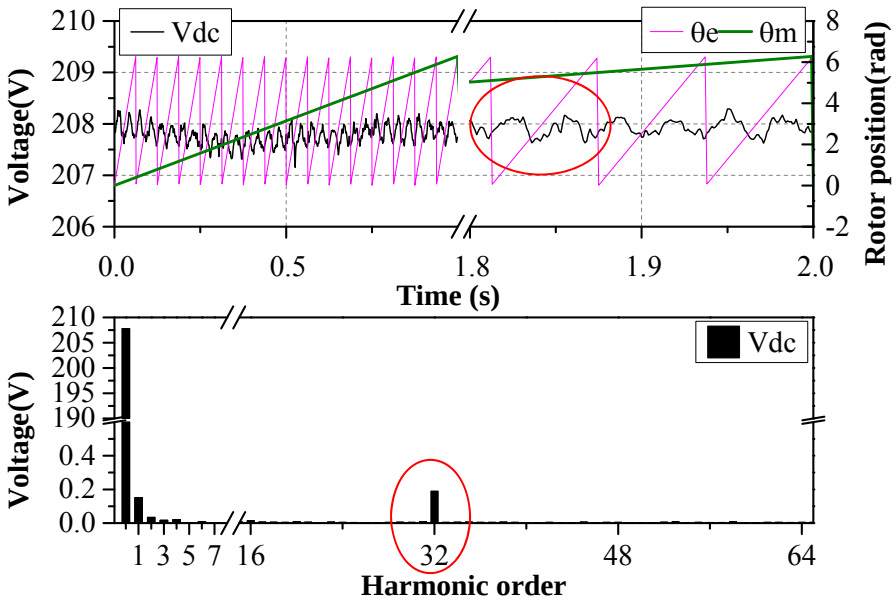
Vdc
θe
θm
Voltage(V)
Rotor position(rad)
Time (s)
Vdc
Voltage(V)
Harmonic order

(c)

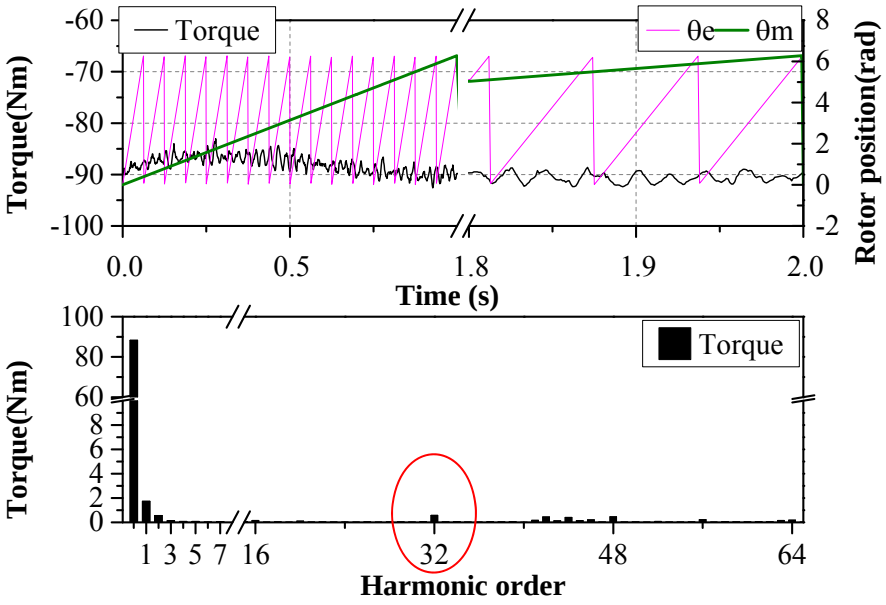

(d)

Fig.5.5 Experimental results of the balanced current control, harmonic analysis based on mechanical frequency (Without compensation). (a) Phase currents. (b) Power and harmonic analysis. (c) DC bus voltage and harmonic analysis. (d) Torque and harmonic analysis.

5.2.4.1.2 Instantaneous Power Control without Compensation

In this experiment, the instantaneous power control in Chapter 4 is employed. The speed is regulated to be 60rpm by the servo machine. The average active and reactive power reference in Fig.4.3(a) are assigned to -400W and 0W respectively. The experiment results have been illustrated in Fig.4.5. For the convenience of comparison with the proposed compensation, the phase currents, power, and DC bus voltage in the instantaneous power control are repeated in Fig.5.6(a), (b) and (c) respectively. Meanwhile, the measured torque is shown in Fig.5.6(d). As can be seen from Fig.5.6(b), the average p_2 is -400W, which means the instantaneous power control is quite effective. Compared with the 2h power in Fig.5.5(b), those harmonics in Fig.5.6(b) are well suppressed. Since the *N*-sequence currents are introduced to suppress the 2h power, the phase currents in Fig.5.6(a) are slightly unbalanced if they are compared with that in Fig.5.5(a). Compared with the 2h DC bus voltage in Fig.5.5(c), the 2h DC bus voltage in Fig.5.6(c) is suppressed effectively. However, the introduced *N*-sequence currents interact with the back-EMFs, resulting in some 2h torque, Fig.5.6(d).

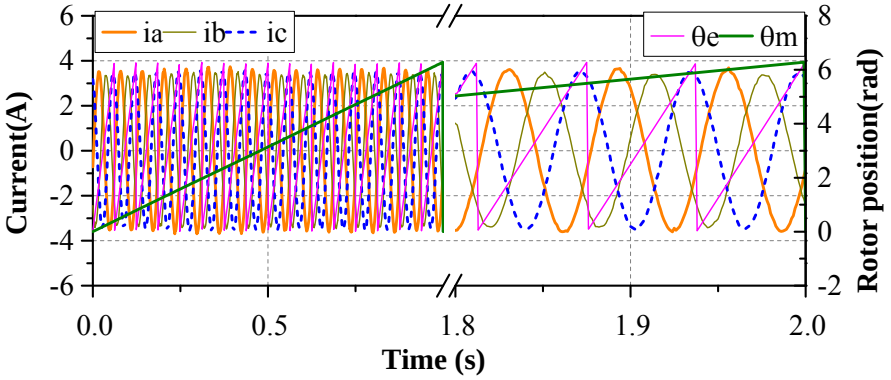
ia
ib
ic
θe
θm
Current(A)
Rotor position(rad)
Time (s)

(a)

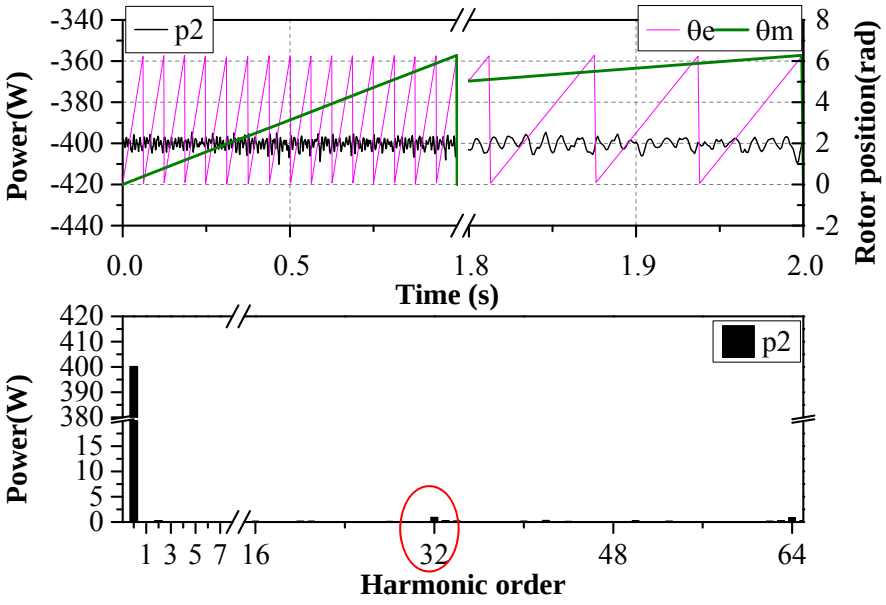
p2
θe
θm
Power(W)
Rotor position(rad)
Time (s)
p2
Power(W)
Harmonic order

(b)

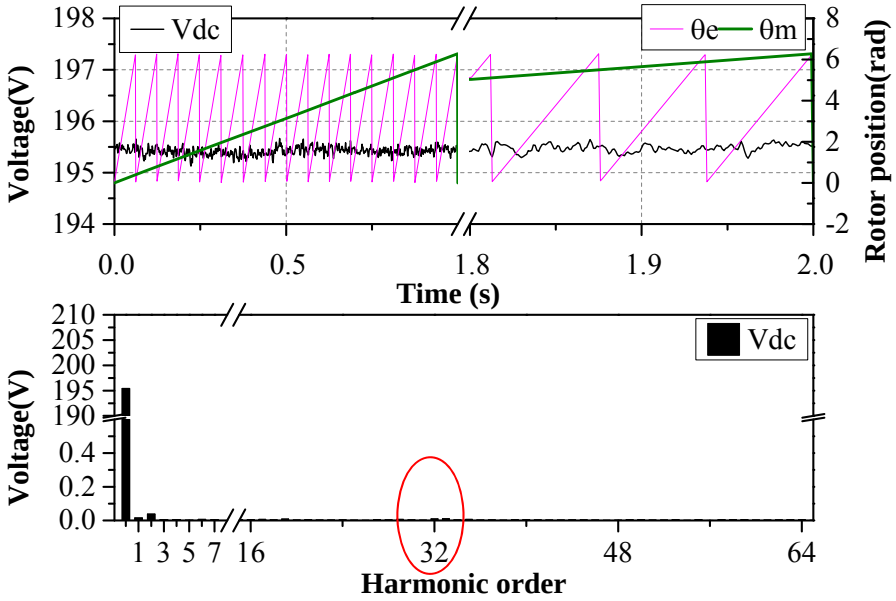
Vdc
θe
θm
Voltage(V)
Rotor position(rad)
Time (s)
Vdc
Voltage(V)
Harmonic order

(c)

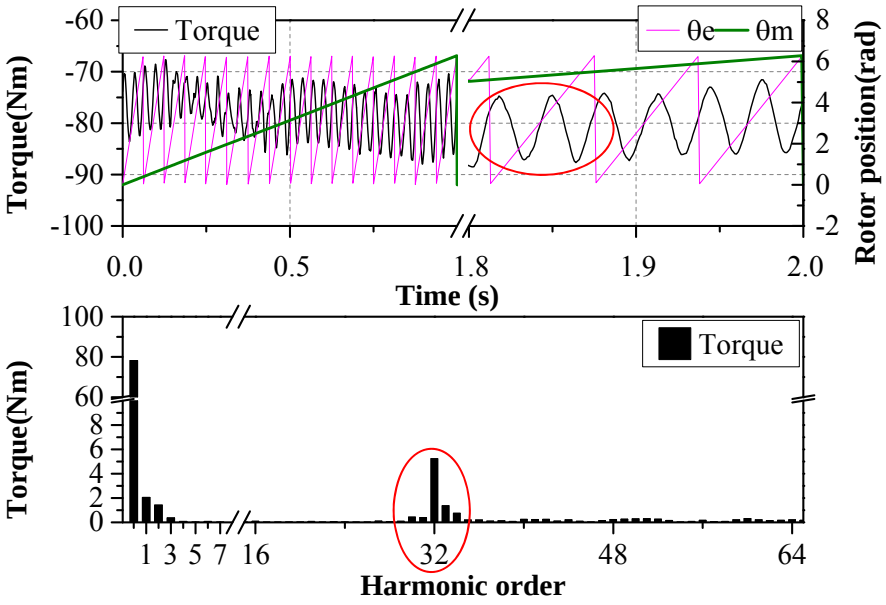

(d)

Fig.5.6 Experimental results of the instantaneous power control, harmonic analysis based on mechanical frequency (Without compensation). (a) Phase currents. (b) Power and harmonic analysis. (c) DC bus voltage and harmonic analysis. (d) Torque and harmonic analysis.

5.2.4.1.3 Proposed Power Control with Compensation

In this experiment, the compensation unit will be employed for the compensation of the 2h power from PMSG. The experimental results of the propose method with compensation are shown in Fig.5.7. The speed is 60rpm, which is controlled by the servo machine. The reference power is -400W and it is regulated very well, as can be seen from Fig.5.7(g) that the average instantaneous power p_{2m} is equal to -400W. However, there is 2h power in p_{2m} because no *N*-sequence currents are injected into the stator currents to suppress the 2h power, Fig.5.7(a). With the compensation current, Fig.5.7(e), flowing through the compensation unit, the power p_{2c} in the compensation unit can be shown in Fig.5.7(h). It can be seen that there is also 2h power in p_{2c}. The amplitude and phase of the 2h power in p_{2m} and p_{2c} are equal and anti-phase respectively, Fig.5.7(f). Therefore, the 2h power ripple in p_2 ($=p_{2m} + p_{2c}$) is cancelled, Fig.5.7(b), and the 2h DC bus voltage ripple can be suppressed effectively, Fig.5.7(c). As only *P*-sequence currents in the stator currents and the back-EMFs are quite balanced, the 2h torque in Fig.5.7(d) is much smaller than that in Fig.5.6(d).

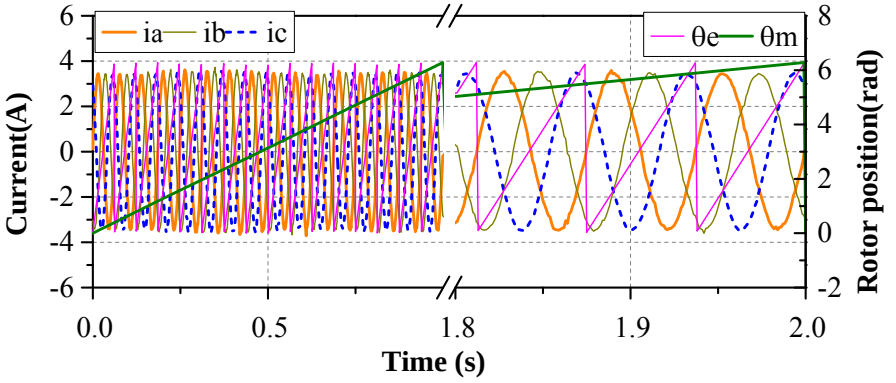
ia
ib
ic
θe
θm
Current(A)
Rotor position(rad)
Time (s)

(a)

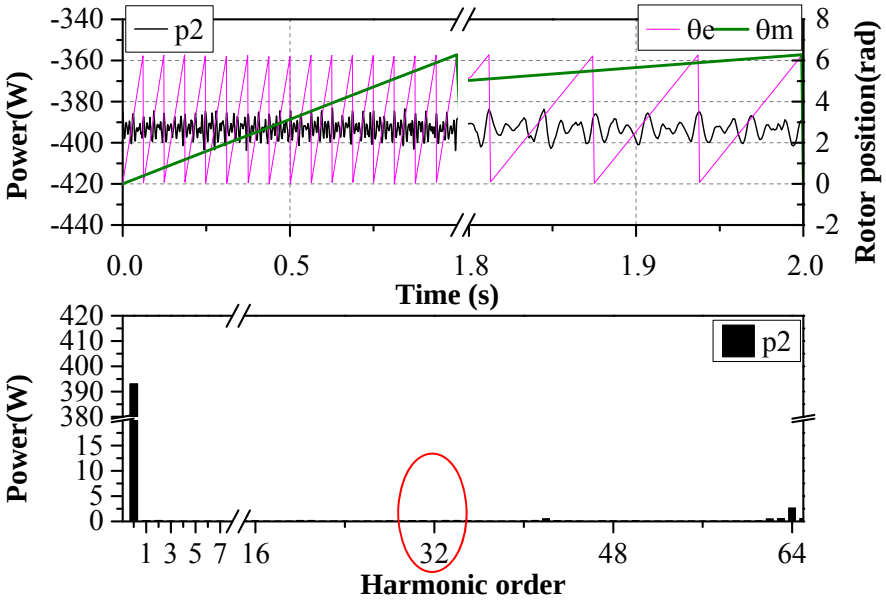
p2
θe
θm
Power(W)
Rotor position(rad)
Time (s)
p2
Power(W)
Harmonic order

(b)

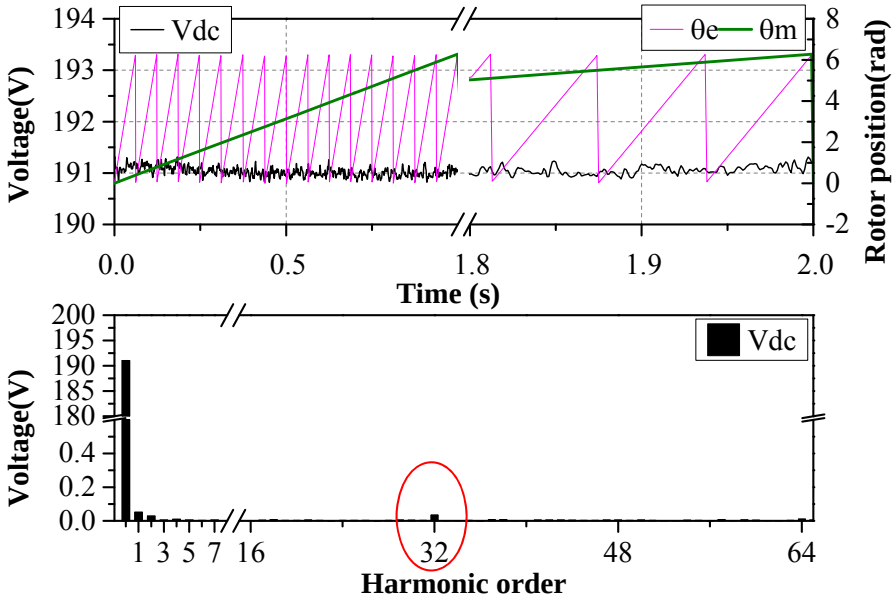
Vdc
θe
θm
Voltage(V)
Rotor position(rad)
Time (s)
Vdc
Voltage(V)
Harmonic order

(c)

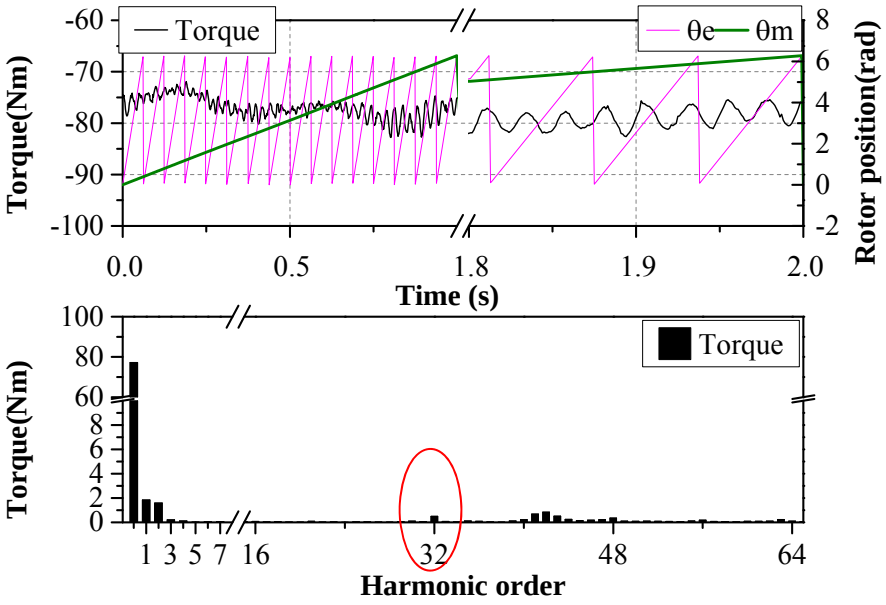
Torque
θe
θm
Torque(Nm)
Rotor position(rad)
Time (s)
Torque
Torque(Nm)
Harmonic order

(d)

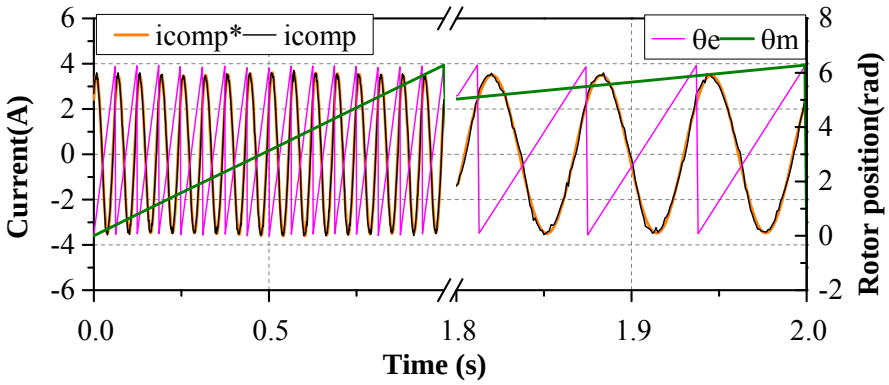
icomp*
icomp
θe
θm
Current(A)
Rotor position(rad)
Time (s)

(e)

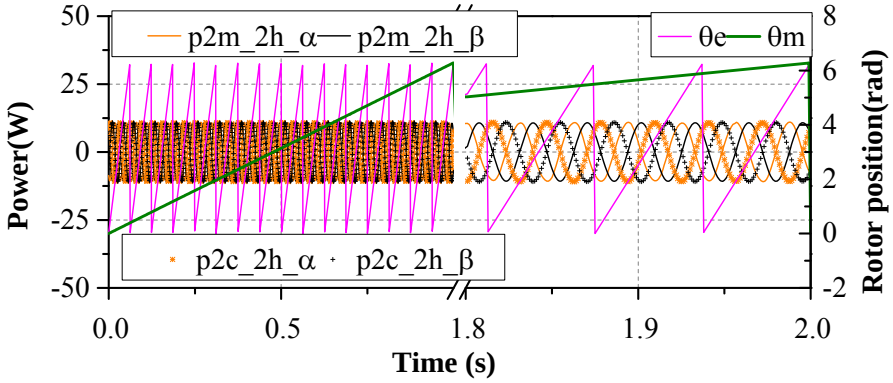
p2m_2h_α
p2m_2h_β
θe
θm
p2c_2h_α
p2c_2h_β
Power(W)
Rotor position(rad)
Time (s)

(f)

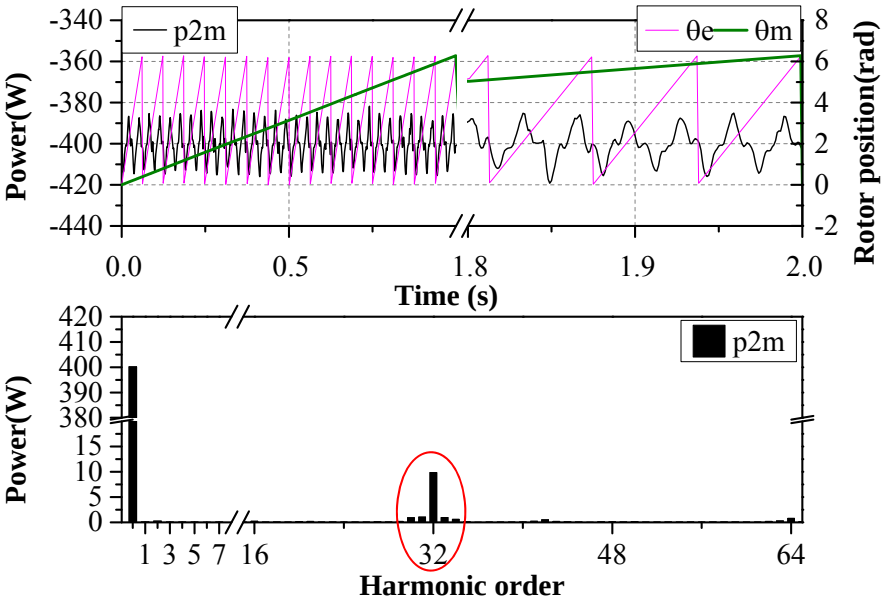

(g)

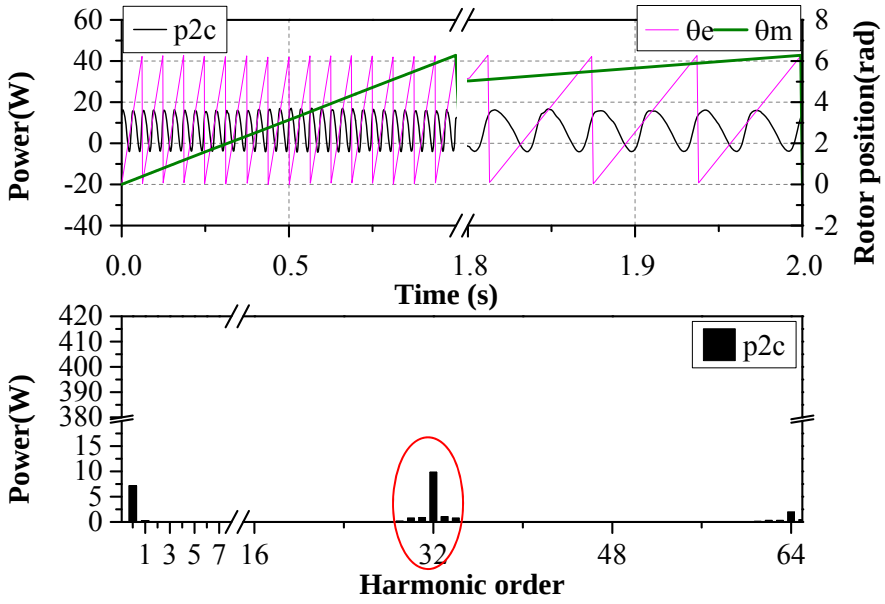

(h)

Fig.5.7 Experimental results of the proposed method, harmonic analysis based on mechanical frequency (Constant average output power control, with compensation). (a) Phase currents. (b) Power and harmonic analysis. (c) DC bus voltage and harmonic analysis. (d) Torque and harmonic analysis. (e) Currents of compensator. (f) Profile of 2h power ripple. (g) Power p_{2m} ripple and harmonic analysis. (h) Power p_{2c} ripple and harmonic analysis.

5.2.4.2 Introduced Asymmetries

To verify the proposed method is effective under different kinds of asymmetries, an extra inductor is deliberately connected with phase *A*, *B*, or *C* respectively in series. The inductance

and inherent resistance of the extra inductor are 5.63mH and 1.15Ω respectively. The different scenarios are listed in TABLE 5.3.

The experimental results of proposed method are shown in Fig.5.8. It can be seen that no matter the balanced current control (M1) or instantaneous power control (M2) is employed, the 2h DC bus voltage (or power) and torque ripple cannot be suppressed simultaneously without compensation in all cases. With the proposed method (M3), those 2h components can be suppressed simultaneously in all cases.

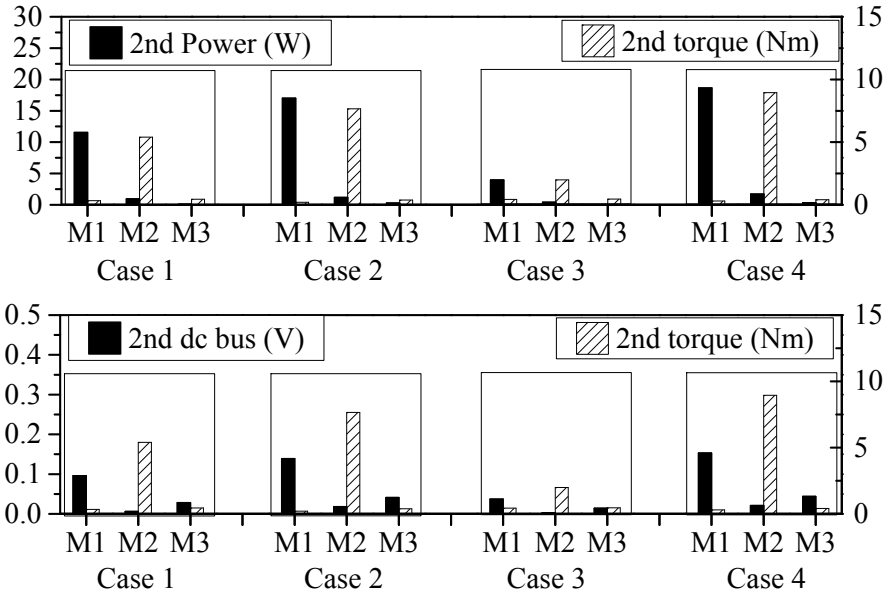

Fig.5.8 Comparison of 2h power, DC bus voltage ripple and torque ripple with/without proposed method (**M1**: balanced current control without compensation; **M2**: instantaneous power control without compensation; **M3**: average output power control with compensation).

TABLE 5.3

DIFFERENT CASES OF ASYMMETRIES

Cases No	DESCRIPTION
Case 1	Inherent asymmetry
Case 2	Extra asymmetry when the inductor is connected with phase *A*
Case 3	Extra asymmetry when the inductor is connected with phase *B*
Case 4	Extra asymmetry when the inductor is connected with phase *C*

5.2.4.3 At Different Speeds

The amplitudes of the 2h power without and with compensation at different speeds are shown in Fig.5.8. It can be seen that the 2h power is reduced significantly at different speeds after compensation. Consequently, the 2h DC bus voltage will be correspondingly suppressed according to (4.6). This experiment shows that the proposed method is effective at different speeds.

It is worth noting the dynamics of the compensation depends on how fast to extract the 2h power, how fast to determine the compensation current reference, and how fast to regulate the compensation current. However, due to the huge inertia of the wind turbine system, the electrical system could be treated as a constant speed system and the dynamics of the control of compensation unit will not be a big issue.

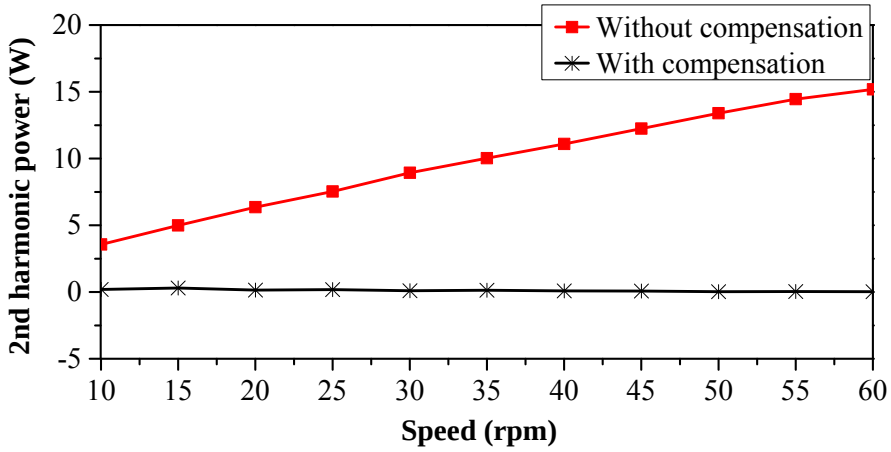

Fig.5.9 Without/with compensation in parallel at different speeds (i_q= -4A, inherent asymmetry).

5.2.5 Summary

An effective method of suppressing the 2h DC bus voltage pulsation in the asymmetric PMSG system considering the torque ripple is investigated in this section. This method does not involve the control of the grid side at all. With the information of the 2h power of the PMSG, the specific fundamental compensation current is obtained by two PI controllers and then injected into the compensation unit with Topology-*RL*. The 2h power generated by the PMSG can be compensated by the 2h power generated by the compensation unit. Consequently, the 2h DC bus voltage can be suppressed. The effectiveness of the proposed method has been verified by elaborate experiments on the prototype PMSG with inherent asymmetries and with introduced asymmetries deliberately.

5.3 Compensation in Parallel (Topology-*RLE*)

5.3.1 Introduction

In Section 5.2 of Chapter 5, to suppress the 2h DC bus voltage and 2h torque of asymmetric PMSG without deterioration of current THD of grid side, the undesired 2h power is transferred to a compensation unit (Topology-*RL*) in parallel with the DC bus. As detailed in Section 5.2, the compensation unit is constructed by an H-bridge and a compensation inductor. To compensate the 2h power due to the asymmetries, the fundamental current is injected into the compensation unit. As the compensation current is fundamental current and the terminal voltage of the compensation inductor is fundamental voltage, the H-bridge can be considered as DC/AC compensation converter and the compensation inductor can be considered as ac storage device. As the major purpose of the inductor is to exchange the 2h power with the DC bus and the size of the compensation inductor depends on the energy stored in the inductor, the inductor could be bulky if there are serve asymmetries in the system. Meanwhile to determine the compensation current to compensate the 2h power, two PI controllers are employed to regulate the amplitude and offset angle of the compensation current reference, which is complicated.

In this section, an improved method of suppressing the 2h DC bus voltage for asymmetric PMSG system will be investigated. It combines the topology of compensation unit with DC voltage source in [132] and the method of disposing of the pulsating power in [133] and in Section 5.2. It will be found that the improved method is superior to the method in Section 5.2 in terms of control complexity, current rating, inductor size, extra copper loss and the number of power switches, which will be analyzed in detail in Section 5.3.2. Meanwhile, it has the same advantages as the method in Section 5.2, such as avoiding the current THD of the grid side and torque ripple of machine side, suppression of the 2h DC bus voltage and no software modification in the grid side.

Firstly, the difference between the method in Section 5.2 and the improved method in this section will be analyzed in detail in Section 5.3.2. After the introduction of the corresponding implementation of the improved method, the comparative experiments will be conducted, which show clearly the differences between the method in Section 5.2 and the improved method in this section, and the effective of suppressing the 2h DC bus voltage will be verified under different conditions of asymmetries.

5.3.2 Compensation Principle

The proposed compensation unit with Topology-*RLE* is shown in Fig.5.10. It is constructed by half-bridge switches, an inductor and a DC voltage source, where the R_{comp} is the inherent resistance of the inductor and the DC voltage source could be a battery or super-capacitor. Since the components in the compensation unit are inherent resistor (R), inductor (L) and DC voltage source (E), the topology of the compensation unit in Fig.5.10 is designated as Topology-*RLE*.

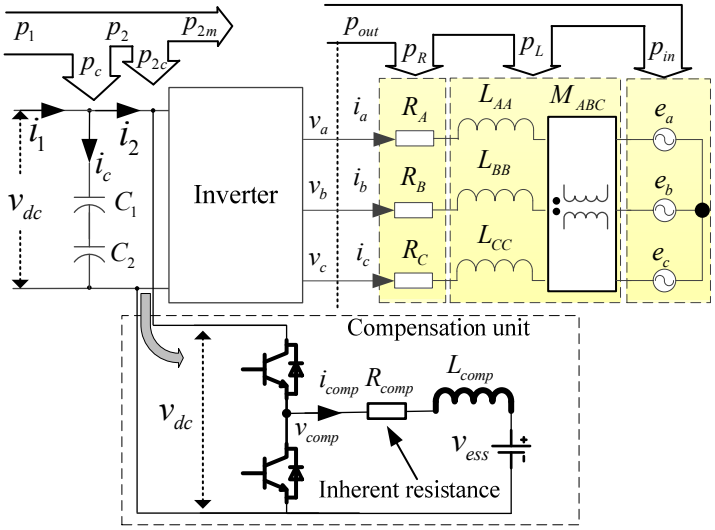

Fig.5.10 Topology of the proposed compensation in parallel (Topology-*RLE*).

In the compensation unit with Topology-*RL*, Fig.5.1, the fundamental current is injected into the compensation unit; the 2h power in the inductor is employed to compensate the 2h power from the asymmetric PMSG. However, in the compensation unit with Topology-*RLE*, Fig.5.10, the 2h power in the DC voltage source v_{ess} in Fig.5.10 will be employed to compensate the 2h power from the asymmetric PMSG. Since the voltage of the DC voltage source v_{ess} is constant, the compensation current should be the 2h current.

In theory, the 2h current flowing through the inductor in Fig.5.10 will result in the fourth harmonic power. To eliminate this fourth harmonic power, the fourth harmonic current should be injected into the compensation current so that it can be compensated by the fourth harmonic power from DC voltage source. Therefore, to eliminate the 2h power, the second, fourth, eighth…, harmonic currents should be injected into the compensation unit in theory. In this case, the regulation of the compensation current will be very complicated. In reality, the DC bus voltage v_{ess} is usually much higher than the voltage across the inductor v_{RL}, the

power in the inductor is negligible. In this case, only the 2h current injected into the compensation unit will be satisfactory.

Since the 2h power is mainly compensated by the power flowing through v_{ess}, the major purpose of the inductor in Fig.5.10 is just for filtering the current, which is unlike the major purpose of the inductor in Fig.5.1 for exchanging the 2h power. Generally, the size of inductors is proportional to the stored maximum energy. Therefore, the size of inductor in Fig.5.10 can be much smaller than that in Fig.5.1.

As detailed in Section 5.2, the compensation current for the compensation unit with Topology-*RL* is fundamental current. To determine the compensation current reference, two proportional-integral (PI) controllers were employed to regulate the amplitude and phase angle of the current reference respectively, which is complicated. In this section, it will be find it is easy to get the compensation current reference without two PI controllers in section 5.3.3.

Overall, the comparison of the Topology-*RL* and the Topology-*RLE* can be summarized in TABLE 5.4.

5.3.3 Implementation

5.3.3.1 Proposed control

The control scheme of the proposed method can be illustrated in Fig.5.11. In the same way as the control method in Section 5.2, the instantaneous average power control without *N*-sequence currents injection, Fig.5.3(a), is employed to control the average active power of the PMSG without ruining the 2h torque. The PI-R control [108-110] is employed to suppress the 2h currents in *dq*-frame to suppress the *N*-sequence currents under asymmetric conditions.

The current reference for the compensation unit can be simply expressed as (5.19) if the power of inductor is negligible.

$$i_{comp}{}^{*} = p_{2c\_2h\_\alpha}{}^{*} \Big/ v_{ess} \tag{5.19}$$

where $p_{2c\_2h\_\alpha}{}^{*}$ is the 2h power should be compensated. Compared with the current reference obtained by two PI controllers in Section 5.2, the determination of current reference in the proposed method is much simpler.

TABLE 5.4

COMPARISON OF TOPOLOGY-*RL* AND TOPOLOGY-*RLE*

Items	Topology-*RL*	Topology-*RLE*
Topology	H-bridge + inductor	Half-bridge + inductor + DC voltage source
Type of energy conversion in the compensation unit	DC/AC	DC/DC
Energy storage device	Inductor	DC voltage source
Type of compensation current	Fundamental (1f)	2f+4f+8f+… in theory 2f if v_{ess}>>v_{RL}
Implementation	Complicated	Complicated if $V_{ess} \approx v_{RL}$ Simple if $v_{ess} >> v_{RL}$
Compensation current	Large	Small
Size of inductor	Large	Small

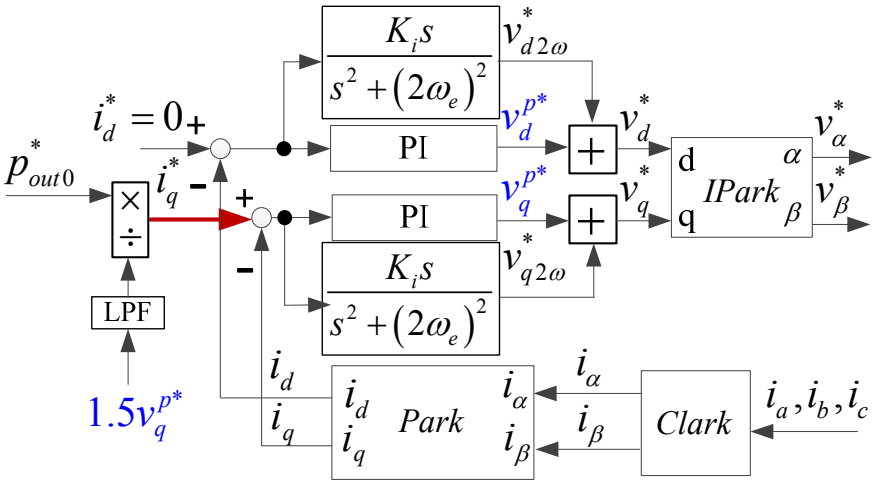

(a)

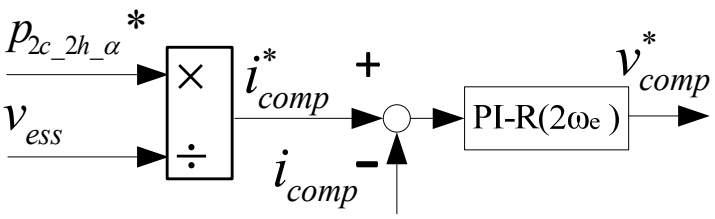

(b)

Fig.5.11 Proposed compensation method for topology-*RLE*. (a) Control block diagram of PMSG. (b) Control of the proposed method.

After the determination of the compensation current reference, the PI-R controller [108-110] with resonant control at the center frequency of $2\omega_e$ is employed to regulate the second harmoic current without tracing error.

5.3.3.2 Extraction of Second Harmonic Power

To compensate the 2h power from the asymmetric PMSG by compensation unit with Topology-*RLE*, the 2h power from the asymmetrical PMSG should be extracted first. In this section, two methods will be introduced; the first one is the SOGI method, which is the same method as that in Fig.5.2 in Section 5.2, and the second one is direct calculation without SOGI.

5.3.3.2.1 Method 1 - Filter with SOGI

The 2h power can be extracted by cascade-SOGI, which can be illustrated in Fig.5.2(a) in Section 5.2. Therefore, the whole flowchart of the compensation method can be illustrated in Fig.5.12. As can be seen from Fig.5.12, the whole flowchart includes two parts: the first is the 2h power reference generation and the second is the regulation of compensation current. The dynamic of the compensation method depends on how fast to extract the 2h power and how fast to regulate the compensation current. The low dynamic performance of cascade-SOGI will compromise the dynamic performance of the whole compensation system.

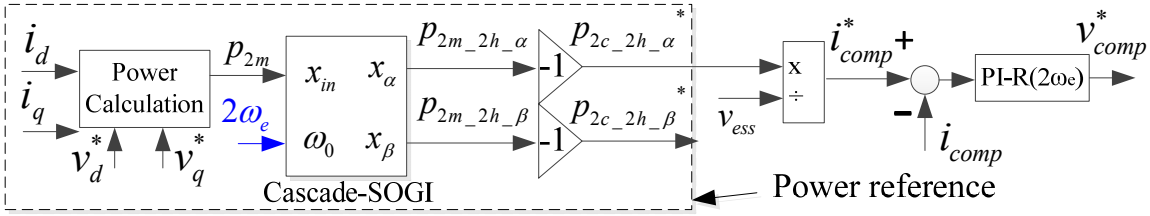

Fig.5.12 Method 1 for Topology-*RLE* with SOGI.

5.3.3.2.2 Method 2 - Calculation without SOGI

As shown in Fig.5.12, the dynamic performance of the compensation method maybe compromised by the cascade-SOGI. To improve the dynamic performance of the compensation method, the cascade-SOGI has better be removed. Actually, from (4.22), the 2h power from the PMSG can be expressed as

$$p_{2m\_2h\_\alpha} = p_{out\_c2}\cos(2\theta_e) + p_{out\_s2}\sin(2\theta_e) \tag{5.20}$$

where p_{out_c2} and p_{out_s2} can be deduced from (4.24) and expressed as (5.21) if the *P*-sequence and *N*-sequence currents are fairly regulated.

$$\begin{bmatrix} p_{out\_c2} \\ p_{out\_s2} \end{bmatrix} = \frac{3}{2}\begin{bmatrix} v_d^{n*} & v_q^{n*} & v_d^{p*} & v_q^{p*} \\ v_q^{n*} & -v_d^{n*} & -v_q^{p*} & v_d^{p*} \end{bmatrix}\begin{bmatrix} i_d^{p*} \\ i_q^{p*} \\ i_d^{n*} \\ i_q^{n*} \end{bmatrix} \tag{5.21}$$

Meanwhile, the 2h power lags $p_{2m\_2h\_\alpha}$ 90° can be expressed as

$$p_{2m\_2h\_\beta} = p_{out\_c2}\sin(2\theta_e) - p_{out\_s2}\cos(2\theta_e) \tag{5.22}$$

Therefore, the 2h powers can be obtained directly from (5.20), (5.21) and (5.22). If the (5.20)~(5.22) are employed to obtain the 2h power of PMSG, the whole compensation method with Topology-*RLE* can be illustrated in Fig.5.13. Compared with the 2h power reference from cascade-SOGI, this method is simpler. Meanwhile, as the 2h power reference can be obtained without cascade-SOGI, the dynamic performance is expected to be better.

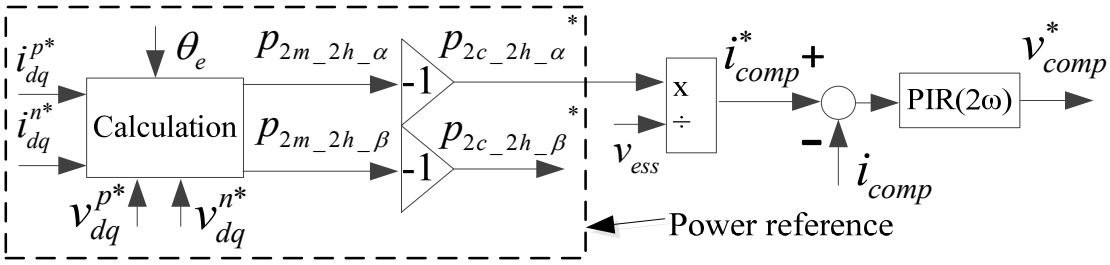

Fig.5.13 Method 2 for Topology-*RLE* without SOGI.

It is worth noting the Method 2 can also be employed to extract the 2h power from the PMSG in the compensation with Topology-*RL*. However, it could not be applied to extract the 2h power from the compensation unit. Therefore, the Method 1 with SOGI is still necessary in the compensation with Topology-*RL*.

5.3.4 Experiment Investigation

The test rig is demonstrated in Fig.5.14, where the prototype asymmetric PMSG is coupled with a servo machine, which is used to simulate the wind turbine. A power resistor R_L (100 Ω) is parallel with the DC bus to consume the power generated by the PMSG. The inductor in the compensation unit is the same as that compensation inductor used in Fig.5.4，Section 5.2. The voltage of the DC voltage source is 48V in this case study. The power generated by the PMSG is p_{2m} and the power transferred to the compensation unit is p_{2c}.

The prototype PMSG and the servo machine are shown in Fig.B.2, where the prototype PMSG is a dual 3-phase PMSG. However, to investigate the compensation effect on the asymmetric 3-phase PMSG, the second set of 3-phase windings in the prototype dual 3-phase

PMSG is disconnected deliberately. Therefore, as shown in Fig.C.1, there are apparent inherent asymmetries in the system.

It is worth noting that the number of pole pairs of the prototype machine is 16. Therefore, the 32nd harmonic in the following harmonic analyses based on the mechanical frequency indicates the 2h electrical frequency.

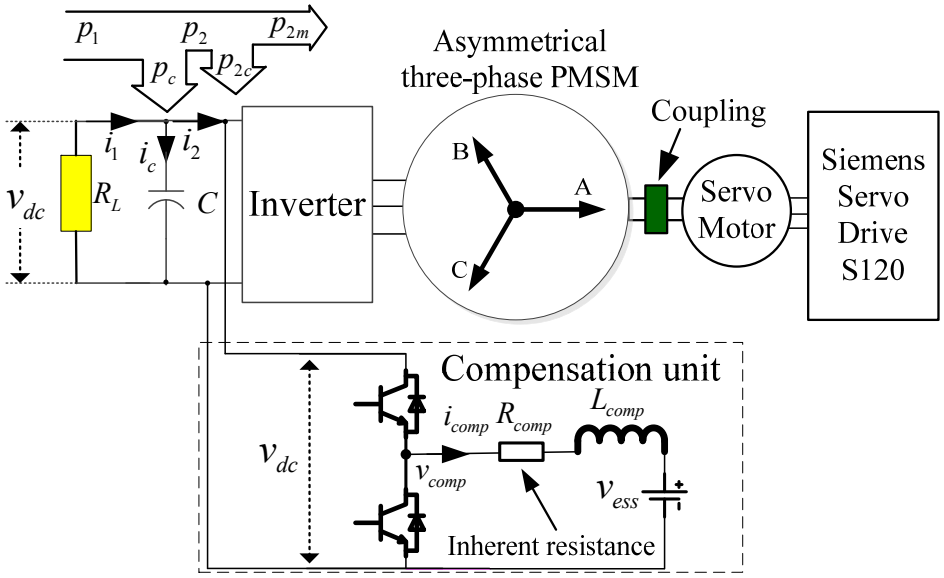

Fig.5.14 Test rig of compensation in parallel with Topology-*RLE*.

5.3.4.1 Compensation with Topology-*RLE*

In the experiment of compensation with Topology-*RLE*, the Method 1 in Fig.5.12 is adopted; the voltage of the DC voltage source is 48V in this case study. The speed is regulated to 60rpm by the servo machine.

The experimental results are shown in Fig.5.15. The reference output active power in Fig.5.11(a) is -400W. As can be seen from Fig.5.15(g), the average instantaneous power in p_{2m} is -400W, which means the average power is fairly regulated. However, there is 2h power in p_{2m} due to the asymmetries and no *N*-sequence currents are injected into the stator currents to compensate the 2h power. The power p_{2c} from the compensation unit is shown in Fig.5.15(h), it can be seen that there is also 2h power in p_{2c} with the 2h compensation current in Fig.5.15(e). However, the phase angle of the 2h power in p_{2m} and p_{2c} are anti-phase, Fig.5.15(f). Therefore, the 2h power in p_2 ($=p_{2m}+p_{2c}$) are cancelled, Fig.5.15(b), and then the 2h DC bus voltage can be suppressed effectively, Fig.5.15(c). As only *P*-sequence currents are injected into the PMSG and the 3-phase back-EMFs are balanced, the 2h torque can be avoided, Fig.5.15(d).

The experimental results of the 2h power, 2h DC bus voltage, 2h torque in Fig.5.15 are similar to those results in the compensation with Topology-*RL* in Fig.5.7. But it is worth noting that there is apparent average power in p_{2c}, Fig.5.7(h), which is due to the copper loss of the inherent resistance in the compensation inductor with large compensation current shown in Fig.5.7(a), while the average power in p_{2c}, Fig.5.15(h) is negligible since the compensation current, Fig.5.7 (e), is very small. Therefore, the power p_2 in Fig.5.7(b) is smaller than that in Fig.5.15(b), and the average DC bus voltage in Fig.5.7(c) is smaller than that in Fig.5.15(c) due to less average power flows towards the DC bus capacitor, although the average power generated by the PMSG in Fig.5.7(g) and Fig.5.7(g) are the same.

As the compensation current with Topology-*RLE* decreases, the power rating of the half-bridge switches in the compensation unit will decrease. Meanwhile, the inductor size will decrease as well because it is generally proportional to the energy stored in the inductor. Therefore, the proposed method of compensation in parallel with Topology-*RLE* is a competitive alternative to the Topology-*RL* although the DC bus voltage source is involved.

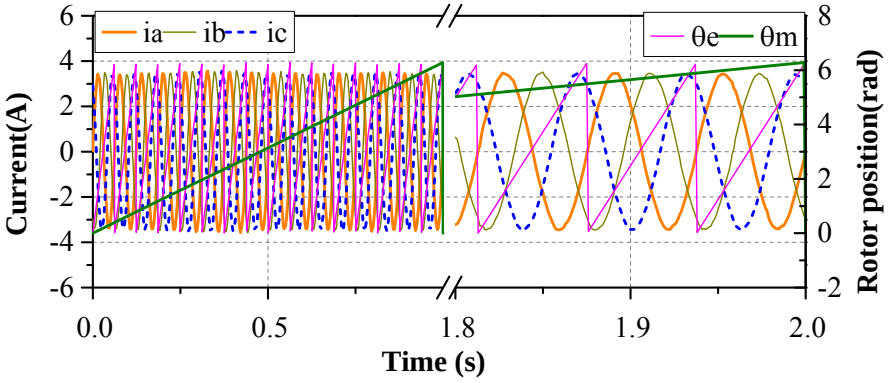
ia
ib
ic
θe
θm
Current(A)
Rotor position(rad)
Time (s)

(a)

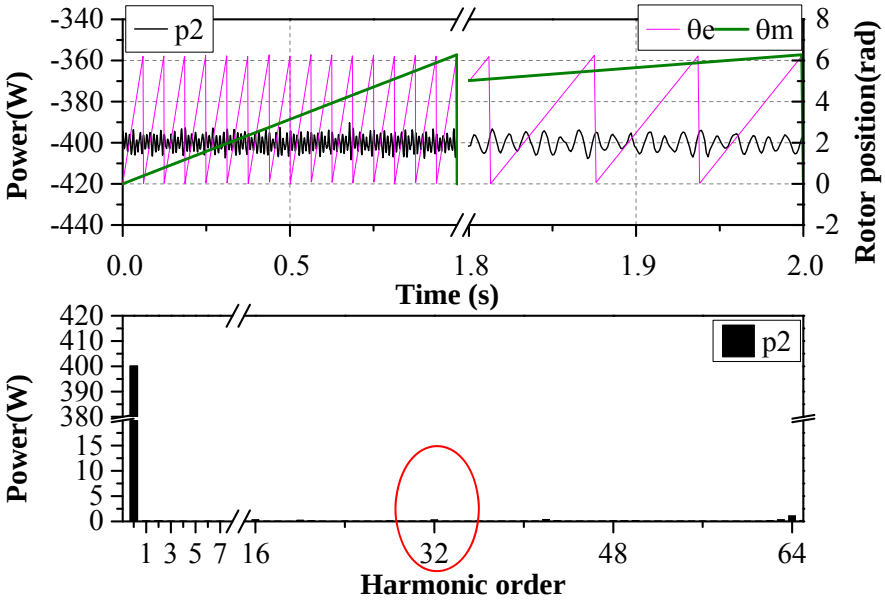
p2
θe
θm
Power(W)
Rotor position(rad)
Time (s)
p2
Power(W)
Harmonic order

(b)

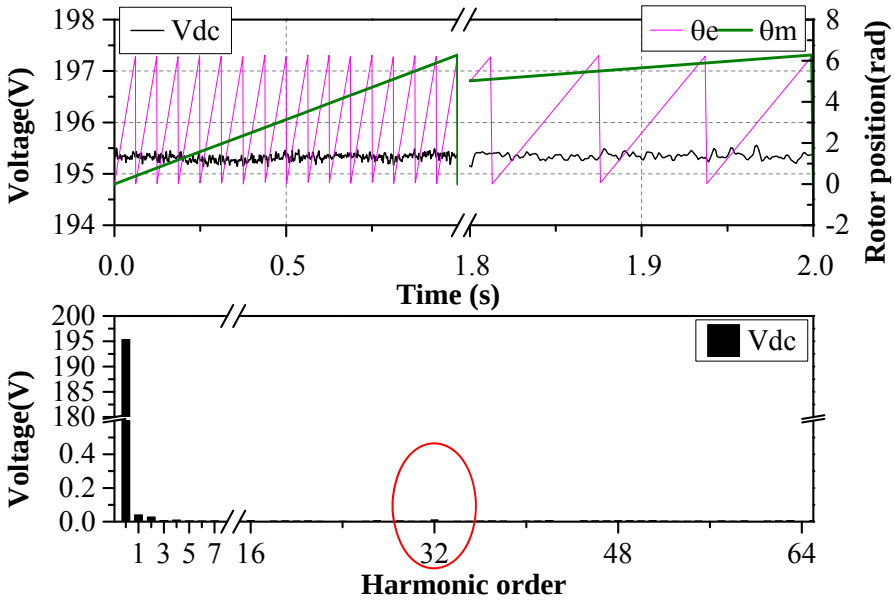
Vdc
θe
θm
Voltage(V)
Rotor position(rad)
Time (s)
Vdc
Voltage(V)
Harmonic order

(c)

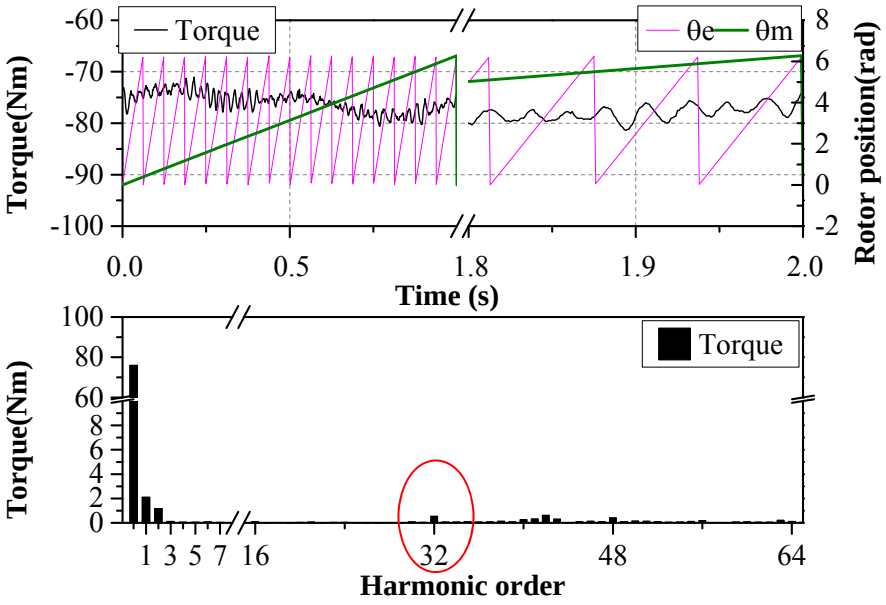
Torque
θe
θm
Torque(Nm)
Rotor position(rad)
Time (s)
Torque
Harmonic order

(d)

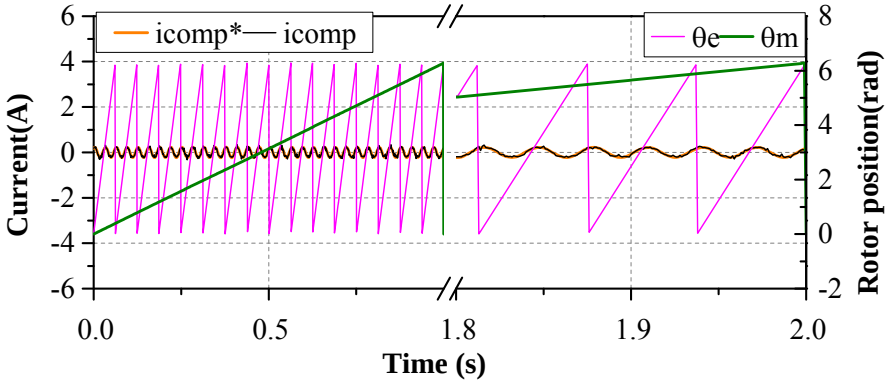
icomp*
icomp
θe
θm
Current(A)
Rotor position(rad)
Time (s)

(e)

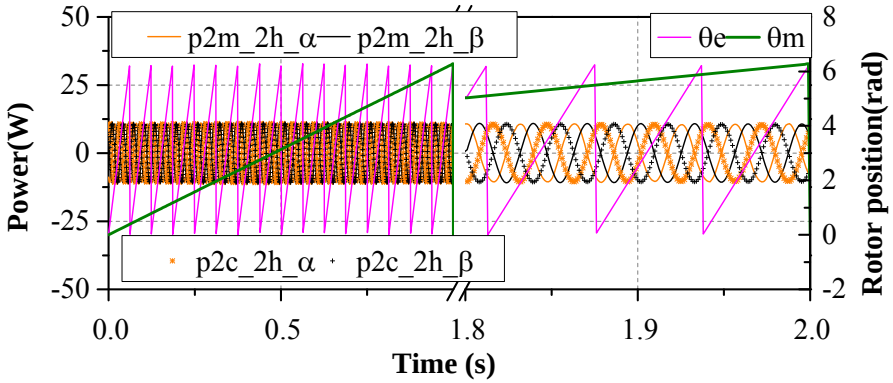
p2m_2h_α
p2m_2h_β
θe
θm
p2c_2h_α
p2c_2h_β
Power(W)
Rotor position(rad)
Time (s)

(f)

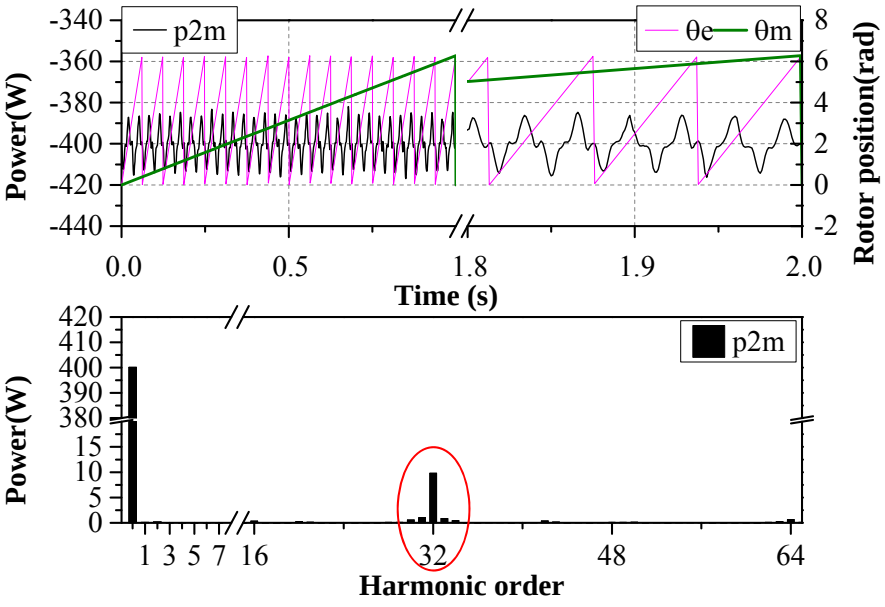

(g)

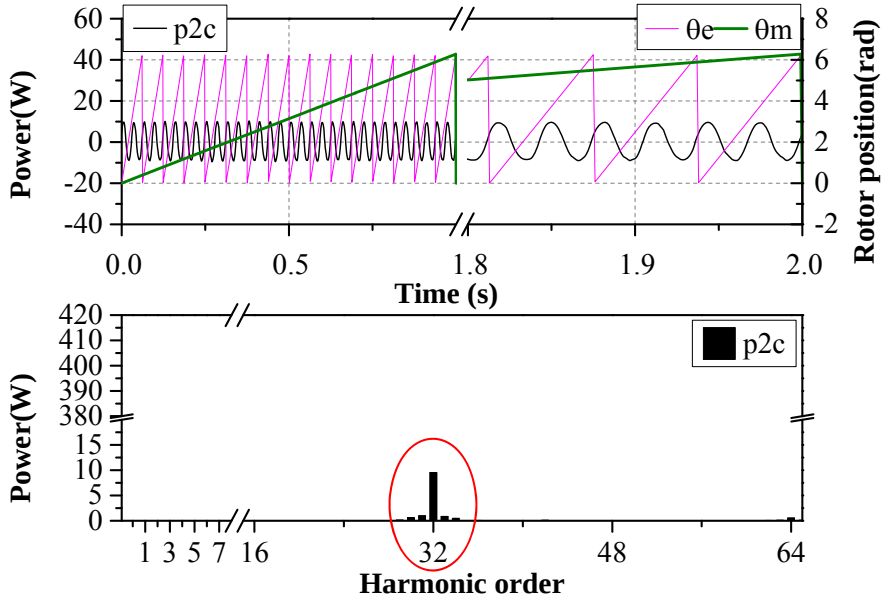

(h)

Fig.5.15 Experimental results with compensation of Topology-*RLE*, harmonic analysis based on mechanical frequency. (a) Phase currents. (b) Power and harmonic analysis. (c) DC bus voltage and harmonic analysis. (d) Measured torque and harmonic analysis. (e) Currents of compensator. (f) Profile of 2h power. (g) Power p_{2m} and harmonic analysis. (h) Power p_{2c} and harmonic analysis.

5.3.4.2 Comparison of Method 1 and Method 2

The second harmonic power references from Method 1 with SOGI in Fig.5.12 and from the Method 2 without SOGI in Fig.5.13 will be compared in this section.

5.3.4.2.1 Comparison of 2h power Extraction

The Fig.5.16(a) and (b) shows the comparison of the 2h power from Method 1 and Method 2 during steady state and dynamic state respectively, where "@SOGI" means the measured results from Method 1, while "@Cal" means the measured results from the Method 2.

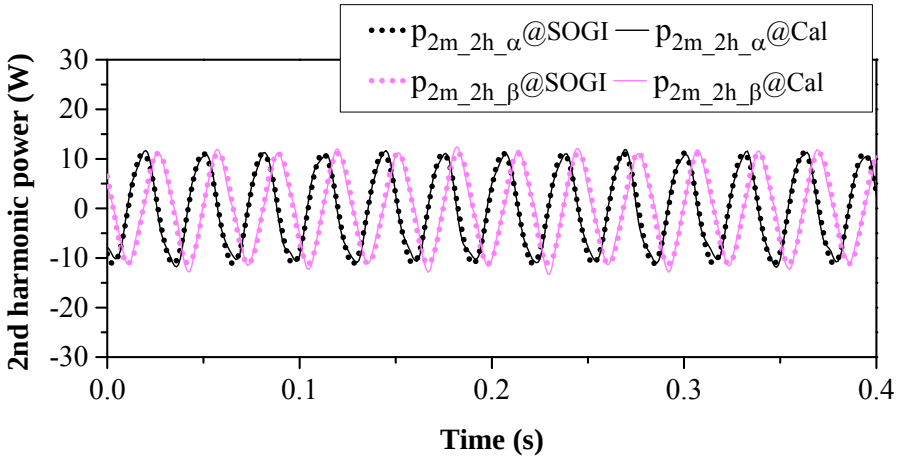

(a)

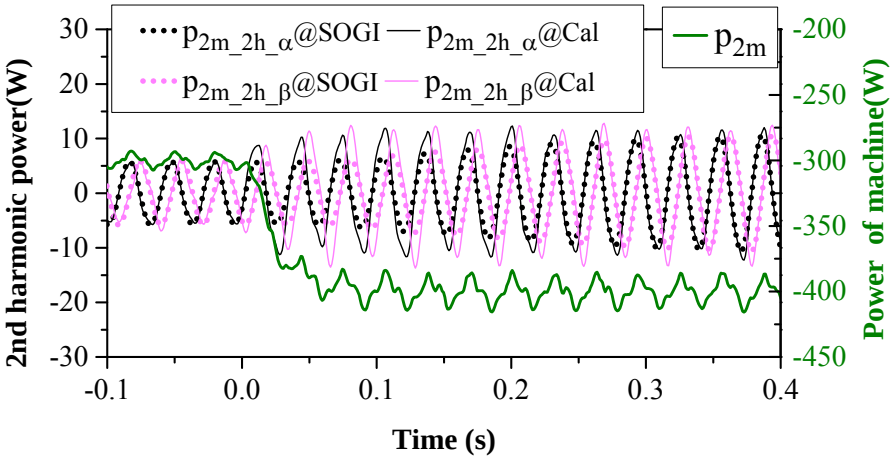

(b)

Fig.5.16 Comparison of 2h power from Cascade-SOGI and calculation. (a) Steady state (average power=-400W, 60rpm). (b) Dynamic state (step power response from -300W to -400W, 60rpm).

As can be seen from Fig.5.16(a), the 2h powers from Method 2 are equivalent to that from Method 1 at the steady state. During the transition in Fig.5.16(b), the 2h power in the

PMSG's power p_{2m} becomes stable at the time of 0.1s, so as the 2h powers from Method 2, while the 2h powers from Method 1 increase step by step until they have equivalent amplitude as that from Method 2 at the time of 0.4s.

This experiment shows that the 2h power from the Method 1 and Method 2 can represent the 2h power from the PMSG at the steady state operation, and the Method 2 has better dynamic performance than the Method 1 during the transit operation. Therefore, the dynamic performance of Method 2 in Fig.5.13 is supposed to be better than that in Fig.5.12.

5.3.4.2.2 Comparison of Dynamic Performance

Since the 2h power reference from the cascade-SOGI in Fig.5.12 and from the calculation in Fig.5.13 at the steady state in Fig.5.16(a) are almost the same, the compensation effect of Method 1 and Method 2 should be the same as well. By elaborated experiments at the steady state, it has been verified that the experimental results of Method 2 are similar as those of the Method 1, and both methods can suppress the 2h power and DC bus voltage effectively. The experimental results of Method 1 at the steady state have been detailed in Section 5.3.4.1. For simplicity, the detailed experimental results of Method 2 at steady state will not be presented here anymore. In this section, the dynamic performance of Method 1 and Method 2 will be compared through power step response and speed step response.

When the average active power reference in Fig.5.11(a) is stepped from -300W to -400W, the power step response of the Method 1 and Method2 are shown in Fig.5.17(a) and Fig.5.17(b) respectively, and the compensation current response are shown in Fig.5.17(c) and Fig.5.17(d) respectively. By comparison of Fig.5.17(c) and Fig.5.17(d), it can be observed that the compensation current response of Method 2 is faster than Method 1 with shorter settling time. Consequently, the 2h power with Method 2, Fig.5.17(b), is suppressed more quickly than that in Method 1, Fig.5.17(a). Therefore, in terms of the dynamic performance of the 2h power compensation, Method 2 is better than that of Method 1.

When the speed is stepped from 40rpm to 60rpm by the servo machine, the power responses of Method 1 and Method 2 are shown in Fig.5.18(a) and (b) respectively, and the compensation current responses are shown in Fig.5.18(c) and Fig.5.18(d) respectively. Similar to the dynamic performance comparison in the power step response, Fig.5.17, the dynamic performance of Method 2 in the speed step response is superior to that of Method 1.

In summary, the power step response and speed step response show that Method 2 has superior dynamic performance to the Method 1 as no SOGI is involved in Method 2.

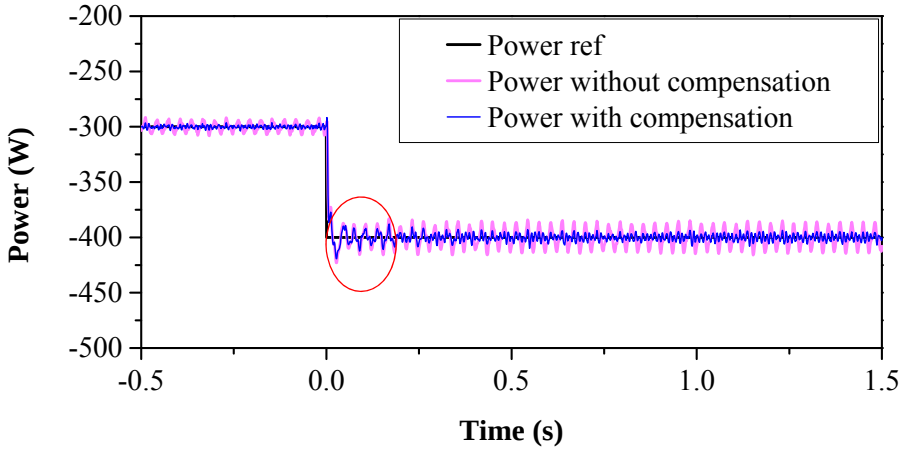
Power ref
Power without compensation
Power with compensation
Power (W)
-200
-250
-300
-350
-400
-450
-500
-0.5
0.0
0.5
1.0
1.5
Time (s)

(a)

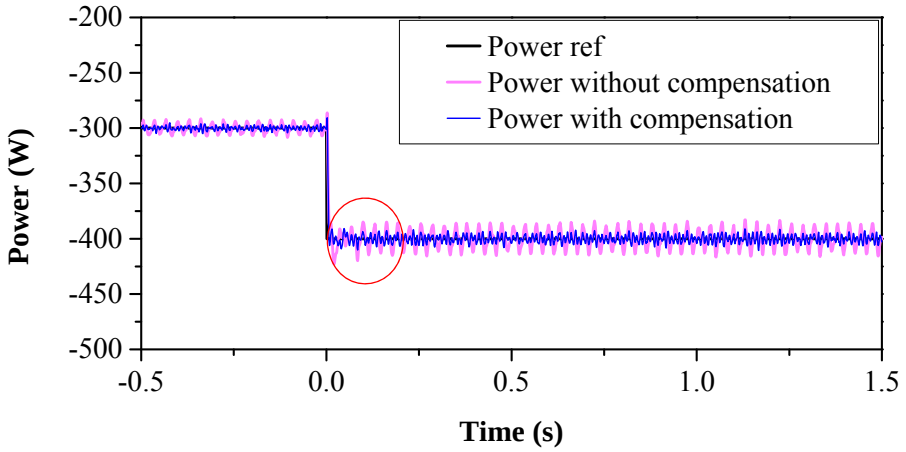
Power ref
Power without compensation
Power with compensation
Power (W)
-200
-250
-300
-350
-400
-450
-500
-0.5
0.0
0.5
1.0
1.5
Time (s)

(b)

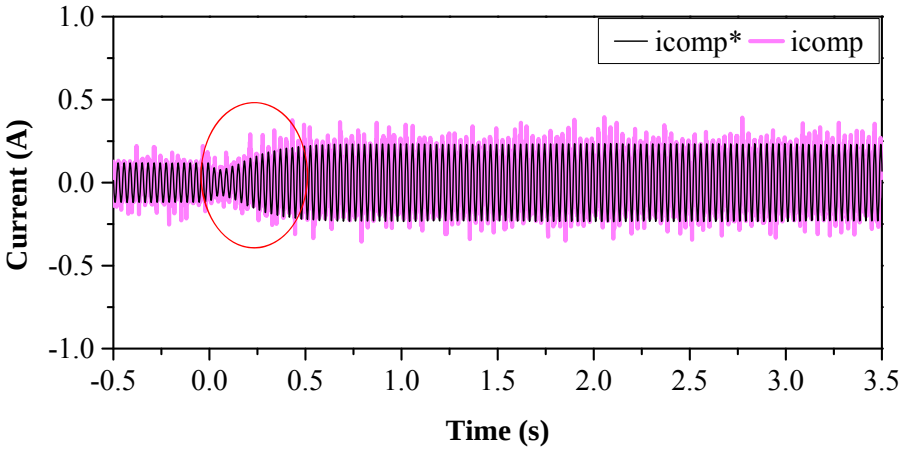
icomp*
icomp
Current (A)
1.0
0.5
0.0
-0.5
-1.0
-0.5
0.0
0.5
1.0
1.5
2.0
2.5
3.0
3.5
Time (s)

(c)

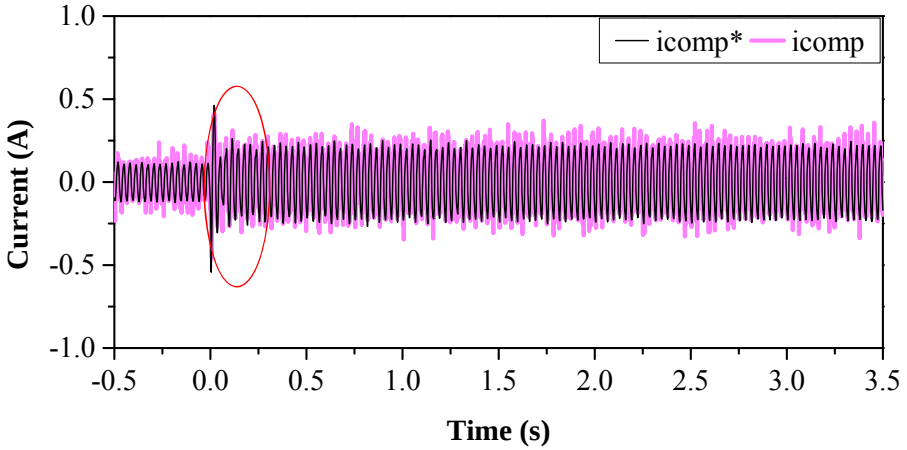

(d)

Fig.5.17 Step response when the power reference is stepped from -300W to -400W (Topology-*RLE*). (a) Power response of Method 1. (b) Power response of Method 2. (c) Compensation current of Method 1. (d) Compensation current of Method 2.

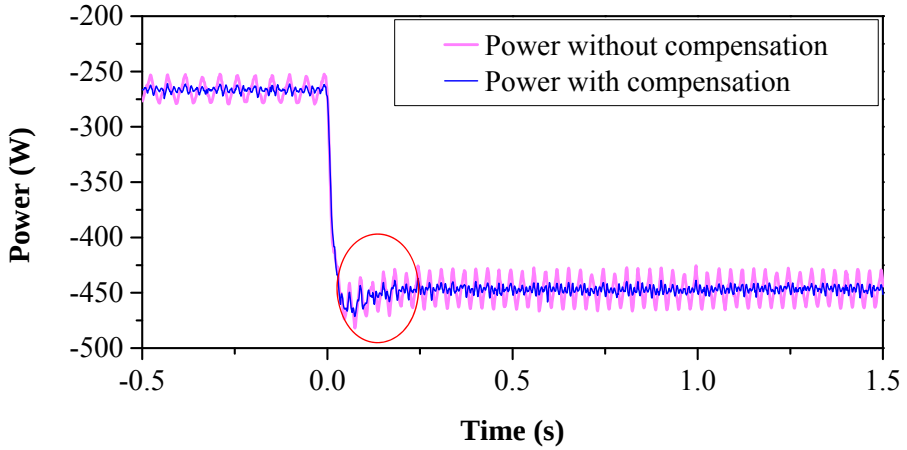

(a)

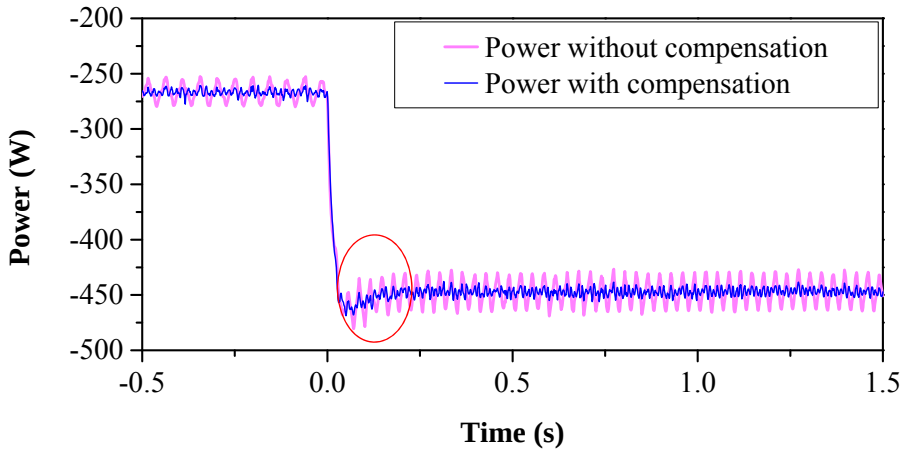

(b)

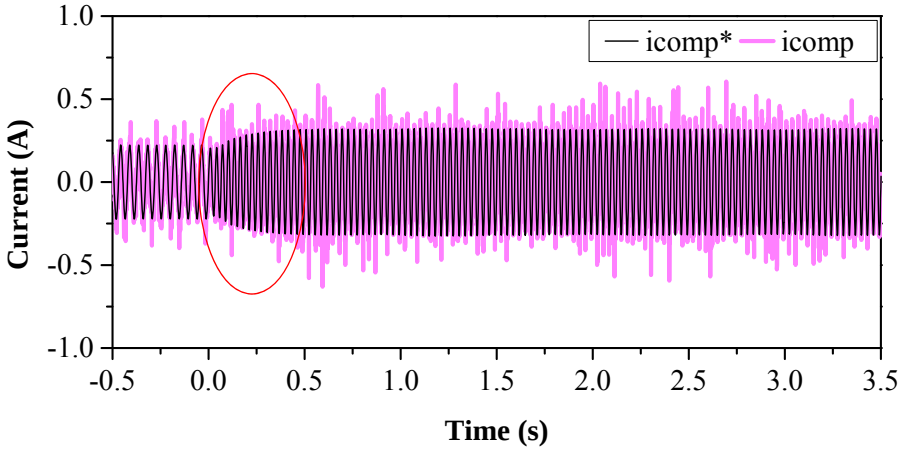

(c)

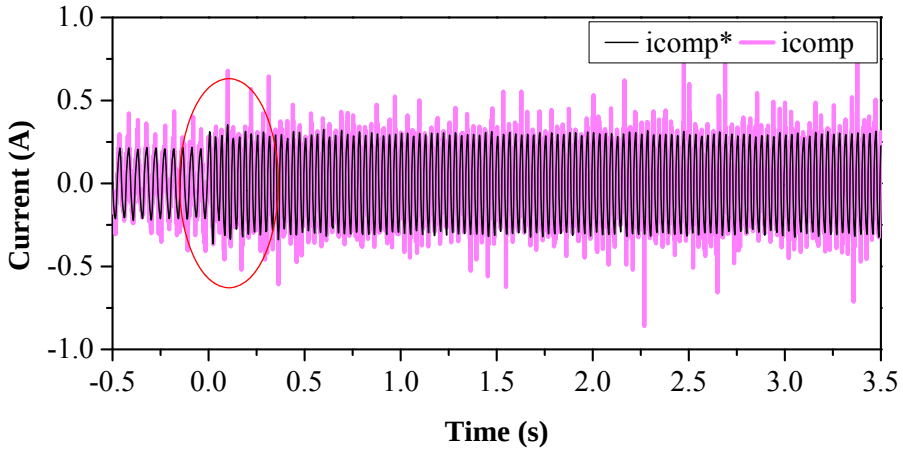

(d)

Fig.5.18 Step response when the speed is stepped from 40rpm to 60rpm by the load motor (Topology-*RLE*). (a) Power response of Method 1. (b) Power response of Method 2. (c) Compensation current of Method 1. (d) Compensation current of Method 2.

5.3.4.3 Introduced Asymmetries

To verify the proposed method is applicable to different asymmetries, an extra inductor is deliberately connected with phase A, B, or C in series respectively. The equivalent inductance and resistance in the inductor are 5.63mH and 1.15Ω respectively. The different scenarios of asymmetries can be listed as TABLE 5.3.

To demonstrate the proposed method can suppress the 2h power, DC bus voltage and the 2h torque, the performance will be compared between the balanced current control (M1), instantaneous power control (M2) and the proposed method (M3). The experimental results are shown in Fig.5.19. As can be seen that the 2h torque in all cases are suppressed by M1,

while the 2h power and DC bus voltage are obvious. In contrast, the 2h torque ripples in all cases are apparent when M2 is employed, while the 2h power and DC bus voltage are suppressed effectively. With the proposed compensation, the 2h DC bus voltage, power and torque can be suppressed simultaneously.

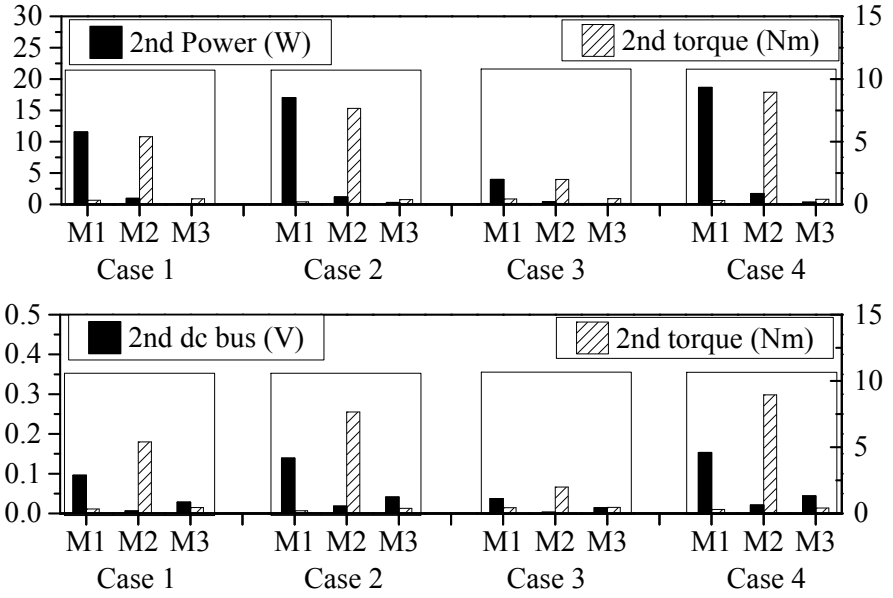

Fig.5.19 Comparison of 2h power, DC bus voltage and torque with/without proposed method (**M1**: balanced current control without compensation; **M2**: instantaneous power control without compensation; **M3**: average output power control with *RLE* compensation.

5.3.4.4 At Different Speeds

The amplitudes of the 2h power without and with compensation at different speeds are shown in Fig.5.9. It can be seen that the 2h power is reduced significantly at different speeds after compensation. Consequently, the 2h DC bus voltage will be correspondingly suppressed according to (4.6). This experiment shows that the proposed method is effective at different speeds.

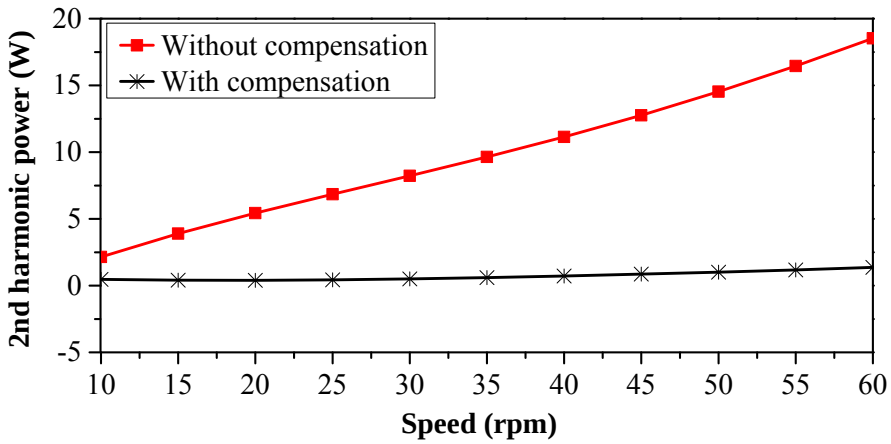

Fig.5.20 Without/with compensation in parallel at different speeds (i_q= -4A, inherent asymmetry).

5.3.5 Summary

An improved compensation in parallel with DC bus aiming for suppressing the 2h DC bus voltage and torque in the asymmetric PMSG is investigated in this section. Compared with the compensation in parallel in Section 5.2, the proposed method has only half power switch numbers and has lower compensation current. Consequently, it has benefits of lower power rating, lower power loss of the power switches, and lower copper loss of the compensation unit and smaller size of the compensation inductor. It could be a competitive method although the DC bus voltage source is involved.

5.4 Conclusion

With the proposed compensation in parallel with DC bus, the 2h DC bus voltage and torque can be suppressed simultaneously. Two power topologies designated as Topology-*RL* and Topology-*RLE* are investigated and their corresponding control methods have been presented. In the proposed method, the *N*-sequence is not involved for consideration of the 2h torque. Meanwhile, the 2h power resulted from the asymmetries is transferred to the compensation unit in parallel with the DC bus. Consequently, the 2h DC bus voltage is effectively suppressed. The effectiveness of the proposed method has been verified on a prototype asymmetric PMSG with inherent asymmetries and introduced asymmetries deliberately.

Chapter 6 Control of Asymmetric PMSG with Compensation in Series

6.1 Introduction

In Chapter 5, the control of asymmetric PMSG with compensation in parallel with the DC bus has been investigated. To suppress the 2h DC bus voltage and 2h torque ripple of the PMSG without deterioration of current THD of the grid side, the undesired 2h power due to asymmetries is transferred to the compensation unit in parallel with the DC bus, Fig.5.1 with Topology-*RL* or Fig.5.10 with Topology-*RLE*. The 2h power from the PMSG and 2h power from the compensation unit have the same amplitude but they are anti-phase. Thus, the 2h power flowing towards the DC bus capacitors is cancelled.

The compensation in parallel is a competitive solution in terms of suppressing the undesired 2h power and DC bus voltage, the 2h torque of the PMSG, and the current THD of grid side. To fulfill this method, some hardware such as power switches, compensation inductor, and DC voltage source are required. Meanwhile, a specific compensation current profile together with the corresponding current regulation is required, which increases the system complexity.

In [153], a method of correcting the unbalanced load condition by means of an additional unbalanced load was studied. The compensation is illustrated in Fig.6.1, where an additional load is connected between an appropriate pair of phases. Although the current of i_a, i_b and i_c are unbalanced due to the unbalanced load, the current of i_a'', i_b'', and i_c'' after compensation are balanced.

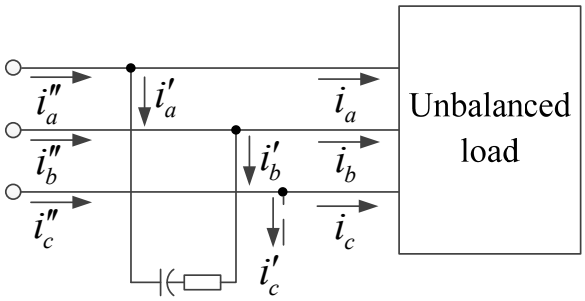

Fig.6.1 Circuit diagram with added load [153].

The method demonstrated in Fig.6.1 is a passive compensation that does not require any software modification. However, when the unbalanced load is asymmetric PMSG, whose frequency and voltage vary with the speed, it is impossible to find an appropriate unbalanced passive load that is in parallel with the unbalanced PMSG and make the whole load balanced.

In this chapter, the passive unbalanced load connected in series with the PMSG to compensate the unbalanced impedances in PMSG will be investigated. It will be found that the asymmetric 3-phase system with unbalanced resistances, unbalanced self-inductances, or even unbalanced mutual inductances can be modified to a balanced system with external circuits in series as shown in Fig.6.2. It will be proved in theory from the perspective of the 2h inductances in *dq*-frame and the 2h power. Therefore, the 2h power due to the asymmetries can be suppressed without any software modifications. Then the optimized inductance in the external circuits in theory and the non-linearity of the compensation inductor in practice will be analyzed in detail. Finally, the feasibility of this compensation method is validated by elaborate experiments at different speeds and loads, although the effectiveness may be slightly affected by the non-linearity of the compensation inductance in practice.

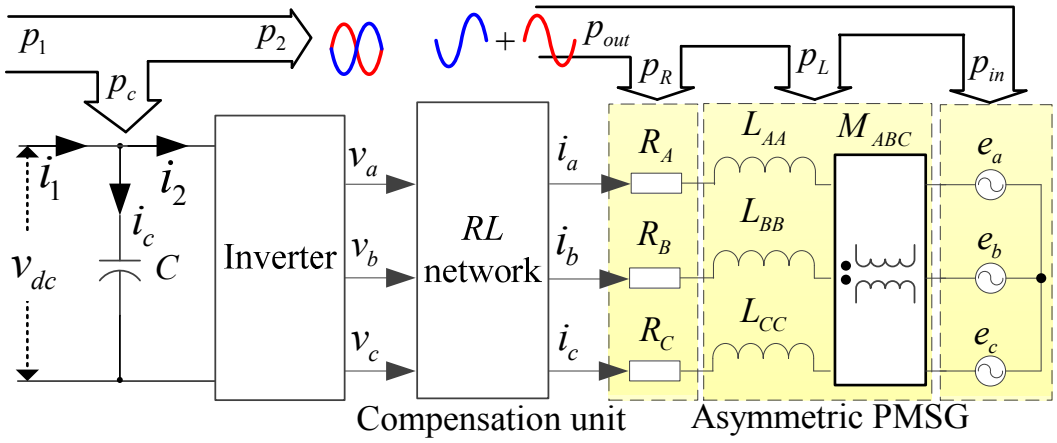

Fig.6.2 Compensation by external circuits in series.

6.2 Principle of Compensation

The general compensation unit in series with *RL* network can be illustrated in Fig.6.3, where ΔR_{Ax}, ΔL_{Ax}, ΔR_{Bx}, ΔL_{Bx}, ΔR_{Cx}, ΔL_{Cx} are the resistances and inductances in the compensation unit in series with each phase.

If the resistances of 3-phase windings and the average self-inductances are unbalanced, which can be modeled as (2.20)~(2.23) and (2.24)~(2.27), the asymmetries can be easily compensated by introduced external resistors and inductors; For the sake of simplicity, only the compensation of unbalanced average mutual inductances will be discussed in the following section.

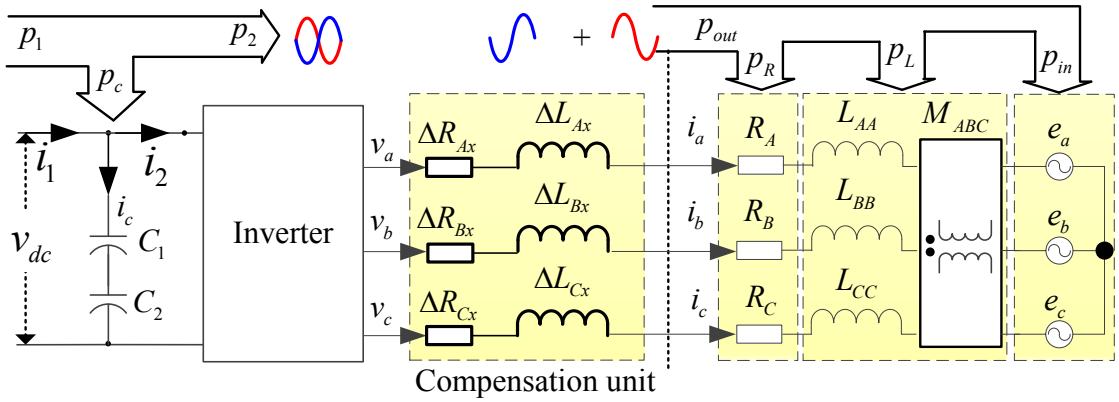

Fig.6.3 Compensation in series for asymmetric PMSM.

6.2.1 Perspective of the Mathematical Model

If the 2h impedances of the asymmetric PMSG in *dq*-frame can be cancelled by the 2h impedances of introduced external circuit in series in Fig.6.2, there will no 2h impedances in *dq*-frame after compensation, which means the original asymmetric system can be modified to a balanced 3-phase system. Consequently, the 2h DC bus voltage and torque ripple can be suppressed naturally.

When the average mutual inductances are unbalanced and modeled as (2.28)~(2.31), as introduced in Section 3.2.3.2 of Chapter 3, the inductance matrix in *dq*-frame can be deduced as

$$\begin{aligned}\left[L_{dq}\right]=\begin{bmatrix}L_d & M_{dq}\\ M_{qd} & L_q\end{bmatrix}&=\left(L_0+\frac{1}{2}M_0\right)I_2+\left(\frac{1}{2}L_2+M_2\right)J_2\\&+\left(\frac{1}{6}\left(\Delta M_{AB0}+\Delta M_{BC0}+\Delta M_{AC0}\right)I_2\right)\\&+\frac{1}{3}\Delta M_{BC0}M_1\left(2\theta_e+0\theta_s\right)\\&+\frac{1}{3}\Delta M_{AC0}M_1\left(2\theta_e+4\theta_s\right)\\&+\frac{1}{3}\Delta M_{AB0}M_1\left(2\theta_e+8\theta_s\right)\end{aligned}\tag{6.1}$$

where $M_1(\theta)$ is expressed as (3.12) and repeated as (6.2) for convenience.

$$M_1(\theta)=\begin{bmatrix}-\cos(\theta) & \sin(\theta)\\ \sin(\theta) & \cos(\theta)\end{bmatrix} \tag{6.2}$$

(6.1) indicates that there are 2h inductances in the inductance matrix in *dq*-frame when the mutual inductances are unbalanced. Therefore, with balanced 3-phase currents injection, there will be 2h voltages in *dq*-frame. Consequently, it will result in 2h power flowing through the DC bus capacitors.

Assuming the introduced inductance matrix of the compensation unit in *abc*-frame can be expressed as [ΔL_{Ax}, 0, 0; 0, ΔL_{Bx}, 0; 0, 0, ΔL_{Cx}], the introduced inductances in *dq*-frame can be deduced as

$$\begin{aligned}\begin{bmatrix}\Delta L_d & \Delta M_{dq}\\ \Delta M_{qd} & \Delta L_q\end{bmatrix} = & \frac{\Delta L_{Ax}}{3} I_2 - \frac{\Delta L_{Ax}}{3} M(2\theta_e + 0\theta s)\\ & + \frac{\Delta L_{Bx}}{3} I_2 - \frac{\Delta L_{Bx}}{3} M(2\theta_e + 4\theta s)\\ & + \frac{\Delta L_{Cx}}{3} I_2 - \frac{\Delta L_{Cx}}{3} M(2\theta_e + 8\theta s)\end{aligned} \tag{6.3}$$

Therefore, the *dq*-axis inductances of the modified system can be expressed as

$$\begin{aligned}\begin{bmatrix}L_d & M_{dq}\\ M_{qd} & L_q\end{bmatrix} + \begin{bmatrix}\Delta L_d & \Delta M_{dq}\\ \Delta M_{qd} & \Delta L_q\end{bmatrix} = & \left(L_0 + \frac{1}{2}M_0\right) I_2 + \left(\frac{1}{2}L_2 + M_2\right) J_2\\ & + \frac{\Delta M_{BC0} + 2\Delta L_{Ax}}{6} I_2 + \frac{\Delta M_{BC0} - \Delta L_{Ax}}{3} M(2\theta_e + 0\theta s)\\ & + \frac{\Delta M_{CA0} + 2\Delta L_{Bx}}{6} I_2 + \frac{\Delta M_{AC0} - \Delta L_{Bx}}{3} M(2\theta_e + 4\theta s)\\ & + \frac{\Delta M_{AB0} + 2\Delta L_{Cx}}{6} I_2 + \frac{\Delta M_{AB0} - \Delta L_{Cx}}{3} M(2\theta_e + 8\theta s)\end{aligned} \tag{6.4}$$

If $\Delta L_{Cx}=\Delta M_{AB0}$, $\Delta L_{Ax}=\Delta M_{BC0}$ and $\Delta L_{Bx}=\Delta M_{CA0}$, (6.4) can be simplified as

$$\left\{\begin{bmatrix}L_d & M_{dq}\\ M_{qd} & L_q\end{bmatrix} + \begin{bmatrix}\Delta L_d & \Delta M_{dq}\\ \Delta M_{qd} & \Delta L_q\end{bmatrix}\right\} = \left(L_0 + \frac{1}{2}\begin{pmatrix}M_0 + \Delta M_{AB0} +\\ \Delta M_{BC0} + \Delta M_{AC0}\end{pmatrix}\right) I_2 + \left(\frac{1}{2}L_2 + M_2\right) J_2 \tag{6.5}$$

As shown in (6.5), with the introduced compensation inductors in series, there are no 2h inductances in the inductance matrix in *dq*-frame. Therefore, the system is modified to a balanced system.

6.2.2 Perspective of the 2h Power

In the asymmetric PMSG system with unbalanced impedances, if the 2h harmonic power due to the asymmetric impedances can be compensated by the 2h power of introduced external circuit in series in Fig.6.2, the 2h power following towards the DC bus capacitors can be suppressed.

Assuming the currents are balanced under the i_d=0 control, and they can be expressed as

$$[i]=\begin{bmatrix} i_a \\ i_b \\ i_c \end{bmatrix}=I_{1p}\begin{bmatrix} \cos(\theta_e-0\theta_s+\pi/2) \\ \cos(\theta_e-4\theta_s+\pi/2) \\ \cos(\theta_e-8\theta_s+\pi/2) \end{bmatrix} \tag{6.6}$$

where I_{1p} is the amplitude of fundamental current, then the 2h power due to the unbalanced mutual inductances ΔM_{AB0}, ΔM_{BC0} and ΔM_{CA0} can be expressed as (2.44), (2.45) and (2.46) respectively and repeated as (6.7), (6.8) and (6.9) respectively for convenience.

$$\Delta p_{M\_AB}=\frac{1}{2}\omega_e\Delta M_{AB0}I_{1p}^2\cdot\cos(2\theta_e-1\theta_s) \tag{6.7}$$

$$\Delta p_{M\_BC}=\frac{1}{2}\omega_e\Delta M_{BC0}I_{1p}^2\cdot\cos(2\theta_e+3\theta_s) \tag{6.8}$$

$$\Delta p_{M\_AC}=\frac{1}{2}\omega_e\Delta M_{CA0}I_{1p}^2\cos(2\theta_e-5\theta_s) \tag{6.9}$$

If an external inductor with inductance of ΔL_{Ax} is connected with phase A in series, the power of the inductor can be expressed as

$$\Delta p_{L\_A}=[i]^T\frac{d}{dt}\left(\begin{bmatrix} \Delta L_{Ax} & 0 & 0 \\ 0 & 0 & 0 \\ 0 & 0 & 0 \end{bmatrix}[i]\right)=-\frac{1}{2}\omega_e\Delta L_{Ax}I_{1p}^2\cos(2\theta_e+3\theta_s) \tag{6.10}$$

In the same way, if external inductors ΔL_{Bx} and ΔL_{Cx} are connected in series with phases B and C respectively, the 2h power of those inductors can be expressed as (6.11) and (6.12) respectively.

$$\Delta p_{L\_B}=-\frac{1}{2}\omega_e\Delta L_{Bx}I_{1p}^2\cos(2\theta_e-5\theta_s) \tag{6.11}$$

$$\Delta p_{L\_C}=-\frac{1}{2}\omega_e\Delta L_{Cx}I_{1p}^2\cos(2\theta_e-1\theta_s) \tag{6.12}$$

Then it can be found that

$$\Delta p_{M\_AB} + \Delta p_{L\_C} = \frac{1}{2}\omega_e \left(\Delta M_{AB0} - \Delta L_{Cx}\right) I_{1p}^2 \cos\left(2\theta_e - 1\theta_s\right) \tag{6.13}$$

$$\Delta p_{M\_BC} + \Delta p_{L\_A} = \frac{1}{2}\omega_e \left(\Delta M_{BC0} - \Delta L_{Ax}\right) I_{1p}^2 \cos\left(2\theta_e + 3\theta_s\right) \tag{6.14}$$

$$\Delta p_{M\_AC} + \Delta p_{L\_B} = \frac{1}{2}\omega_e \left(\Delta M_{AC0} - \Delta L_{Bx}\right) I_{1p}^2 \cos\left(2\theta_e - 5\theta_s\right) \tag{6.15}$$

Therefore, if $\Delta L_{Cx} = \Delta M_{AB0}$, $\Delta L_{Ax} = \Delta M_{BC0}$ and $\Delta L_{Bx} = \Delta M_{CA0}$, the 2h power resulted from unbalanced average mutual inductances can be compensated completely by the introduced external inductors.

6.2.3 Summary

In summary, the unbalanced resistances, unbalanced average self-inductances, and mutual-inductances can be compensated by external *RL* network in series. Overall, the asymmetric 3-phase system with unbalanced impedances can be modified to balanced 3-phase system by external *RL* network. The parameters of the external circuits can be summarized in TABLE 6.1 if the asymmetries are modeled in Section 2.3.

Compared with the compensation in parallel in Fig.5.1 and Fig.5.10, the proposed method is much simpler, which does not need any power switches and any algorithm modifications. However, since the compensation in series is a passive compensation, the compensation effect may be affected by the non-linearity of compensation inductor, which will be detailed in Section 6.3.2 and verified by experiments in Section 6.4.1.

TABLE 6.1

COMPENSATION IN SERIES

Items	Asymmetries	Compensation
Resistances	Unbalanced resistance of phase A	$\Delta R_{Ax} = \Delta R_{A0}$
	Unbalanced resistance of phase B	$\Delta R_{Bx} = \Delta R_{B0}$
	Unbalanced resistance of phase C	$\Delta R_{Cx} = \Delta R_{C0}$
Self-inductances	Unbalanced self-inductance of phase A	$\Delta L_{Ax} = \Delta L_{A0}$
	Unbalanced self-inductance of phase B	$\Delta L_{Bx} = \Delta L_{B0}$
	Unbalanced self-inductance of phase C	$\Delta L_{Cx} = \Delta L_{C0}$
Mutual inductances	**Unbalanced mutual inductances between phase A and B**	$\boldsymbol{\Delta L_{Cx} = \Delta M_{AB0}}$
	Unbalanced mutual inductances between phase B and C	$\boldsymbol{\Delta L_{Ax} = \Delta M_{BC0}}$
	Unbalanced mutual inductances between phase A and C	$\boldsymbol{\Delta L_{Bx} = \Delta M_{AC0}}$

6.3 Compensation for the Prototype PMSG

According to the modeling of unbalanced average mutual inductances (2.28)~(2.31), at least one among the average mutual inductances of ΔM_{AB0}, ΔM_{BC0}, and ΔM_{CA0} is zero in the worst case. Therefore, only maximum two external inductors are required for compensating the unbalanced mutual inductances of the prototype PMSG completely.

To investigate the compensation in series in the asymmetric 3-phase PMSG system, only the first set of 3-phase windings in the dual 3-phase PMSG, Fig.B.3, is employed. The measured no-load self-inductances and mutual inductances in the single set of the prototype dual 3-phase PMSG at the frequency of 120Hz by HIOKI LCR meter IM3533-01 and the corresponding curve fitting are shown in Fig.C.1(a), while the corresponding harmonic analysis is shown in Fig.C.1(b). As shown in Fig.C.1(a) and (b), it is apparent that the average mutual inductance of M_{AB} is not equal to those of M_{CA} and M_{BC}, which is the dominant inherent asymmetry. Consequently, there are apparent 2h components in the *dq*-axis inductances, Fig.C.1(d).

According to the measured no-load inductances in Fig.C.1 and the inductance modeling of (2.14) and (2.15), the inductances of the prototype machine and the inherent asymmetry can be obtained and shown in TABLE 6.2. In the case study of the asymmetric prototype PMSG in single 3-phase mode, the 2h power resulted from the unbalanced impedances can be compensated by two external inductors connected with phase *A* and phase *B* respectively. The general compensation circuit in Fig.6.3 for the prototype PMSG can be simplified to Fig.6.4. With consideration of the internal resistance ΔR in the compensation inductors, an extra resistor should be connected with phase C in series in theory to keep the resistance network balanced.

TABLE 6.2

NO-LOAD INDUCTANCES OF THE PROTOTYPE PMSG

Inductances	Values
DC self-indutance (mH)	$L_0=L_{A0}= L_{B0}= L_{C0} =17.960$
2nd self-inductance(mH)	$L_{A2}= L_{B2}= L_{C2}= 1.146$
DC mutual-inductance (mH)	$M_0 = M_{AB0}=1.049;\ M_{CA0}= M_{BC0}= 10.825$
2nd mutual-inductance(mH)	$M_2=M_{AB2}= M_{CA2}= M_{BC2}= -1.272$
Inherent asymmetry	$\Delta M_{AB0}=0mH;\ \Delta M_{BC0}=\Delta M_{CA0}=$ 9.776mH

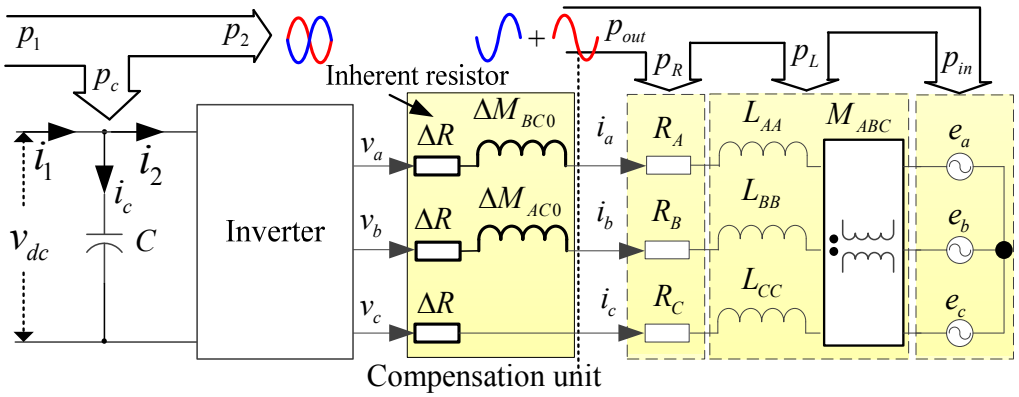

Fig.6.4 Proposed compensation unit in series for the prototype PMSG.

6.3.1 Optimized Compensation Inductance

When the balanced currents of 4A (generation mode, i_q=-4A) are injected into the stator currents, the active power flowing towards the DC bus from the PMSG is shown in Fig.6.5(b), where there is considerable 2h power due to the unbalanced mutual inductances. The *dq*-axis currents are shown in Fig.6.5(a), where there are no 2h currents in the *dq*-axis currents, which means the injected currents are quite balanced and sinusoidal.

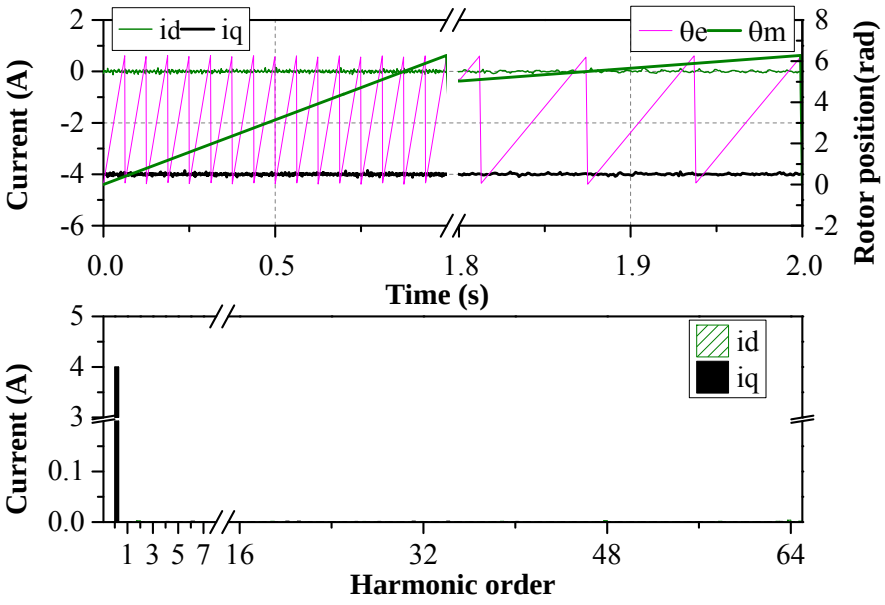

(a)

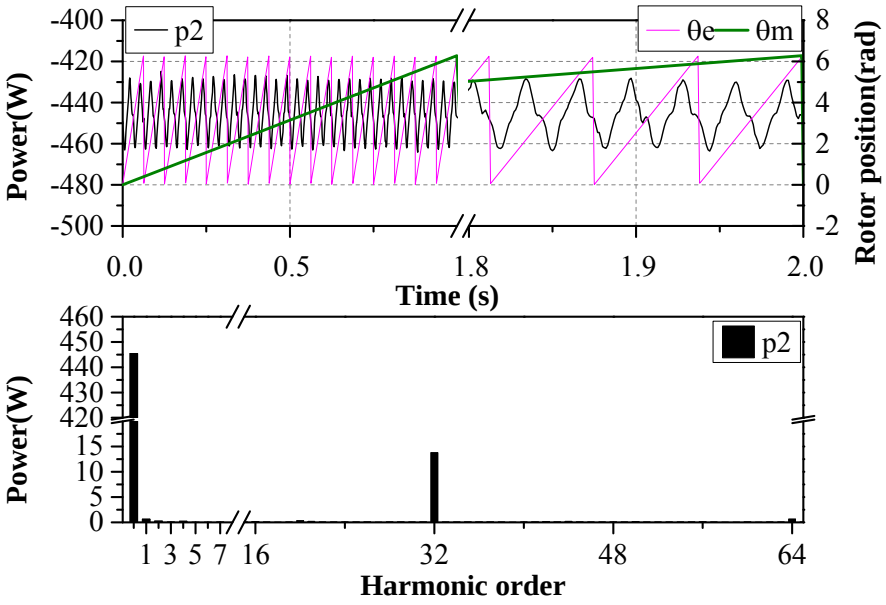

(b)

Fig.6.5 Experiments with inherent asymmetry. (a) Currents. (b) Second harmonic power.

The extracted 2h power p_{2_2h} from the power p_2 generated by PMSG at the speed of 60rpm can be illustrated in Fig.6.6. To compensate the 2h power properly, the external inductor in Fig.6.4 with optimized inductance of 18.8mH under the rated load is required. The 2h power $p_{2\_2h\_comp}$ from the compensation unit and the 2h power after compensation ($p_{2\_2h} + p_{2\_2h\_comp}$) can also be shown in Fig.6.6. After compensation, the total 2h power is suppressed significantly. However, it is worth noting that there is still residual 2h power after compensation because p_{2_2h} and $p_{2\_2h\_comp}$ are not exactly anti-phase, which is due to other insignificant asymmetries in the system, such as the trivial unbalanced resistances, self-inductances and 3-phase back-EMFs.

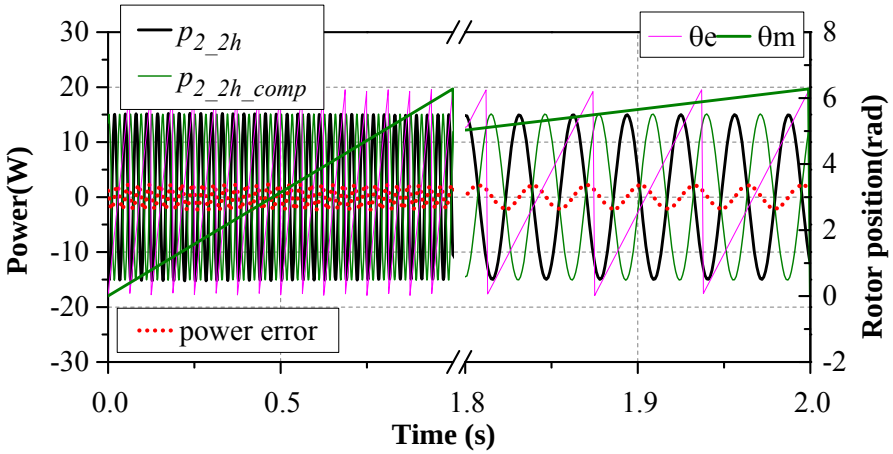

Fig.6.6 2h power (extracted vs. compensation) with optimized compensation inductance of 18.8mH (-4A, 60rpm).

6.3.2 Non-linearity of Compensation Inductor

The compensation inductor employed in this case study is shown in Fig.6.7. It can be flexibly configured as Tap-5mH, Tap-10mH, Tap-15mH or Tap-20mH respectively. In reality, the inductances at different loads depend on the *B-H* curve of the material used in the inductor. If the *B-H* curve is non-linear, the inductance will be non-linear as well [154]. To investigate the non-linearity of the inductance under different load conditions, the inductances are measured by HIOKI LCR meter IM3533-01, HIOKI LCR HiTESTER 3522, and AC test respectively.

Fig.6.7 Compensation inductor.

In the AC test, the inductor is energized with a controllable AC voltage source, and then the impedance can be obtained by

$$Z = \sqrt{(\omega L)^2 + R^2} = \frac{V}{I} \tag{6.16}$$

where ω, V, and I are the fundamental frequency, voltage and current respectively, R is the resistance at the test frequency. Thus, the inductance can be obtained by

$$L = \sqrt{Z^2 - R^2} / \omega \tag{6.17}$$

Take the measured inductance under the load of RMS 2.789A (peak 3.94A) as an example, the measured voltage and current of the compensation inductor are shown in Fig.6.8. The harmonic analyses of the voltage and current are listed in TABLE 6.3. The fundamental voltage and current are $13.9901V$ and $3.9447A$. Assuming the resistance is varied from $0.5*R_0$ to $2*R_0$ (R_0 is the resistance at the ambient temperature), which may be due to temperature variation, the inductance can be calculated as shown in TABLE 6.4. Since the

impedance Z is much bigger than the resistance, the inductance is varied from 34.5389mH ~ 34.6493mH, which has very trivial variation. It indicates the inductance measurement is credible even without consideration of temperature variation.

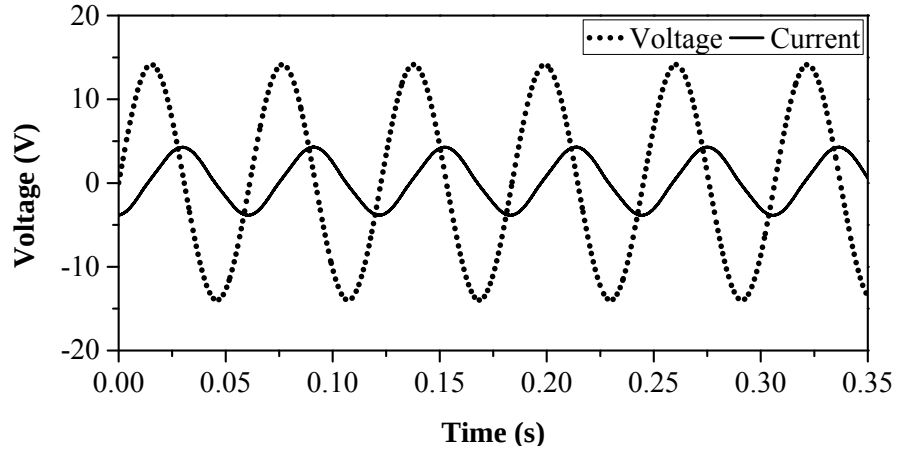

(a)

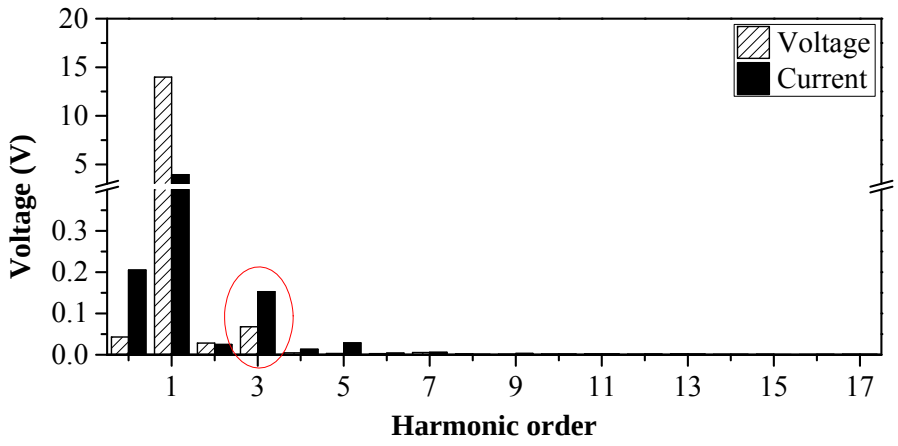

(b)

Fig.6.8 Inductance measurement by AC test. (a) Measured voltage and current. (b) Harmonic analysis of voltage and current.

If the inductance of the compensation inductor is linear, the expected harmonic voltages with the measured current flowing through the inductor can be shown in Fig.6.9. For example, the expected third harmonic voltage will be 1.625V, which has a huge difference from the actual measured third harmonic voltage (0.0679V) in TABLE 6.3. This phenomenon indicates the inductance is non-linear.

Since the maximum RMS current of IM3533-01 and HiTESTER 3522 in constant current mode are 50mA and 100mA respectively, the measurements by IM3533-01 and HIOKI LCR HiTESTER 3522 are conducted until the limit. To obtain the inductances under heavy load conditions (>100mA), the inductances are measured by AC test.

TABLE 6.3

FFT ANALYSIS UNDER THE LOAD OF RMS 2.789A

Harmonic order	Voltage(V)	Current(A)	Harmonic order	Voltage(V)	Current(A)
0	0.0430	0.2052	9	0.0015	0.0029
1	**13.9901**	**3.9447**	10	0.0018	0.0016
2	0.0284	0.0250	11	0.0022	0.0020
3	**0.0679**	**0.1529**	12	0.0016	0.0011
4	0.0045	0.0133	13	0.0022	0.0014
5	0.0032	0.0287	14	0.0012	0.0008
6	0.0028	0.0038	15	0.0017	0.0005
7	0.0055	0.0057	16	0.0008	0.0006
8	0.0022	0.0007	17	0.0017	0.0009

TABLE 6.4

INDUCTANCE MEASUREMENT AT THE RATED LOAD

Voltage(V)	Current(A)	Frequency(Hz)	Z(Ω)	R(Ω)	L(mH)
13.9901	3.9447	16.2870	3.5466	0.1460 (1.0*R_0)	34.6272
13.9901	3.9447	16.2870	3.5466	0.0730 (0.5*R_0)	34.6493
13.9901	3.9447	16.2870	3.5466	0.2920 (2.0*R_0)	34.5389

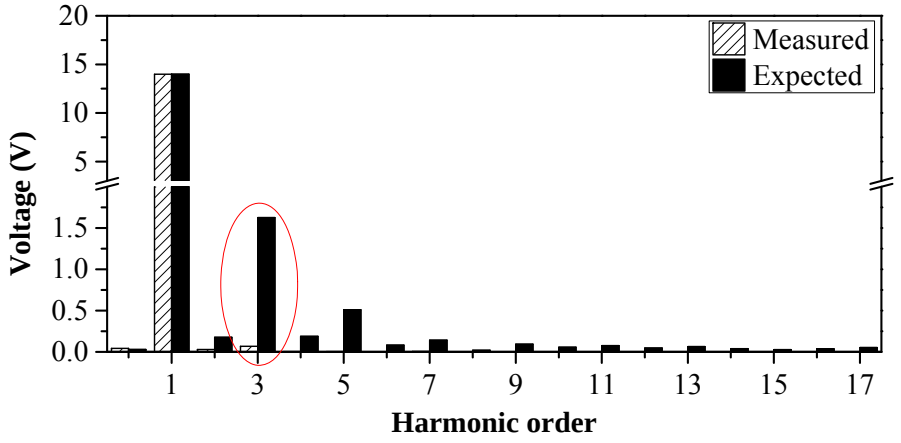

Fig.6.9 Measured harmonic voltages and expected harmonic voltages with same current if the inductance is linear.

The measured inductances under different load conditions at the frequency of 16Hz are plotted in Fig.6.10. As can be seen from Fig.6.10, the inductances measured by IM 3533-01, HiTESTER 3522 and AC test under light load conditions match each other, which show the credibility of the measurement of the AC test. Meanwhile, it clearly shows that the inductance of the employed compensation inductor is non-linear.

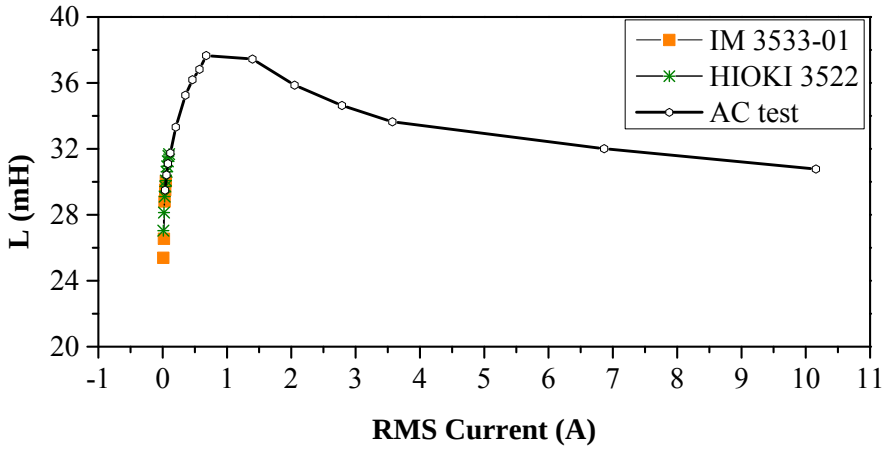

(a)

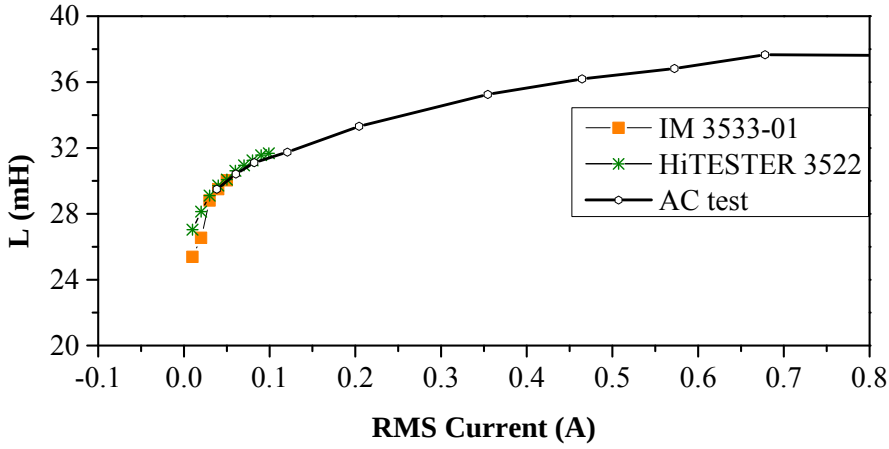

(b)

Fig.6.10 Measured indutances under different load conditions (Tap-20mH). (a) Inductance vs. load (full range). (b) Inductance vs. load (Zoom in).

6.3.3 Extra Copper Loss

Since the external inductors are connected in series with phases, the power rating of the compensation inductors and resistors in the compensation unit should be the same as the power rating of the PMSG. Therefore, the copper loss of the compensation unit and the PMSG can be expressed as (6.18) and (6.19) respectively.

$$\Delta P_{copper} = 1.5 I_1^2 \Delta R \tag{6.18}$$

$$P_{copper} = 1.5 I_1^2 R \tag{6.19}$$

where I_1=4A is the peak value of the rated phase current, ΔR is the inherent resistance of the compensation inductor, R is the resistance of the phase winding of the PMSG. Therefore, the copper loss ratio can be expressed as

$$\Delta P_{copper} \Big/ P_{copper} = \Delta R \Big/ R \tag{6.20}$$

The measured resistances of the compensation inductor and the prototype PMSG by HIOKI LCR meter IM3533-01 are shown in TABLE 6.5, and then the introduced copper loss can be estimated and listed in TABLE 6.5 if the compensation inductor is configured with different taps. It is worth noting that Tap-20mH//20mmH in TABLE 6.5 means two Tap-20mH terminals are connected in parallel and they are treated as a unity inductor.

As can be seen from the TABLE 6.5, the extra power loss from the compensation unit will not exceed 4% of the copper loss of the PMSG.

TABLE 6.5

MEASURED RESISTANCES AND ESTIMATED COPPER LOSS

Tap	ΔR@Compensation inductor (Ω)	R@PMSG (Ω)	Copper loss ratio
Tap-5mH	0.066	3.93	1.68%
Tap-10mH	0.096	3.93	2.44%
Tap-15mH	0.121	3.93	3.08%
Tap-20mH	0.146	3.93	3.72%
Tap-20mH//20mmH	0.077	3.93	1.96%

6.4 Experiments

The test rig is illustrated in Fig.6.11. The asymmetric PMSG employed for this study is the dual 3-phase PMSG in single 3-phase mode, whose measured inductances are shown in Fig.94. The PMSG is coupled with a servo machine driven by the Siemens servo drive S120, which is used to simulate the wind turbine. A power resistor R_L(100Ω) is parallel with the DC bus to consume the power generated by the PMSG in generation mode. A dedicated compensation unit shown in Fig.6.4 is connected with the PMSG in series.

The control is conducted based on dSPACE DS1006. The design parameters of the prototype PMSG are listed in TABLE B. 1 and measured parameters are detailed in Appendix C. It is worth noting that the number of the pole pairs of the prototype machine is 16.

Therefore, the 32nd harmonic in the following harmonic analyses based on the mechanical frequency indicates the 2h component in electrical frequency.

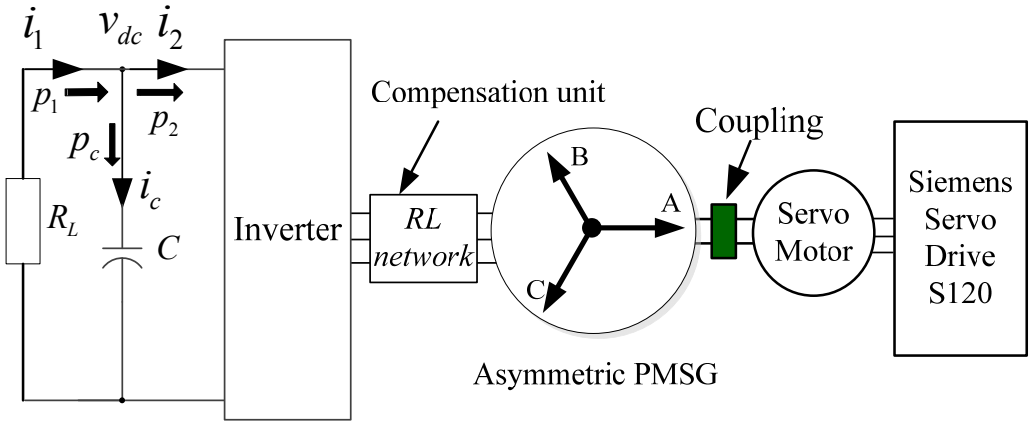

Fig.6.11 Illustration of test rig with compensation in series.

6.4.1 Influence of Non-linearity of Compensation Inductor

From the measured inductance of the compensation inductor in Fig.6.10, it can be concluded that the inductance of Tap-10mH (half of the inductance of Tap-20mH) is closer to the optimized inductance in Fig.6.6 than other Taps. Thus, Tap-10mH is the best candidate for the compensation inductor in the compensation unit in series. In theory, the 2h powers with the configuration of Tap-10mH and the Tap-20mH//20mH (two Tap-20mH in parallel) should be the same without consideration of non-linearity. However, due to the different non-linearity of the compensation inductances, Fig.6.12, there is slight difference between these two cases.

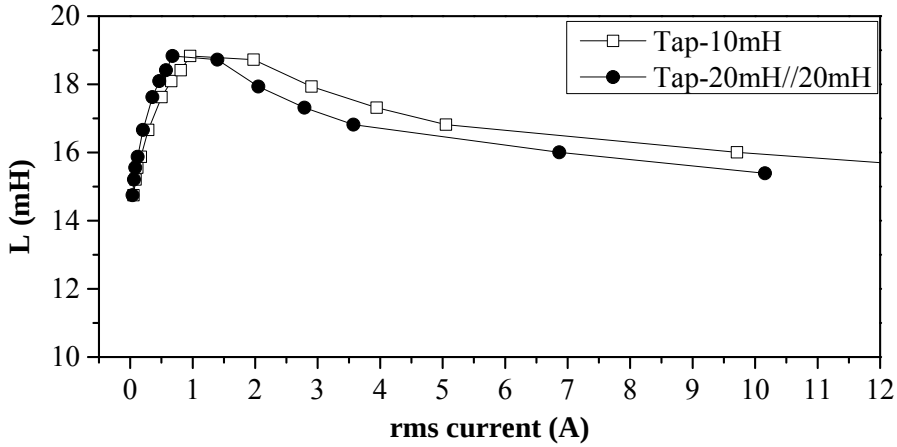

Fig.6.12 Different non-linearity of the compensation inductance (Tap-10mH vs. Tap-20mH//20mH).

The 2h powers without and with compensation under different *q*-axis current conditions at the speed of 60 rpm are shown in Fig.6.13. The compensation inductor configured as Tap-10mH and Tap-20mH//20mH are applied for compensation in series in the experiments respectively. As can be seen from Fig.6.13 that there is approximate 2.5W 2h power difference under rated current conditions between the configuration of Tap-10mH and the Tap-20mH//20mH, which is 0.16% of the rated power. The compensation effect is slightly affected by the non-linearity of the compensation inductor. Nevertheless, the 2h powers are reduced significantly after compensation no matter the inductor is configured as Tap-10mH or Tap-20mH//20mH.

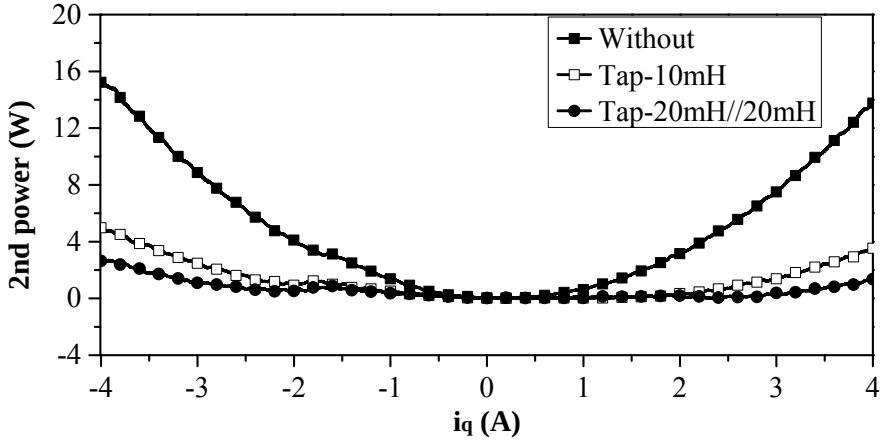

Fig.6.13 2h powers without/with compensation under different loads.

The harmonic analyses of the *dq*-axis voltages under rated load condition without/with compensation are shown in Fig.6.14. As shown in Fig.6.14(a), the 2h voltages in *dq*-frame without compensation are balanced, whose amplitudes are equal to each other. Correspondingly, the third harmonic phase voltages in Fig.6.15(a) are subtle, which indicates the armature reaction effect in the prototype PMSG is negligible. However, when the compensation inductors (Tap-10mH or tap-20mH//20mH) are connected in series, it can be seen that there are apparent third harmonic phase voltages, Fig.6.15(b) and (c) compared with that in Fig.6.15(a), which result in the unbalanced 2h voltages in *dq*-frame, Fig.6.14(b) and (c). When there are third harmonic voltages in the phase voltages, they will interact with the fundamental currents, which will result in a small portion of 2h power. Consequently, the 2h powers with the Tap-10mH and the Tap-20mH//20mH in Fig.6.13 are slightly different.

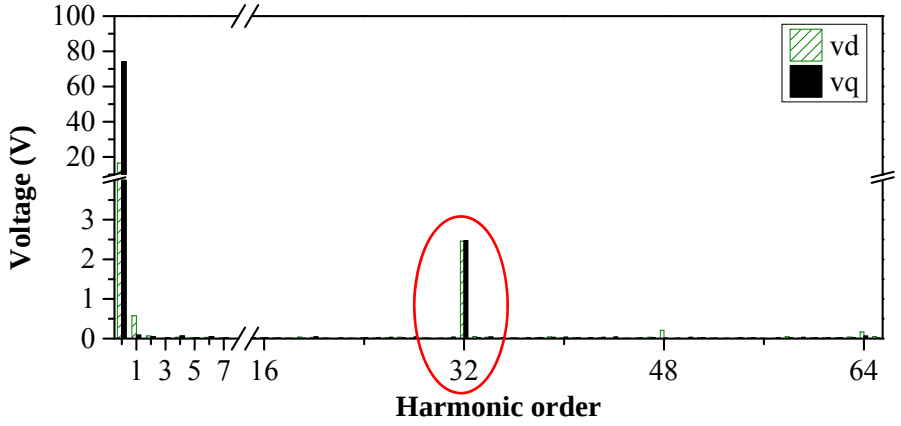

(a)

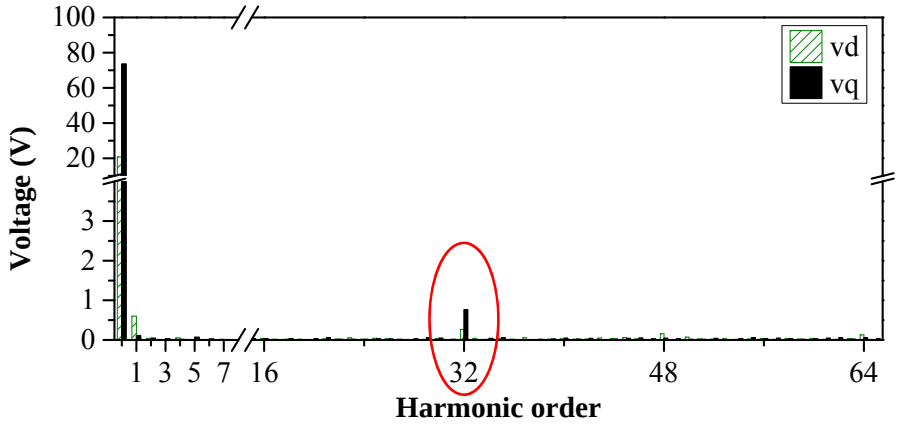

(b)

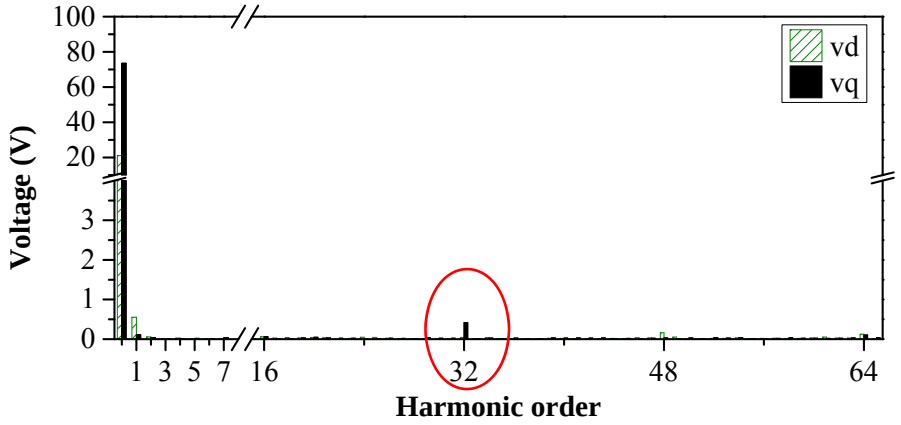

(c)

Fig.6.14 Harmonic analysis of *dq*-axis voltages based on mechanical frequency. (a) Without compensation (balanced 2nd harmonics). (b) With compensation of Tap-10mH (unbalanced 2nd harmonics). (c) With compensation of Tap-20//20mH (unbalanced 2nd harmonics)

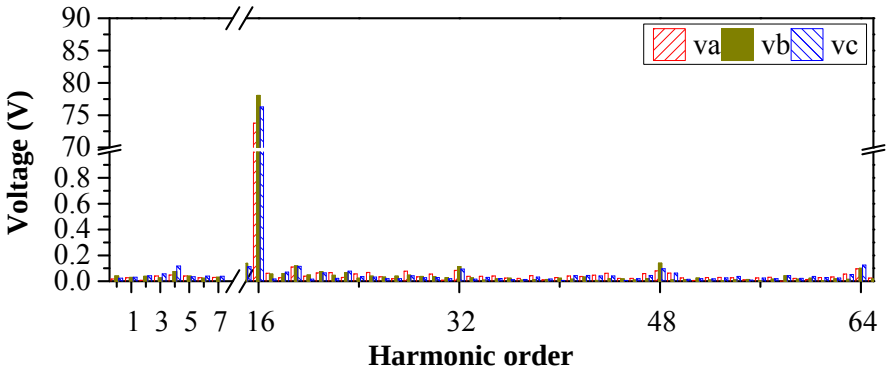

(a)

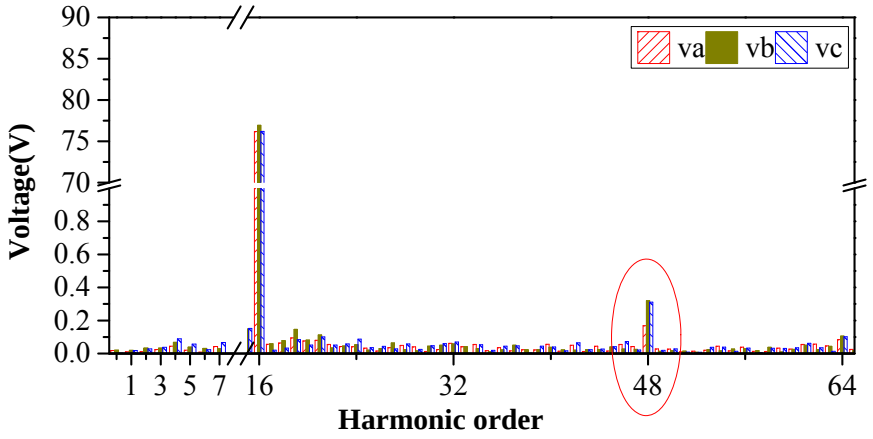

(b)

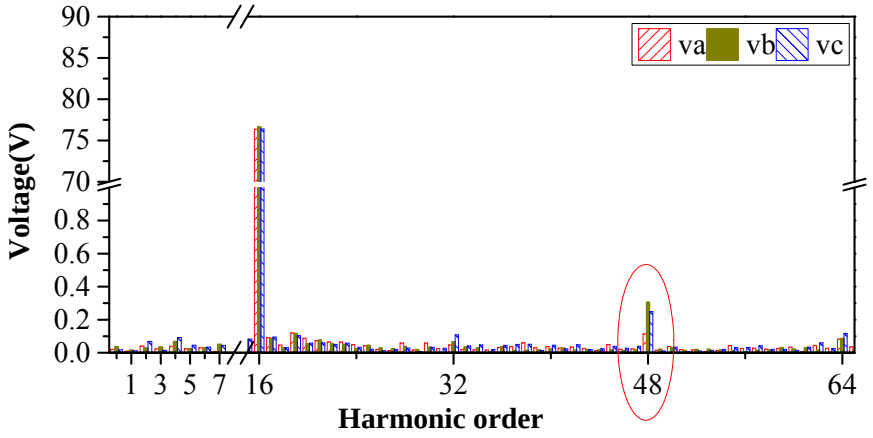

(c)

Fig.6.15 Harmonic analysis of phase voltages in *abc*-frame based on mechanical frequency. (a) Without compensation. (b) With compensation of Tap-10mH ($\pm 3\omega_e$ voltages). (c) With compensation of Tap-20//20mH ($\pm 3\omega_e$ voltages).

6.4.2 Results without/with Compensation

As shown in Fig.6.13, the configuration of Tap-20mH//20mH has better performance than the Tap-10mH in terms of the suppression of 2h power, Fig.6.13. Therefore, the configuration of Tap-20mH//20mH will be employed for compensation in this experiment.

The results without/with compensation will be compared in this section. The drive works in balanced current control mode by adopting the PI-R control in PSRF in Fig.3.6. The *d*-axis and *q*-axis current references are assigned to 0A and -4A respectively. The speed is regulated to be 60 rpm by the servo machine. The experimental results of balanced current control without compensation have been presented in Fig.4.4 in Section 4.5.1. For the convenience of comparison with the proposed method with compensation, the phase currents, power, and DC bus voltage of the balanced current control without compensation are repeated in Fig.6.16(a), (c), and (d) respectively. Meanwhile, the *dq*-axis voltages are shown in Fig.6.16(b).

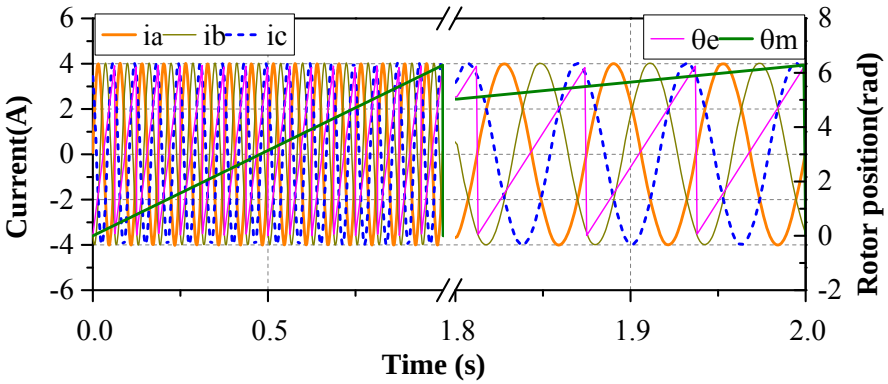

(a)

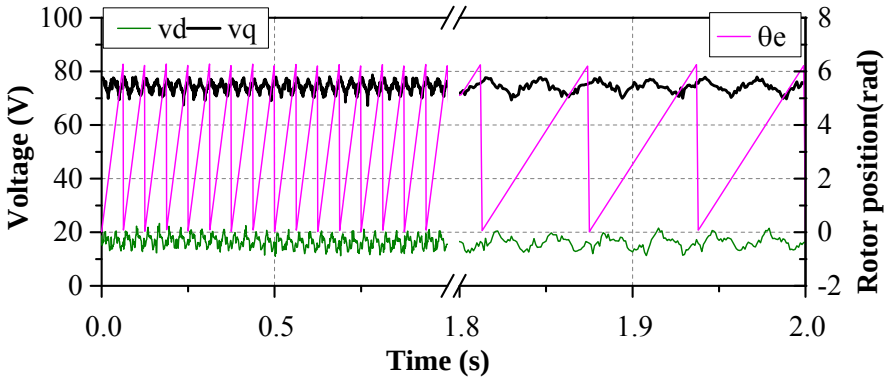

(b)

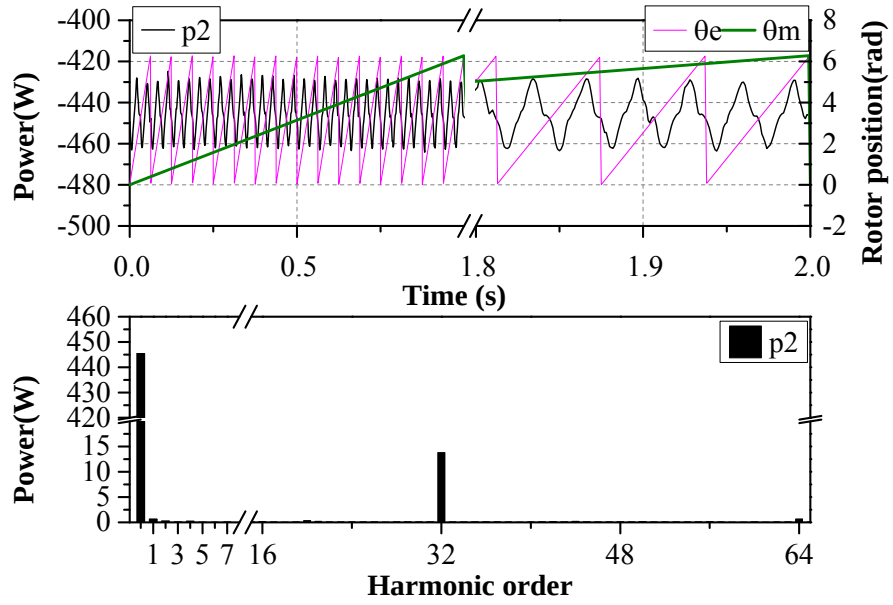

(c)

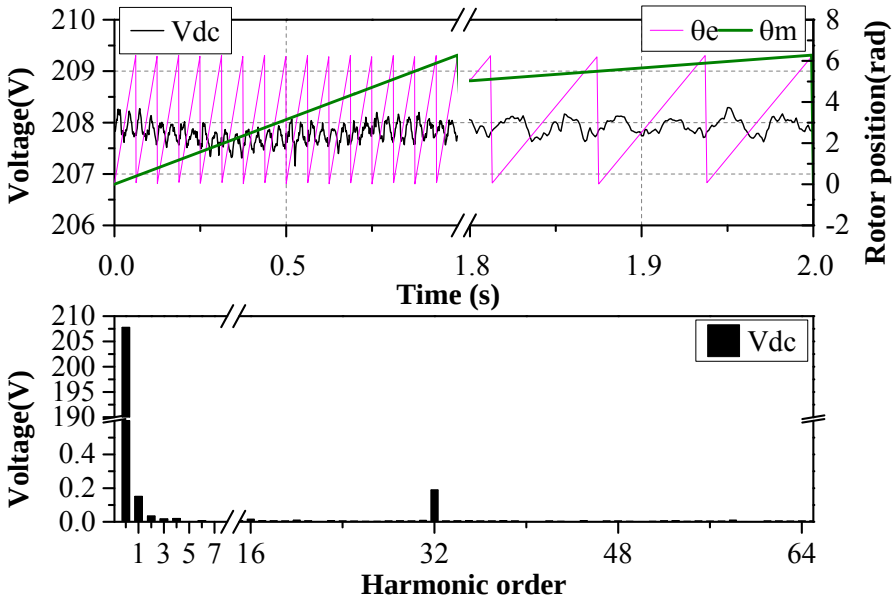

(d)

Fig.6.16 Balanced current control without compensation @60rpm. (a) Currents. (b) Voltages. (c) Power. (d) DC bus voltage.

The experiment results with compensation are shown in Fig.6.17. As can be seen from Fig.6.16(a) and Fig.6.17(a), the 3-phase currents are quite sinusoidal, balanced and fairly regulated. Due to the inherent asymmetric impedances of the prototype machine shown in Fig.C.1, the output voltages without compensation are unbalanced, which is implied by the apparent 2h *dq*-axis voltages in *dq*-frame, Fig.6.16(b). Consequently, it will result in 2h power flowing towards the DC bus capacitors, Fig.6.16(c), and corresponding 2h DC bus voltage, Fig.6.16(d).

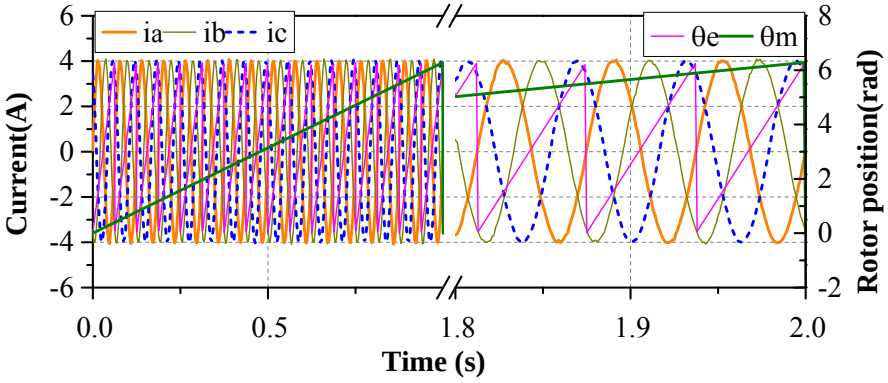
ia
ib
ic
θe
θm
Current(A)
Rotor position(rad)
Time (s)

(a)

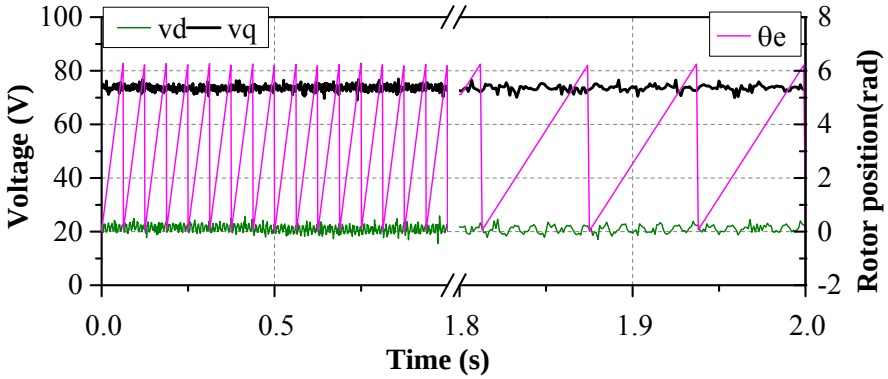
vd
vq
θe
Voltage (V)
Rotor position(rad)
Time (s)

(b)

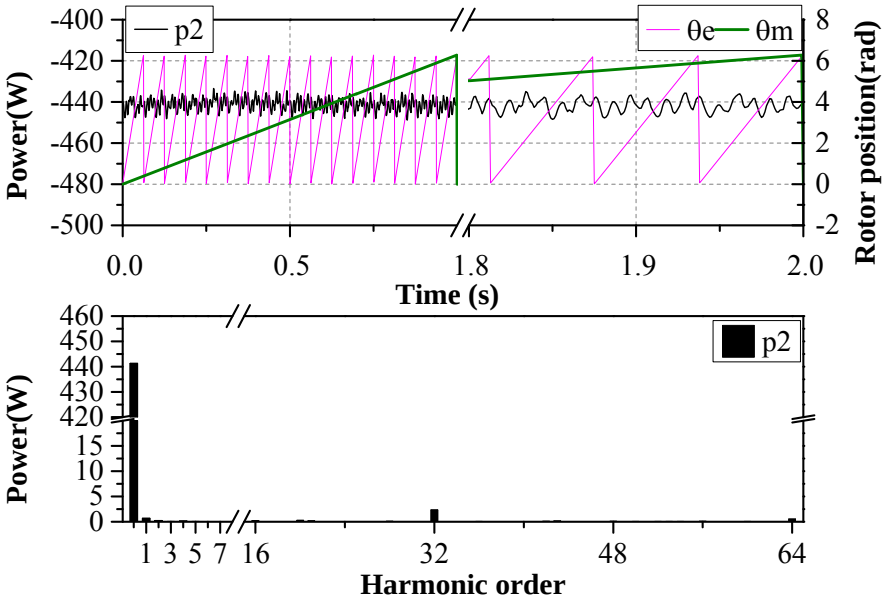
p2
θe
θm
Power(W)
Rotor position(rad)
Time (s)
p2
Power(W)
Harmonic order

(c)

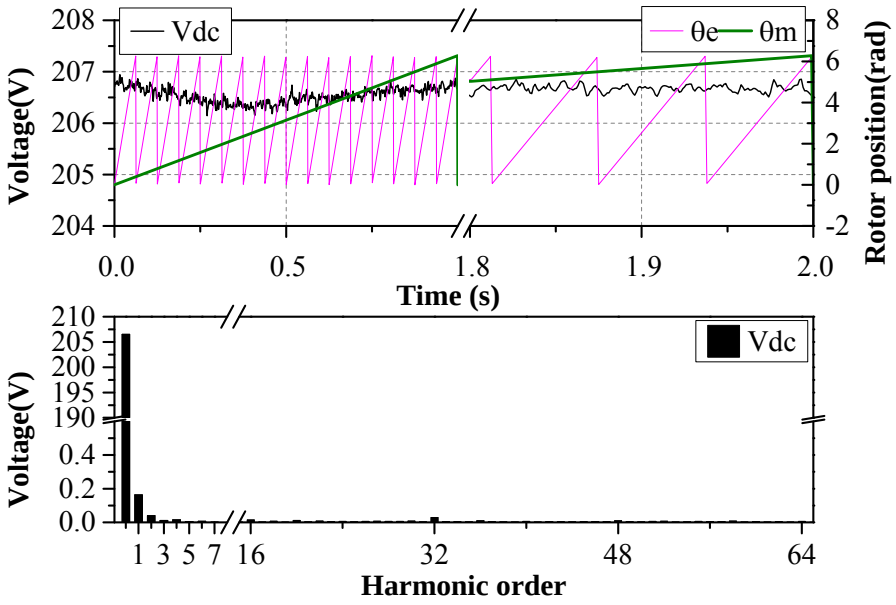

(d)

Fig.6.17 Balanced current control with compensation @60rpm. (a) Currents. (b) Voltages in *dq*-frame. (c) Power. (d) DC bus voltage.

With the proposed compensation in series, the 2h voltages in the *dq*-axis voltages in Fig.6.17(b) are suppressed significantly compared with that in Fig.6.16(b), which means the system is more balanced after compensation. The 2h power flowing towards the DC bus capacitors, Fig.6.17(c), is reduced significantly compared with that in Fig.6.16(c). Therefore, the 2h DC bus voltage, Fig.6.17(d), is correspondingly suppressed and smaller than that in Fig.6.16(d).

6.4.3 Feasibility at Different Speeds and Loads

To verify that the proposed method is feasible under different load conditions, the experiments under different load conditions (i_q from -4A to 4A) at the speed of 60rpm are conducted. The 2h powers without and with compensation are shown in Fig.6.13. Compared with the 2h power without compensation, the 2h power with compensation is reduced significantly. According to (4.6), the 2h DC bus voltage will be correspondingly suppressed.

To verify the proposed method is feasible at different speeds, the experiments at different speeds under rated current (-4A) conditions are conducted as well. The measured 2h power with rated current (i_q=-4A) at different speeds are shown in Fig.6.18, which shows that the 2h power is reduced significantly at different speeds with compensation in series. As the 2h power decreases, according to (4.6), the 2h DC bus voltage will be correspondingly

suppressed as well. Overall, the system is more balanced than the original system after the compensation.

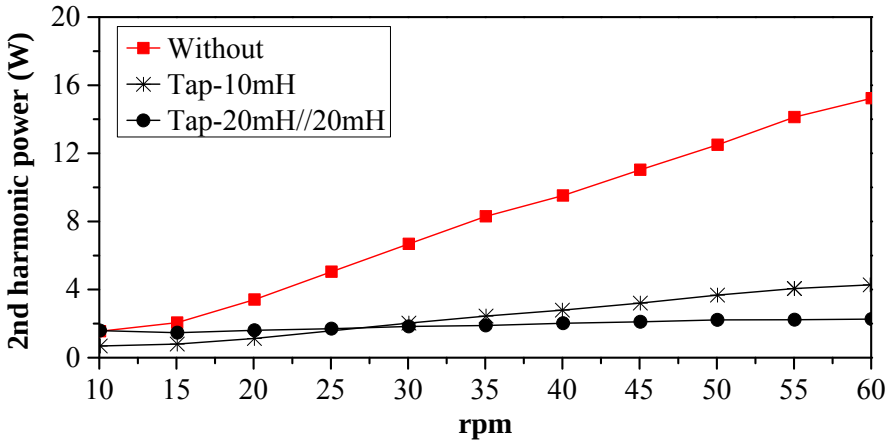

Fig.6.18 2h power without/with compensation at different speeds (i_q=-4A).

6.5 Conclusion

In this chapter, the unbalanced impedances in the asymmetric 3-phase PMSG compensated by external circuits in series is investigated. From the perspective of the 2h inductances in *dq*-frame and the 2h power, it has been demonstrated that the original unbalanced 3-phsae system with unbalanced resistances, unbalanced self-inductances or even unbalanced mutual inductances can be modified to a balanced system by introduced external circuits in series in theory. With the compensation, the 2h power and DC bus voltage can be suppressed significantly. The proposed method is simple, which does not need extra power switches and any algorithm modifications as the compensation in parallel. The feasibility of this compensation is verified by elaborate experiments at different speeds and under different load conditions, although the compensation effective may be slightly affected by the non-linearity of the compensation inductance in practice.

Chapter 7 Control of Asymmetric Dual 3-Phase PMSG System with One Channel Failed

7.1 Introduction

In Chapter 5, the control of asymmetric single 3-phase PMSG with compensation in parallel is investigated, while in Chapter 6, the control of asymmetric 3-phase PMSG with compensation in series is investigated. Both the compensation in parallel and in series can suppress the 2h DC bus voltage and torque in the PMSG system with asymmetric impedances. In this chapter, the research of suppressing the 2h DC bus voltage and torque ripple will be extended to dual 3-phase PMSG system.

As the power level of wind turbines increases while considering the operational current limit of power devices [155, 156], the multi-phase machine and parallel two-level BTB converters [3] present a potential solution. One typical wind turbine drive system configured with dual 3-phase PMSG is shown in Fig.7.1, where two identical windings of dual 3-phase PMSG are supplied independently by two BTB inverters [10, 157, 158]. The DC buses of the two BTB inverters are isolated. In some cases, when one of the two BTB inverters is failed, only the healthy channel can keep working with only half power rating, while the remaining healthy set of 3-phase windings may be asymmetric, which will result in system asymmetries [79, 80, 159-162]. Consequently, it will result in the 2h DC bus voltage, 2h torque ripple and increased current THD of grid side.

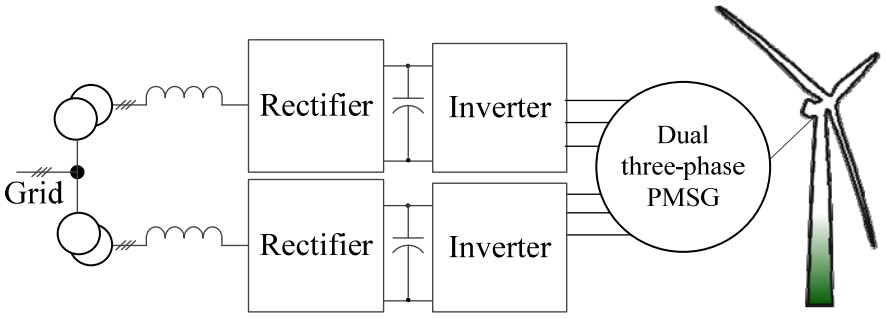

Fig.7.1 Dual 3-phase PMSG wind turbine drive system.

In dual 3-phase PMSG drive system, the two sets of 3-phase windings may be physically separated. As shown in Fig.7.2, the windings of the first and the second set of the prototype dual 3-phase PMSG are denoted by the solid and dotted line respectively. When both

channels work normally with the same currents, the dual 3-phase PMSG can be treated as balanced single 3-phase machine with two sets in parallel and has symmetrical winding topology. For each phase winding, the other two phase-windings are always next to it. However, when one set of 3-phase windings, one channel of the rectifier or inverter units is failed, only the other healthy channel can keep working. If the set of 3-phase windings in the fault channel are disconnected, e.g., the second set is disconnected, as shown in Fig.7.2, the winding topology of the first set is asymmetric which results in unbalanced inductances, Fig.93. Therefore, the system will work under asymmetric conditions. In this case, the *N*-sequence currents and the 2h power will be produced under conventional current control. The undesired *N*-sequence currents will result in the 2h torque ripple, while the undesired 2h power will flow through the DC bus capacitors and result in the 2h DC bus voltage ripple [113, 114, 143], capacitor power losses, temperature rise, and reduced lifetime [93].

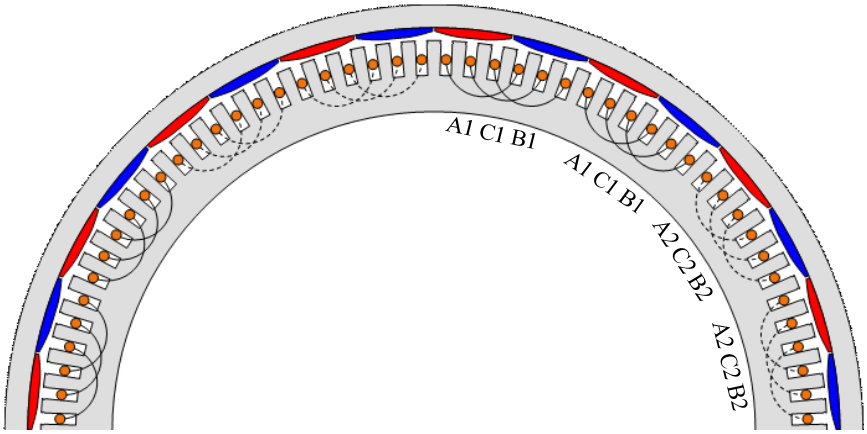

Fig.7.2 Winding topology of the prototype dual 3-phase PMSG.

To suppress the 2h DC bus voltage and torque ripple in the asymmetric PMSG system without deterioration of current THD of grid side, a compensation unit with H-bridge switches and compensation inductor (Topology-*RL*) in parallel with the DC bus is introduced in the Section 5.2 of Chapter 5. However, this method requires some extra hardware investment. Meanwhile, how to transfer the 2h power to the compensation unit is very complicated. An alternative compensation unit with half-bridge, inductor, and DC voltage source (Topology-*RLE*) in parallel with the DC bus is introduced in section 5.3 of Chapter 5. It has the same principle of transferring the 2h power to the compensation unit, but it is superior to the Topology-*RL* because of its half-bridge power switches, smaller compensation current, smaller copper loss, smaller size of inductor and simpler control. However, it still requires extra hardware investment and compensation current regulation, particularly a DC voltage source, which increases the cost of the whole system and complexity.

In Chapter 6, an external resistor and inductor (*RL)* network connected in series with the asymmetric PMSG is employed to compensate the unbalanced impedances of PMSG. With the introduced asymmetric *RL* network, the original unbalanced system is modified to a balanced 3-phase system after compensation. Therefore, with the balanced currents injection, the 2h power and DC bus voltage can be suppressed. Compared with the compensation in parallel in Chapter 5, the most attractive advantage is that no software modifications and extra power switches are required. However, it requires two external inductors with the same power rating of the machine. Meanwhile, how to activate the compensation circuit is a serious issue as it is not required in normal operation.

When one channel in Fig.7.1 is failed, e.g., the rectifier, inverter, or the one set of dual 3-phase PMSG is failed, the methods in Chapter 5 and Chapter 6 can be applied to suppress the 2h DC bus voltage and torque ripple without deterioration of the current THD of grid side. However, those methods require extra hardware investment that increases the system cost.

By utilizing the 3-phase winding, rectifier, or inverter in the faulty channel that are still functional, there could be some more economical solutions that can suppress the 2h DC bus voltage and torque ripple. In this chapter, three control methods aiming for suppressing the 2h DC bus voltage and torque ripple with minimum or without any hardware investment will be investigated when one channel in Fig.7.1 is failed.

7.2 Different Scenarios of Faults

7.2.1 One Faulty Channel of 3-phase Windings

When one set of 3-phase windings fails, as illustrated in Fig.7.3, the faulty set cannot transfer power from the wind to the grid anymore, and only the other healthy channel can keep working with half rated power. In this case, the dual 3-phase drive system becomes asymmetric single 3-phase PMSG drive system. To suppress the 2h DC bus voltage and torque ripple, the compensation in parallel in Chapter 5 and compensation in series in Chapter 6 can be adopted.

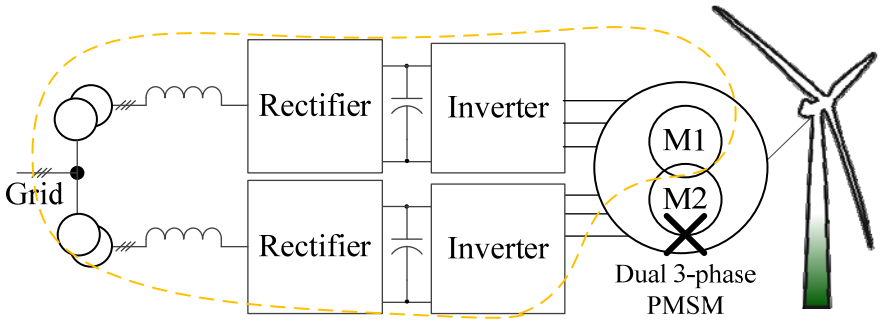

Fig.7.3 Dual 3-phase PMSG wind turbine drive system with one faulty set of 3-phase windings.

7.2.2 One Faulty Channel of Inverter

As illustrated in Fig.7.4, when one channel of inverter units fails, the power from wind cannot be transferred to grid side through the faulty inverter any more. In this case, if the set of 3-phase windings in the faulty channel is disconnected, the compensation in parallel in Chapter 5 and compensation in series in Chapter 6 can be adopted to suppress the 2h DC bus voltage and torque ripple. Alternatively, the two sets of 3-phase windings can be connected in parallel, then the dual 3-phase PMSG is turned into a balanced single 3-phase PMSG with two branches in parallel, then the 2h DC bus voltage and 2h torque ripple can be suppressed naturally. Although the power capability of the machine can be fully utilized, only one set of inverter and rectifier in the healthy channel can deliver the power from the machine to the grid side. Therefore, the power rating is reduced to half rated power of the original system.

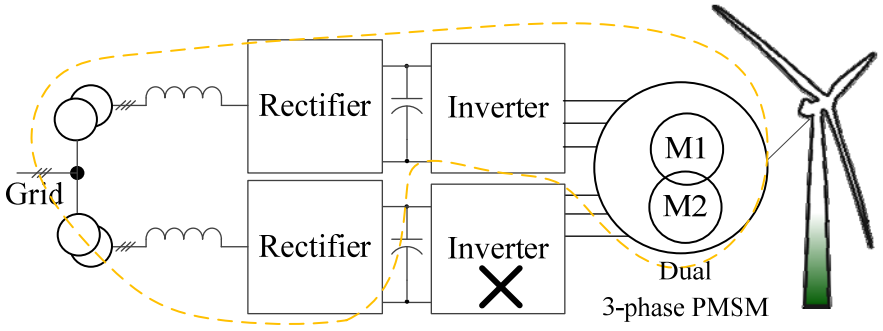

Fig.7.4 Dual 3-phase PMSG wind turbine drive system with one faulty channel of inverter.

7.2.3 One Faulty Channel of Rectifier

When one channel of rectifier fails as illustrated in Fig.7.5, the wind power cannot be transferred through the faulty rectifier. In this case, to suppress the 2h DC bus voltage and 2h torque ripple, the compensation in parallel in Chapter 5 and compensation in series in

Chapter 6 can be adopted without utilizing the set of windings and inverter in the faulty channel. Or alternatively, the two sets can be connected in parallel, and then the dual 3-phase PMSG is modified to the symmetrical single 3-phase PMSG. Except that, the two separate DC buses can be connected together, with the two sets supplied with same currents, the dual 3-phase PMSG is actually equivalent to the systematical single 3-phase PMSG. However, as only one channel of rectifier can be employed to deliver the power, the power rating is reduced to half rated power of original system.

Compared with the compensation in parallel in Chapter 5 and compensation in series in Chapter 6, to implement the method of two sets in parallel or the DC buses in parallel, the hardware modification is much less since it only requires some power relays to connect the two sets in parallel or the DC buses in parallel together. Nevertheless, it still requires hardware investment, to further reduce the cost, in this chapter, another method will be proposed without any hardware investment and configuration at all, which will be detailed in the next section.

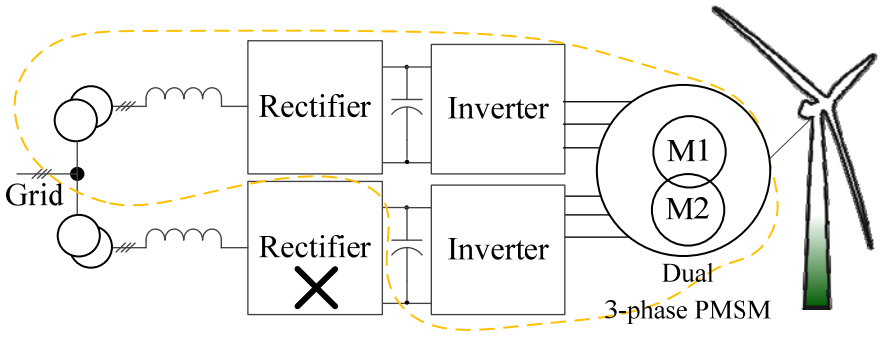

Fig.7.5 Dual 3-phase PMSG wind turbine drive system with one faulty channel of rectifier.

7.3 Proposed Methods

As all aforementioned methods of compensation in parallel, compensation in series, two sets in parallel, and DC buses in parallel are all applicable for the scenario of one channel of rectifier fails, this scenario is chosen for investigation. Since the compensation in parallel has been discussed in Chapter 5 and the compensation in series has been discussed in Chapter 6, three other methods will be discussed in this section.

7.3.1 Method 1- Two Sets in Parallel

The Method 1 is illustrated in Fig.7.6(a), where the two sets of dual 3-phase PMSG windings are connected in parallel, both the two sets of 3-phase windings are employed to

transfer power from the wind turbine to the DC bus capacitors. However, since only one channel of rectifier and inverter is keep working, due to the power rating limit of the rectifier and inverter, the power volume of whole system is only half of the original system.

Since the two sets of dual 3-phase machine are in parallel, the original dual 3-phase machine actually becomes a single 3-phase machine with symmetrical winding topology due to two branches in parallel Fig.7.2. Therefore, the inductances are balanced as shown in Fig.C.2. Consequently, the 2h power and DC bus voltage can be suppressed. Meanwhile, compared with the methods in Chapter 5 and Chapter 6, where only one set of windings is employed to transfer power, the equivalent resistance of two sets in parallel is only half of that in the single set. Therefore, the copper loss is also halved compared with the methods in Chapter 5 and Chapter 6.

7.3.2 Method 2- Two DC Buses in Parallel

Method 2 is illustrated in Fig.7.6(b), where the DC buses in two channels are connected together. Both two sets of windings and inverters are employed to transfer the power from the wind turbine to the DC bus capacitors. However, since only one channel of rectifier is kept working, due to the power rating limit of the rectifier, the power volume of whole system is only half of the original system.

In Method 2, if the two sets of 3-phase windings are supplied with the same currents by two independent drives, the dual 3-phase machine can be treated as a balanced single 3-phase machine as that in Method 1. Therefore, the 2h power and DC bus voltage will be suppressed and the copper loss is also only half of that in the methods in Chapter 5 and Chapter 6.

7.3.3 Method 3- *N*-sequence Currents Compensation

The third method is illustrated in Fig.7.6(c), which does not require any extra hardware investment. When the second rectifier fails, Fig.7.6(c), only the first channel of rectifier will deliver the energy generated by the PMSG from the DC bus capacitors to the grid side. If the balanced currents are injected into the first set, the 2h power due to the asymmetries will flow into the DC bus. As the rectifier is trying to regulate the DC bus voltage, it will transfer the 2h power to the gird side and then ruin the current THD of grid side. Therefore, to avoid the deterioration of current THD of grid side, the instantaneous power control should be employed to suppress the 2h power generated by the first set of 3-phase windings. Consequently, the 2h DC bus voltage in the healthy channel can be suppressed.

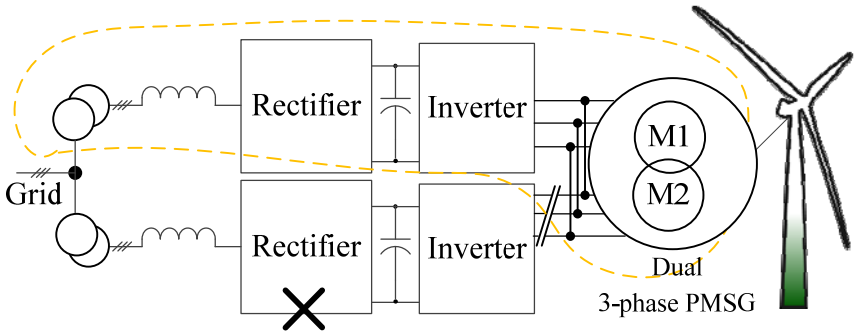

(a)

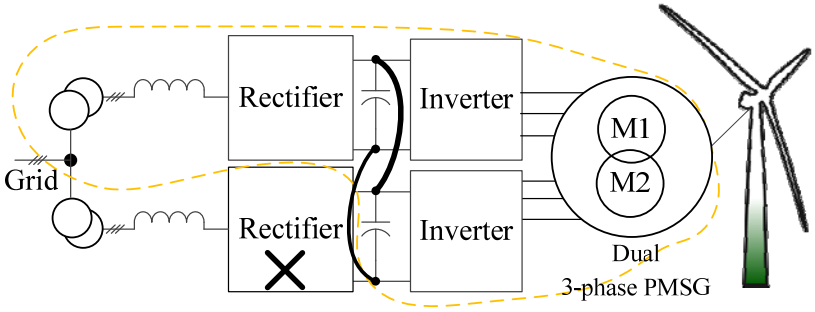

(b)

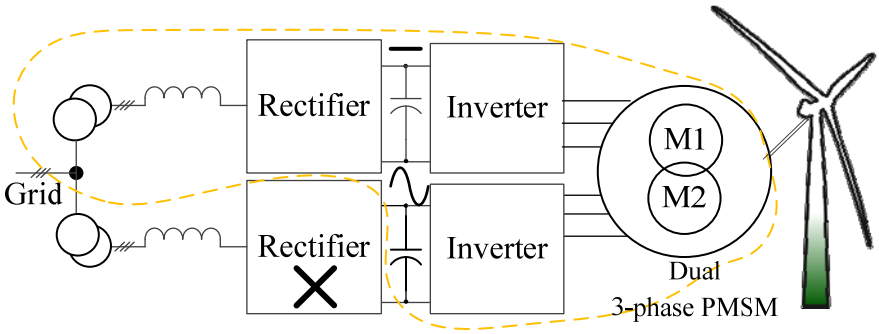

(c)

Fig.7.6 Dual 3-phase PMSG drive system with one faulty rectifier. (a) Method 1: Two sets in parallel. (b) Method 2: DC buses in parallel. (c) Method 3: *N*-sequence currents compensation.

However, as introduced in Chapter 2, the *N*-sequence currents in instantaneous power control will interact with the 3-phase back-EMFs and then 2h torque will be produced. To mitigate the 2h torque from the first set due to the *N*-sequence currents, the second set of 3-phase windings and inverter can be utilized to cancel the 2h torque.

Since the 2h torque is mainly contributed by the *N*-sequence currents, if the *N*-sequence currents in the first set are compensated by *N*-sequence currents in the second set, the 2h torque from the first set can be compensated by the 2h torque from the second set.

Consequently, the total 2h torque can be suppressed. Based on this principle, the whole control of Method 3 can be illustrated in Fig.7.7. This method is designated as *N*-sequence currents compensation.

As shown in Fig.7.7, the first inverter works in constant power control mode by instantaneous power control, while the second inverter works in constant DC bus voltage mode. As detailed in Chapter 4, with the power reference for the first set, the *P*-sequence current references in PSRF i_{d1}^{p*}, i_{q1}^{p*} and the *N*-sequence current references in NSRF i_{d1}^{n*}, i_{q1}^{n*} can be derived by (4.25). i_{d1}^{n*} and i_{q1}^{n*} are converted to *N*-sequence current references in PSRF $i_{d2\omega1}^{*}$ and $i_{q2\omega1}^{*}$ by $T_{dq}(2\theta_e)$, where $T_{dq}(\theta)$ is the standard Park transformation (A.7). Then $i_{d2\omega1}^{*}$ and $i_{q2\omega1}^{*}$ are deducted from the current references for the second set. Therefore, the *N*-sequence currents of the first set can be compensated by the *N*-sequence currents of the second set.

To suppress the undesired 2h current reference in i_{q2}^{*} from the DC bus voltage PI control of the second set which will produce the 2h torque, the bandwidth of the DC bus voltage PI controller should be low. As the second rectifier is isolated from the grid, it will not contribute the energy transition anymore. The energy is only consumed by the balanced resistors which are connected in parallel with the DC bus capacitors in reality. Usually, the resistance of the balanced resistors is very large and the consumed energy is negligible. Therefore, the average value of the active current i_{q2}^{*} will be very small.

As the *N*-sequence currents are introduced in the second set to cancel the 2h torque produced by the first set, there will be 2h power flowing into the DC bus of the second set, which will result in the 2h DC bus voltage. However, compared with the 2h DC bus voltage in the first channel, the 2h DC bus voltage in the second set would not result in the deterioration of the current THD of grid side.

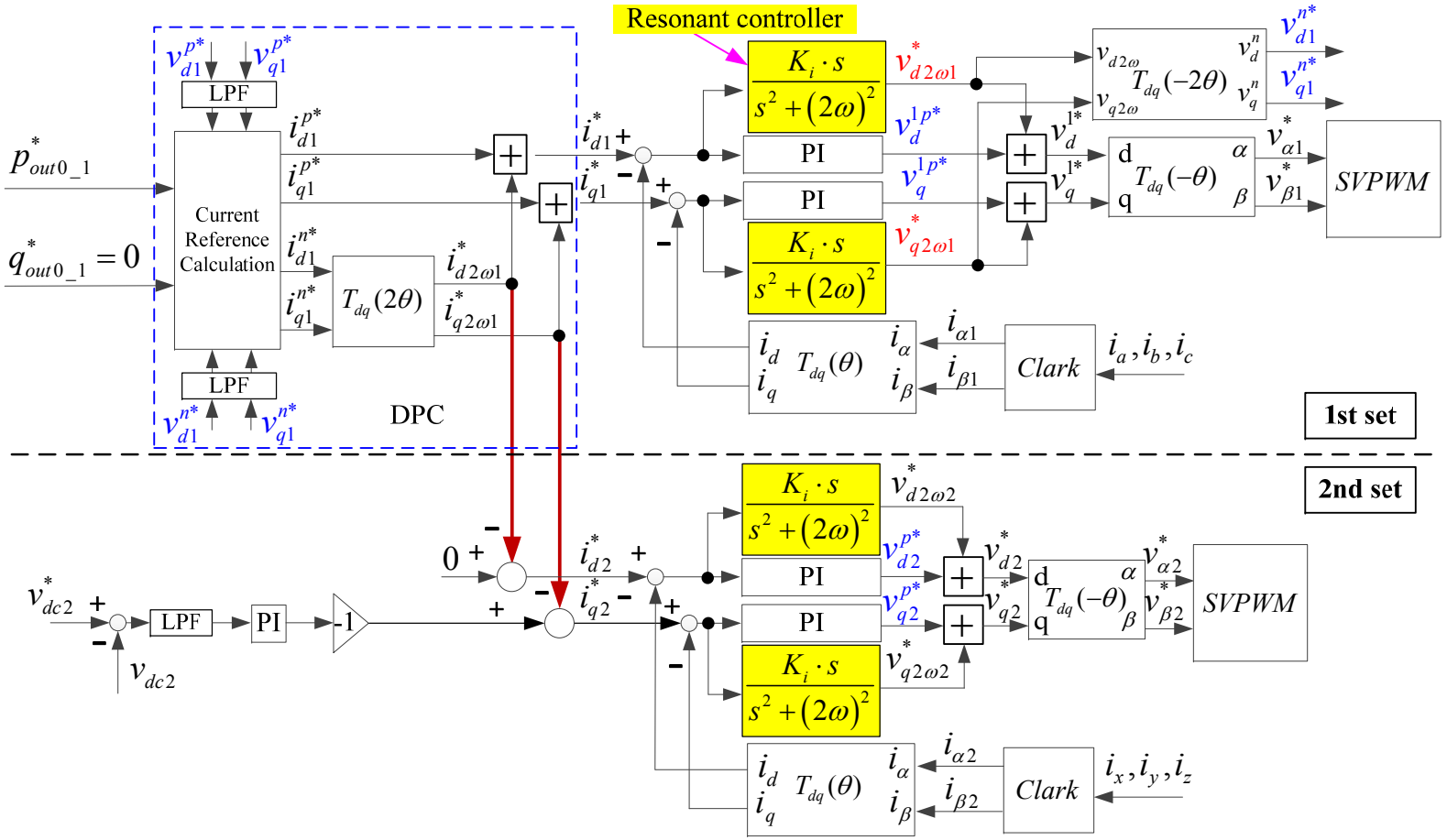

Fig.7.7 Proposed Method 3 of *N*-sequence currents compensation.

7.3.4 Summary

In the proposed three methods in this chapter, only some power relays are required to connect two sets of the machine in parallel in Method 1 and to connect the DC buses in parallel in Method 2. The copper loss is also only the half of that in Chapter 5 and Chapter 6. Meanwhile, the extra hardware investment in Method 1 and Method 2 is much lower. Furthermore, the cost can be further reduced by Method 3 without any hardware investment. However, in terms of control complexity, the methods of compensation in series in Chapter 6 and the proposed Method 1 and Method 2 in this chapter are simpler without any software modifications.

The methods which are applicable to suppress the 2h DC bus voltage and torque ripple in different scenarios of one channel failure can be summarized in TABLE 7.1.

TABLE 7.1 METHODS FOR DIFFERENT SCENARIOS

SCENARIOS	Methods
One faulty set of 3-phase windings	1. Compensation in parallel 2. Compensation in series
One faulty channel of inverter	1. Compensation in parallel 2. Compensation in series 3. Method 1(Two sets in parallel)
One faulty channel of rectifier	1. Compensation in parallel 2. Compensation in series 3. Method 1(Two sets in parallel) 4. Method 2(DC buses in parallel) 5. Method 3(*N*-sequence currents compensation)

7.4 Experiments

The prototype dual 3-phase PMSG is shown in Fig.B.2 and the design parameters are shown in TABLE B. 1. The measured no-load inductances of the first set and of the two sets in parallel at the frequency of 120Hz are shown in Fig.C.1 and Fig.C.2 respectively. As can be seen from Fig.C.1(a) and corresponding harmonic analysis Fig.C.1(b), it is apparent that the mutual inductances are unbalanced as the average mutual inductance M_{AB} is not equal to average mutual inductance M_{CA} and M_{BC}. When the two sets are in parallel, it can be seen from the measured inductances Fig.C.2(a) and corresponding harmonic analysis Fig.C.2(b) that the asymmetry of the mutual inductances is much smaller.

The test rigs for Methods 1, 2 and 3 are illustrated in Fig.7.8(a), (b) and (c) respectively. The prototype dual 3-phase PMSG is coupled with a servo machine, which is used to simulate the wind turbine. The servo machine is driven by the Siemens servo drive S120. In this case study, the second rectifier in Fig.7.6 is assumed to be failed. Therefore, the second channel cannot transfer the power generated by the dual 3-phase PMSG to grid side anymore. In the first channel, to simulate the first rectifier transferring the power from the DC bus capacitors to the grid side, a power resistor R_L (100Ω) is used to consume the power generated by the PMSG. In the second channel in Fig.7.8, R_1 and R_2 are balancing resistors to balance the voltages of DC bus capacitors.

It is worth noting that the number of pole pairs of the prototype machine is 16, therefore, the 32nd harmonic in the following harmonic analyses based on the mechanical frequency indicates the 2h component in electrical frequency.

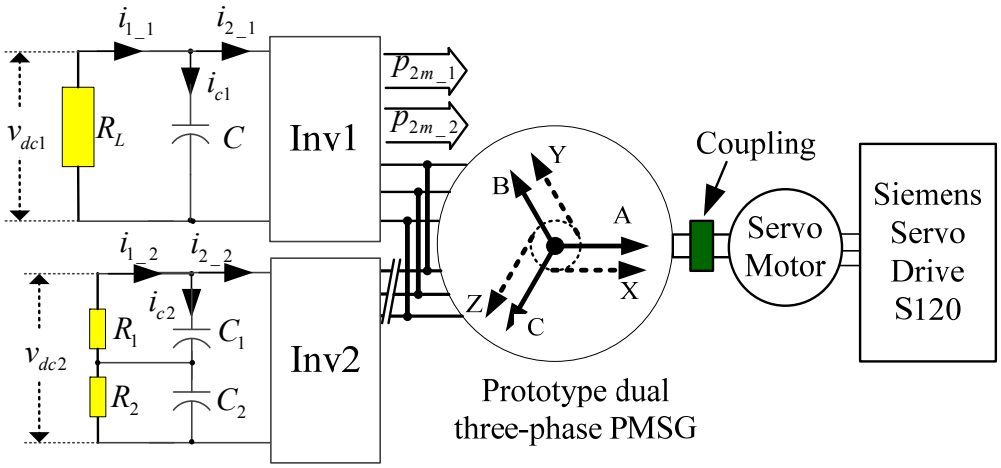

(a)

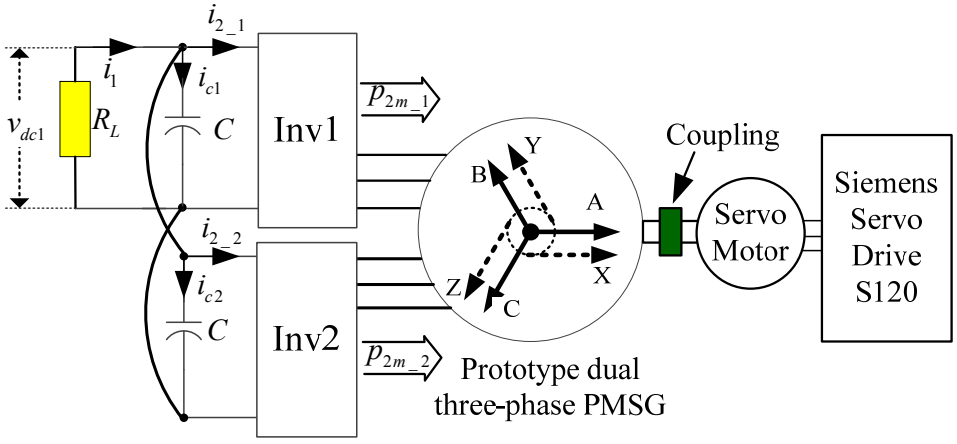

(b)

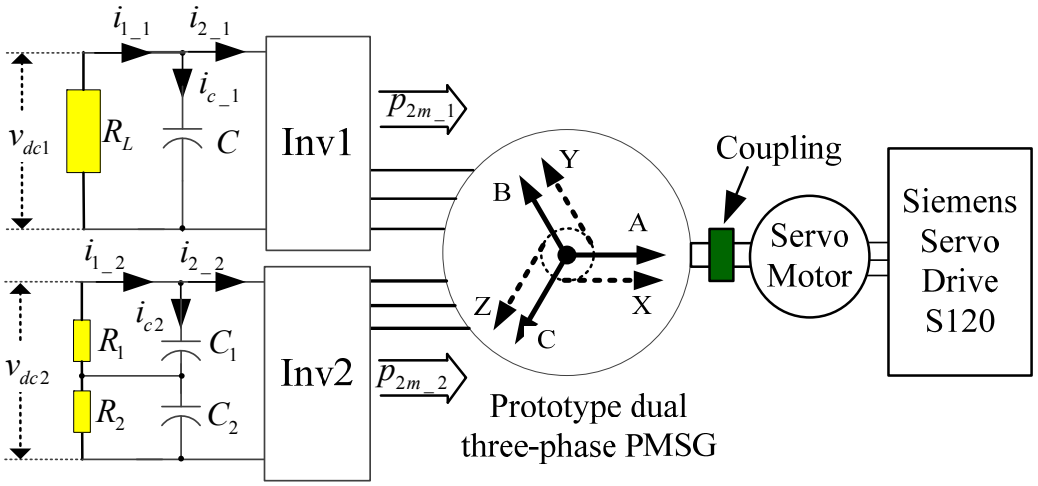

(c)

Fig.7.8 Illustration of test rig. (a) Method 1- Two sets in parallel. (b) Method 2 – DC buses in parallel. (c) Method 3- *N*-sequence current compensation.

7.4.1 Method 1- Two Sets in Parallel

As the two sets of 3-phase wingdings are connected in parallel in this method, the dual 3-phase PMSG can be treated as a single 3-phase PMSG. Therefore, those current control strategies for single 3-phase machine can be employed here. In this experiment, the balanced current control PI-R in PSRF is employed and the *q*-axis current reference is -4A. The speed is regulated to 60rpm by the servo machine.

The experimental results of Method 1 are shown in Fig.7.9. As only one inverter works and the two sets of 3-phase windings are connected in parallel, the inverter currents (the sum currents of two sets) rather than the phase currents in each set are measured. The inverter currents are shown in Fig.7.9(a), which is twice of the phase currents in each set in the Method 2, Fig.7.10(a). The sum of *dq*-axis currents of each set are shown in Fig.7.9(b), where there are no 2h currents, and consequently, the 2h torque in Fig.7.9(e) is insignificant. The sum of instantaneous power generated by the two sets is shown in Fig.7.9(c), which is twice of the power of each set in Method 2, Fig.7.10(c). As almost no 2h power generated by the two sets in parallel, Fig.7.10(c), the 2h DC bus voltage in Fig.7.10(d) is negligible.

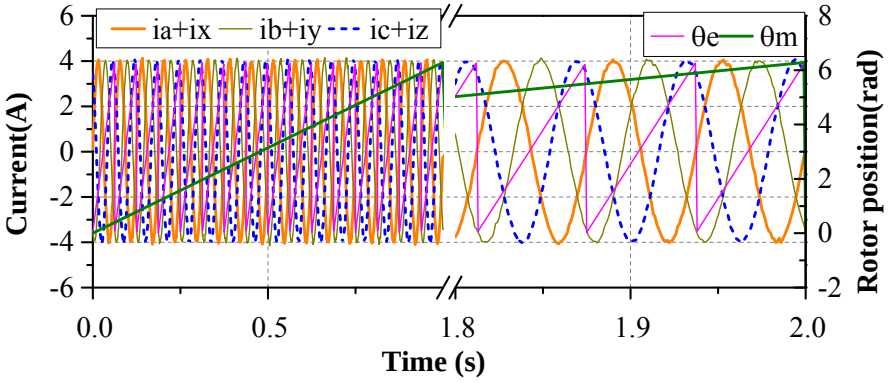
ia+ix
ib+iy
ic+iz
θe
θm
Current(A)
Rotor position(rad)
Time (s)

(a)

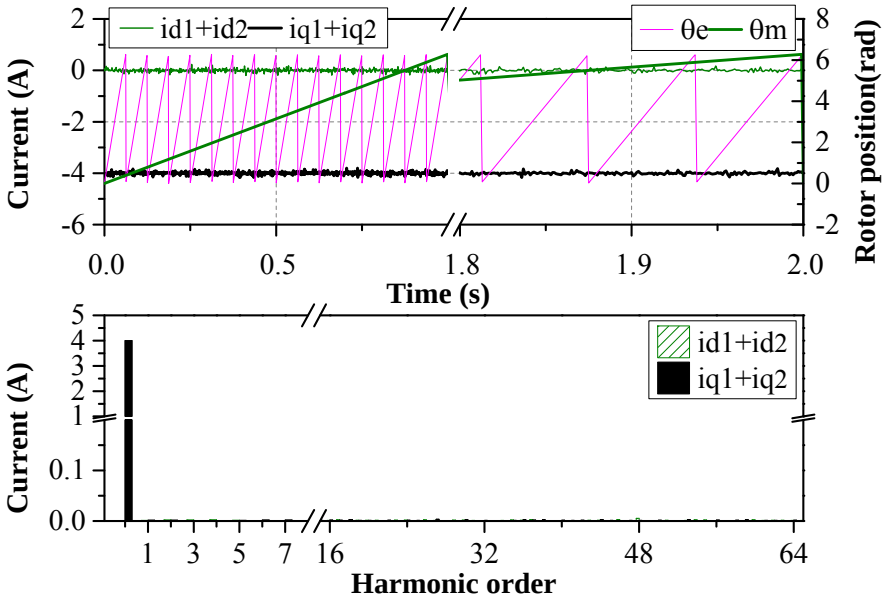
id1+id2
iq1+iq2
θe
θm
Current (A)
Rotor position(rad)
Time (s)
id1+id2
iq1+iq2
Current (A)
Harmonic order

(b)

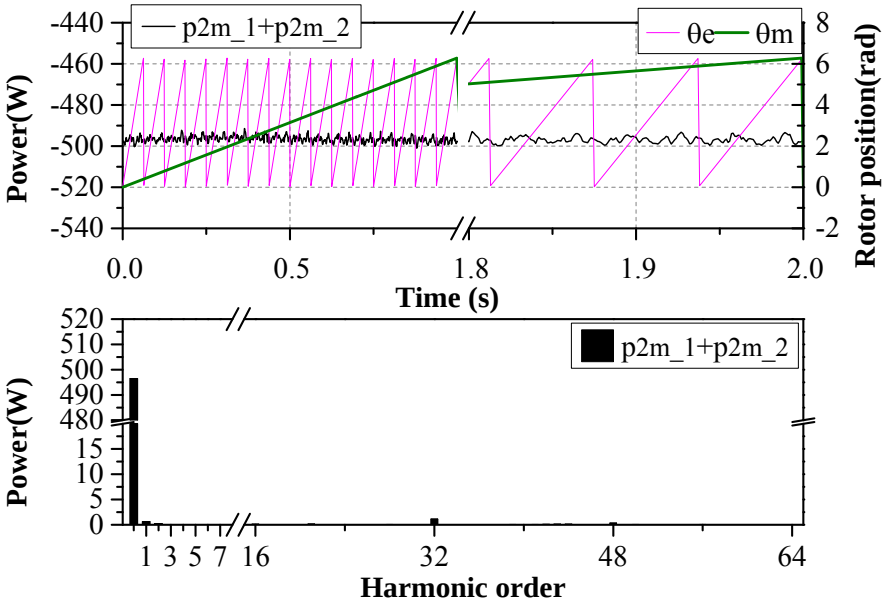
p2m_1+p2m_2
θe
θm
Power(W)
Rotor position(rad)
Time (s)
p2m_1+p2m_2
Power(W)
Harmonic order

(c)

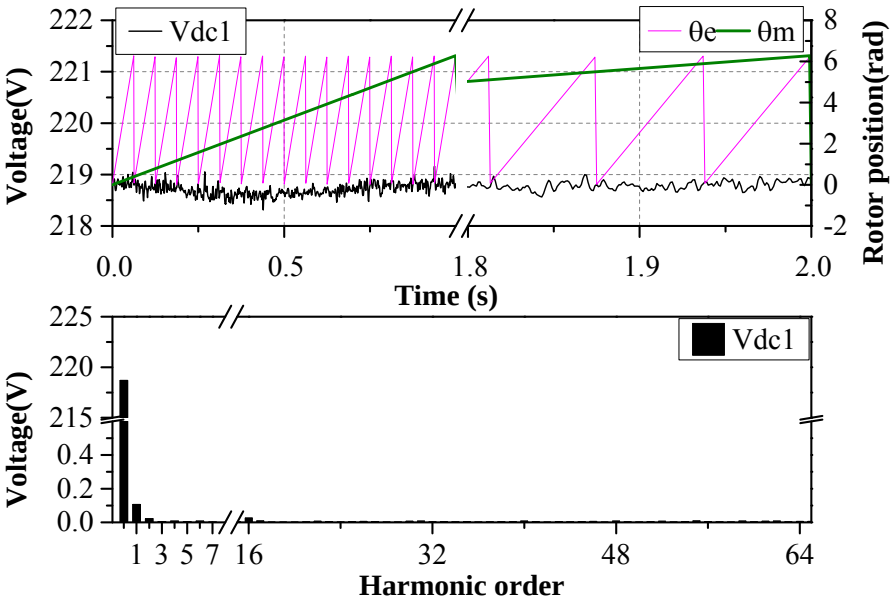

(d)

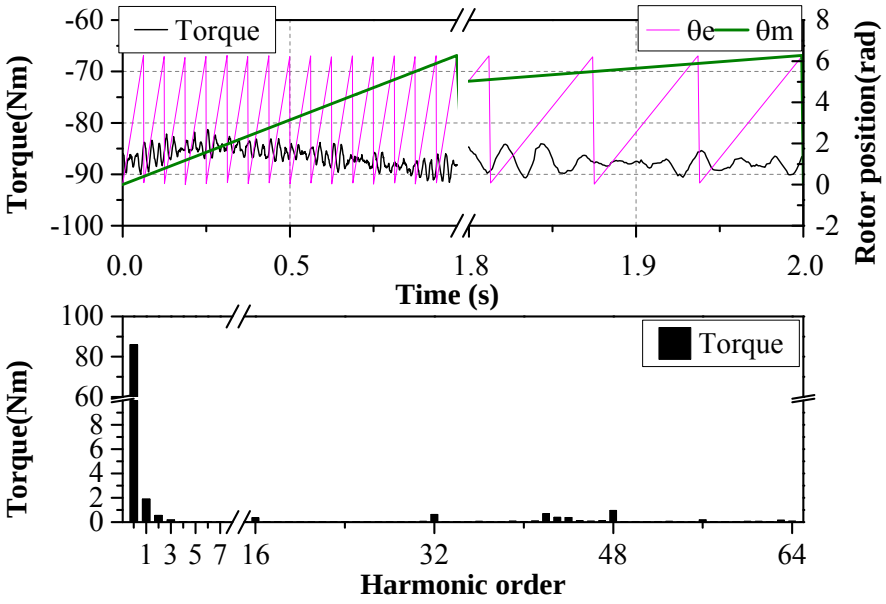

(e)

Fig.7.9 Experimental results with Method 1. (a) Phase currents. (b) Currents in *dq*-frame. (c) Power. (d) DC bus voltage. (e) Torque.

7.4.2 Method 2- Two DC Buses in Parallel

In this experiment, the speed is regulated to 60rpm by the servo machine. The 2-individual current control [163], which controls the *dq*-axis current for each set individually, is applied to the dual 3-phase PMSG. The drive works in balanced current control mode, where the PI-R control in PSRF is employed for each set. As there are two inverters working together in

Method 2, to achieve the equivalent power as that in Method 1, the current reference for each inverter is -2A in Method 2.

The experimental results of Method 2 are shown in Fig.7.10. The phase currents in Fig.7.10(a) shows that the currents of each set are equal to each other. The *dq*-axis currents are shown in Fig.7.10(b), where the 2h currents in *dq*-frame are negligible. Since the two sets have same currents, the instantaneous power of the first set is equal to that of the second set, Fig.7.10(c). As the 2h power in each set is negligible, Fig.7.10(c), the total 2h power flowing into the DC bus is trivial, and therefore, the 2h DC bus voltage in Fig.7.10(d) is insignificant. As there are no *N*-sequence currents in the two sets of 3-phase windings, the 2h torque in Fig.7.10(e) is also suppressed effectively.

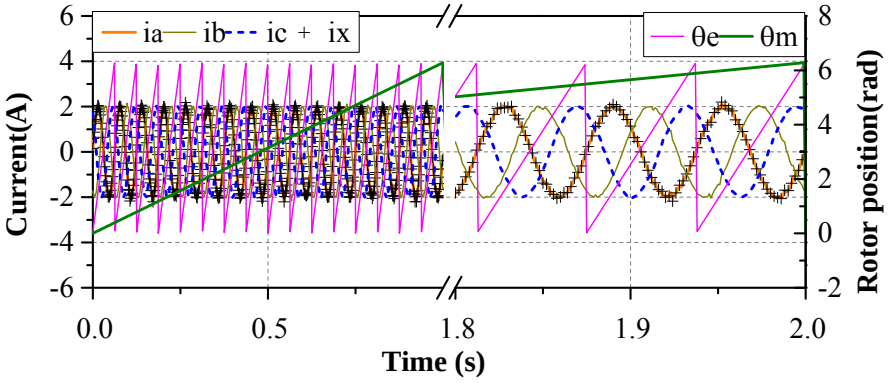

(a)

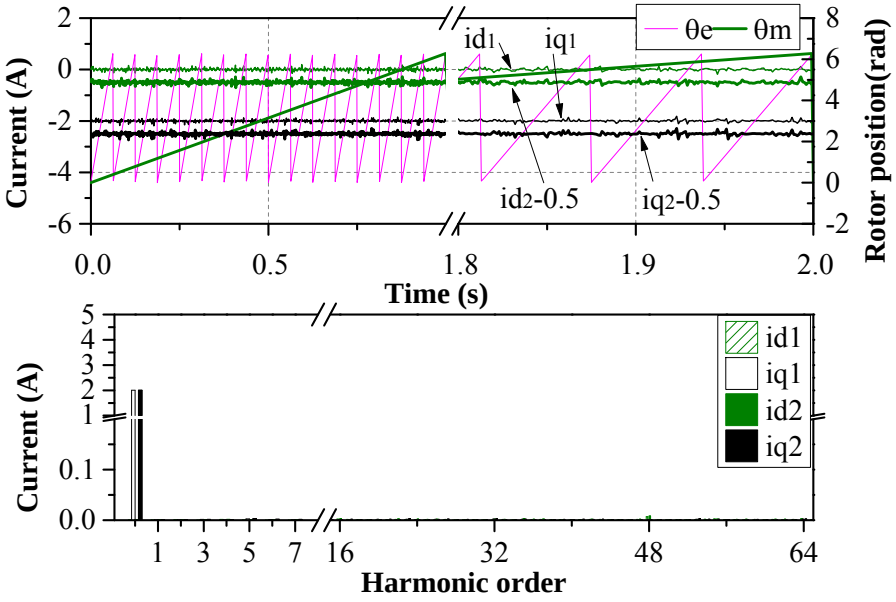

(b)

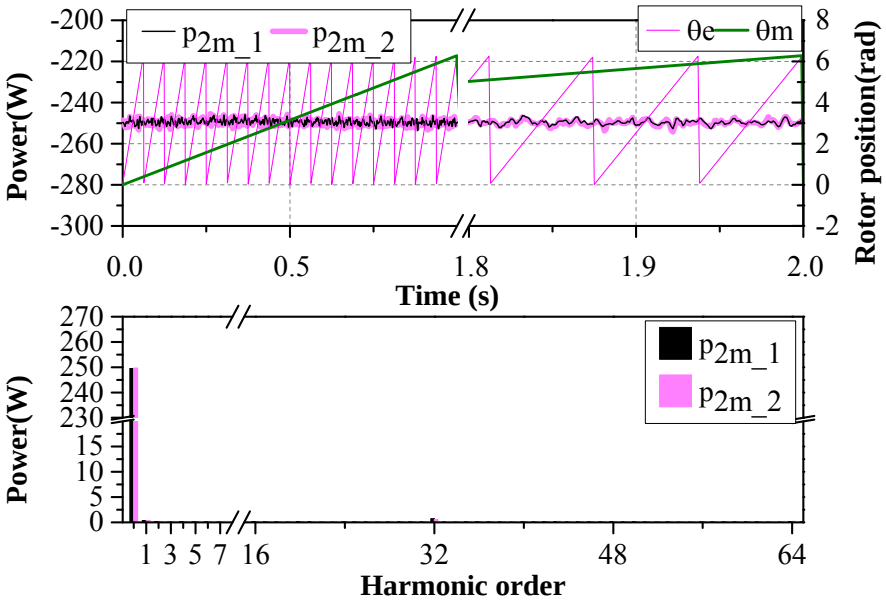
p2m_1
p2m_2
θe
θm
Power(W)
Rotor position(rad)
Time (s)
Harmonic order

(c)

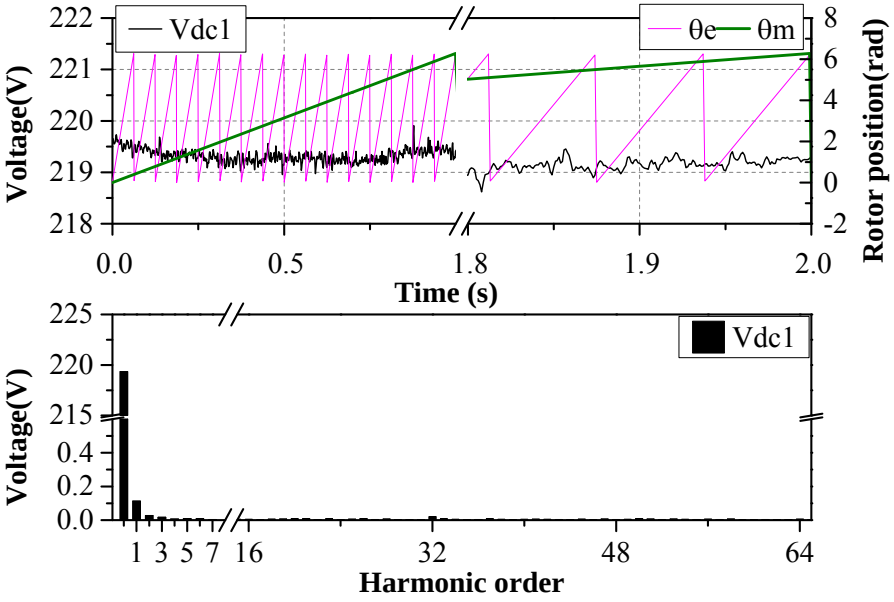
Vdc1
θe
θm
Voltage(V)
Rotor position(rad)
Time (s)
Harmonic order

(d)

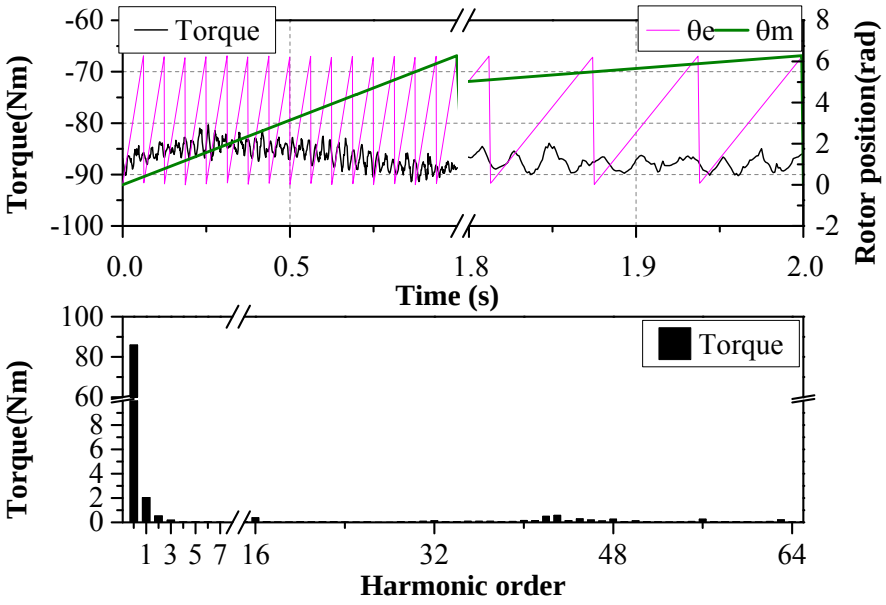

(e)

Fig.7.10 Experimental results with Method 2. (a) Phase currents. (b) Currents in *dq*-frame. (c) Power. (d) DC bus voltage. (e) Torque.

7.4.3 Method 3- *N*-sequence Currents Compensation

In this experiment, the speed is regulated to 60rpm by the servo machine. The first drive works in constant power control mode with instantaneous power control and the power reference $p_{out0\_1}^{*}$ in Fig.7.7 is -400W. The second drive works in constant DC-bus voltage control mode and the DC bus voltage reference is 200V in this case study. The experimental results of the first set and the second set are shown in Fig.7.11 and Fig.7.12 respectively.

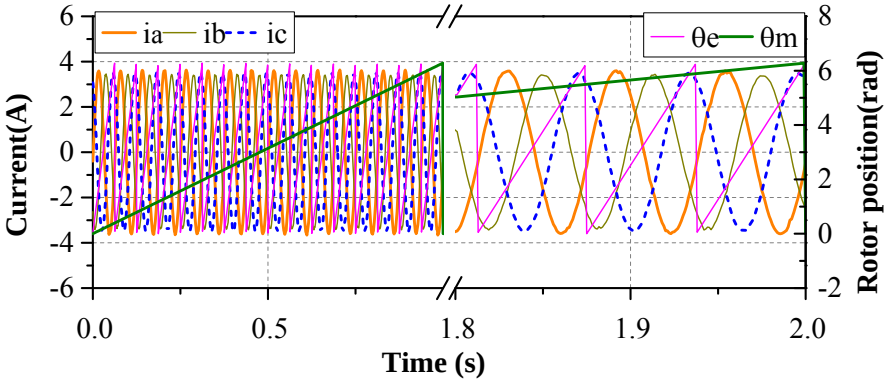

(a)

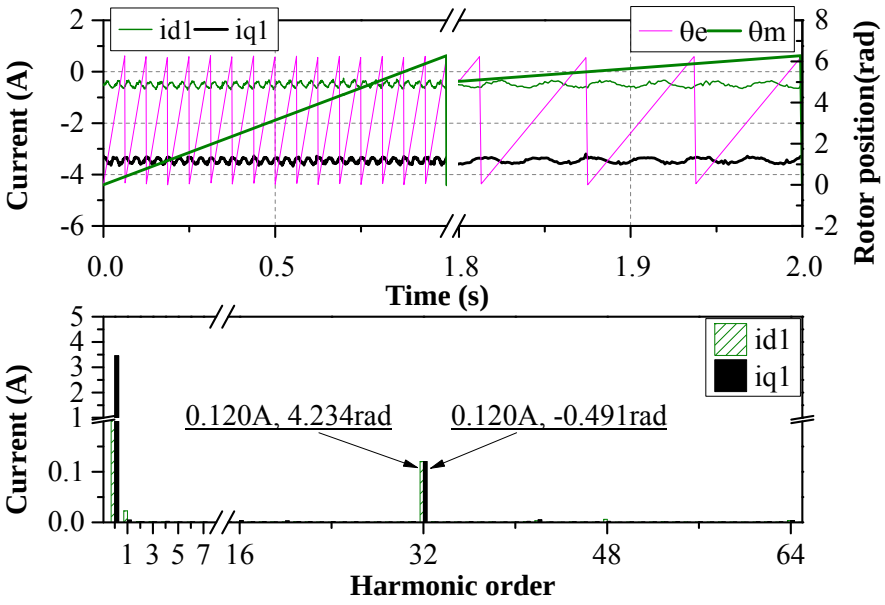
id1
iq1
θe
θm
Current (A)
Rotor position(rad)
Time (s)
id1
iq1
0.120A, 4.234rad
0.120A, -0.491rad
Current (A)
Harmonic order

(b)

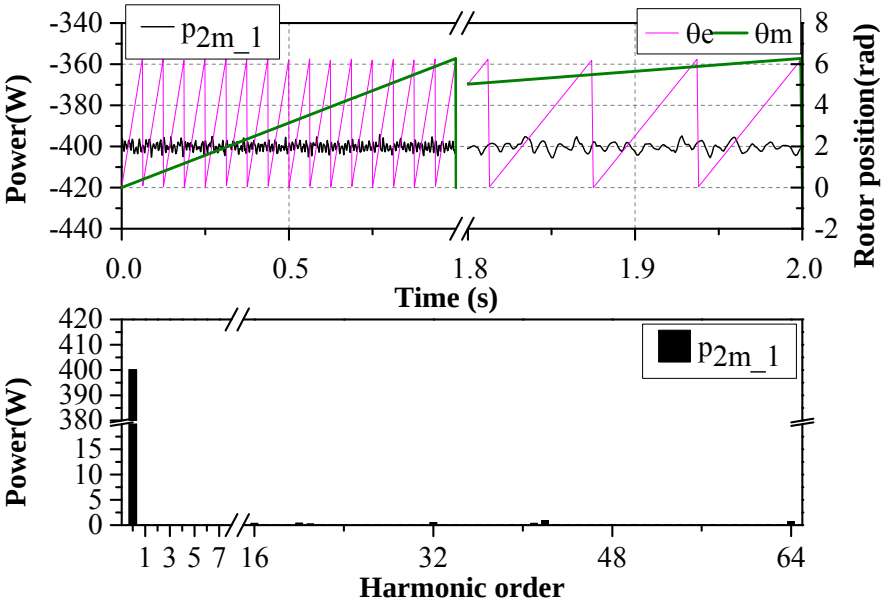
p2m_1
θe
θm
Power(W)
Rotor position(rad)
Time (s)
p2m_1
Power(W)
Harmonic order

(c)

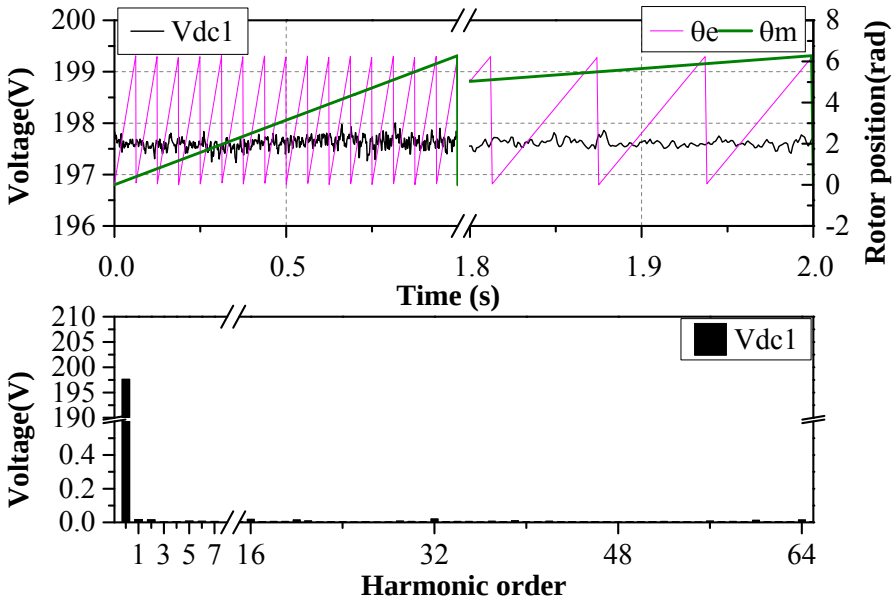

(d)

Fig.7.11 Experimental results of the 1st inverter with proposed Method 3. (a) Currents in *abc*-frame. (b) Currents in *dq*-frame. (c) Power. (d) DC bus voltage.

As the *N*-sequence currents are involved in the instantaneous power control, the phase currents of the first set are slightly unbalanced in Fig.7.11(a). In terms of the *dq*-axis currents, there are apparent 2h currents in Fig.7.11(b). As shown in Fig.7.11(c), the instantaneous active power is around -400W, according to the corresponding harmonic analysis, the 2h power is negligible, which shows that the power is regulated fairly well by the instantaneous power control. Consequently, the 2h DC bus voltage V_{dc1} in the first channel, Fig.7.11(d), is suppressed as well. Since the 2h power flowing towards the DC bus has been suppressed, the current THD of grid side will be not ruined.

The phase currents of the second set are shown in Fig.7.12(a). It can be seen that the current of phase X lags that of the phase Y, that means the N-sequence currents rather than the *P*-sequence currents in the second set are dominant. From the *dq*-axis currents in Fig.7.12(b), it can be seen that the amplitude of 2h currents are the same as that in the first set in Fig.7.11(b). However, the 2h currents in the first set and the second set are anti-phase. Therefore, the total 2h currents can be cancelled. As the *N*-sequence currents are injected into the second set, it can be seen that there is apparent 2h power in Fig.7.12(c), consequently, there is obvious 2h DC bus voltage in V_{dc2}, Fig.7.12(d).

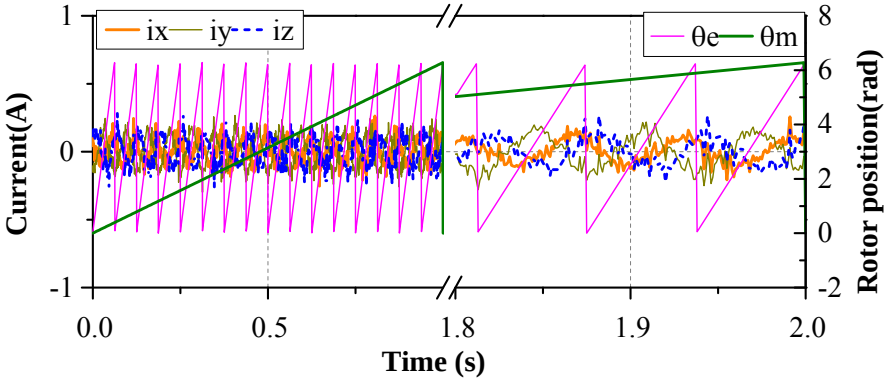
ix
iy
iz
θe
θm
Current(A)
Rotor position(rad)
Time (s)

(a)

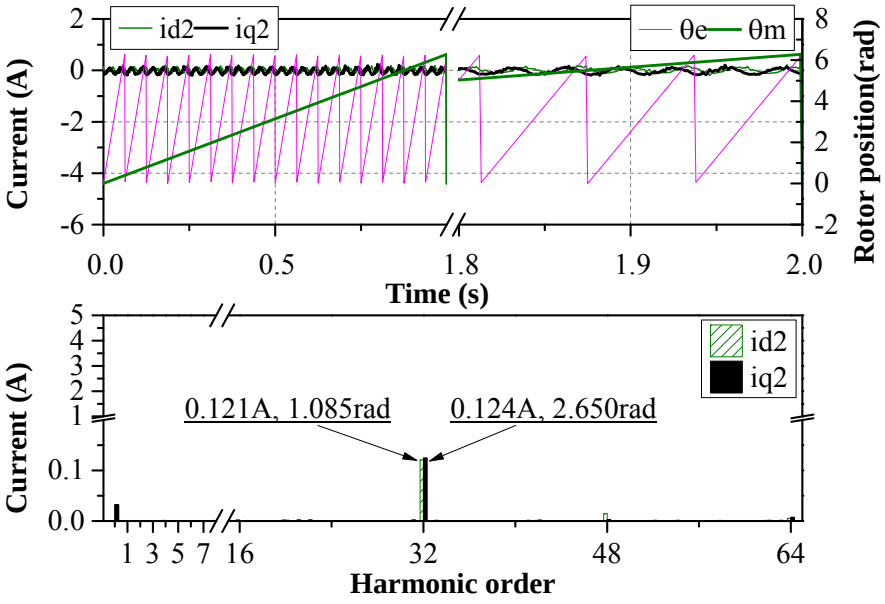
id2
iq2
θe
θm
Current (A)
Rotor position(rad)
Time (s)
0.121A, 1.085rad
0.124A, 2.650rad
Harmonic order

(b)

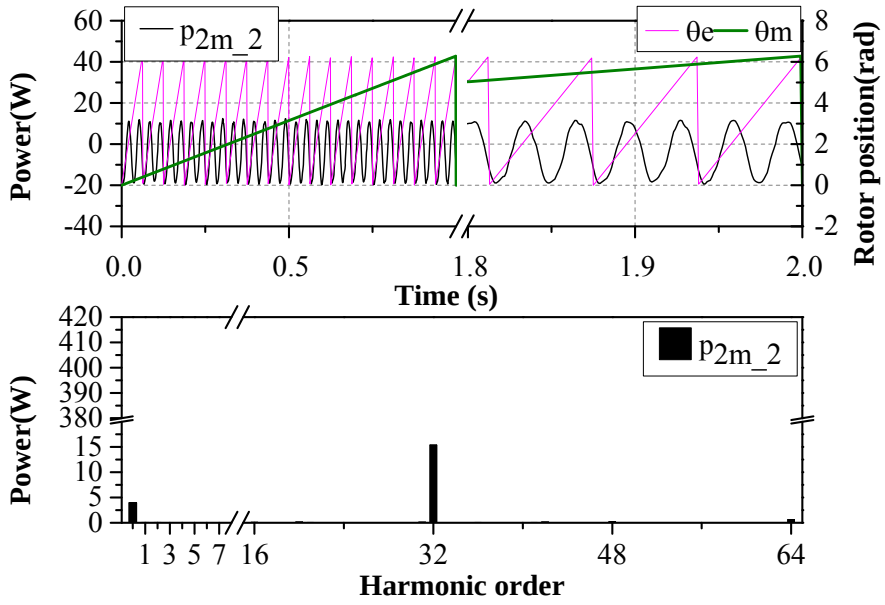
p2m_2
θe
θm
Power(W)
Rotor position(rad)
Time (s)
Harmonic order

(c)

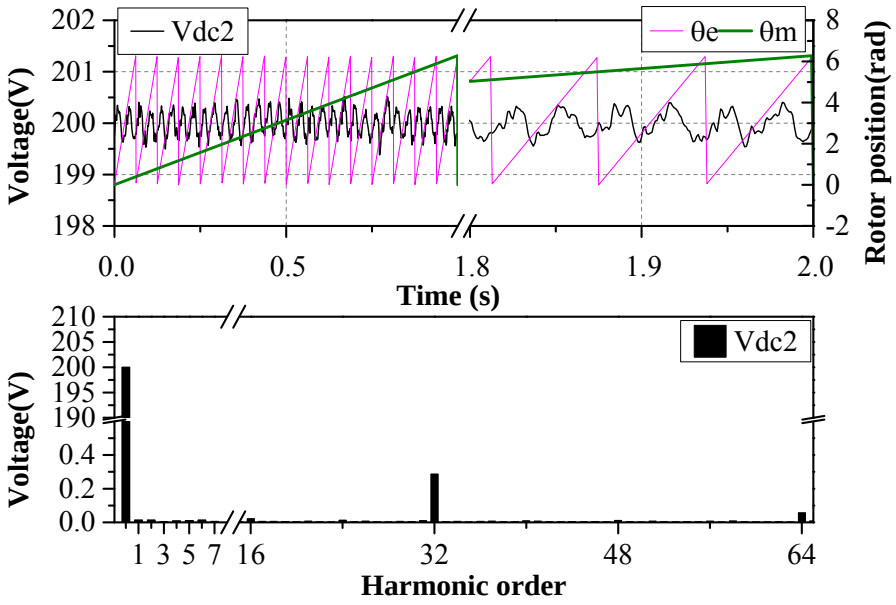

(d)

Fig.7.12 Experimental results of the 2nd inverter with proposed Method 3. (a) Phase currents. (b) Currents in *dq*-frame. (c) Power. (d) DC bus voltage.

The torque of the first set with instantaneous power control is shown in Fig.5.6(d). For the convince of discussion, it is repeated here as Fig.86(a). The measured torque with the proposed Method 3 is shown in Fig.7.13(b). As the *N*-sequence currents in the first set are compensated by the *N*-sequence currents in the second set, the 2h torque generated by the first set is compensated by the 2h torque generated by the second set. Consequently, the 2h torque in total is suppressed effectively, Fig.7.13(b).

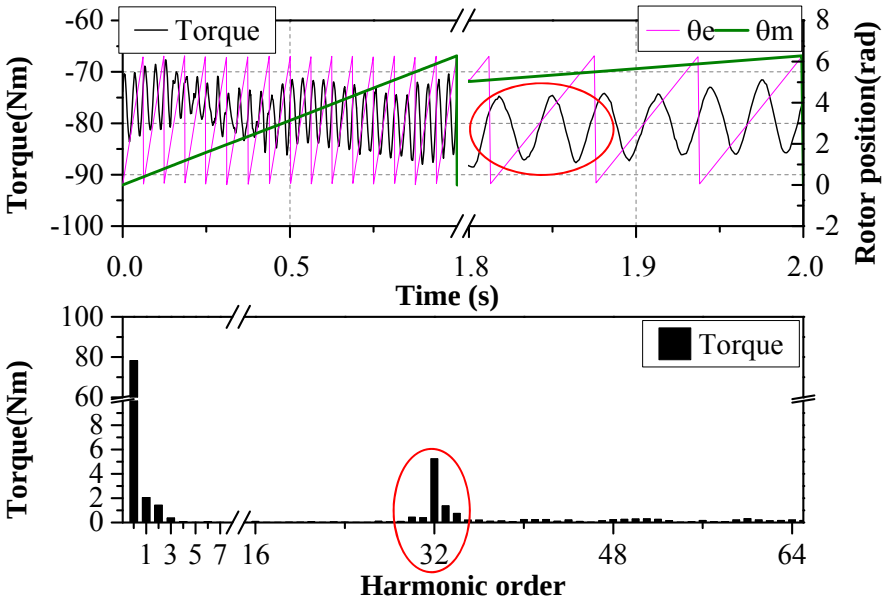

(a)

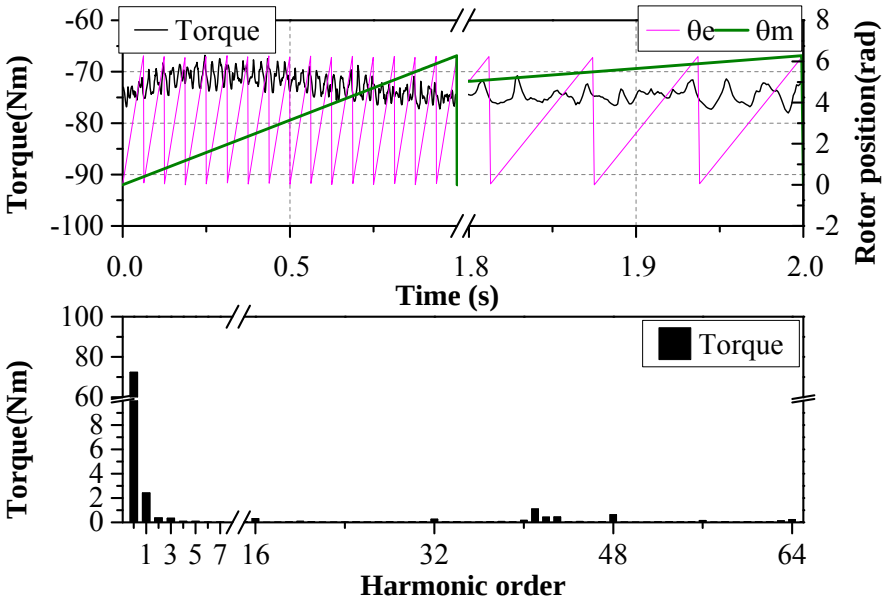

(b)

Fig.7.13 Torque. (a) Single set with instantaneous power control. (b) Proposed Method 3.

The disadvantage of the proposed Method 3 is that there is 2h DC bus pulsation in the DC bus capacitors in the second channel. However, since the 2h DC bus voltage in the first channel is suppressed, the deterioration of current THD of grid side is avoided. Considering the torque ripple is suppressed as well without any hardware investment, the proposed Method 3 is still a competitive method.

7.4.4 Comparison

The measured DC bus voltage and torque with balanced current control and instantaneous power control are shown in Fig.5.5 and Fig.5.6 respectively. As can be seen from the experimental results in Fig.5.5, the 2h torque under balanced current control in Fig.5.5(d) is very small, while the 2h DC bus voltage is significant, Fig.5.5(c). In contrast, the 2h DC bus voltage in instantaneous power control is suppressed effectively, Fig.5.6(c), while the 2h torque is deteriorated significantly, Fig.5.6(d). Neither of these two methods can deal with the 2h DC bus voltage and the 2h torque simultaneously.

As shown in Fig.7.9(d), Fig.7.10(d), and Fig.7.11(d), the 2h DC bus voltage has been suppressed effectively by the proposed Methods 1, 2 and 3 respectively. From the Fig.7.9(e), Fig.7.10(e), and Fig.7.13(b), it can be seen that the 2h torque has been suppressed effectively by the proposed Methods 1, 2 and 3 respectively. Therefore, the proposed methods can suppress the 2h DC bus voltage and torque simultaneously.

7.5 Conclusion

In this chapter, three methods of suppressing the 2h DC bus voltage and torque ripple are investigated when one channel of the dual 3-phase PMSG drive system fails. In Method 1 of two sets of dual 3-phase windings in parallel and Method 2 of DC buses in parallel, the 2h DC bus voltage and torque ripple can be suppressed as the dual 3-phase PMSG can be treated as a balanced single 3-phase PMSG. In the Method 3, with the instantaneous power control applying for the first set of dual 3-phase PMSG, the 2h power and DC bus voltage in the first channel can be suppressed effectively; while the 2h torque generated by the first set is then cancelled by the second set with *N*-sequence currents compensation. With the proposed methods, the 2h DC bus voltage in the first channel can be suppressed without deterioration of current THD of the grid side and the 2h torque is also suppressed effectively.

Chapter 8 General Conclusions

8.1 Introduction

This thesis focuses on the control of asymmetric PMSG system accounting for the 2h torque and 2h DC bus voltage. A comprehensive and systematic investigation has been undertaken. It includes the balanced current control, the improved power control and the 2h power compensation in the asymmetric single 3-phase PMSG system, and finally the research is extended to the asymmetric dual 3-phase PMSG system with one channel failed.

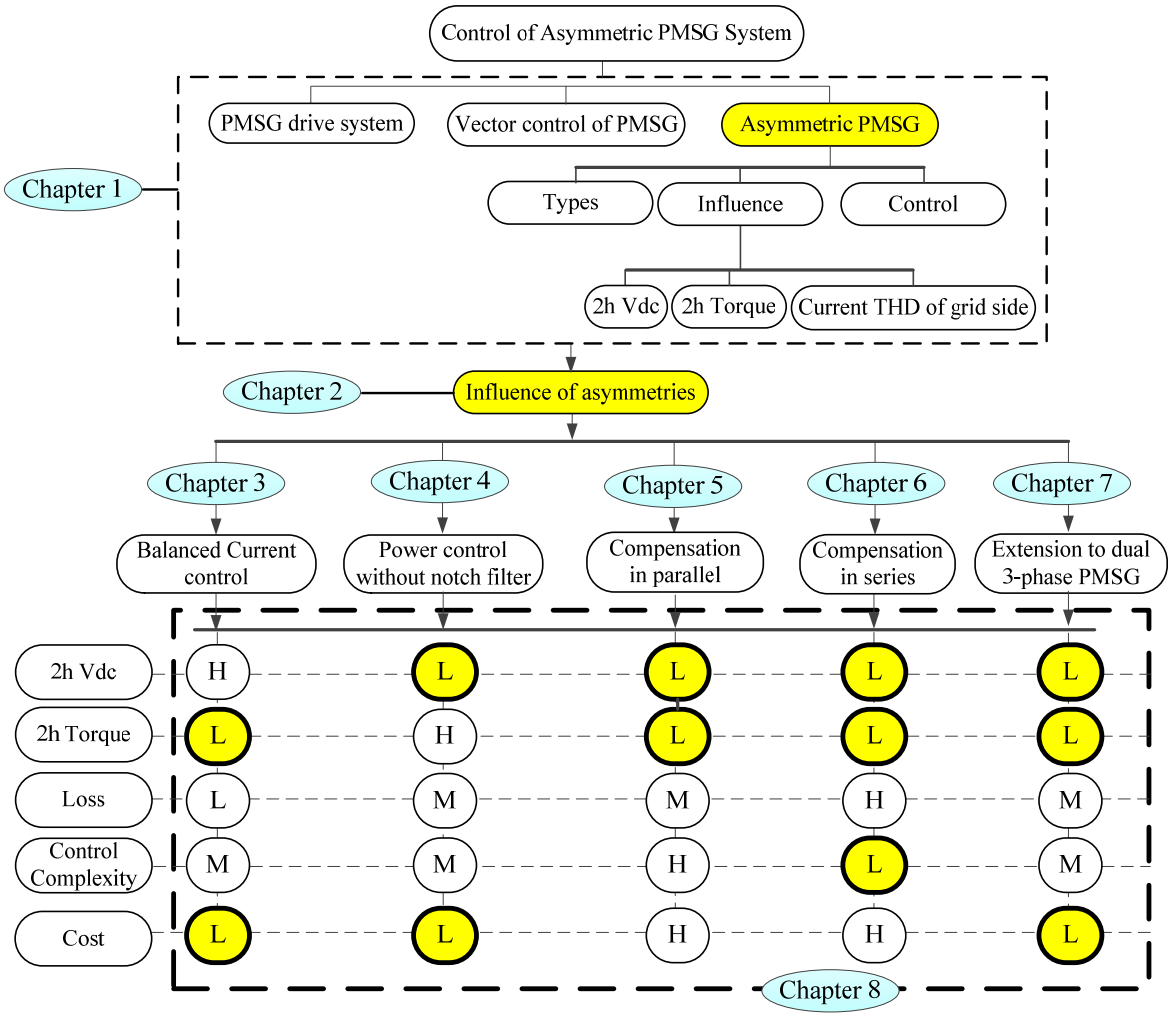

H=High; M=Medium; L=Low

Fig.8.1 Research structure and key features of each method.

From the aspects of the 2h DC bus voltage, 2h torque ripple, copper loss, control complexity and system cost, the brief summary of each control method introduced in this thesis is shown at the bottom of Fig.8.1, where the merits of them are highlighted as yellow.

8.1.1 Current Control of Asymmetric PMSG

The conventional PI current control in *dq*-frame is not applicable to suppress the *N*-sequence currents of asymmetric PMSG due to its limited bandwidth and non-linear impedances in *dq*-frame. Three typical balanced current control methods, including PR control in *αβ*-frame, dual current control, and PI-R control in PSRF are reviewed and evaluated, which can suppress the *N*-sequence currents effectively. The relationship between these methods is revealed for the first time and can be summarized in TABLE 3.2. It can be concluded that

- The conventional current control is not applicable in the asymmetric system for suppressing the *N*-sequence currents;
- PR control in *αβ*-frame, dual current control, and PI-R control in PSRF are all capable of suppressing the *N*-sequence currents;
- The PR control in *αβ*-frame is equivalent to the dual current control in theory;
- The performance of PR control in *αβ*-frame is compromised in practice due to the ideal integral in the resonant control is replaced by an approximated low-pass filter transfer function;
- The proportional gain of dual current control in PSRF and NSRF should be reduced to the half of the proportional gain in PR control in *αβ*-frame and PI-R control in PSRF;
- PR control in *αβ*-frame, dual current control, and PI-R control in PSRF are robust to different asymmetries.

It is worth noting the balanced current control can only be applied to reduce the torque ripple of the asymmetric PMSG with unbalanced impedances. If the 3-phase back-EMFs are unbalanced, the 2h torque ripple can be resulted from the interaction of *P*-sequence currents and *N*-sequence back-EMFs.

The major problem of the balanced current control is that 2h power will be produced and consequently result in the 2h DC bus voltage ripple.

8.1.2 Instantaneous Power Control of Asymmetric PMSG

An improved instantaneous power control without sequential component decomposers is

proposed to suppress the 2h DC bus voltage under generalized unbalanced conditions. The *P*-sequence and *N*-sequence output voltages are essential for the calculation of the *P*- and *N*-sequence current references in the instantaneous power control. In the previous researches, the *P*- and *N*-sequence output voltages were usually extracted by some sequential decomposers, such as the time delaying method, notch filter method, or dual second-order generalized integrator (DSOGI) method, etc. In the proposed method, based on the PI-R($2\omega_e$) control in PSRF to regulate the *P*-sequence current and *N*-sequence currents, the *P*-and *N*-sequence output voltages are simply obtained from the output of the PI controller and resonant controller respectively. With the proposed instantaneous power control, the 2h power and the DC bus voltage can be suppressed effectively under generalized unbalanced conditions. The features of the proposed method can be summarized as

- Effective suppression of the 2h power and DC bus voltage;
- Simple, no sequential component decomposers such as the time delaying method, notch filter method, or dual second-order generalized integrator (DSOGI) method;
- Robust to unbalanced impedances and unbalanced back-EMFs;
- Based on output power control;
- Simple implementation and current reference calculation;

The problem of the proposed method is that it cannot achieve unity input power factor as the back-EMFs are usually unknown in 3-phase PMSG system without the access of neutral point. If the back-EMFs are known, the input-output-power control can be adopted. However, the sequential component decomposers are then required to extract the *P*-sequence and *N*-sequence back-EMFs.

Another problem of the proposed method is that the 2h torque ripple will be resulted from *N*-sequence currents although the *N*-sequence currents in instantaneous power control are helpful to suppress the 2h power.

8.1.3 Control of Asymmetric PMSG (Compensation in Parallel)

By transferring the undesired 2h power from asymmetric PMSG to the compensation unit in parallel with the DC bus rather than the grid side, the 2h DC bus voltage and 2h torque ripple can be suppressed simultaneously without ruining the current THD of grid side. Two power topologies of the compensation unit designated as Topology-*RL* and Topology-*RLE* and corresponding control method have been investigated. The comparison of the Topology-*RL* and the Topology-*RLE* can be summarized in TABLE 5.4 and repeated as follows.

TABLE 8.1

COMPARISON OF TOPOLOGY-*RL* AND TOPOLOGY-*RLE*

Items	Topology-*RL*	Topology-*RLE*
Topology	H-bridge + inductor	Half-bridge + inductor + DC voltage source v_{ess}
Type of energy conversion in the compensation unit	DC/AC	DC/DC
Energy storage device	Inductor	DC voltage source
Type of compensation current	Fundamental (1f)	2f+4f+8f+… in theory 2f if $v_{ess}>>v_{RL}$
Implementation	Complicated	Complicated if $V_{ess} \approx v_{RL}$ Simple if $v_{ess} >> v_{RL}$
Compensation current	Large	Small
Size of inductor	Large	Small

The Topology-*RL* is constructed by full H-bridge switches and a compensation inductor. The main role of the inductor is acting as a passive energy storage device to exchange the 2h power with the DC bus. To compensate the 2h power from PMSG, the compensation current should be fundamental current and the 2h powers from the compensation unit and from PMSG should have same amplitude but anti-phase. Two PI controllers are employed to determine the amplitude and phase angle of the compensation current reference. As the size of inductor depends on the energy stored in the inductor, the inductor could be bulky if the asymmetries are very serve.

The Topology-*RLE* is constructed by half-bridge switches, an inductor, and a DC voltage source. The DC voltage source acts as the storage device which exchanges 2h power with the DC bus. The main role of the inductor acts as current filter rather than storage device. As the voltage of DC voltage source is far higher than the voltage across the inductor, the compensation current is much smaller than that in Topology-*RL*, albeit with the requirement of an extra DC voltage source. Therefore, the size of inductor is smaller than that in Topology-*RL*. Although the second, fourth, eighth,…, harmonic currents should be injected into the compensation unit to thoroughly compensate the 2h power from the PMSG in theory, actually, the 2h current injection is satisfactory as the power generated by the inductor is negligible.

The advantages of compensation in parallel can be summarized as below

- 2nd harmonic power suppressed;
- 2nd harmonic DC bus voltage suppressed;
- 2nd harmonic torque avoided;
- Without deterioration of current THD in grid side;
- Feasible for different impedance asymmetries;
- No involvement of the control in the grid side.

The disadvantages of the compensation in parallel can be listed as

- Extra hardware investment, such as power switches, compensation inductor, DC source, etc.;
- Regulation of compensation current;
- Increased system complexity.

8.1.4 Control of Asymmetric PMSG (Compensation in Series)

The original unbalanced 3-phase PMSG system with asymmetric impedances (unbalanced resistances, unbalanced self-inductances, or even unbalanced mutual inductances) can be modified to balanced system by adding an unbalanced 3-phase *RL* network connected in series with the PMSG. From the perspective of 2h inductances in *dq*-frame, the 2h impedances of the PMSG are cancelled by the 2h impedances of the introduced unbalanced *RL* network. From the perspective of 2h power, the 2h power generated by the PMSG is compensated by the 2h power generated by the introduced unbalanced *RL* network. Therefore, the *N*-sequence currents and the 2h power due to the system asymmetries can be suppressed naturally without any software modifications.

The advantages of compensation in series can be summarized as below

- 2nd harmonic power suppressed;
- 2nd harmonic DC bus voltage suppressed;
- 2nd harmonic torque not ruined;
- Without ruining current THD in grid side;
- No extra power switches;
- No compensation current regulation;
- No software modification;
- Robust under different load and at different speeds.

The disadvantages of compensation in series can be summarized as below

- Extra hardware such as two external inductors in the compensation unit;
- Slightly affected by the non-linearity of compensation inductor;
- Compensation effect may be compromise by the saturation of PMSG.

8.1.5 Control of Asymmetric Dual 3-Phase PMSG System with One Channel Failed

To suppress the 2h DC bus voltage and 2h torque ripple in the dual 3-phase PMSG system with one channel failed, the compensation in parallel in Chapter 5 and the compensation in series in Chapter 6 can be employed if the faulty channel is disconnected. In addition, three more methods, i.e. the dual sets in parallel, DC buses in parallel and *N*-sequence currents compensation, are investigated for reduced cost. It has been verified that these three methods are also applicable to suppress the 2h DC bus voltage and the 2h torque ripple simultaneously. Method 1 of two sets in parallel and Method 2 of DC buses in parallel only require power relays to connect the two sets or two DC buses together. Meanwhile, they do not require any software modification. Method 3 of *N*-sequence currents compensation does not require any hardware investment at all. The comparisons of these different methods can be listed in TABLE 8.2.

TABLE 8.2

COMPARISON OF DIFFERENT METHODS

Compensation	Hardware	Software	Cost
Compensation in parallel (Topology-*RL*)	1. H-bridge switches 2. Inductor 3. Power relays	Compensation current regulation	High
Compensation in parallel (Topology-*RLE*)	1. Half-bridge switches 2. Inductor 3. DC voltage source 4. Power relays	Compensation current regulation	High
Compensation in series	1. 2 inductors 2. Power relays	No	High
Method 1 (Two sets in parallel)	Power relays	No	Low
Method 2 (DC buses in parallel)	Power relays	No	Low
Method 3 (*N*-sequence currents compensation)	No	*N*-sequence current compensation	No

8.2 Future work

In this thesis, to suppress the 2h DC bus voltage and torque ripple without deterioration of current THD of grid side, the unbalanced impedances of asymmetric PMSG is accounted. However, how to suppress the 2h DC bus voltage and torque ripple when the back-EMFs are unbalanced is not investigated. As the back-EMFs are usually unknown without the access of the neutral point in reality, it will be a very challenge work without the information of back EMFs.

The 2h power in the DC bus compensated by the compensation unit in parallel has been investigated. In theory, the compensation principle can be extended to other harmonics that are not investigated in this thesis.

Usually, the flux-weakening control utilizes the output voltages to determinate the flux-weakening current in the flux-weakening current control. As the voltages of asymmetric PMSG are unbalanced, how to deal with the unbalanced voltages in flux-weakening control will be an interesting and challenge work.

Therefore, the proposed future research can be summarized as

- Suppress the torque ripple when the back-EMFs are unbalanced;
- Other power harmonics compensated in parallel;
- Flux-weakening control of asymmetric PMSG;

Appendix A. Coordinate Transformation for 3-Phase System

The relationship between the stationary reference frame $\alpha\beta$-frame and the 3-phase coordinate system frame (*abc*-frame) in single 3-phase system is shown in Fig.A.1, which can be expressed as

$$F_{\alpha\beta} = \frac{2}{3}\left(F_a + F_b e^{j2\pi/3} + F_b e^{j4\pi/3}\right) = F_\alpha + jF_\beta \tag{A.1}$$

where F_a, F_b, and F_c represent the phase components in abc-frame respectively, F_α and F_β are the α-axis and β-axis components, which can be obtained by the phasor projected to $\alpha\beta$-frame.

According to the vector control theory for 3-phase machine, the components in *abc*-frame can be converted to components in $\alpha\beta$-frame by Clark transformation, which can be expressed as

$$\begin{bmatrix} F_\alpha \\ F_\beta \end{bmatrix} = T_{\alpha\beta} \begin{bmatrix} F_a \\ F_b \\ F_c \end{bmatrix} \tag{A.2}$$

where

$$T_{\alpha\beta} = \frac{2}{3}\begin{bmatrix} 1 & \cos(4\theta_s) & \cos(8\theta_s) \\ 0 & \sin(4\theta_s) & \sin(8\theta_s) \end{bmatrix} \tag{A.3}$$

where $\theta_s = \pi/6$. The inverse Clark transformation can be expressed as

$$\begin{bmatrix} F_a \\ F_b \\ F_c \end{bmatrix} = T_{\alpha\beta\_inv} \begin{bmatrix} F_\alpha \\ F_\beta \end{bmatrix} \tag{A.4}$$

where

$$T_{\alpha\beta\_inv} = \begin{bmatrix} 1 & 0 \\ \cos(4\theta_s) & \sin(4\theta_s) \\ \cos(8\theta_s) & \sin(8\theta_s) \end{bmatrix} \tag{A.5}$$

The relationship between $\alpha\beta$-frame and *dq*-frame is shown in Fig.A.2. By applying standard Park transformation to variables in $\alpha\beta$ frame, the projection of phasor $F_{\alpha\beta}$ on the *d*-axis and *q*-axis of *dq*-frame can be expressed as (A.6)

$$\begin{bmatrix} F_d \\ F_q \end{bmatrix} = T_{dq}(\theta) \begin{bmatrix} F_\alpha \\ F_\beta \end{bmatrix} \tag{A.6}$$

where

$$T_{dq}(\theta)=\begin{bmatrix}\cos(\theta) & \sin(\theta)\\ -\sin(\theta) & \cos(\theta)\end{bmatrix} \tag{A.7}$$

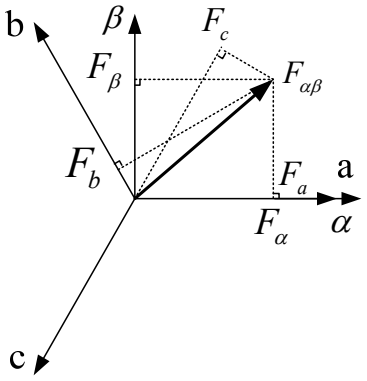

Fig.A.1 Clark transformation.

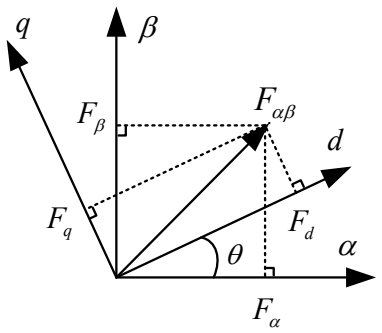

Fig.A.2 Park transformation.

(A.6) can also be rewritten as

$$F_{dq}=e^{-j\theta}F_{\alpha\beta} \tag{A.8}$$

where

$$F_{dq}=F_d+jF_q \tag{A.9}$$

$$F_{\alpha\beta}=F_\alpha+jF_\beta \tag{A.10}$$

The inverse Park transformation can be expressed as

$$\begin{bmatrix}F_\alpha\\ F_\beta\end{bmatrix}=T_{dq}(\theta)^{-1}\begin{bmatrix}F_d\\ F_q\end{bmatrix} \tag{A.11}$$

where

$$T_{dq}(\theta)^{-1}=T_{dq}(-\theta)=\begin{bmatrix}\cos(\theta) & -\sin(\theta)\\ \sin(\theta) & \cos(\theta)\end{bmatrix} \tag{A.12}$$

(A.11) can also be rewritten as

$$F_{\alpha\beta}=e^{j\theta}F_{dq} \tag{A.13}$$

Appendix B. Description of Test Rig

The experiment system is constructed based on dSPACE DS1006 control system, which is suitable for rapid research development and prototype verification. The setup of whole experiment test system is shown in Fig.B.1. The analog signals from current sensor, torque transducer and DC bus voltage sensor are converted to digital signals by the DS2004 high-speed A/D board, and then transferred to the DS1006 processor board. The DS3001 incremental encoder board is in charge of measuring the rotor position from the encoder and then sends the information to DS1006 processor board. Therefore, through the DS2004 and DS3001, the DS1006 gets all the information such as rotor position, currents, and DC bus voltage which are necessary for vector control. To output desired voltages, the DS1006 processor board outputs PWM duty to DS5101 module, which will generate six channels of PWM signals according to the received PWM duty, and then the inverter will output PWM voltages according to the PWM signals received.

The test rig is shown in Fig.B.2. The prototype asymmetric PMSG is coupled with a servo machine driven by the Siemens servo drive S120, which is used to simulate the wind turbine. The encoder MHGE 400 with hollow shaft is employed to measure the rotor position and speed, while the torque transducer is employed to measure the PMSG's torque. A power resistor R_L (100 Ω) is parallel with the DC bus in each set to consume the power generated by the generator.

The prototype PMSG is a dual 3-phase PMSM with 96 slots/32 poles and zero shifted angle between two sets of 3-phase windings. The corresponding winding topology is shown in Fig.B.3, where the first and second winding sets are denoted by the solid and dotted line respectively. When the two sets are healthy and work together with the same current in each set, the dual 3-phase PMSG can be treated as a symmetrical single 3-phase machine with two branches in parallel. However, when one set fails, e.g. the second set fails and only the first set (A1,B1,C1) keeps working, the winding topology is asymmetric, which results in unbalanced mutual inductances as shown in Appendix C.

In the experiments in Chapter 3, Chapter 4, Chapter 5, and Chapter 6, to verify the research on single 3-phase PMSG, the second set of 3-phase windings in the prototype dual 3-phase PMSG is disconnected deliberately.

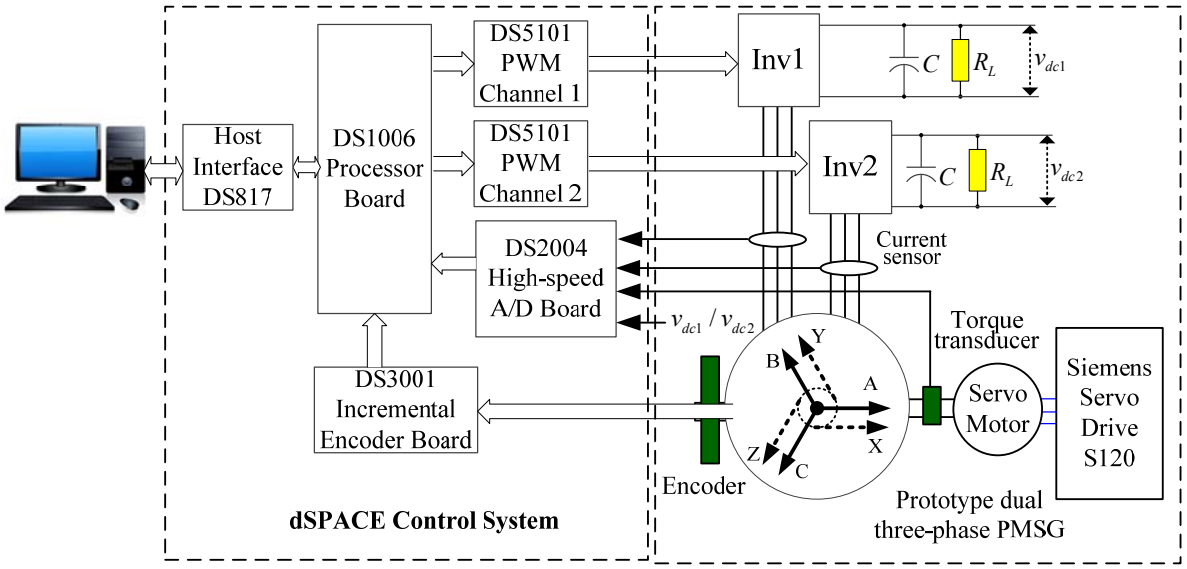

Fig.B.1 Setup of experimental system.

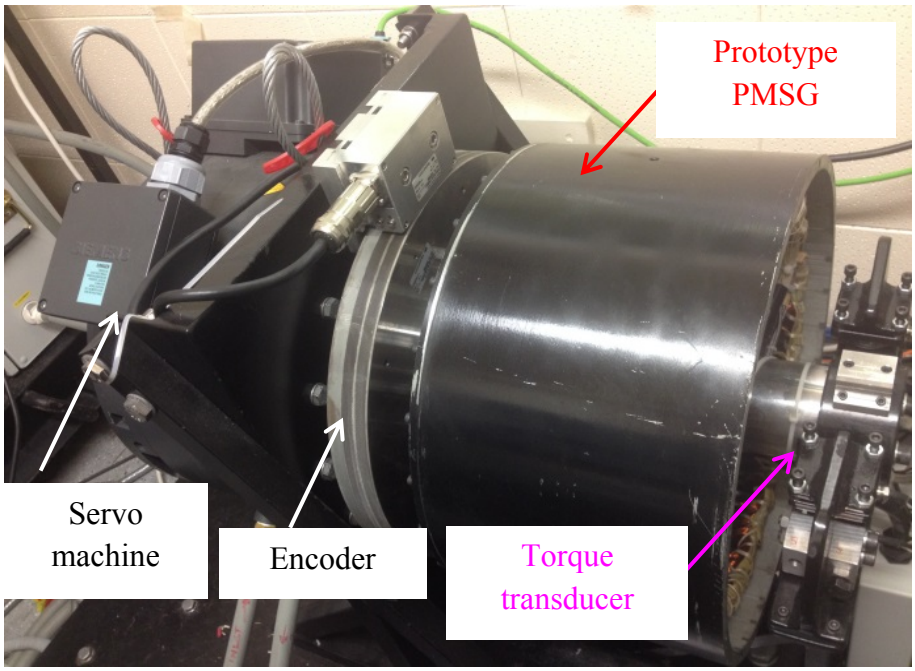

Fig.B.2 Test rig.

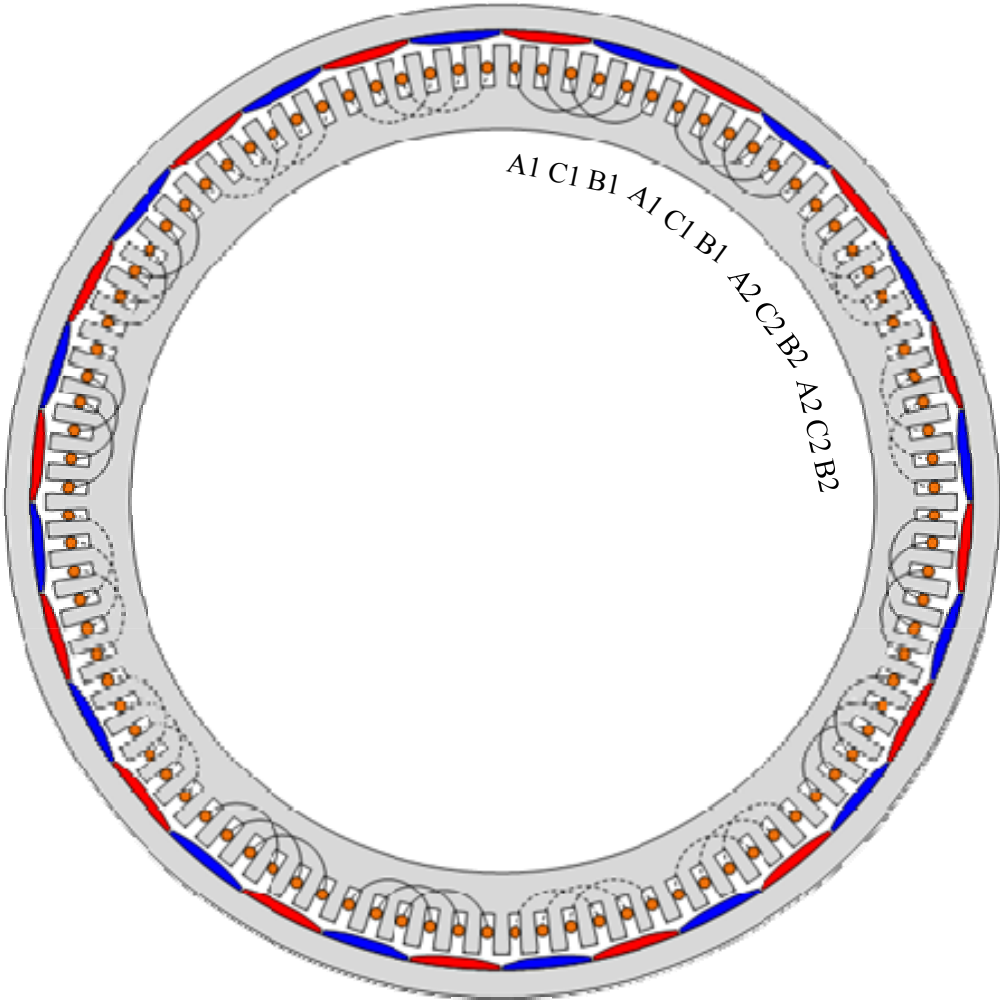

Fig.B.3 Winding topology of the dual 3-phase PMSM prototype.

The design parameters are shown in TABLE B. 1

TABLE B. 1

DESIGN PARAMETERS OF THE PROTOTYPE DUAL 3-PHASE PMSM

Parameters	Value	Parameters	Value
Pole pairs	16	No-load PM Flux linkage (Wb)	0.9
Resistance (Ω)	3.76	Shifted angle between two sets	0
Rated RMS current (A)	2.83	Encoder resolution	4096
Rated speed(rpm)	170	Rated frequency(Hz)	45.33
Rated torque(Nm)	171	Rated power(kW)	3

Appendix C. Inherent Asymmetries of the Prototype PMSG

In this section, the inherent asymmetries of the prototype PMSG will be presented, which include the inherent asymmetries in the resistances, inductances and back-EMFs. Since the first set and the second set are identical, the measurements of resistances, inductances and back-EMFs in each set are only conducted on the first set.

C.1 Resistances

The resistances of the 3-phase windings in the first set of prototype machine are listed in TABLE C. 1, which are measured by the HIOKI LCR meter IM3533-01. It can be seen from TABLE C. 1 that the resistance network is fairly balanced because the maximum difference between the phase resistances and the average resistance is only 0.02 Ω, which is only 0.5% of the average resistance and is negligible.

TABLE C. 1
RESISTANCES OF THE PROTOTYPE MACHINE

Resistances	Values
R_A :Resistance of phase A(Ω)	3.94
R_B :Resistance of phase B(Ω)	3.95
R_C :Resistance of phase C(Ω)	3.91
R_{avg}:Average resistance *(Ω)*	3.93

C.2 Inductances

The inductances of the first set are measured by HIOKI LCR meter IM3533-01 in constant current mode (10mA). The measured results and the fitted curve of inductances at the frequency of 120Hz are shown in Fig.C.1(a), while the corresponding harmonic analyses are shown in Fig.C.1(b). As can be seen from Fig.C.1(b), the self-inductances are quite balanced with approximately the same DC value and 2h components, while the mutual inductances are obviously unbalanced as the average mutual inductance in M_{AB} is significantly different with that in M_{CA} and M_{BC}.

Since the phase self-inductances and mutual inductances as function of angle have been measured. According to (3.10), the inductance in $\alpha\beta$-frame can be obtained. Hereafter, the inductances in dq-frame can be obtained according to (3.34). The inductances in $\alpha\beta$-frame

and in *dq*-frame are shown in Fig.C.1(c) and (d) respectively. As there are apparent inherent asymmetry of mutual inductances, L_d, L_q, and M_{dq} in *dq*-frame have apparent 2h inductances, which is in accordance with (3.38).

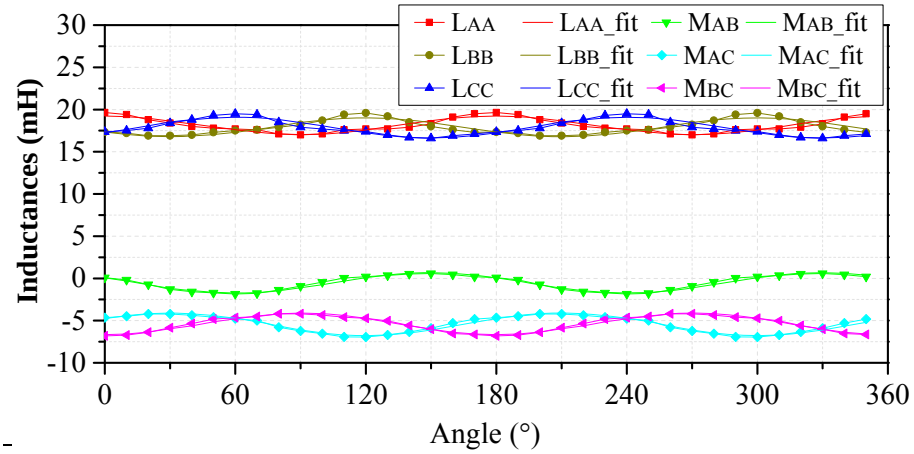

(a)

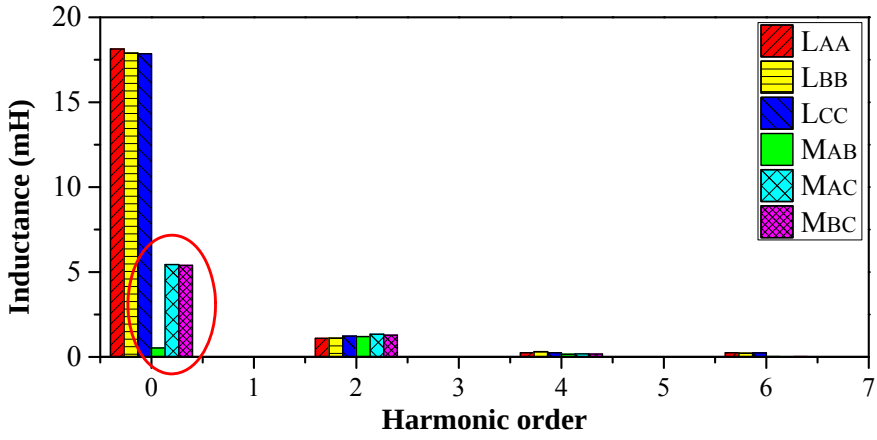

(b)

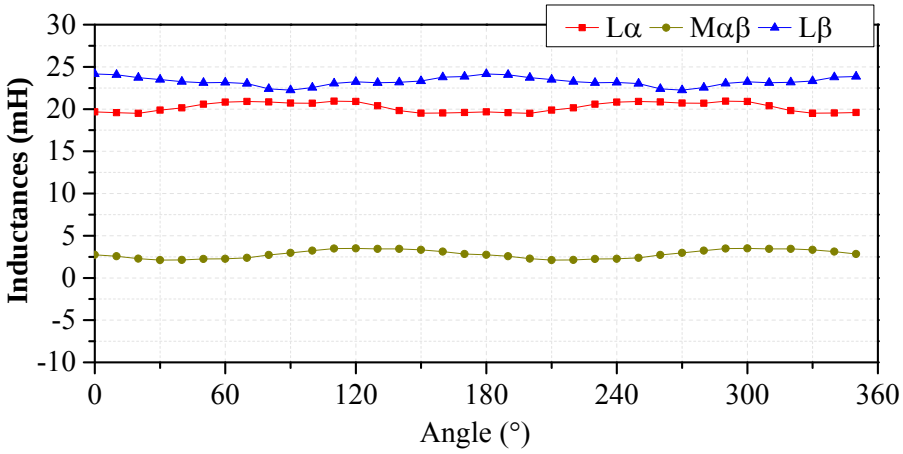

(c)

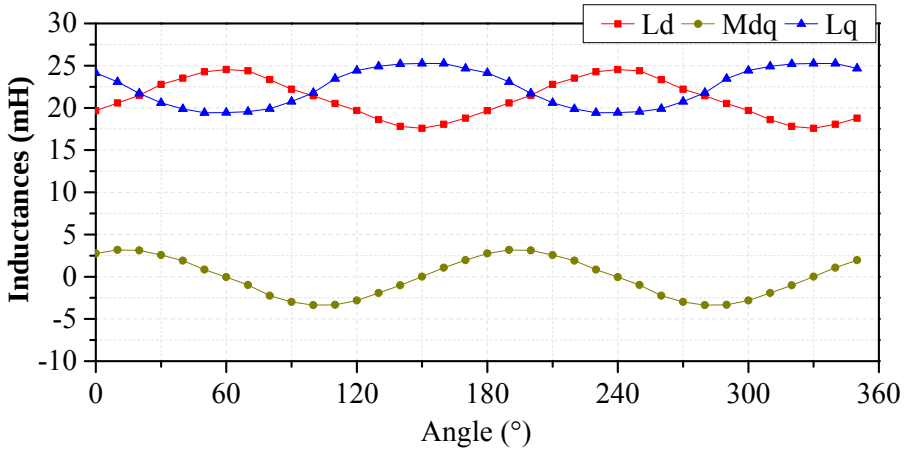

(d)

Fig.C.1 Measured inductances of the first set. (a) Measured inductances. (b) FFT analysis of measured inductances. (c) Inductances in *αβ*-frame. (c) Inductances in *dq*-frame.

The inductances of the two sets in parallel are measured by HIOKI LCR meter IM3533-01 in constant current mode (10mA). The measured results and the fitted curve of inductances at the frequency of 120Hz are shown in Fig.C.2(a), while the corresponding harmonic analyses are shown in Fig.C.2(b). The inductances in *αβ*-frame and in *dq*-frame are shown in Fig.C.2(c) and (d) respectively. As can be seen from Fig.C.2(b), the self-inductances are quite balanced with approximately the same DC and 2h components, and meanwhile, the mutual inductances are much more balanced than that in Fig.C.1(a). Consequently, the 2h inductances in L_d, L_q, and M_{dq}, Fig.C.2(d) are much smaller than that in Fig.C.1(d).

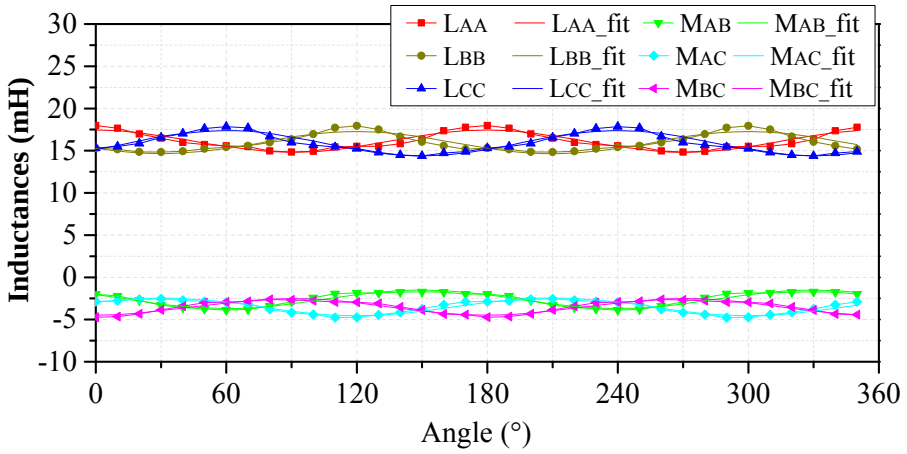

(a)

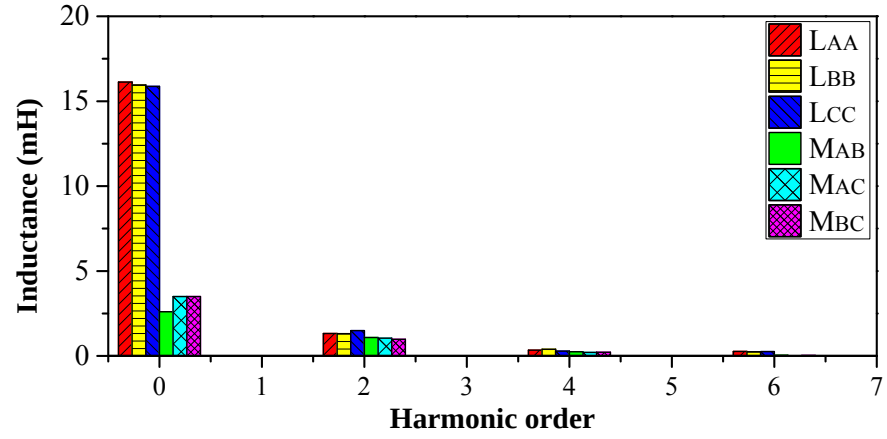

(b)

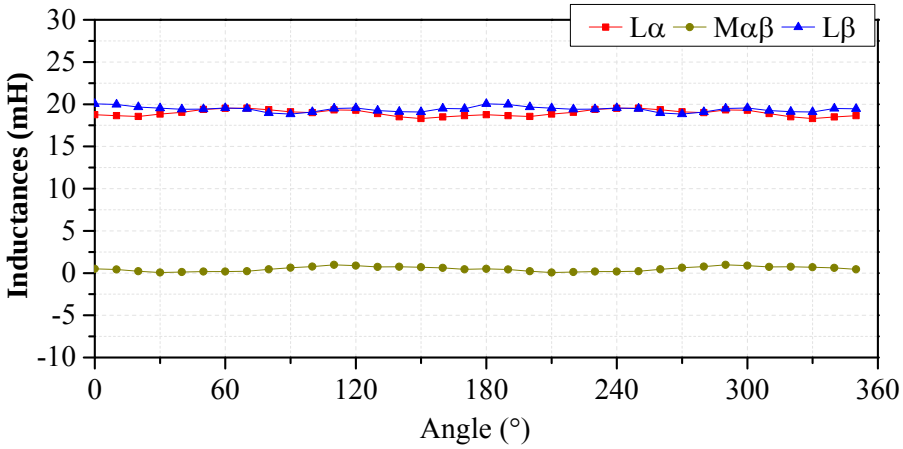

(c)

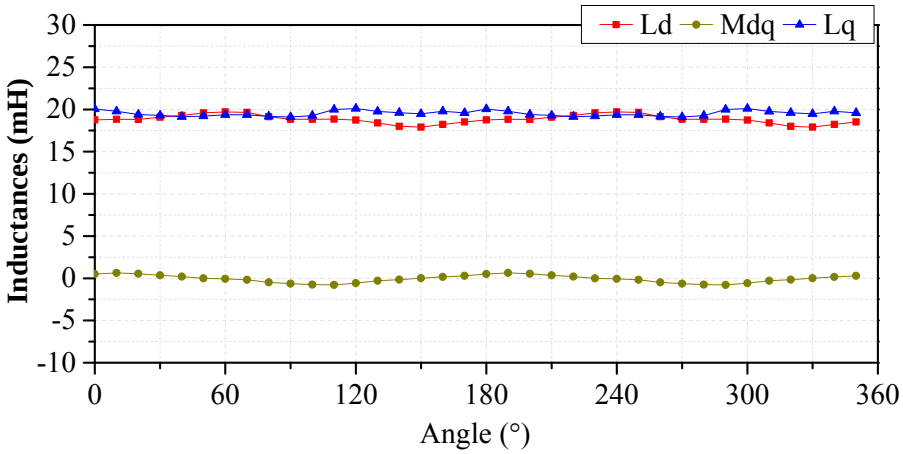

(d)

Fig.C.2 Measured inductances with two sets in parallel. (a) Measured inductances. (b) FFT analysis of measured inductances. (c) Inductances in *αβ*-frame. (c) Inductances in *dq*-frame.

According the modeling of self-inductances(2.14), mutual inductances (2.15) and measured results of inductances in Fig.C.1 and Fig.C.2, the coefficients of the inductances of the prototype machine can be summarized in TABLE C. 2.

TABLE C. 2

COEFFICIENTS OF INDUCTANCES OF THE PROTOTYPE MACHINE

Inductances (mH)	Single set	Two sets in parallel
DC self-inductance	L_{A0}= 18.131 L_{B0}= 17.897 L_{C0}=17.853	L_{A0}= 16.129 L_{B0}= 15.956 L_{C0}=15.874
2h self-inductance	L_{A2}= 1.096 L_{B2}= 1.116 L_{C2}= 1.226	L_{A2}= 1.322 L_{B2}= 1.311 L_{C2}= 1.492
DC mutual-inductance	M_{AB0}=1.049 M_{BC0}=10.776 M_{CA0}= 10.873	M_{AB0}=5.199 M_{BC0}=6.999 M_{CA0}= 6.986
2h mutual-inductance	M_{AB2}= -1.201 M_{CA2}= -1.336 M_{BC2}= -1.278	M_{AB2}= -1.088 M_{CA2}= -1.046 M_{BC2}= -0.979

For simplicity, the coefficients in TABLE C. 2 can be simplified in TABLE C. 3 with average value.

TABLE C. 3

MODELING OF INDUCTANCES OF THE PROTOTYPE MACHINE

Inductances (mH)	Single set	Two sets in parallel
DC self-inductance	L_0=L_{A0}= L_{B0}= L_{C0} =17.960	L_0=L_{A0}= L_{B0}= L_{C0} = 15.987
2h self-inductance	L_{A2}= L_{B2}= L_{C2}= 1.146	L_{A2}= L_{B2}= L_{C2}= 1.375
DC mutual-inductance	M_0 = M_{AB0}=1.049 M_{CA0}= M_{BC0}= 10.825	M_0=M_{AB0}= M_{CA0}= M_{BC0}=6.395
2h mutual-inductance	M_{AB2}= M_{CA2}= M_{BC2}= -1.272	M_{AB2}= M_{CA2}= M_{BC2}= -1.038

C.3 Back-EMFs

The measured back-EMFs of the first set at the speed of 60rpm are shown in Fig.C.3(a), while the harmonic analyses of the back-EMFs are shown in Fig.C.3(b). As can be seen from

the harmonic analysis, the average back EMFs is 92.29V, the maximum deviation from the average back EMFs is 0.153V, which is 0.17% of the average back EMFs and indicates that the back-EMFs are quite balanced despite of the 3-phase windings asymmetry.

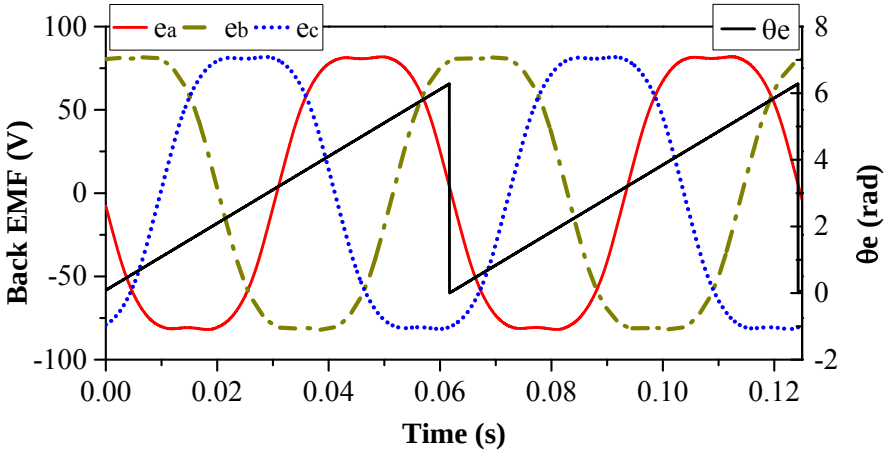

(a)

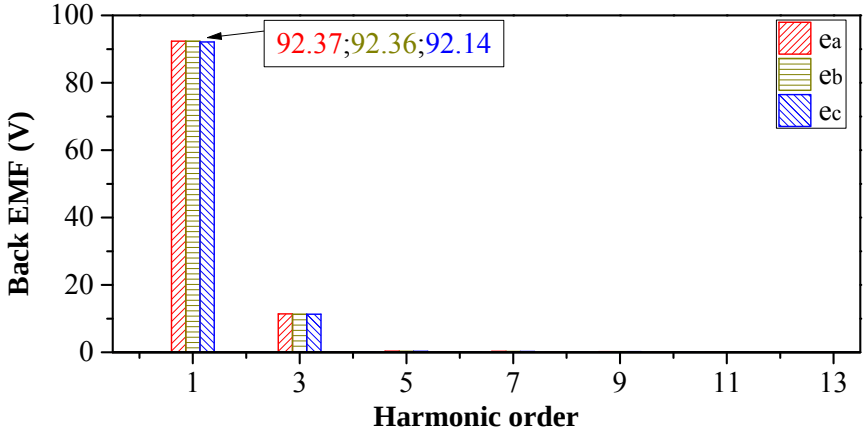

(b)

Fig.C.3 Back-EMFs of the prototype machine. (a) Waveform of the back-EMFs. (b) Harmonic analyses of back-EMFs.

Appendix D. Current Control For Dual 3-Phase PM Synchronous Motors Accounting For Current Unbalance and Harmonics

This appendix proposes an improved vector space decomposition current control scheme for dual 3-phase permanent magnet (PM) synchronous motors having two sets of 3-phase windings spatially shifted by 30 electrical degrees. A PI and resonant (2nd) controller is developed for eliminating the current unbalance in $\alpha\beta$ sub-plane, which is effective irrespective of the degree of current unbalance, whilst PI plus multi-frequency resonant (2nd and 6th) control is employed to eliminate the current unbalance, the 5th and 7th current harmonics in z_1z_2 sub-plane. Compared with existing methods only accounting for current unbalance in z_1z_2 sub-plane, the proposed method has taken into account the current unbalances in both z_1z_2 and $\alpha\beta$ sub-planes and can eliminate them simultaneously at the steady state of operation. Consequently, the full compensation of current unbalance can be achieved, by which both the current unbalance between two sets and current unbalance between phase windings in each set are eliminated. Meanwhile, the 5th and 7th current harmonics caused by non-sinusoidal back EMF and inverter non-linearity can also be fully compensated. The effectiveness of proposed method is verified by a set of comparative experiments on a prototype dual 3-phase PM machine system. It shows that fully balanced currents without the 5th and 7th current harmonics at the steady state of operation can be achieved.

D.1 Introduction

Dual 3-phase motor drives exhibit outstanding advantages [155, 156, 164-167], such as reduced phase current rating, low DC link current harmonics, less torque ripples, improved efficiency [167], excellent fault tolerant characteristics and higher reliability at system level. Consequently, dual 3-phase motor drives are widely used for electric ship propulsion, locomotive traction, electric and hybrid electric vehicles, “more-electric” aircraft [168], wind power generation [169] and high-power industrial applications, etc.

In 1993, the dual 3-phase induction machine fed by two sets of voltage source inverters was investigated in [170], as shown in Fig.D.1, one set being designated as ABC, the other set as XYZ shifted by 30° electrical degrees. Due to the configuration of induction motor having two sets of balanced windings, with phase shift of 30° electrical degrees, sixth harmonic

torque pulsations produced by two sets of windings respectively are anti-phase and therefore can be completely eliminated [155].

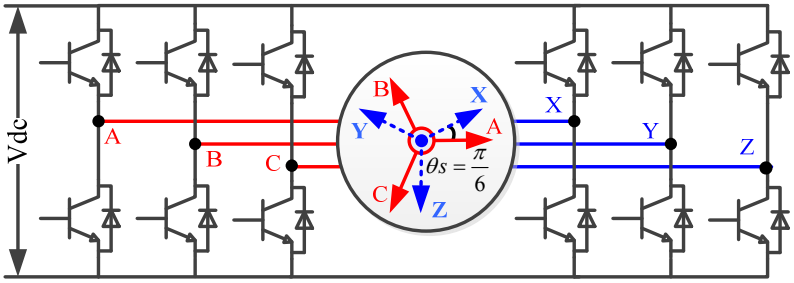

Fig.D.1 Dual 3-phase system [170].

Nowadays, numerous control strategies such as direct torque control (DTC), predictive control and vector control have been developed for dual 3-phase driver system. The DTC has the advantages of low machine parameter dependence and fast dynamic torque response and its application in drive control of dual 3-phase induction motor was discussed in [171]. In order to obtain equivalent dynamic torque response as DTC, a preferred alternative is the predictive control, which has been applied in dual 3-phase drives in recent research [172-176]. However, its applicability is hindered due to high cost in computation, whereas the vector control is popular thanks to its simplicity.

The conventional vector space decomposition (VSD) control for dual 3-phase induction motor was introduced in [177]. According to matrix transformation, the fundamental and harmonics in voltage, current, and flux vectors were projected to three sub-planes viz. $\alpha\beta$, z_1z_2, o_1o_2, which were orthogonal to each other. Therefore, the induction motor could be controlled separately in these sub-planes with full decomposition. However, the impedance in z_1z_2 sub-plane, related with the leakage inductance and phase winding resistance [177-179], is very small. Consequently, even if there are only small 5th and 7th voltage harmonics in z_1z_2 sub-plane, the resulting 5th and 7th current harmonics will be very large. Although they are not related to the electromechanical energy conversion [177], it will affect the total harmonic distortion (THD) and efficiency. In order to suppress the 5th and 7th voltage harmonics, several PWM strategies [177] [180-183] were introduced to synthesize the voltage command in $\alpha\beta$ sub-plane and maintain zero voltage in z_1z_2 sub-plane during each PWM period. However, there are still abundant 5th and 7th current harmonics due to the inverter non-linearity [86].

The conventional VSD current control scheme for dual 3-phase motor has only two current

regulators [177], The voltage references in $\alpha\beta$ sub-plane were regulated by PI controller while the voltage references in z_1z_2 sub-plane were assigned to zero with the assumption that the system is symmetrical. In this case, the currents in z_1z_2 sub-plane were not controlled by closed loop. Since there are inevitable asymmetries in reality, there will be fundamental currents in z_1z_2 sub-plane [184]. This will cause current unbalance, i.e. the currents of phase ABC and phase XYZ are unbalanced - not only the current amplitudes of two sets are not equal, but also the phase displacement will not be exactly 30° electrical degrees [184]. In order to achieve balanced currents, current control schemes with current unbalance compensation are needed in real applications.

In fact, the conventional VSD current control is not sufficient for regulating all the current components (currents in $\alpha\beta$ and z_1z_2 sub-plane). In order to control the current of dual 3-phase machine effectively, 4 current regulators at a minimum are needed in reality [185], which can be mainly categorized into two types.

The first type is the double synchronous reference frames current control, which controls the two sets of windings separately, as presented in [163, 165] for induction motors and in [166, 186] for permanent magnet (PM) motors. The two individual current controllers in the double synchronous reference frames share the same current reference from a speed controller. Although this method can provide excellent performance for current unbalance compensation between two sets, it cannot compensate the current unbalance between phase windings in each set. Meanwhile, there are mutual coupling voltages between two sets of 3-phase windings, which are hard to compensate completely, and hence, its dynamic torque performance may be affected. In order to eliminate the effect of mutual coupling between two sets of windings, an additional matrix was introduced in [136]. The original double synchronous frames were converted to new double synchronous frames without mutual coupling between two frames. Consequently, this improved double synchronous frames model is actually equivalent to the VSD model with full decomposition. It could produce good dynamic torque performance and exhibit the capability of compensating the current unbalance [187]. However, only PI control was employed for current unbalance compensation, which was incapable to eliminate the current unbalance caused by different type of asymmetries due to limited bandwidth [86]. Meanwhile, the 5th and 7th current harmonics were only suppressed to some extent due to the limited bandwidth of PI control.

The second type is the VSD current control with unbalance compensation. The method presented in [188] was based on the conventional VSD current control [177], of which two

additional PI regulators are used for current unbalance compensation. This method could provide excellent dynamic torque performance without the influence of coupling voltages between two sets. However, the current unbalance was compensated by forcing the *d-q* axis currents of the second set to follow those of the first set, the control performance may deteriorate if the current of the first set is distorted.

The current unbalance can also be compensated by minimizing the currents in z_1z_2 sub-plane to be zero. In [189], currents in z_1z_2 sub-plane were controlled by a proportional-resonant (PR) current controller to eliminate the fundamental current in z_1z_2 sub-plane [184], by which the current unbalance between two sets could be consequently eliminated. However, the current unbalance between phase windings in each set as well as the 5th and 7th current harmonics were not taken into account.

In [86], the 5th and 7th current harmonics caused by the inverter non-linearity were compensated for a dual 3-phase induction machine drive system. Meanwhile, a generic modeling of asymmetry of a dual 3-phase phase system was presented, which included both the asymmetry between two sets and asymmetry in each set. Due to different type of asymmetries, positive and negative sequence currents could be generated in z_1z_2 sub-plane [190]. A combination of anti-synchronous PI and synchronous PI could be a good alternative to achieve the optimal compensation of current unbalance in z_1z_2 sub-plane [86]. However, the current harmonics in $\alpha\beta$ sub-plane caused by asymmetry, which corresponds to current unbalance between phase windings in each set, are not considered. Meanwhile, it is only focused on six-phase induction machines.

In this appendix, an improved VSD current control scheme for dual 3-phase PMSMs accounting for the current unbalance and the 5th and 7th current harmonics is proposed. Compared with the method presented in [17], the proposed method has taken into account the compensation of current unbalance in both z_1z_2 sub-plane and $\alpha\beta$ sub-plane, which correspond to the current unbalance between two sets and between phase windings in each set, respectively. In addition, the influence of the non-sinusoidal back electromotive force (EMF) of permanent magnet synchronous machine (PMSM) and inverter non-linearity, which generates the 5th and 7th current harmonics, is also investigated in details. The current unbalance in z_1z_2 sub-plane and the 5th and 7th current harmonics is simply compensated by extending the method presented in [17] to dual 3-phase PMSM while the current unbalance in $\alpha\beta$ sub-plane is compensated by a proposed 2nd order harmonic compensator. The effectiveness of proposed method is finally verified by a set of comparative experiments on a

prototype dual 3-phase PMSM, which shows that the proposed current control has excellent performance at the steady state of operation although the dynamic torque performance will be slightly influenced.

D.2 Mathematical Model of Dual 3-phase PMSM

Generally, there are two types of mathematical model for dual 3-phase motor. The first is the 2-individual single 3-phase model [163, 165, 166, 186], which treats dual 3-phase motor as two single 3-phase motors with coupling between two sets. The second is VSD model, which treats the dual 3-phase motor as one unit with different harmonics in different sub-planes [177]. The VSD model is prevailing because of its total decomposition, clear harmonics mapping, and easy to extend to multi-phase motor system.

According to VSD theory for dual 3-phase motor, through matrix transformation, the variables in real frame are mapped to three orthogonal sub-planes $\alpha\beta$, z_1z_2, o_1o_2 and different harmonics are mapped to different sub-planes [177]. The fundamental and $(12k\pm1)$th, k=1, 2, 3… harmonics were projected to $\alpha\beta$ sub-plane, the $(6k\pm1)$th, k=1, 3, 5… harmonics, including 5th and 7th harmonics, were mapped to z_1z_2 sub-plane, and the zero sequence current harmonics ($3k$th current harmonics, k=0,1,2…) were mapped to o_1o_2 sub-plane. The transformation can be described as (D.1)

$$\begin{bmatrix} F_\alpha & F_\beta & F_{z1} & F_{z2} & F_{o1} & F_{o2} \end{bmatrix}^T = [T_6] \cdot \begin{bmatrix} F_a & F_x & F_b & F_y & F_c & F_z \end{bmatrix}^T \tag{D.1}$$

where F stands for voltage, current, or flux; a, b, and c stand for each phase of the first set of 3-phase windings; x, y, and z stand for the second set of 3-phase windings. The matrix $[T_6]$ can be expressed as (D.2)

$$[T_6] = \frac{1}{3}\begin{bmatrix} 1 & \cos(\theta_s) & \cos(4\theta_s) & \cos(5\theta_s) & \cos(8\theta_s) & \cos(9\theta_s) \\ 0 & \sin(\theta_s) & \sin(4\theta_s) & \sin(5\theta_s) & \sin(8\theta_s) & \sin(9\theta_s) \\ 1 & \cos(5\theta_s) & \cos(8\theta_s) & \cos(\theta_s) & \cos(4\theta_s) & \cos(9\theta_s) \\ 0 & \sin(5\theta_s) & \sin(8\theta_s) & \sin(\theta_s) & \sin(4\theta_s) & \sin(9\theta_s) \\ 1 & 0 & 1 & 0 & 1 & 0 \\ 0 & 1 & 0 & 1 & 0 & 1 \end{bmatrix} \tag{D.2}$$

where $\theta_s = \pi/6$. In the three sub-planes, the $\alpha\beta$ sub-plane is related with electromechanical energy conversion, the currents in z_1z_2 sub-plane make no contribution for torque generation if the flux is sinusoidal, and there are no currents in o_1o_2 sub-plane for 3-phase system [177].

After the variables in $\alpha\beta$ sub-plane are obtained, by applying Park transformation(A.6), the synchronous mathematical model in dq-frame can be obtained. Assuming that the induced back EMF is sinusoidal, eddy current and hysteresis losses, mutual leakage inductance, and saturation are neglected, two sets of windings are symmetric, the voltage equation in dq-frame, z_1z_2 sub-plane and o_1o_2 sub-plane of the ideal dual 3-phase PMSM can be expressed as (D.3)-(D.5) respectively [191].

$$\begin{bmatrix} v_d \\ v_q \end{bmatrix} = \begin{bmatrix} \left(R_s + (L_{sl} + 3L_d) \cdot p\right) i_d \\ \left(R_s + (L_{sl} + 3L_q) \cdot p\right) i_q \end{bmatrix} + \begin{bmatrix} v_{ffd\_d} \\ v_{ffd\_q} \end{bmatrix} \tag{D.3}$$

$$\begin{bmatrix} v_{z1} \\ v_{z1} \end{bmatrix} == \begin{bmatrix} R_s + L_{sl} \cdot p & 0 \\ 0 & R_s + L_{sl} \cdot p \end{bmatrix} \begin{bmatrix} i_{z1} \\ i_{z2} \end{bmatrix} \tag{D.4}$$

$$\begin{bmatrix} v_{o1} \\ v_{o1} \end{bmatrix} == \begin{bmatrix} R_s + L_{sl} \cdot p & 0 \\ 0 & R_s + L_{sl} \cdot p \end{bmatrix} \begin{bmatrix} i_{o1} \\ i_{o2} \end{bmatrix} \tag{D.5}$$

where

$$\begin{bmatrix} v_{ffd\_d} \\ v_{ffd\_q} \end{bmatrix} = \omega \begin{bmatrix} -(L_{sl} + 3L_q) i_q \\ (L_{sl} + 3L_d) i_d \end{bmatrix} + \omega \begin{bmatrix} 0 \\ \psi_{fd} \end{bmatrix} \tag{D.6}$$

where p is differential operator, R_s is the stator winding resistance. L_{sl} is the stator leakage inductance. L_d and L_q are the dq-axis self-inductances of each phase respectively. ψ_{fd} is the permanent magnet flux. ω is the electrical angular speed. i_d, v_d, i_q, and v_q are the dq-axis currents and voltages for dual 3-phase machine respectively. v_{ffd_d} and v_{ffd_q} are the decoupling voltages in dq-frame. i_{z1}, i_{z2}, v_{z1} and v_{z2} are the currents and voltages in z_1z_2 sub-plane respectively. i_{o1}, i_{o2}, v_{o1} and v_{o2} are the currents and voltages in o_1o_2 sub-plane respectively.

The equivalent circuit for (D.3)-(D.5) can be expressed in Fig.D.2. From Fig.D.2, it can be seen that the control for dual 3-phase PMSM is decomposed completely. The vector control for dual 3-phase PMSM could be as simple as vector control for single 3-phase PMSM.

D.3 Proposed Current Control Scheme

In this section, the principle of current unbalance compensation will be firstly introduced, and then two major sources causing 5th and 7th current harmonics will be analyzed in details. Followed by the principle of 5th and 7th current harmonics compensation, an improved VSD current scheme accounting for current unbalance and 5th and 7th current harmonics will be proposed.

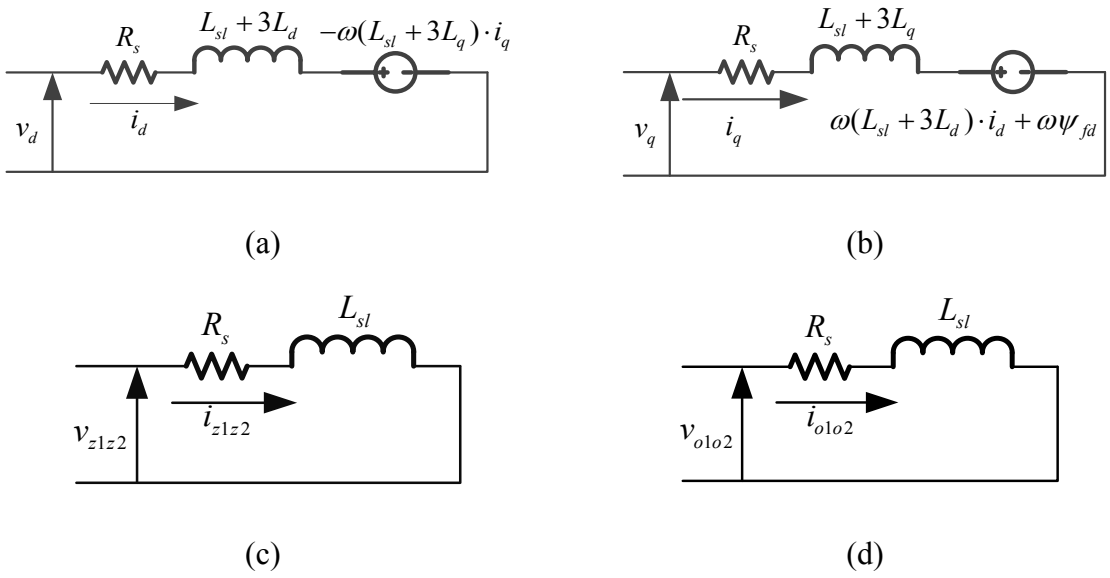

Fig.D.2 Equivalent circuits for dual 3-phase PMSM. (a) *d*-axis equivalent circuit in *αβ* sub-plane, (b) *q*-axis equivalent circuit in *αβ* sub-plane, (c) Equivalent circuit in z_1z_2 sub-plane, (d) Equivalent circuit in o_1o_2 sub-plane.

A. Current Unbalance Compensation

The asymmetry in dual 3-phase driver system is inevitable due to the asymmetry between two sets of windings, asymmetry between windings in each set and asymmetry in power inverter. According to [86], the unbalanced currents can be expressed as a combination of positive and negative sequence currents, which are caused by different type of asymmetry [190]. When $i_d=0$ control strategy is employed, the unbalanced currents of each set can be expressed as (assuming no phase angle lead/lag between positive and negative sequence current for simplicity).

$$i_{\alpha\beta 1}=k_1 I_m\cdot e^{j\left(\theta+\frac{\pi}{2}\right)}+k_2 I_m\cdot e^{-j\left(\theta+\frac{\pi}{2}\right)} \tag{D.7}$$

$$i_{\alpha\beta 2}=k_3 I_m\cdot e^{j\left(\theta+\frac{\pi}{2}\right)}+k_4 I_m\cdot e^{-j\left(\theta+\frac{\pi}{2}\right)} \tag{D.8}$$

where coefficients k_i, i=1, 2, 3,4, depend on the type of the asymmetry [86]. $i_{\alpha\beta 1}$ and $i_{\alpha\beta 2}$ are the currents of phase ABC and phase XYZ in *αβ* frame respectively. θ is the rotor position.

The variables in z_1z_2 sub-plane can be converted to a new frame, designated as *dqz* frame, by using the matrix conversion of $[T_{dqz}]$.

$$\left[T_{dqz}\right]=\begin{bmatrix}-\cos\theta & \sin\theta\\ \sin\theta & \cos\theta\end{bmatrix} \tag{D.9}$$

$$\begin{bmatrix} F_{dz} \\ F_{qz} \end{bmatrix} = \begin{bmatrix} T_{dqz} \end{bmatrix} \begin{bmatrix} F_{z1} \\ F_{z2} \end{bmatrix} \tag{D.10}$$

where F is v, i, or ψ, which is corresponding with voltage, current, and stator flux, respectively.

From (D.7), (D.8) and the inverse Clark transformation, the current of each phase can be obtained. Then, i_{z1} and i_{z2} can be calculated by (D.1) and expressed as (D.11). It can be seen there are fundamental currents in z_1z_2 sub-plane, which is in accordance with [184].

$$\begin{bmatrix} i_{z1} \\ i_{z2} \end{bmatrix} = -\frac{I_m}{2} \left(\underbrace{\begin{bmatrix} (k_1 - k_3)\sin(\theta) \\ (k_1 - k_3)\cos(\theta) \end{bmatrix}}_{\text{Negative sequence}} + \underbrace{\begin{bmatrix} (k_2 - k_4)\sin(\theta) \\ -(k_2 - k_4)\cos(\theta) \end{bmatrix}}_{\text{Positive sequence}} \right) \tag{D.11}$$

After the transformation(D.10), i_{dz} and i_{qz} in dqz frame can be expressed as

$$\begin{bmatrix} i_{dz} \\ i_{qz} \end{bmatrix} = \frac{I_m}{2} \left(\underbrace{\begin{bmatrix} 0 \\ -(k_1 - k_3) \end{bmatrix}}_{\text{DC}} + \underbrace{(k_2 - k_4) \begin{bmatrix} \sin(2\theta) \\ \cos(2\theta) \end{bmatrix}}_{\text{Second order}} \right) \tag{D.12}$$

It can be seen that negative and positive sequence currents in (D.11) are converted to DC currents and 2nd order harmonics in (D.12) in dqz frame respectively. By eliminating the DC values and 2nd order current harmonics in dqz frame, the current unbalance in z_1z_2 sub-plane can be eliminated. It is equivalent to the method presented in [86], where combination of synchronous frame PI and anti-synchronous frame PI were used to obtain full compensation of current unbalance in z_1z_2 sub-plane.

If the current unbalance in z_1z_2 sub-plane is eliminated, i_{dz} and i_{qz} will be zero. In this case, the following equation can be obtained from (D.12)

$$k_1 = k_3, \quad k_2 = k_4 \tag{D.13}$$

Equation (D.13) means the unbalance between two sets of 3-phase windings is eliminated, and two sets have same positive and same negative sequence currents. However, it does not mean k_2 and k_4 are zero. If k_2 and k_4 are non-zero, negative sequence currents will still exist in (D.7) and (D.8), which indicates the phase currents in each set are still unbalanced.

In [86], the current unbalance in z_1z_2 sub-plane was considered. However, the current unbalance in $\alpha\beta$ sub-plane was not considered. When the currents are unbalanced, there will

have positive and negative sequence currents in $\alpha\beta$ sub-plane as well. From (D.7), (D.8) and the inverse Clark conversion, the current of each phase can be obtained. Then, i_α and i_β can be calculated by (D.1) and expressed as

$$\begin{bmatrix} i_\alpha \\ i_\beta \end{bmatrix} = \frac{I_m}{2}\left(\underbrace{\begin{pmatrix} -(k_1+k_3)\cdot\sin(\theta) \\ (k_1+k_3)\cdot\cos(\theta) \end{pmatrix}}_{\text{Positive sequence}} + \underbrace{\begin{pmatrix} -(k_2+k_4)\cdot\sin(\theta) \\ -(k_2+k_4)\cdot\cos(\theta) \end{pmatrix}}_{\text{Negative sequence}} \right) \tag{D.14}$$

By applying Park transformation (A.6) to (D.14), the dq-axis currents can be expressed as (D.15).

$$\begin{bmatrix} i_d \\ i_q \end{bmatrix} = \frac{I_m}{2}\left(\underbrace{\begin{bmatrix} 0 \\ k_1+k_3 \end{bmatrix}}_{\text{DC}} - \underbrace{(k_2+k_4)\begin{bmatrix} \sin(2\theta) \\ \cos(2\theta) \end{bmatrix}}_{\text{Second order}} \right) \tag{D.15}$$

From (D.15), it can be seen that when there are negative sequence currents in each set caused by asymmetry, the 2nd order current harmonics may exist in dq-axis currents ($k_2 + k_4 \neq 0$). If the 2nd order harmonics in dq-frame are eliminated as well, which means:

$$k_2 + k_4 = 0 \tag{D.16}$$

by combining (D.13) and (D.16) together, the following equations can be obtained:

$$k_1 = k_3, \quad k_2 = k_4 = 0 \tag{D.17}$$

In this case, $i_{\alpha\beta 1}$ in (D.7) will be equal to $i_{\alpha\beta 2}$ in (D.8). Meanwhile, there are only positive sequence currents exist, which means the currents are totally balanced, viz. balance between two sets and between windings in each set.

The current unbalance in $\alpha\beta$ sub-plane has significant influence on torque ripple. For example, the 2nd order torque ripple will be generated due to the interaction between the negative sequence currents and positive sequence fluxes in $\alpha\beta$ sub-plane. If the current unbalance can be completely compensated, there are only positive sequence currents in $\alpha\beta$ sub-plane. If the fluxes are unbalanced, there will have positive and negative sequence fluxes in $\alpha\beta$ sub-plane, which have similar expression as (D.14). The positive sequence currents in $\alpha\beta$ sub-plane will interact with positive and negative sequence fluxes in $\alpha\beta$ sub-plane and generate average torque and 2nd order torque ripple. However, if the fluxes are balanced and

the asymmetry is caused by resistor or inverter asymmetry, there are only positive sequence fluxes in $\alpha\beta$ sub-plane. In this case, the 2nd order torque ripple will not be generated.

B. Fifth and Seventh Current Harmonics Compensation

In [86], a 6th order resonant controller was employed to compensate the 5th and 7th current harmonics caused by dead-time effect for asymmetric 6-phase machine. However, for the dual 3-phase PMSM, the 5th and 7th current harmonics are not only resulted from the inverter non-linearity, but also from the non-sinusoidal back EMF.

1) Due to Non-Sinusoidal Back EMF

There are the 5th and 7th harmonics in the back EMF inevitably in reality [166]. The back EMFs of phase A and phase X of the prototype machine are shown in Fig.D.3 (a). The line back EMFs of phase ABC are shown in Fig.D.3(b). From Fig.D.3(b), it can be seen that the line back EMF profiles are not pure sinusoidal, with abundant harmonics, being dominated by the 5th and 7th harmonics, as shown in Fig.D.3 (c). After matrix transformation (D.2) and (D.10), the 5th and 7th flux harmonics are mapped to the 6th flux harmonics ψ_{fdz} and ψ_{fqz} in dqz frame, Fig.D.3 (d).

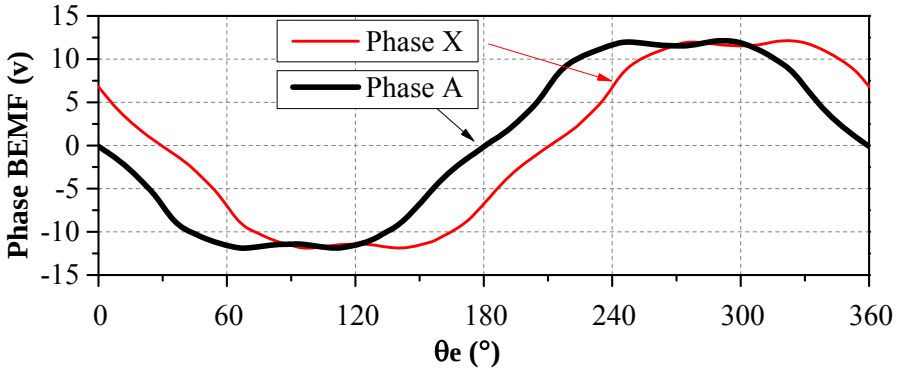

(a)

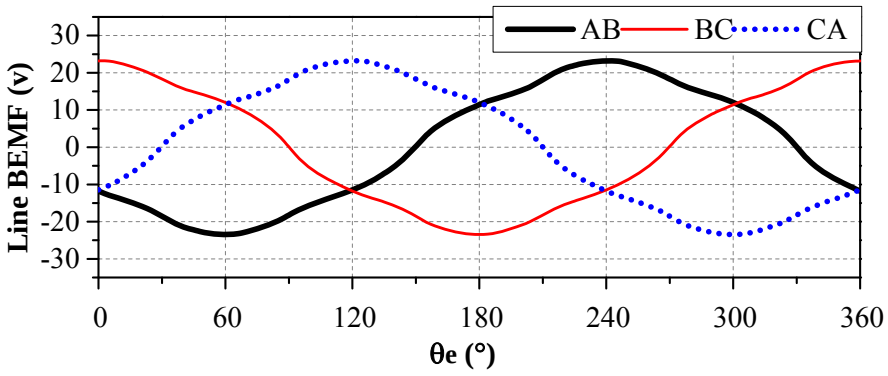

(b)

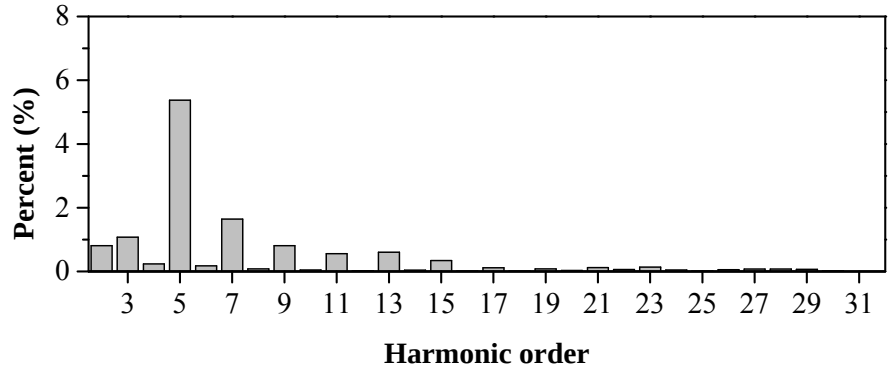

(c)

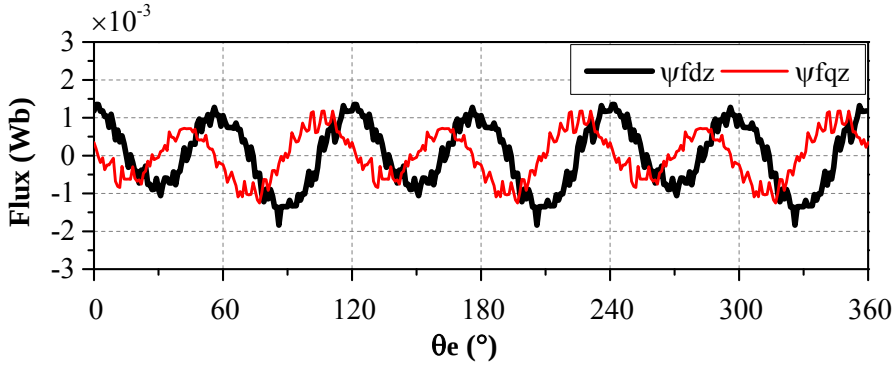

(d)

Fig.D.3 Measured back EMFs. (a) Phase back EMF, (b) Line back EMF between Phases A and B, (c) Harmonic analysis of line back EMF between Phases A and B, (d) Flux in *dqz* frame obtained from measured back EMFs.

2) Due to Inverter Non-linearity

According to [192, 193], the distorted phase voltage caused by inverter non-linearity is related with the phase current direction, which can be simplified as

$$V_{phs\_dead} = sign(i_{phs}) * V_{dead} \tag{D.18}$$

where *phs* stands for phase A, B, C, X, Y, or Z, V_{dead} stands for the magnitude of distorted voltage caused by inverter non-linearity.

Assuming V_{dead} is equal to 2V, from the harmonic analysis of V_{A_dead} shown in Fig.D.4(a), it can be seen that abundant odd voltage harmonics exist in V_{A_dead}. Since the fundamental distorted voltages can be effectively compensated by PI controller and the 3rd voltage harmonics have no influence in the 3-phase system, the 5th and 7th voltage harmonics will have dominant effect on current harmonics.

The distorted voltages for each single 3-phase system in *dq*-frame are shown in Fig.D.4(b) when the $i_d=0$ control strategy is employed. DV_{d1}, DV_{q1}, DV_{d2} and DV_{q2} are the distorted *dq*-axis voltages for phase ABC and XYZ respectively. The abundant 6th voltage harmonics caused by inverter non-linearity will cause the 6th current harmonics in *dq*-axis currents of each single 3-phase.

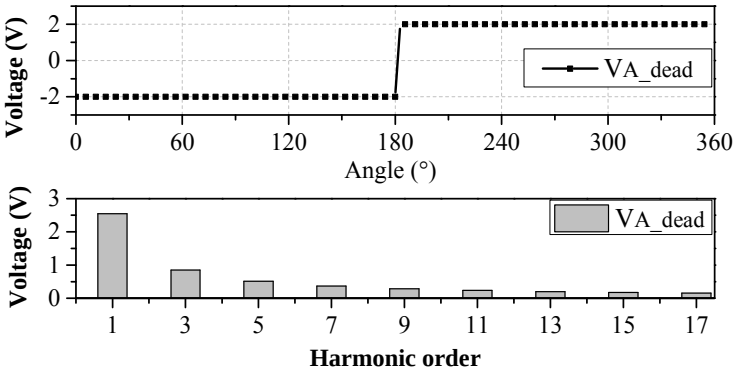

(a)

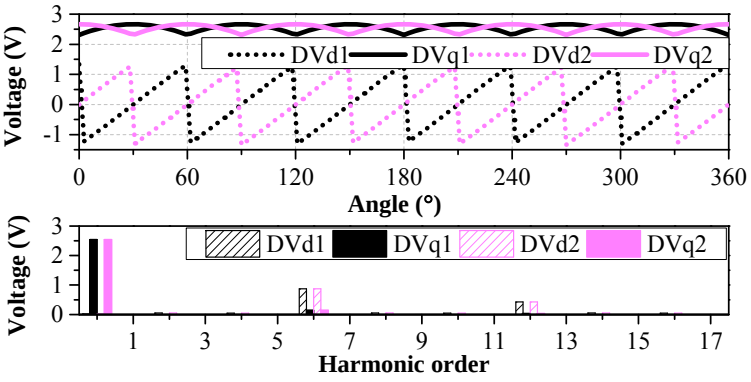

(b)

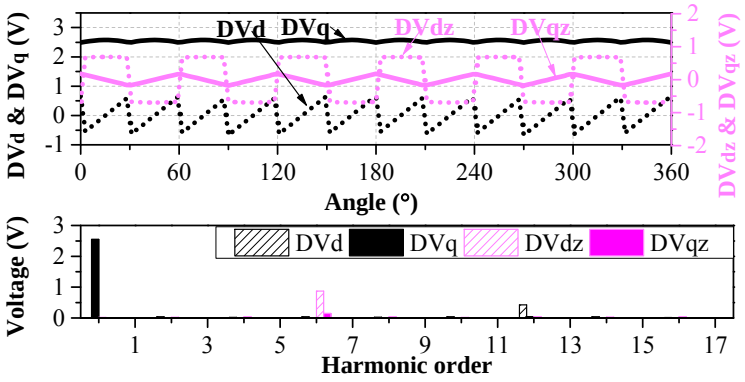

(c)

Fig.D.4 Distorted voltage caused by non-linearity of inverter. (a) Harmonic analysis for distorted voltage for phase A, (b) Distorted voltages in *dq*-axis for each set of single 3-phase, (c) Distorted voltage in *dq*-frame and *dqz* frame for dual 3-phase.

The distorted voltages in *dq*-frame and *dqz* frame for dual 3-phase system are shown in Fig.D.4(c). DV_d and DV_q are the distorted *dq*-axis voltages for dual 3-phase system. It is worth noting that there are no 6th voltage harmonics in DV_d and DV_q, while the 12th voltage harmonics are significant. It means it will cause the 12th current harmonics in *dq*-axis currents for a dual 3-phase system. DV_{dz} and DV_{qz} are the distorted voltages in *dqz* frame, and the 6th voltage harmonics are dominant in *dqz* frame, Fig.D.4(c), which will generate corresponding current harmonics in *dqz* frame.

3) Principle of Fifth and Seventh Current Harmonics Compensation

Considering the non-sinusoidal back EMF and inverter non-linearity, the 5th and 7th current harmonics in phase currents are inevitable. In order to reduce the current total harmonic distortion and increase efficiency, they should be eliminated.

Assuming the 5th and 7th harmonics in the phase current, voltage or flux can be expressed as (D.19)

$$\begin{bmatrix} F_a \\ F_x \\ F_b \\ F_y \\ F_c \\ F_z \end{bmatrix} = F_5 \begin{bmatrix} \cos((5\theta)+\theta_5) \\ \cos(5(\theta-\theta_s)+\theta_5) \\ \cos(5(\theta-4\theta_s)+\theta_5) \\ \cos(5(\theta-5\theta_s)+\theta_5) \\ \cos(5(\theta-8\theta_s)+\theta_5) \\ \cos(5(\theta-9\theta_s)+\theta_5) \end{bmatrix} + F_7 \begin{bmatrix} \cos((7\theta)+\theta_7) \\ \cos(7(\theta-\theta_s)+\theta_7) \\ \cos(7(\theta-4\theta_s)+\theta_7) \\ \cos(7(\theta-5\theta_s)+\theta_7) \\ \cos(7(\theta-8\theta_s)+\theta_7) \\ \cos(7(\theta-9\theta_s)+\theta_7) \end{bmatrix} \tag{D.19}$$

where θ_5 and θ_7 are the offset electrical angles of the 5th and 7th harmonics respectively. F_5 and F_7 are the amplitudes of the 5th and 7th harmonics respectively.

By converting the variables of each set shown in (D.19) to *dq*-frame respectively, the following relationship can be obtained.

$$\begin{cases} F_{d1\_6th} = -F_{d2\_6th} = F_5 \cdot \cos(6\theta+\theta_5) + F_7 \cdot \cos(6\theta+\theta_7) \\ F_{q1\_6th} = -F_{q2\_6th} = -F_5 \cdot \sin(6\theta+\theta_5) + F_7 \cdot \sin(6\theta+\theta_7) \end{cases} \tag{D.20}$$

where F_{d1_6th} and F_{q1_6th} are *dq*-axis 6th harmonics for phase ABC, F_{d2_6th} and F_{q2_6th} are *dq*-axis 6th harmonics for phase XYZ. The equation (D.20) means the 5th and 7th harmonics in real frame are converted to 6th harmonics in *dq*-axis for single 3-phase ABC and XYZ respectively, they have same amplitude, but anti-phase.

By applying matrix (D.2) to (D.19), the 5th and 7th harmonics will be projected to z_1z_2 sub-plane, and then by applying (D.9) to variables in z_1z_2 sub-plane, the 5th and 7th harmonics

will be converted to the 6th harmonics in *dqz* frame. It can be concluded that the 6th current harmonics in *dqz* frame have the following relationship.

$$\begin{bmatrix} i_{dz\_6th} \\ i_{qz\_6th} \end{bmatrix} = -\begin{bmatrix} i_{d1\_6th} \\ i_{q1\_6th} \end{bmatrix} = \begin{bmatrix} i_{d2\_6th} \\ i_{q2\_6th} \end{bmatrix} \tag{D.21}$$

From (D.21), it can be seen that by suppressing the 6th current harmonics in *dqz* frame, the 6th current harmonics in *dq*-frame for each set can be suppressed simultaneously. Consequently, the 5th and 7th current harmonics in each phase can be suppressed simultaneously.

C. Proposed Current Control Scheme

The PI controller is incapable of eliminating AC errors because of its limited bandwidth. To eliminate AC errors in steady state operation, the PR control, which could track sinusoidal signal reference with zero error if the reference signal had a fixed frequency, was introduced in [96-98]. The modified PI control with resonant control (PI-R) was used widely in 3-phase grid current control when the grid voltage was unbalanced or not sinusoidal [106, 109, 194-199]. In this appendix, the resonant control will be employed to eliminate the current unbalance and the 5th and 7th current harmonics.

The proposed current control scheme is shown in Fig.D.5. i_{dz}^{*} and i_{qz}^{*} are assigned to zero aiming for current unbalance and the 5th and 7th current harmonics compensation in z_1z_2 sub-plane. Since there are no currents flowing in o_1o_2 sub-plane, the voltages in o_1o_2 sub-plane are assigned to zero. Compared with the conventional VSD current scheme [177], current control in *dqz* frame is included, PI control is used to regulate the DC error, while the multi-frequency resonant controls are used to eliminate the 2nd and 6th current harmonics in *dqz* frame.

Unlike the method presented in [86], which only considered the current unbalance in z_1z_2 sub-plane for dual 3-phase induction motor system, the proposed method considers the current unbalance in z_1z_2 and $\alpha\beta$ sub-plane for dual 3-phase PMSM simultaneously. The proposed resonant control is employed to eliminate the 2nd order current harmonics in *dq*-frame caused by current unbalance.

It is worth noting that the practical resonant control is usually implemented by replacing the ideal integral with an approximated low-pass filter transfer function [96]. The gains and cut-off frequency of low-pass filter are very important considering the stability [96]. However, it

is beyond the scope of this appendix. For simplicity, the cut-off frequency is chosen as 1/200 times of resonant frequency, and the integral gain of resonant control is set to be the same as the integral gain of PI control [86].

By matrix (D.22) conversion, the output of current controllers for i_{dz}, i_{qz} are converted to v_{z1}^*, v_{z2}^*.

$$\left[T_{dqz}\right]^{-1} = \left[T_{dqz}\right]^{T} = \begin{bmatrix} -\cos\theta & \sin\theta \\ \sin\theta & \cos\theta \end{bmatrix} \tag{D.22}$$

After all the voltages of six-dimensions v_α^*, v_β^*, v_{z1}^*, v_{z2}^*, v_{o1}^*, v_{o2}^* are obtained, the phase voltage references can be obtained by the inverse [T_6] transformation (D.23), and then, the conventional SVPWM strategy is applied for PWM generation.

$$[T_6]^{-1} = 3\left[T_6\right]^{T} \tag{D.23}$$

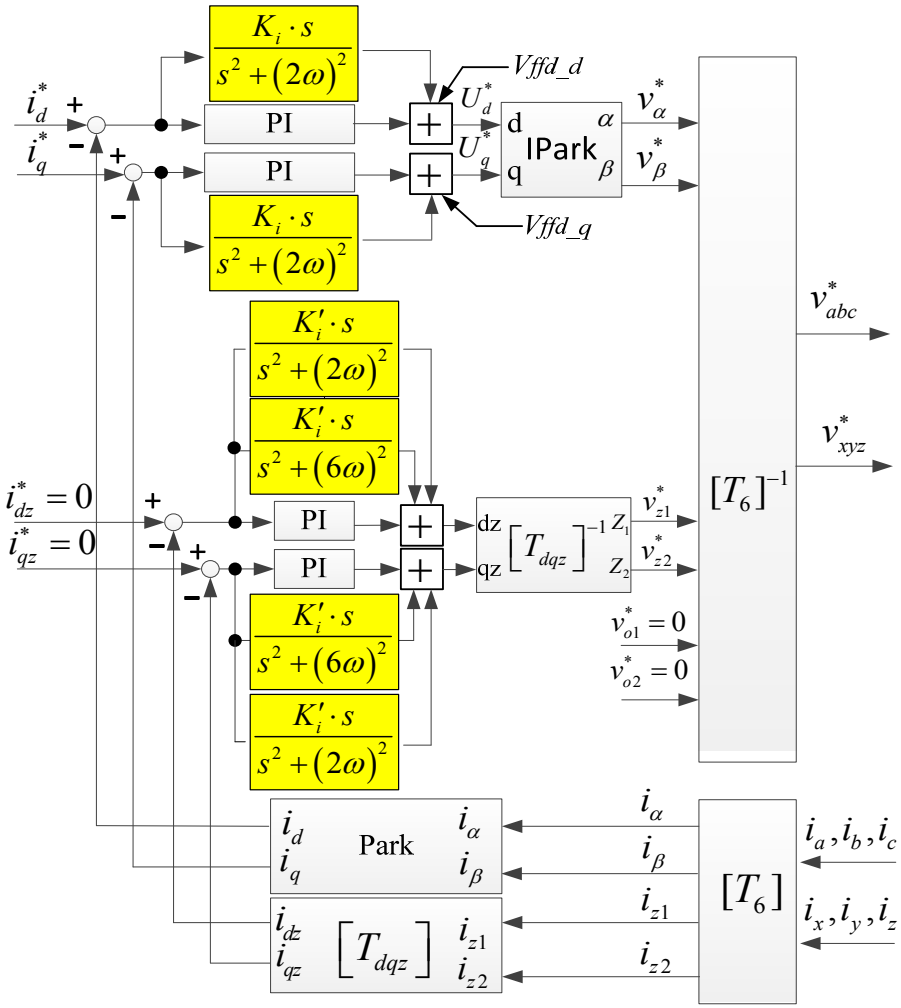

Fig.D.5 Current control flowchart of proposed method.

D.4 Experiments

The hardware platform to evaluate the effectiveness of the proposed method is constructed based on dSPACE DS1005. The experimental setup is shown in Fig.D.6. The prototype dual 3-phase PMSM is coupled with a permanent magnet DC motor, which is connected with an adjustable power resistor used as load. The dual 3-phase driver is constructed by two single 3-phase drives, which have same power inverter topology as Fig.D.1. The calculation rate of the current loop is configured to be 10 kHz, which is the same as the PWM frequency. The currents are sampled by DS2002 A/D board in dSPACE system, which has 16-bit resolution. The corresponding current sample resolution is 0.38mA. The 2μs dead-time is used to avoid short-circuit of power switching bridge. Two independent SVPWM modulators for each single 3-phase are used for PWM generation. The design parameters of prototype dual 3-phase PMSM are shown in TABLE D. 1. The design principle of PI parameters is the same as that in [70] and the overall time delay including the PWM output delay, current sampling delay and processing delay, is approximately 1.5 times of PWM period. Thus, the optimized PI parameters can be derived by setting the damping factor to 0.707 and are listed in TABLE 3.3.

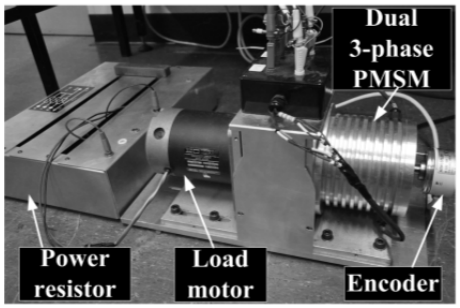

(a)

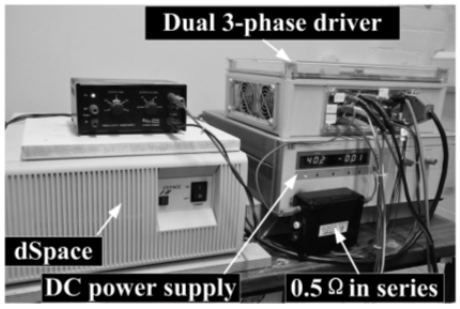

(b)

Fig.D.6 Experimental setup for dual 3-phase PMSM drive. (a) Test dual 3-phase PMSM, (b) Dual 3-phase drive system.

TABLE D. 1

PARAMETERS OF PROTOTYPE DUAL 3-PHASE PMSM

Parameters	Value
Resistance (Ω)	1.096
Leakage inductance (mH)	0.875
d-axis self-inductance (mH)	2.141
q-axis self-inductance (mH)	2.141
Flux linkage (Wb)	0.075
Pole pairs	5
Power (W)	240
DC link voltage(V)	40

TABLE D. 2 PARAMETERS OF REGULATORS

Parameters	Value
Proportional gain of PI in *dq*-frame	24.33
Integral gain of PI in *dq*-frame	3654.43
Integral gain of resonant controller in *dq*-frame	3654.43
Proportional gain of PI in *dqz* frame	2.92
Integral gain of PI in *dqz* frame	3654.43
Integral gain of resonant controller in *dqz* frame	3654.43

A. Fifth and Seventh Current Harmonics Compensation

In this experiment, the driver works in constant current control mode without/with the 5th and 7th current harmonics compensation, and i_q reference is 1.5A. The test results without compensation are shown in Fig.D.7. It can be seen that the currents of phases A and X are not pure sinusoidal, Fig.D.7(a), and the 5th and 7th current harmonics are dominant. After i_{z1}, i_{z2} are transformed to i_{dz}, i_{qz} in Fig.D.7(b), obvious 6th harmonics can be found in i_{dz}, i_{qz}. It can also be seen that the *dq*-axis currents i_{d1}, i_{d2} in Fig.D.7(c) and i_{q1}, i_{q2} in Fig.D.7(d) for each set have 6th current harmonics, but they are anti-phase, which is in accordance with (D.20). Consequently, there is no 6th current harmonic in i_d and i_q for dual 3-phase system.

The test results with compensation are shown in Fig.D.8. The current profiles of phase A and X in Fig.D.8(a) are more sinusoidal than that in Fig.D.7(a) due to the 6th current harmonics of i_{dz}, i_{qz} in Fig.D.8(b) are eliminated. The 6th current harmonics in *d*-axis current

i_{d1} and i_{d2} for each single 3-phase in Fig.D.8(c) are effectively suppressed compared with those in Fig.D.7(c). The 6th current harmonics in q-axis current i_{q1} and i_{q2} for each single 3-phase in Fig.D.8(d) are effectively suppressed compared with those in Fig.D.7(d).

It is worth noting that i_d and i_q in Fig.D.8 are corresponding to the right y-axis of Fig.D.8 (c) and (d), respectively. An interesting phenomenon is that i_d in Fig.D.7(c) and Fig.D.8(c) has distinct 12th current harmonics, while i_q in Fig.D.7(d) and Fig.D.8(d) does not have apparent 12th current harmonic. This is because the 12th voltage harmonics caused by inverter non-linearity in d-axis is larger than that in q-axis, as shown in Fig.D.4(c).

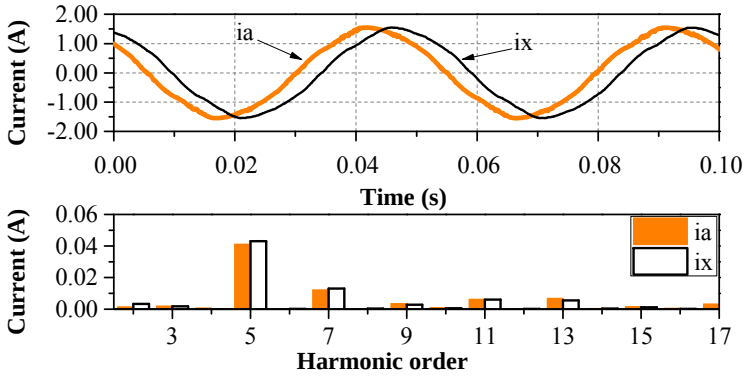

(a)

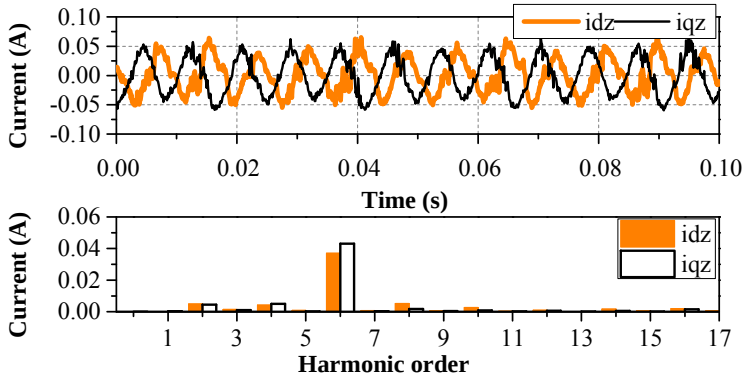

(b)

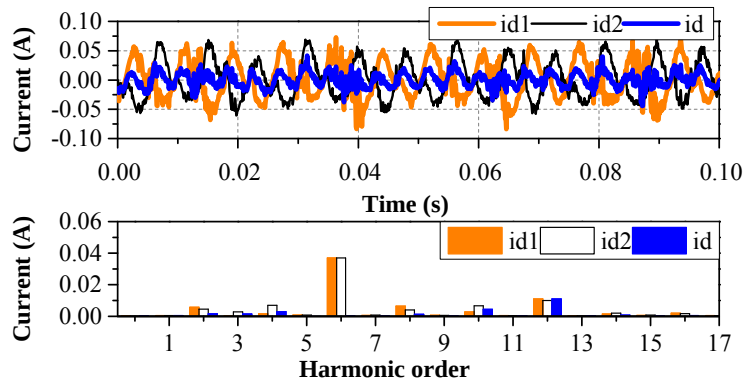

(c)

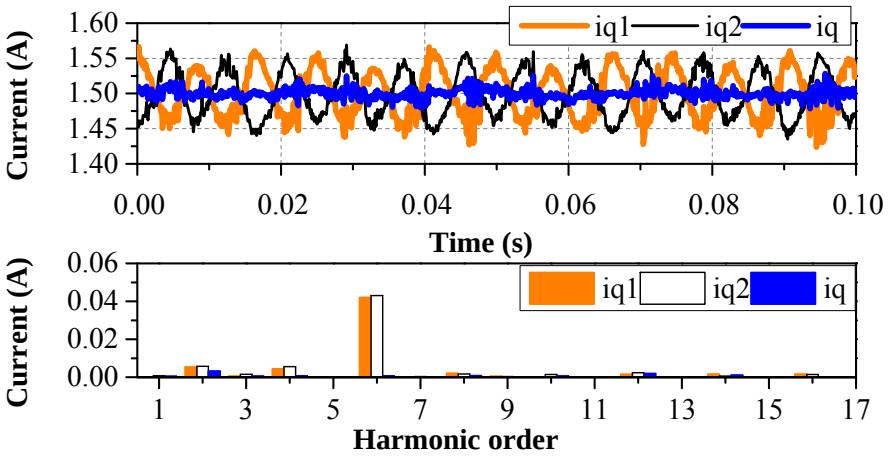

(d)

Fig.D.7. Measured results without 5th and 7th harmonics compensation. (a) Phase A and X current and harmonic analysis, (b) i_{dz} and i_{qz} and harmonic analysis, (c) d-axis current and harmonic analysis, (d) q-axis current and harmonic analysis

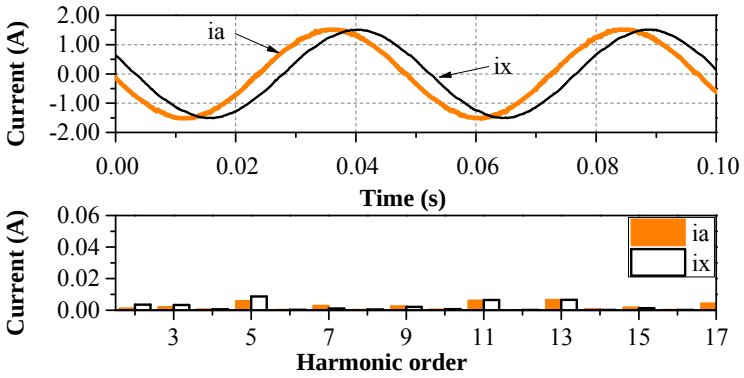

(a)

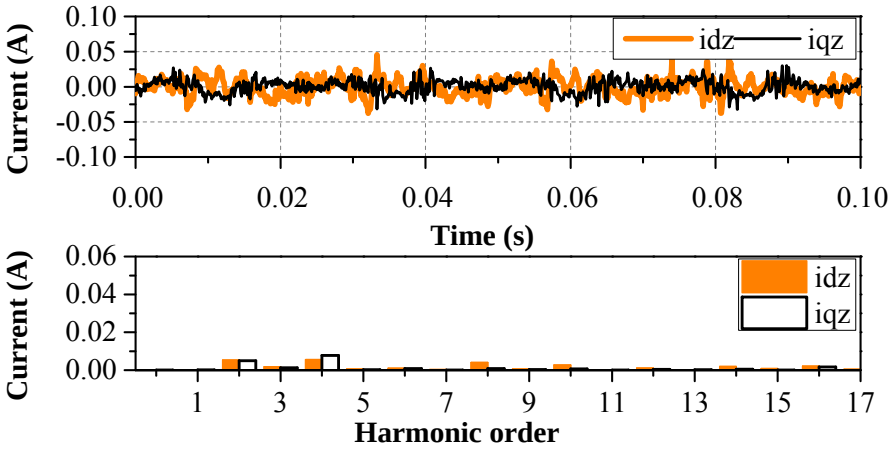

(b)

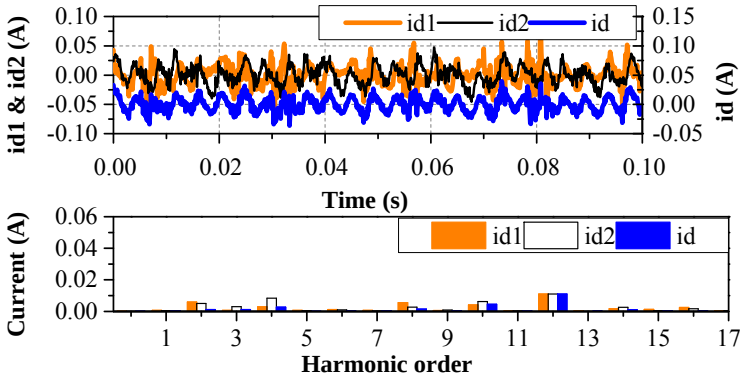

(c)

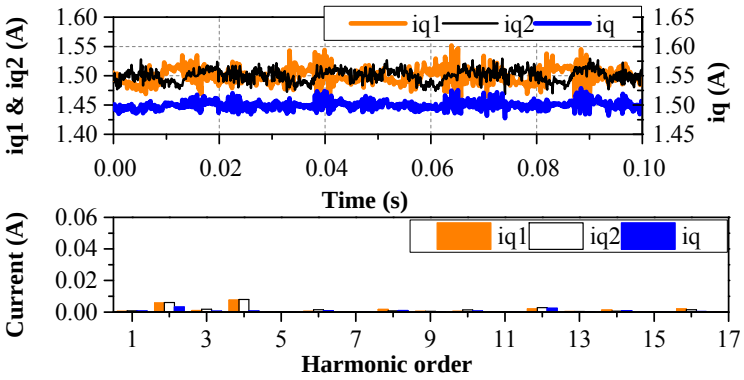

(d)

Fig.D.8 Measured results of proposed method with the 5th and 7th harmonics compensation (a) Phase A and X current and harmonic analysis, (b) i_{dz} and i_{qz} and harmonic analysis, (c) *d*-axis current and harmonic analysis, (d) *q*-axis current and harmonic analysis.

B. Current Unbalance Compensation in Steady State Operation

In this experiment, a 0.5Ω resistor is deliberately connected in series with phase A. The system works in constant current mode, and the reference of i_a is 1.5A. The measured phase current and i_{dz}, i_{qz} of conventional VSD current control without current control in z_1z_2 sub-plane are shown in Fig.D.9(a)(b) respectively. Fig.D.9 (a) shows that i_a and i_x are seriously unbalanced. i_{dz} and i_{qz} have obvious 6th current harmonics in Fig.D.9 (b). From the harmonic analysis of i_{dz} and i_{qz} shown in the lower part of Fig.D.9 (b), it can be seen that the 6th current harmonics, DC value and 2nd order current harmonics are dominant. The i_d and i_q current profiles and corresponding harmonic analysis are shown in Fig.D.9 (c) and Fig.D.9 (d) respectively. It can been seen that there are the 2nd current harmonics in i_d and i_q, which is in accordance with (D.15).

The experimental results with PI-R(6th) control in *dqz* frame are shown in Fig.D.10, which shows that the phase current profiles in Fig.D.10(a) have been improved significantly

compared with those in Fig.D.9(a). In addition, as can be seen from Fig.D.10 (b), the dominant DC value and 6th current harmonic in i_{dz} and i_{qz} have been eliminated compared with those in Fig.D.9(b). Furthermore, it is also evident that the 2nd current harmonics in Fig.D.10 (b) are suppressed greatly compared with that in Fig.D.9(b). However, from Fig.D.10 (b), there are still residual 2nd current harmonics in i_{dz} and i_{qz} while there are also residual 2nd current harmonics in i_d and i_q, as shown in Fig.D.10 (c) and Fig.D.10 (d).

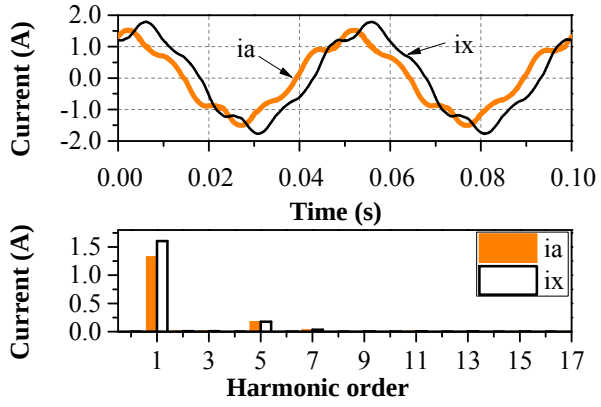

(a)

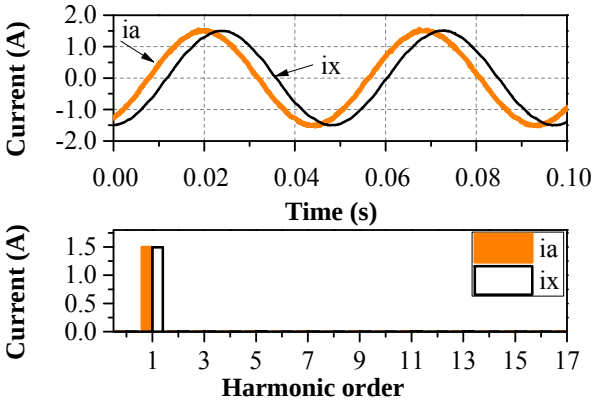

(a)

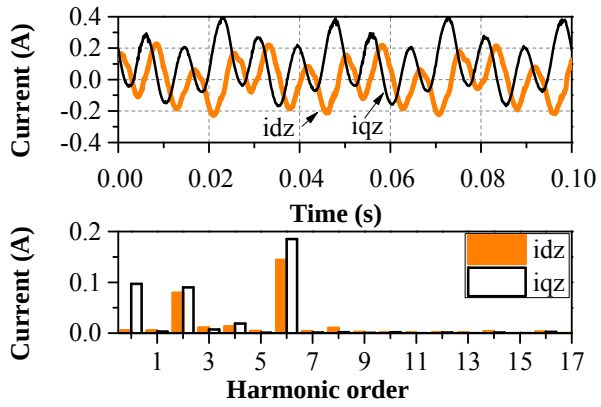

(b)

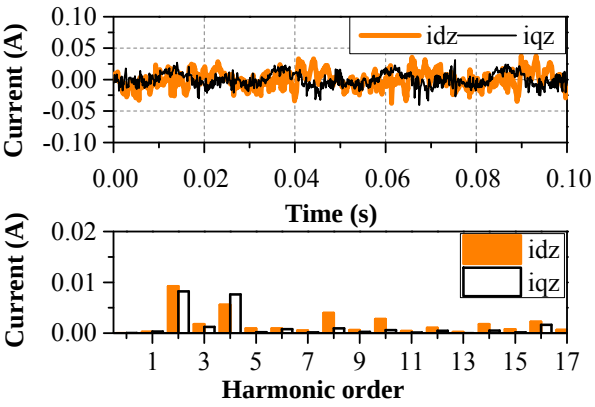

(b)

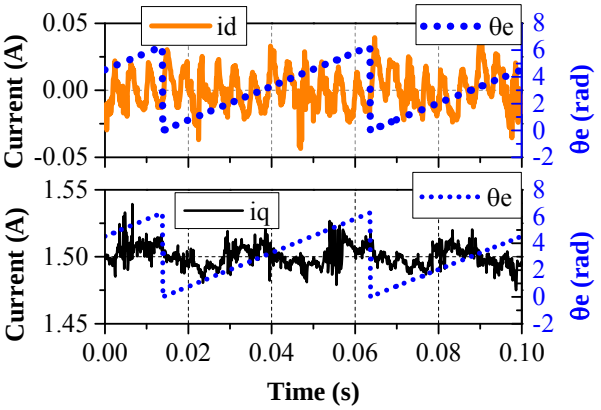

(c)

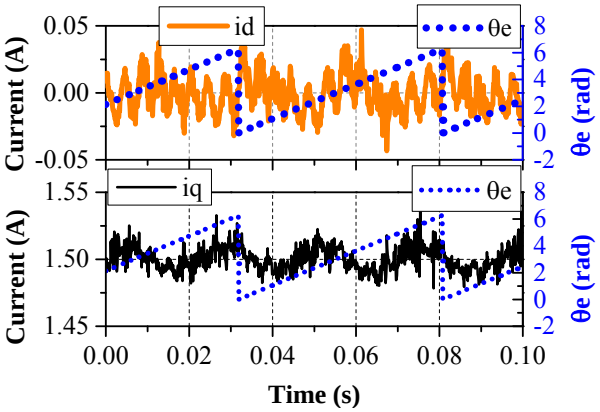

(c)

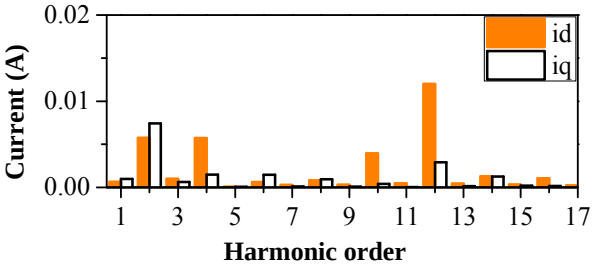

(d)

Fig.D.9 Measured results without current control in z_1z_2 sub-plane and PI control in *dq*-frame with an additional resistor 0.5Ω in series with phase A (a) Phase A and X currents and harmonic analysis, (b) i_{dz} and i_{qz} and harmonic analysis, (c) i_d and i_q, (d) Harmonic analysis of i_d and i_q.

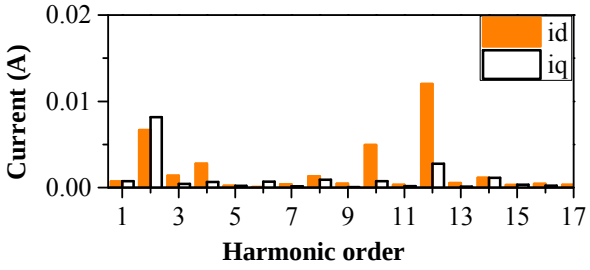

(d)

Fig.D.10 Measured results with PI-R(6th) control in *dqz* frame and PI control in *dq*-frame with an additional resistor 0.5Ω in series with phase A (a) Phase A and X currents and harmonic analysis, (b) i_{dz} and i_{qz} and harmonic analysis, (c) i_d and i_q, (d) Harmonic analysis of i_d and i_q.

To eliminate the 2nd current harmonics in *dqz* frame, the PI-R(6th) control in *dqz* frame with an additional 2nd order resonant control in *dqz* frame is employed, which is equivalent to the method presented in [86]. As can be seen from the experimental results shown in Fig.D.11, it is evident that although the phase current profiles shown in Fig.D.11(a) change insignificantly compared with those in Fig.D.10(a), the 2nd current harmonics in i_{dz} and i_{qz} shown in Fig.D.11(b) have been eliminated effectively compared with those in Fig.D.10(b). However, there are still slight 2nd current harmonics in i_d and i_q, as can be seen from Fig.D.11(c) and Fig.D.11(d).

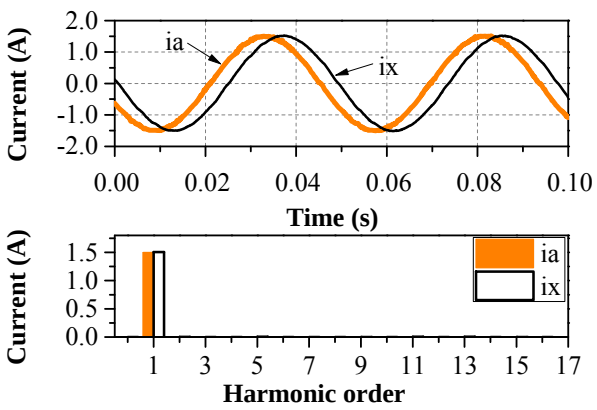

(a)

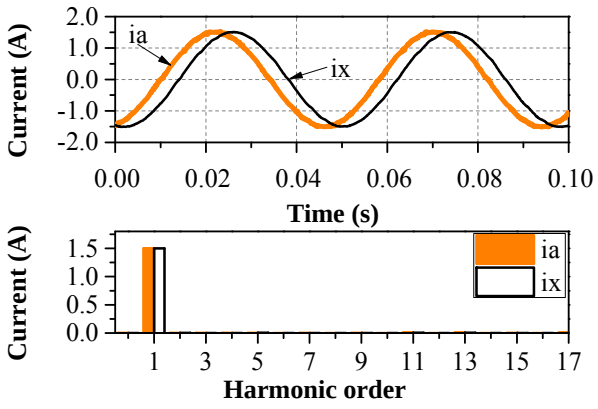

(a)

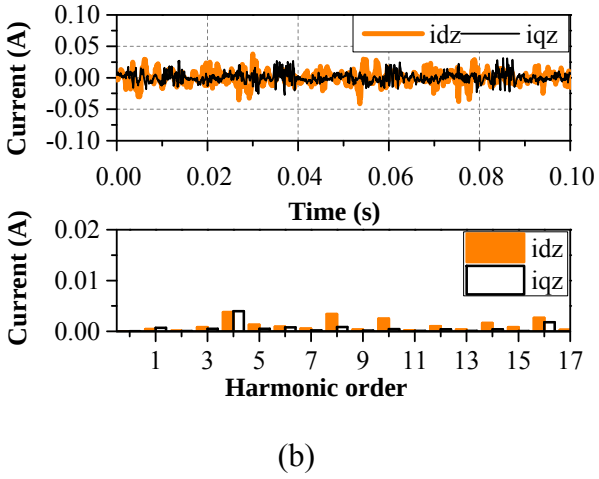

(b)

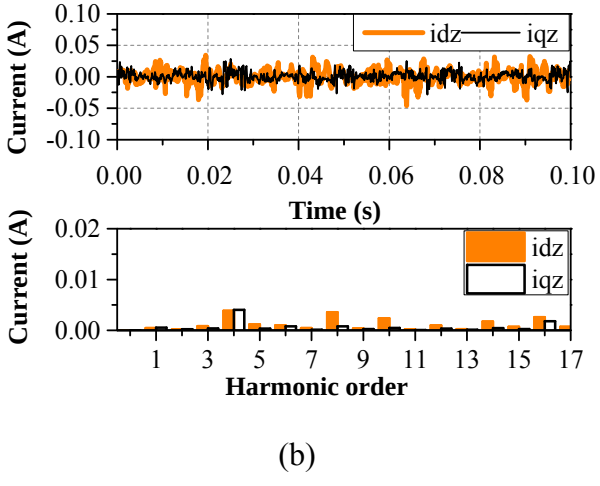

(b)

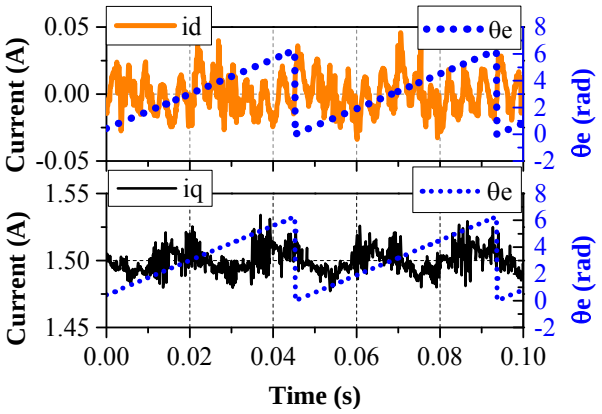

(c)

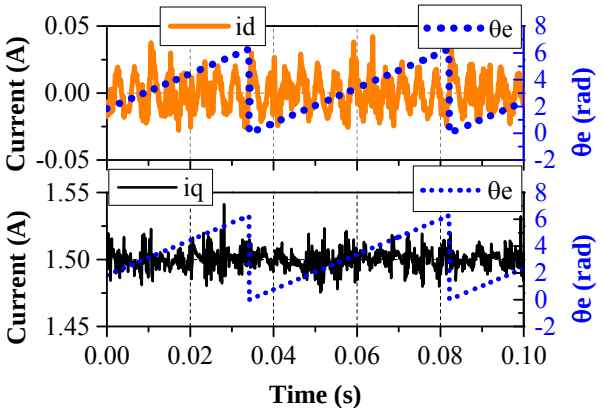

(c)

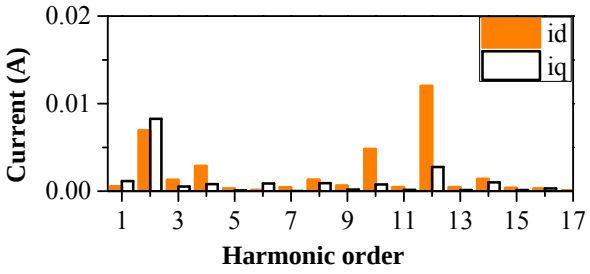

(d)

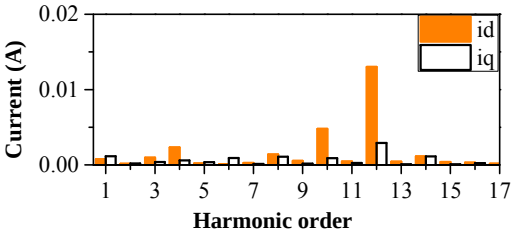

(d)

Fig.D.11 Measured results with PI-R(6th+2nd) control in z_1z_2 frame and PI control in dq-frame with an additional resistor 0.5Ω in series with phase A. (a) Phase A and X currents and harmonic analysis, (b) i_{dz} and i_{qz} and harmonic analysis, (c) i_d and i_q, (d) Harmonic analysis of i_d and i_q.

Fig.D.12 Measured results of proposed current scheme with an additional resistor 0.5Ω in series with phase A. (a) Phase A and X currents and harmonic analysis, (b) i_{dz} and i_{qz} and harmonic analysis, (c) i_d and i_q, (d) Harmonic analysis of i_d and i_q.

The measured phase currents with the proposed method are shown in Fig.D.12(a) and are

very sinusoidal. i_{dz}, i_{qz} and corresponding harmonic analysis are shown in Fig.D.12(b), it can be seen that the DC value, the 2nd current harmonics and 6th current harmonics are eliminated. Furthermore, from the i_d and i_q current profiles in Fig.D.12(c) and corresponding harmonic analysis in Fig.D.12(d), it can be seen the 2nd current harmonics in *dq*-frame are eliminated effectively as well.

In some applications, the bandwidth of PI control may be relatively low due to the low PWM switching frequency [70], especially in high power applications. In order to extend the current unbalance compensation strategy in some applications with low bandwidth and to demonstrate a clearer effect of the proposed 2nd order current harmonic compensation in *dq*-frame when the system is asymmetry, the experiment with reduced gains and lower bandwidth is conducted and shown in Figs. 12 and 13. The PI-R gain values in *dq*-frame are deliberately reduced to 1/10 of that shown in TABLE 3.3, while the gain values in *dqz* frame remain the same.

The experimental results with PI-R (6th and 2nd) control in *dqz* frame and PI control in *dq*-frame, which is equivalent to the method presented in [17], are shown in Fig.D.13. From Fig.D.13(b), it can be seen that the 2nd current harmonics in *dqz* frame are eliminated, whereas the current unbalance in *αβ* sub-plane is still significant, Fig.D.13(a). Consequently, there are still obvious 2nd order current harmonics in *dq*-frame, Fig.D.13(c) and (d). The experimental results with the proposed method including the compensation of the 2nd order current harmonics in *dq*-frame, are shown in Fig.D.14. It can be seen that the 2nd current harmonics in *dqz* frame are eliminated, Fig.D.14(b), while the 2nd order current harmonics in *dq*-frame are also eliminated as shown in Fig.D.14 (c) and (d). Consequently, as can be seen from Fig.D.14(a), the currents in *αβ* sub-plane will be balanced.

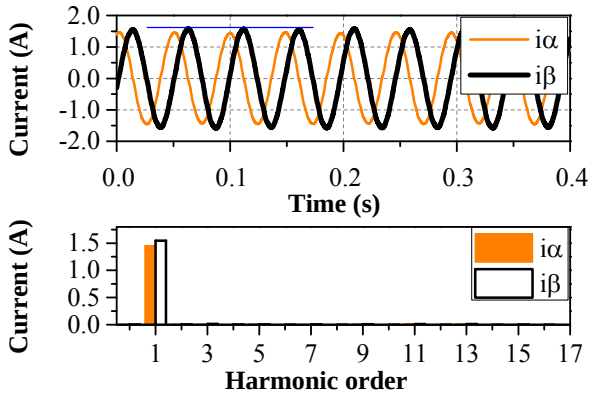

(a)

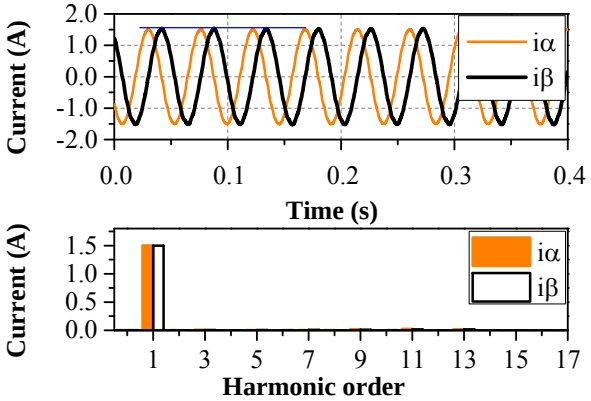

(a)

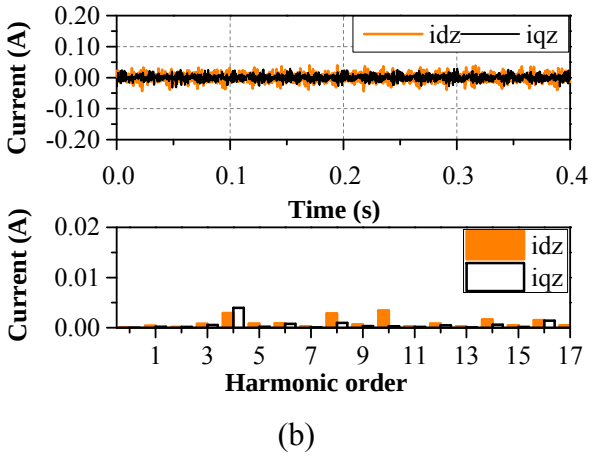

(b)

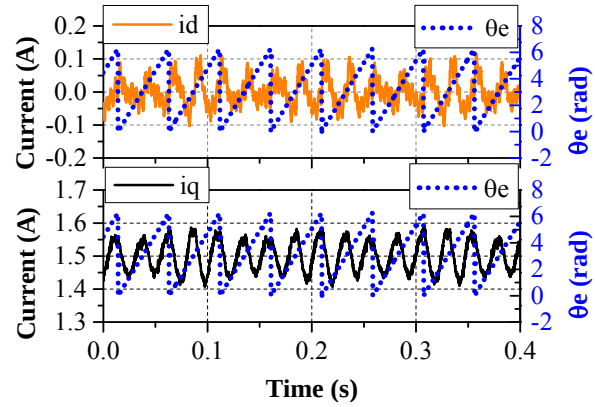

(c)

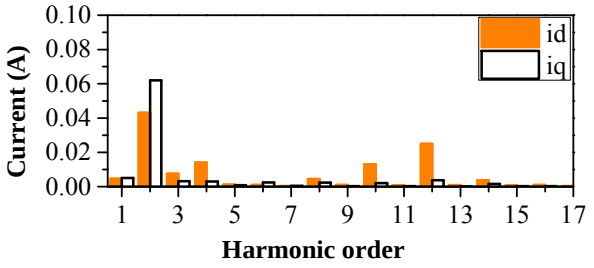

(d)

Fig.D.13 Measured results with PI+R(6th+2nd) control in *dqz* frame and PI control in *dq*-frame with an additional resistor 0.5Ω in series with phase A. (a) Currents in *αβ* sub-plane and harmonic analysis, (b) i_{dz} and i_{qz} and harmonic analysis, (c) i_d and i_q, (d) Harmonic analysis of i_d and i_q.

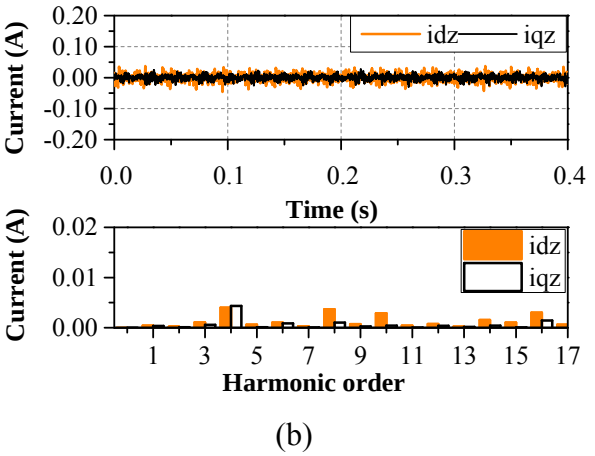

(b)

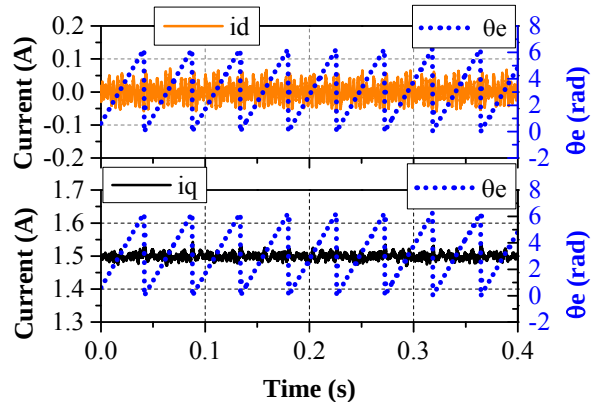

(c)

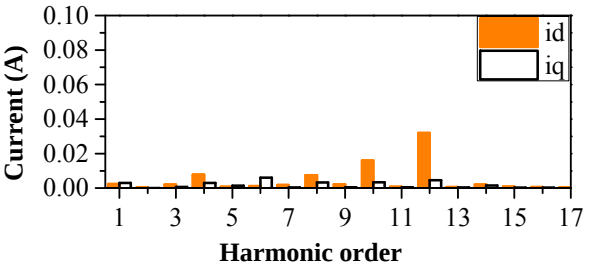

(d)

Fig.D.14 Measured results of proposed current scheme with an additional resistor 0.5Ω in series with phase A. (a) Currents in *αβ* sub-plane and harmonic analysis, (b) i_{dz} and i_{qz} and harmonic analysis, (c) i_d and i_q, (d) Harmonic analysis of i_d and i_q.

Overall, the proposed current control could be regarded as a competitive alternative for the elimination of current balance of dual 3-phase PMSM. Although the complexity of the

current control is increased, this issue can be ignored in reality thanks to the fast development of micro controllers.

C. Dynamic Performance Comparison

Although the proposed method can achieve fully balanced currents, the dynamic performance of drive system will be slightly affected by the extra 2nd order current harmonics compensation in *dq*-frame. The step current response with/without 2nd order resonant control in *dq*-frame is shown in Fig.D.15. The i_q reference current is stepped from 1A to 1.5A. It can be seen that the settling time with compensation is longer than that without compensation because the use of resonant controllers in *dq*-frame will affect the decoupling control of the *dq* current.

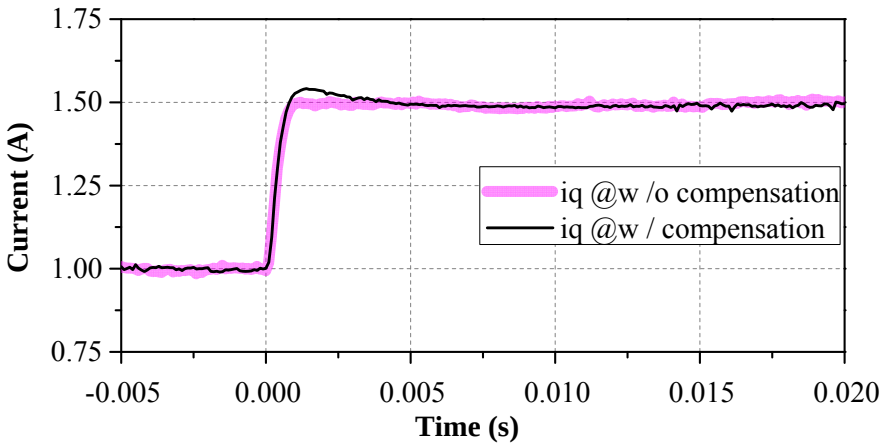

Fig.D.15 Current step response with/without 2nd order harmonics compensation in *dq*-frame in $\alpha\beta$ sub-plane.

D.5 Conclusion

This appendix has proposed an improved VSD current control scheme for dual 3-phase PMSMs having two sets of 3-phase windings spatially shifted by 30 electrical degrees. Compared with existing methods only accounting for current unbalance in z_1z_2 sub-plane, the proposed method has taken into account the current unbalances in both z_1z_2 and $\alpha\beta$ sub-planes and can eliminate them simultaneously at the steady state of operation. Consequently, the full compensation of current unbalance can be achieved, by which both the current unbalance between two sets and current unbalance between windings in each set are eliminated. Meanwhile, the 5th and 7th current harmonics caused by non-sinusoidal back EMF and inverter non-linearity can also be fully compensated. The effectiveness of proposed method is verified by a set of comparative experiments on a prototype dual 3-phase PM machine system. It shows that completely balanced currents without the 5th and 7th current harmonics at the

steady state of operation can be achieved. Since this research only investigates the steady state performance of current control, it will be full of challenge to take into account the improvement of the dynamic torque performance in our future research.

Reference

[1] H. Li and Z. Chen, "Overview of different wind generator systems and their comparisons," *IET Renewable Power Generation,* vol. 2, no. 2, pp. 123-138, 2008.

[2] A. D. Hansen and L. H. Hansen, "Wind turbine concept market penetration over 10 years (1995–2004)," *Wind energy,* vol. 10, no. 1, pp. 81-97, 2007.

[3] F. Blaabjerg and M. Ke, "Future on power electronics for wind turbine systems," *IEEE J. Emerg. Sel. Topics Power Electron.,* vol. 1, no. 3, pp. 139-152, 2013.

[4] F. Blaabjerg, C. Zhe, and S. B. Kjaer, "Power electronics as efficient interface in dispersed power generation systems," *IEEE Trans. Power Electron.,* vol. 19, no. 5, pp. 1184-1194, 2004.

[5] A. Hansen, F. Iov, F. Blaabjerg, and L. Hansen, "Review of contemporary wind turbine concepts and their market penetration," *Wind Engineering,* vol. 28, no. 3, pp. 247-263, 2004.

[6] S. Muller, M. Deicke, and R. W. De Doncker, "Doubly fed induction generator systems for wind turbines," *IEEE Industry Applications Magazine,* vol. 8, no. 3, pp. 26-33, 2002.

[7] J. M. Carrasco, L. G. Franquelo, J. T. Bialasiewicz, E. Galvan, R. C. P. Guisado, M. A. M. Prats, J. I. Leon, and N. Moreno-Alfonso, "Power-electronic systems for the grid integration of renewable energy sources: A survey," *IEEE Trans. Ind. Electron.,* vol. 53, no. 4, pp. 1002-1016, 2006.

[8] F. M. Hughes, O. Anaya-Lara, N. Jenkins, and G. Strbac, "Control of DFIG-based wind generation for power network support," *Power Systems, IEEE Transactions on,* vol. 20, no. 4, pp. 1958-1966, 2005.

[9] D. Santos-Martin, J. L. Rodriguez-Amenedo, and S. Arnaltes, "Providing ride-through capability to a doubly fed induction generator under unbalanced voltage dips," *IEEE Trans. Power Electron.,* vol. 24, no. 7, pp. 1747-1757, 2009.

[10] F. Blaabjerg, M. Liserre, and M. Ke, "Power electronics converters for wind turbine systems," *IEEE Trans. Ind. Appl.,* vol. 48, no. 2, pp. 708-719, 2012.

[11] M. Liserre, R. Cardenas, M. Molinas, and J. Rodriguez, "Overview of multi-MW wind turbines and wind parks," *IEEE Trans. Ind. Electron.,* vol. 58, no. 4, pp. 1081-1095, 2011.

[12] C. Zhe, J. M. Guerrero, and F. Blaabjerg, "A review of the state of the art of power electronics for wind turbines," *IEEE Trans. Power Electron.,* vol. 24, no. 8, pp. 1859-1875, 2009.

[13] H. Polinder, F. F. A. van der Pijl, G. J. de Vilder, and P. J. Tavner, "Comparison of direct-drive and geared generator concepts for wind turbines," *IEEE Trans. Energy Convers.,* vol. 21, no. 3, pp. 725-733, 2006.

[14] K. T. Chau, C. C. Chan, and L. Chunhua, "Overview of permanent-magnet brushless drives for electric and hybrid electric vehicles," *IEEE Trans. Ind. Electron.,* vol. 55, no. 6, pp. 2246-2257, 2008.

[15] C. Yicheng, P. Pillay, and A. Khan, "PM wind generator topologies," *IEEE Trans. Ind. Appl.,* vol. 41, no. 6, pp. 1619-1626, 2005.

[16] J. Y. Chen, C. V. Nayar, and X. Longya, "Design and finite-element analysis of an outer-rotor permanent-magnet generator for directly coupled wind turbines," *IEEE Trans. Magn.,* vol. 36, no. 5, pp. 3802-3809, 2000.

[17] E. Spooner and A. C. Williamson, "Direct coupled, permanent magnet generators for wind turbine applications," *IEE Proc. - Elect. Pow. Appl.,* vol. 143, no. 1, pp. 1-8, 1996.

[18] M. E. Haque, M. Negnevitsky, and K. M. Muttaqi, "A novel control strategy for a variable-speed wind turbine with a permanent-magnet synchronous generator," *IEEE Trans. Ind. Appl.,* vol. 46, no. 1, pp. 331-339, 2010.

[19] K. Tan and S. Islam, "Optimum control strategies in energy conversion of PMSG wind turbine system without mechanical sensors," *IEEE Trans. Energy Convers.,* vol. 19, no. 2, pp. 392-399, 2004.

[20] Z. Chen and E. Spooner, "Grid power quality with variable speed wind turbines," *IEEE Trans. Energy Convers.,* vol. 16, no. 2, pp. 148-154, 2001.

[21] Y. Y. Xia, J. E. Fletcher, S. J. Finney, K. H. Ahmed, and B. W. Williams, "Torque ripple analysis and reduction for wind energy conversion systems using uncontrolled rectifier and boost converter," *IET Renewable Power Generation,* vol. 5, no. 5, pp. 377-386, 2011.

[22] R. Sharma, T. W. Rasmussen, and B. B. Jensen, "Application of a synchronous generator with a boost converter in wind turbines: an experimental overview," *IET Renewable Power Generation,* vol. 6, no. 6, pp. 414-423, 2012.

[23] F. Valenciaga and P. F. Puleston, "High-order sliding control for a wind energy conversion system based on a permanent magnet synchronous generator," *IEEE Trans. Energy Convers.,* vol. 23, no. 3, pp. 860-867, 2008.

[24] North american electric reliability corporation-Accommodating high levels of variable generation [Online]. Available: http://www.nerc.com/files/IVGTF_Report_041609.pdf

[25] W. Quincy and C. Liuchen, "An intelligent maximum power extraction algorithm for inverter-based variable speed wind turbine systems," *IEEE Trans. Power Electron.,* vol. 19, no. 5, pp. 1242-1249, 2004.

[26] E. Koutroulis and K. Kalaitzakis, "Design of a maximum power tracking system for wind-energy-conversion applications," *IEEE Trans. Ind. Electron.,* vol. 53, no. 2, pp. 486-494, 2006.

[27] J. Song-Manguelle, S. Schroder, T. Geyer, G. Ekemb, and J. M. Nyobe-Yome, "Prediction of mechanical shaft failures due to pulsating torques of variable-frequency drives," *IEEE Trans. Ind. Appl.,* vol. 46, no. 5, pp. 1979-1988, 2010.

[28] L. Dessaint, H. Nakra, and D. Mukhedkar, "Propagation and elimination of torque ripple in a wind energy conversion system," *IEEE Power Engineering Review,* vol. PER-6, no. 6, pp. 46-47, 1986.

[29] A. L. Rogers, J. F. Manwell, and S. Wright, "Wind turbine acoustic noise," *Renewable Energy Research Laboratory, Amherst: University of Massachusetts,* 2006.

[30] R. Islam and I. Husain, "Analytical model for predicting noise and vibration in permanent-magnet synchronous motors," *IEEE Transactions on Industry Applications,* vol. 46, no. 6, pp. 2346-2354, 2010.

[31] J. Walsh, I. Bashir, P. R. Thies, L. Johanning, and P. Blondel, "Acoustic emission health monitoring of marine renewables: Illustration with a wave energy converter in Falmouth Bay (UK)," in *OCEANS 2015 - Genova*, 2015, pp. 1-7.

[32] W. Hongjia, Y. Ming, N. Li, and X. Dianguo, "Current-loop bandwidth expansion strategy for permanent magnet synchronous motor drives," in *Proc. the 5th IEEE Conference on Industrial Electronics and Applications (ICIEA)*, 2010, pp. 1340-1345.

[33] F. Van den Berg, E. Pedersen, J. Bouma, and R. Bakker, "WINDFARMperception: visual and acoustic impact of wind turbine of wind turbine farms on residents," *Report FP6-2005-Science-and-Society-20. University of Groningen and Göteborg University,* 2008.

[34] H. Møller and C. S. Pedersen, "Low-frequency noise from large wind turbines," *The Journal of the Acoustical Society of America,* vol. 129, no. 6, pp. 3727-3744, 2011.

[35] D. J. Alberts, "Addressing wind turbine noise," *Report from Lawrence Technological University,* 2006.

[36] S. M. Muyeen, M. H. Ali, R. Takahashi, T. Murata, J. Tamura, Y. Tomaki, A. Sakahara, and E. Sasano, "Comparative study on transient stability analysis of wind turbine generator system using different drive train models," *IET Renewable Power Generation,* vol. 1, no. 2, pp. 131-141, 2007.

[37] J. Sopanen, V. Ruuskanen, J. Nerg, and J. Pyrhonen, "Dynamic torque analysis of a wind turbine drive train including a direct-driven permanent-magnet generator," *IEEE Trans. Ind. Electron.,* vol. 58, no. 9, pp. 3859-3867, 2011.

[38] J. F. Gieras, C. Wang, and J. C. Lai, *Noise of polyphase electric motors*: CRC press, 2005.

[39] Z. Q. Zhu, D. Ishak, D. Howe, and C. Jintao, "Unbalanced magnetic forces in permanent-magnet brushless machines with diametrically asymmetric phase windings," *IEEE Trans. Ind. Appl.,* vol. 43, no. 6, pp. 1544-1553, 2007.

[40] O. Carranza, G. Garcerá, E. Figueres, and L. G. González, "Peak current mode control of three-phase boost rectifiers in discontinuous conduction mode for small wind power generators," *Applied Energy,* vol. 87, no. 8, pp. 2728-2736, 2010.

[41] A. R. Prasad, P. D. Ziogas, and S. Manias, "An active power factor correction technique for three-phase diode rectifiers," *IEEE Trans. Power Electron.,* vol. 6, no. 1, pp. 83-92, 1991.

[42] M. Chinchilla, S. Arnaltes, and J. C. Burgos, "Control of permanent-magnet generators applied to variable-speed wind-energy systems connected to the grid," *IEEE Trans. Energy Convers.,* vol. 21, no. 1, pp. 130-135, 2006.

[43] Q. Wei, Q. Liyan, and R. G. Harley, "Control of IPM synchronous generator for maximum wind power generation considering magnetic saturation," *IEEE Trans. Ind. Appl.,* vol. 45, no. 3, pp. 1095-1105, 2009.

[44] R. Pena, J. C. Clare, and G. M. Asher, "Doubly fed induction generator using back-to-back PWM converters and its application to variable-speed wind-energy generation," *IEE Proc. - Elect. Pow. Appl.,* vol. 143, no. 3, pp. 231-241, 1996.

[45] X. Dawei, L. Ran, P. J. Tavner, and S. Yang, "Control of a doubly fed induction generator in a wind turbine during grid fault ride-through," *IEEE Trans. Energy Convers.,* vol. 21, no. 3, pp. 652-662, 2006.

[46] D. Jingya, D. D. Xu, and W. Bin, "A novel control scheme for current-source-converter-based PMSG wind energy conversion systems," *IEEE Trans. Power Electron.,* vol. 24, no. 4, pp. 963-972, 2009.

[47] Y. Xibo, W. Fei, D. Boroyevich, L. Yongdong, and R. Burgos, "DC-link voltage control of a full power converter for wind generator operating in weak-grid systems," *IEEE Trans. Power Electron.,* vol. 24, no. 9, pp. 2178-2192, 2009.

[48] A. Timbus, M. Liserre, R. Teodorescu, P. Rodriguez, and F. Blaabjerg, "Evaluation of current controllers for distributed power generation systems," *IEEE Trans. Power Electron.,* vol. 24, no. 3, pp. 654-664, 2009.

[49] M. Liserre, F. Blaabjerg, and S. Hansen, "Design and control of an LCL-filter-based three-phase active rectifier," *IEEE Trans. Ind. Appl.,* vol. 41, no. 5, pp. 1281-1291, 2005.

[50] P. Rodriguez, A. V. Timbus, R. Teodorescu, M. Liserre, and F. Blaabjerg, "Flexible active power control of distributed power generation systems during grid faults," *IEEE Trans. Ind. Electron.,* vol. 54, no. 5, pp. 2583-2592, 2007.

[51] F. Blaabjerg, R. Teodorescu, M. Liserre, and A. V. Timbus, "Overview of control and grid synchronization for distributed power generation systems," *IEEE Trans. Ind. Electron.,* vol. 53, no. 5, pp. 1398-1409, 2006.

[52] M. Tsili and S. Papathanassiou, "A review of grid code technical requirements for wind farms," *IET Renewable Power Generation,* vol. 3, no. 3, pp. 308-332, 2009.

[53] I. Trintis, S. Munk-Nielsen, F. Abrahamsen, and P. B. Thoegersen, "Efficiency and reliability improvement in wind turbine converters by grid converter adaptive control," in *Proc. 15th European Conference on Power Electronics and Applications (EPE)*, 2013, pp. 1-9.

[54] U. I. Dayaratne, S. B. Tennakoon, N. Y. A. Shammas, and J. S. Knight, "Investigation of variable DC link voltage operation of a PMSG based wind turbine with fully rated converters at steady state," in *Proc. 14th European Conference on Power Electronics and Applications (EPE)*, 2011, pp. 1-10.

[55] R. Jones, P. Brogan, E. Grondahl, and H. Stiesdal, "Power converters," 2007.

[56] F. Niu, B. Wang, A. S. Babel, K. Li, and E. G. Strangas, "Comparative Evaluation of Direct Torque Control Strategies for Permanent Magnet Synchronous Machines," *IEEE Trans. Power Electron.,* vol. 31, no. 2, pp. 1408-1424, 2016.

[57] S. Bolognani, S. Bolognani, L. Peretti, and M. Zigliotto, "Design and implementation of model predictive control for electrical motor drives," *IEEE Trans. Ind. Electron.,* vol. 56, no. 6, pp. 1925-1936, 2009.

[58] F. Morel, X. Lin-Shi, J.-M. Rétif, B. Allard, and C. Buttay, "A comparative study of predictive current control schemes for a permanent-magnet synchronous machine drive," *IEEE Trans. Ind. Electron.,* vol. 56, no. 7, pp. 2715-2728, 2009.

[59] M. Preindl, E. Schaltz, and P. Thogersen, "Switching frequency reduction using model predictive direct current control for high-power voltage source inverters," *IEEE Trans. Ind. Electron.,* vol. 58, no. 7, pp. 2826-2835, 2011.

[60] T. M. Jahns, G. B. Kliman, and T. W. Neumann, "Interior permanent-magnet synchronous motors for adjustable-speed drives," *IEEE Trans. Ind. Appl.,* vol. IA-22, no. 4, pp. 738-747, 1986.

[61] R. Gabriel, W. Leonhard, and C. J. Nordby, "Field-oriented control of a standard AC motor using microprocessors," *IEEE Trans. Ind. Appl.,* vol. IA-16, no. 2, pp. 186-192, 1980.

[62] Field orientated control of 3-phase AC-motors [Online]. Available: http://www.ti.com/lit/an/bpra073/bpra073.pdf

[63] T. M. Rowan and R. J. Kerkman, "A new synchronous current regulator and an analysis of current-regulated PWM inverters," *IEEE Trans. Ind. Appl.,* vol. IA-22, no. 4, pp. 678-690, 1986.

[64] H. Zhu, X. Xiao, and Y. Li, "Torque ripple reduction of the torque predictive control scheme for permanent-magnet synchronous motors," *IEEE Trans. Ind. Electron.,* vol. 59, no. 2, pp. 871-877, 2012.

[65] M. P. Kazmierkowski and L. Malesani, "Current control techniques for three-phase voltage-source PWM converters: a survey," *IEEE Trans. Ind. Electron.,* vol. 45, no. 5, pp. 691-703, 1998.

[66] H. Le-Huy, K. Slimani, and P. Viarouge, "Analysis and implementation of a real-time predictive current controller for permanent-magnet synchronous servo drives," *IEEE Trans. Ind. Electron.,* vol. 41, no. 1, pp. 110-117, 1994.

[67] D. Casadei, F. Profumo, G. Serra, and A. Tani, "FOC and DTC: two viable schemes for induction motors torque control," *IEEE Transactions on Power Electronics,* vol. 17, no. 5, pp. 779-787, 2002.

[68] A. R. Bergen, *Power systems analysis*: Pearson Education India, 2009.

[69] B. Drury, *Control techniques drives and controls handbook*: IET, 2001.

[70] V. Blasko, V. Kaura, and W. Niewiadomski, "Sampling of discontinuous voltage and current signals in electrical drives: a system approach," *IEEE Trans. Ind. Appl.,* vol. 34, no. 5, pp. 1123-1130, 1998.

[71] Y. Jangho, C. Jintae, L. Sang Bin, and Y. Ji-Yoon, "On-line detection of high-resistance connections in the incoming electrical circuit for induction motors," in *Proc. IEEE International Electric Machines & Drives Conference*, 2007, pp. 583-589.

[72] L. Zarri, M. Mengoni, Y. Gritli, A. Tani, F. Filippetti, G. Serra, and D. Casadei, "Detection and localization of stator resistance dissymmetry based on multiple reference frame controllers in multiphase induction motor drives," *IEEE Trans. Ind. Electron.,* vol. 60, no. 8, pp. 3506-3518, 2013.

[73] M. D. Bryant and M. Jin, "Time-wise increases in contact resistance due to surface roughness and corrosion," *IEEE Transactions on Components, Hybrids, and Manufacturing Technology,* vol. 14, no. 1, pp. 79-89, 1991.

[74] Y. Jangho, C. Jintae, L. Sang Bin, and Y. Ji-Yoon, "Online detection of high-resistance connections in the incoming electrical circuit for induction motors," *IEEE Trans. Ind. Appl.,* vol. 45, no. 2, pp. 694-702, 2009.

[75] D. G. Dorrell and M. Popescu, "Effect of winding asymmetries and winding connection on small synchronous machines," *IEEE Trans. Ind. Appl.,* vol. 47, no. 6, pp. 2453-2459, 2011.

[76] B. Zhao, J. Zou, G. Hao, J. Zou, and Y. Xu, "Asymmetry of inductance and torque ripple of multi-unit permanent magnet synchronous motor," in *Proc. International Conference on Electrical Machines and Systems (ICEMS)*, 2011, pp. 1-4.

[77] T.-C. Lin, Z. Q. Zhu, and J. M. Liu, "Improved rotor position estimation in sensorless controlled permanent magnet synchronous machines having asymmetric-EMF with harmonic compensation," *IEEE Trans. Ind. Electron.,* vol. PP, no. 99, pp. 1-1, 2015.

[78] W. Hao, Z. Zhijing, L. Chengying, and L. Chengwu, "Analysis of inductance variation in permanent magnet linear synchronous motor," in *Proc. International Conference on Mechanic Automation and Control Engineering (MACE)*, 2010, pp. 6299-6302.

[79] M. Barcaro, N. Bianchi, and F. Magnussen, "Analysis and tests of a dual three-phase 12-slot 10-pole permanent-magnet motor," *IEEE Trans. Ind. Appl.,* vol. 46, no. 6, pp. 2355-2362, 2010.

[80] M. Barcaro, N. Bianchi, and F. Magnussen, "Faulty operations of a PM fractional-slot machine with a dual three-phase winding," *IEEE Trans. Ind. Electron.,* vol. 58, no. 9, pp. 3825-3832, 2011.

[81] J. Zou, B. Zhao, Y. Xu, and M. Zhao, "The torque ripple and minimization in multi-unit permanent magnet synchronous motor for electromagnetic thruster," in *Proc. 16th International Symposium on Electromagnetic Launch Technology (EML)*, 2012, pp. 1-6.

[82] Z. Q. Zhu, L. J. Wu, and M. L. Mohd Jamil, "Distortion of back-EMF and torque of PM brushless machines due to eccentricity," *IEEE Trans. Magn.,* vol. 49, no. 8, pp. 4927-4936, 2013.

[83] S. Nandi, H. A. Toliyat, and L. Xiaodong, "Condition monitoring and fault diagnosis of electrical motors-a review," *IEEE Trans. Energy Convers.,* vol. 20, no. 4, pp. 719-729, 2005.

[84] J. Ilsu, H. Byong Jo, and N. Kwanghee, "Dynamic modeling and control for SPMSMs with internal turn short fault," *IEEE Trans. Power Electron.,* vol. 28, no. 7, pp. 3495-3508, 2013.

[85] M. Mengoni, L. Zarri, Y. Gritli, A. Tani, F. Filippetti, and L. Sang Bin, "Online detection of high-resistance connections with negative-sequence regulators in three-phase induction motor drives," *IEEE Trans. Ind. Appl.,* vol. 51, no. 2, pp. 1579-1586, 2015.

[86] H. S. Che, E. Levi, M. Jones, W. P. Hew, and N. A. Rahim, "Current control methods for an asymmetrical six-phase induction motor drive," *IEEE Trans. Power Electron.,* vol. 29, no. 1, pp. 407-417, 2014.

[87] A. H. Abosh and Z. Q. Zhu, "Current control of permanent magnet synchronous machine with asymmetric phases," in *Proc. 7th IET International Conference on Power Electronics, Machines and Drives (PEMD)*, 2014, pp. 1-6.

[88] J. L. Kohler, J. Sottile, and F. C. Trutt, "Alternatives for assessing the electrical integrity of induction motors," *IEEE Trans. Ind. Appl.,* vol. 28, no. 5, pp. 1109-1117, 1992.

[89] H. A. Toliyat and T. A. Lipo, "Transient analysis of cage induction machines under stator, rotor bar and end ring faults," *IEEE Trans. Energy Convers.,* vol. 10, no. 2, pp. 241-247, 1995.

[90] S. Williamson and K. Mirzoian, "Analysis of cage induction motors with stator winding faults," *IEEE Trans. Power App. Syst.,* vol. PAS-104, no. 7, pp. 1838-1842, 1985.

[91] C. L. Fortescue, "Method of symmetrical co-ordinates applied to the solution of polyphase networks," *Transactions of the American Institute of Electrical Engineers,* vol. XXXVII, no. 2, pp. 1027-1140, 1918.

[92] H. De Battista, P. F. Puleston, R. J. Mantz, and C. F. Christiansen, "Sliding mode control of wind energy systems with DOIG-power efficiency and torsional dynamics optimization," *IEEE Transactions on Power Systems,* vol. 15, no. 2, pp. 728-734, 2000.

[93] K. Lee, T. M. Jahns, G. Venkataramanan, and W. E. Berkopec, "DC-bus electrolytic capacitor stress in adjustable-speed drives under input voltage unbalance and sag conditions," *IEEE Trans. Ind. Appl.,* vol. 43, no. 2, pp. 495-504, 2007.

[94] W. Huai and F. Blaabjerg, "Reliability of capacitors for DC-link applications in power electronic converters-an overview," *IEEE Trans. Ind. Appl.,* vol. 50, no. 5, pp. 3569-3578, 2014.

[95] Y. Shaoyong, A. Bryant, P. Mawby, X. Dawei, L. Ran, and P. Tavner, "An industry-based survey of reliability in power electronic converters," *IEEE Trans. Ind. Appl.,* vol. 47, no. 3, pp. 1441-1451, 2011.

[96] D. N. Zmood and D. G. Holmes, "Stationary frame current regulation of PWM inverters with zero steady-state error," *IEEE Trans. Power Electron.,* vol. 18, no. 3, pp. 814-822, 2003.

[97] D. N. Zmood, D. G. Holmes, and G. H. Bode, "Frequency-domain analysis of three-phase linear current regulators," *IEEE Trans. Ind. Appl.,* vol. 37, no. 2, pp. 601-610, 2001.

[98] L. R. Limongi, R. Bojoi, G. Griva, and A. Tenconi, "Digital current-control schemes," *IEEE Ind. Electron. Mag.,* vol. 3, no. 1, pp. 20-31, 2009.

[99] X. Yuan, W. Merk, H. Stemmler, and J. Allmeling, "Stationary-frame generalized integrators for current control of active power filters with zero steady-state error for current harmonics of concern under unbalanced and distorted operating conditions," *IEEE Trans. Ind. Appl.,* vol. 38, no. 2, pp. 523-532, 2002.

[100] J. Hu and Y. He, "Modeling and control of grid-connected voltage-sourced converters under generalized unbalanced operation conditions," *IEEE Trans. Energy Convers.,* vol. 23, no. 3, pp. 903-913, 2008.

[101] D. Roiu, R. I. Bojoi, L. R. Limongi, and A. Tenconi, "New stationary frame control scheme for three-phase PWM rectifiers under unbalanced voltage dips conditions," *IEEE Trans. Ind. Appl.,* vol. 46, no. 1, pp. 268-277, 2010.

[102] S. Hong-Seok and N. Kwanghee, "Dual current control scheme for PWM converter under unbalanced input voltage conditions," *IEEE Trans. Ind. Electron.,* vol. 46, no. 5, pp. 953-959, 1999.

[103] S. Yongsug, V. Tijeras, and T. A. Lipo, "A nonlinear control of the instantaneous power in dq synchronous frame for PWM AC/DC converter under generalized unbalanced operating conditions," in *Proc. Conf. Record of the 37th IAS Annu. Meeting Ind. Appl. Conf.*, 2002, pp. 1189-1196 vol.2.

[104] C. B. Jacobina, M. B. d. Correa, T. M. Oliveiro, A. M. N. Lima, and E. R. Cabral da Silva, "Current control of unbalanced electrical systems," *IEEE Trans. Ind. Electron.,* vol. 48, no. 3, pp. 517-525, 2001.

[105] H. Deng, "Current controller and generator system," ed: Google Patents, 2014.

[106] I. Etxeberria-Otadui, U. Viscarret, M. Caballero, A. Rufer, and S. Bacha, "New optimized PWM VSC control structures and strategies under unbalanced voltage transients," *IEEE Trans. Ind. Electron.,* vol. 54, no. 5, pp. 2902-2914, 2007.

[107] A. G. Yepes, A. Vidal, O. Lopez, and J. Doval-Gandoy, "Evaluation of techniques for cross-coupling decoupling between orthogonal axes in double synchronous reference frame current control," *IEEE Trans. Ind. Electron.,* vol. 61, no. 7, pp. 3527-3531, 2014.

[108] P. Van-Tung and L. Hong-Hee, "Performance enhancement of stand-alone DFIG systems with control of rotor and load side converters using resonant controllers," *IEEE Trans. Ind. Appl.,* vol. 48, no. 1, pp. 199-210, 2012.

[109] J. B. Hu, Y. K. He, L. Xu, and B. W. Williams, "Improved control of DFIG systems during network unbalance using PI-R current regulators," *IEEE Trans. Ind. Electron.,* vol. 56, no. 2, pp. 439-451, 2009.

[110] Y. Hu, Z. Q. Zhu, and K. Liu, "Current control for dual three-phase PM synchronous motors accounting for current unbalance and harmonics," *IEEE J. Emerg. Sel. Topics Power Electron.,* vol. 2, no. 2, pp. 272-284, 2014.

[111] Y. Hu, Z. Q. Zhu, and K. Liu, "Current control for dual three-phase PM synchronous motors accounting for current unbalance and harmonics," *IEEE J. Emerg. Sel. Topics Power Electron.,* vol. PP, no. 99, pp. 1-1, 2014.

[112] R. Reginatto and R. A. Ramos, "On electrical power evaluation in dq coordinates under sinusoidal unbalanced conditions," *IET Generation, Transmission & Distribution,* vol. 8, no. 5, pp. 976-982, 2014.

[113] L. Xiao, S. Huang, and K. Lu, "DC-bus voltage control of grid-connected voltage source converter by using space vector modulated direct power control under unbalanced network conditions," *IET Power Electron.,* vol. 6, no. 5, pp. 925-934, 2013.

[114] Y. Bo, R. Oruganti, S. K. Panda, and A. K. S. Bhat, "An output-power-control strategy for a three-phase PWM rectifier under unbalanced supply conditions," *IEEE Trans. Ind. Electron.,* vol. 55, no. 5, pp. 2140-2151, 2008.

[115] A. Yazdani and R. Iravani, "A unified dynamic model and control for the voltage-sourced converter under unbalanced grid conditions," *IEEE Trans. Power Del.,* vol. 21, no. 3, pp. 1620-1629, 2006.

[116] X. H. Wu, S. K. Panda, and J. X. Xu, "Analysis of the instantaneous power flow for three-phase PWM boost rectifier under unbalanced supply voltage conditions," *IEEE Trans. Power Electron.,* vol. 23, no. 4, pp. 1679-1691, 2008.

[117] P. Rioual, H. Pouliquen, and J.-P. Louis, "Regulation of a PWM rectifier in the unbalanced network state using a generalized model," *IEEE Trans. Power Electron.,* vol. 11, no. 3, pp. 495-502, 1996.

[118] S. Yongsug and T. A. Lipo, "Control scheme in hybrid synchronous stationary frame for PWM AC/DC converter under generalized unbalanced operating conditions," *IEEE Trans. Ind. Appl.,* vol. 42, no. 3, pp. 825-835, 2006.

[119] J. G. Hwang, P. W. Lehn, and M. Winkelnkemper, "Control of grid connected AC-DC converters with minimized DC link capacitance under unbalanced grid voltage condition," in *Proc. European Conf. Power Electron. and Appl.*, 2007, pp. 1-10.

[120] P. Rodriguez, R. Teodorescu, I. Candela, A. V. Timbus, M. Liserre, and F. Blaabjerg, "New positive-sequence voltage detector for grid synchronization of power converters under faulty grid conditions," in *Proc. 37th IEEE Power Electron. Spec. Conf.*, 2006, pp. 1-7.

[121] Z. Li, P. Wang, Y. Li, H. Zhu, and F. Gao, "Control of three-phase PWM rectifier under unbalanced input voltage conditions without sequential component extraction," in *Proc. 14th Int. Power Electron. and Motion Control Conf.*, 2010, pp. T2-179-T2-184.

[122] Z. Li, Y. Li, P. Wang, H. Zhu, C. Liu, and W. Xu, "Control of three-phase boost-type PWM rectifier in stationary frame under unbalanced input voltage," *IEEE Trans. Power Electron.,* vol. 25, no. 10, pp. 2521-2530, 2010.

[123] Y. Jun, L. Hui, L. Yong, and C. Zhe, "An improved control strategy of limiting the DC-link voltage fluctuation for a doubly fed induction wind generator," *IEEE Trans. Power Electron.,* vol. 23, no. 3, pp. 1205-1213, 2008.

[124] N. Hur, J. Jinhwan, and N. Kwanghee, "A fast dynamic DC-link power-balancing scheme for a PWM converter-inverter system," *IEEE Trans. Ind. Electron.,* vol. 48, no. 4, pp. 794-803, 2001.

[125] L. Malesani, L. Rossetto, P. Tenti, and P. Tomasin, "AC/DC/AC PWM converter with reduced energy storage in the DC link," *IEEE Trans. Ind. Appl.,* vol. 31, no. 2, pp. 287-292, 1995.

[126] J. Si-Hun, S. SeoEun, and P. Jung-Wook, "On improving distortion power quality index in distributed power grids," *Smart Grid, IEEE Transactions on,* vol. 4, no. 1, pp. 586-595, 2013.

[127] "IEEE Recommended Practices and Requirements for Harmonic Control in Electrical Power Systems," *IEEE Std 519-1992,* pp. 1-112, 1993.

[128] "IEEE standard for interconnecting distributed resources with electric power systems," *IEEE Std 1547-2003,* pp. 1-28, 2003.

[129] "Electromagnetic compatibility (EMC)—Part 3: Limits-Section VI: Assessment of emission limits for distorting loads in MV and HV power systems," *IEC 61000-3-6,* 1996.

[130] T. Kinjo, T. Senjyu, N. Urasaki, and H. Fujita, "Output levelling of renewable energy by electric double-layer capacitor applied for energy storage system," *IEEE Trans. Energy Convers.,* vol. 21, no. 1, pp. 221-227, 2006.

[131] S. M. Muyeen, R. Takahashi, T. Murata, and J. Tamura, "Integration of an energy capacitor system with a variable-speed wind generator," *IEEE Trans. Energy Convers.,* vol. 24, no. 3, pp. 740-749, 2009.

[132] X. Guoyi, X. Lie, D. J. Morrow, and C. Dong, "Coordinated DC voltage control of wind turbine with embedded energy storage system," *IEEE Trans. Energy Convers.,* vol. 27, no. 4, pp. 1036-1045, 2012.

[133] L. Ma, J. Li, H. Liao, and J. Zhang, "Compensation device used for eliminating second harmonic pulsation in inverter and electrical power system," China Patent CN103872683 A, 2014.

[134] X. Zhao, J. Corda, and T. Mei, "Modelling of the impact of phase asymmetries on the torque waveform of a permanent magnet synchronous motor," *Electrical Engineering Electrical Journal,* vol. 1, 2009.

[135] A. Gebregergis, M. Islam, T. Sebastian, and R. Ramakrishnan, "Evaluation of inductance in a permanent magnet synchronous motor," in *Proc. IEEE Int. Electric Mach. & Drives Conf.*, 2011, pp. 1171-1176.

[136] S. Kallio, M. Andriollo, A. Tortella, and J. Karttunen, "Decoupled d–q model of double-star interior-permanent-magnet synchronous machines," *IEEE Trans. Ind. Electron.,* vol. 60, no. 6, pp. 2486-2494, 2013.

[137] S. Kallio, J. Karttunen, M. Andriollo, P. Peltoniemi, and P. Silventoinen, "Finite element based phase-variable model in the analysis of double-star permanent magnet synchronous machines," in *Proc. International Symposium on Power Electronics, Electrical Drives, Automation and Motion (SPEEDAM)*, 2012, pp. 1462-1467.

[138] A. E. Fitzgerald, C. Kingsley, and S. D. Umans, *Electric machinery*: 6th ed. McGraw-Hill, 2002.

[139] C. D. Schauder and R. Caddy, "Current control of voltage-source inverters for fast four-quadrant drive performance," *IEEE Trans. Ind. Appl.,* vol. IA-18, no. 2, pp. 163-171, 1982.

[140] F. Briz, M. W. Degner, and R. D. Lorenz, "Analysis and design of current regulators using complex vectors," *IEEE Trans. Ind. Appl.,* vol. 36, no. 3, pp. 817-825, 2000.

[141] A. Vidal, F. D. Freijedo, A. G. Yepes, P. Fernandez-Comesana, J. Malvar, O. Lopez, and J. Doval-Gandoy, "Assessment and optimization of the transient response of proportional-resonant current controllers for distributed power generation systems," *IEEE Trans. Ind. Electron.,* vol. 60, no. 4, pp. 1367-1383, 2013.

[142] M. Reyes, P. Rodriguez, S. Vazquez, A. Luna, R. Teodorescu, and J. M. Carrasco, "Enhanced decoupled double synchronous reference frame current controller for unbalanced grid-voltage conditions," *IEEE Trans. Power Electron.,* vol. 27, no. 9, pp. 3934-3943, 2012.

[143] J. Tan, X. Wang, Z. Chen, and M. Li, "Impact of a direct-drive permanent magnet generator (DDPMG) wind turbine system on power system oscillations," in *Proc. IEEE Power and Energy Soc. General Meeting*, 2012, pp. 1-8.

[144] A. W. Green, J. T. Boys, and G. F. Gates, "3-phase voltage sourced reversible rectifier," *IEE Proc. B Elect. Power Appl.,* vol. 135, no. 6, pp. 362-370, 1988.

[145] Y. Ye, M. Kazerani, and V. H. Quintana, "A novel modeling and control method for three-phase PWM converters," in *Proc. IEEE 32nd Annual Power Electronics Specialists Conference (PESC)*, 2001, pp. 102-107 vol. 1.

[146] K. Hyosung, F. Blaabjerg, B. Bak-Jensen, and C. Jaeho, "Instantaneous power compensation in three-phase systems by using p-q-r theory," *IEEE Trans. Power Electron.,* vol. 17, no. 5, pp. 701-710, 2002.

[147] Z. Wei, H. Yanze, L. Xinbo, and Z. Yuanjun, "Switched control of three-phase voltage source PWM rectifier under a wide-range rapidly varying active Load," *IEEE Trans. Power Electron.,* vol. 27, no. 2, pp. 881-890, 2012.

[148] H. Akagi, Y. Kanazawa, and A. Nabae, "Instantaneous reactive power compensators comprising switching devices without energy storage components," *IEEE Trans. Ind. Appl.,* vol. IA-20, no. 3, pp. 625-630, 1984.

[149] H. S. Kim, H. S. Mok, G. H. Choe, D. S. Hyun, and S. Y. Choe, "Design of current controller for 3-phase PWM converter with unbalanced input voltage," in *Proc. 29th Annual IEEE Power Electronics Specialists Conference*, 1998, pp. 503-509 vol.1.

[150] P. Karlsson and J. Svensson, "DC bus voltage control for a distributed power system," *IEEE Trans. Power Electron.,* vol. 18, no. 6, pp. 1405-1412, 2003.

[151] S. Golestan, M. Monfared, F. D. Freijedo, and J. M. Guerrero, "Dynamics assessment of advanced single-phase PLL structures," *IEEE Trans. Ind. Electron.,* vol. 60, no. 6, pp. 2167-2177, 2013.

[152] J. Matas, M. Castilla, J. Miret, L. Garcia de Vicuna, and R. Guzman, "An adaptive prefiltering method to improve the speed/accuracy tradeoff of voltage sequence detection methods under adverse grid conditions," *IEEE Trans. Ind. Electron.,* vol. 61, no. 5, pp. 2139-2151, 2014.

[153] W. K. Sonnemann, "A symmetrical component approach to load balancing," *Electrical Engineering,* vol. 79, no. 4, pp. 294-296, 1960.

[154] L. Guanghao and X. Xiao-Bang, "Improved modeling of the nonlinear B-H curve and its application in power cable analysis," *IEEE Trans. Magn.,* vol. 38, no. 4, pp. 1759-1763, 2002.

[155] K. Gopakumar, S. Sathiakumar, S. K. Biswas, and J. Vithayathil, "Modified current source inverter fed induction motor drive with reduced torque pulsations," *IEE Proc. B Elect. Power Appl.,* vol. 131, no. 4, pp. 159-164, 1984.

[156] E. Levi, "Multiphase electric machines for variable-speed applications," *IEEE Trans. Ind. Electron.,* vol. 55, no. 5, pp. 1893-1909, 2008.

[157] B. Andresen and J. Birk, "A high power density converter system for the Gamesa G10x 4,5 MW wind turbine," in *Proc. European Conference on Power Electronics and Applications*, 2007, pp. 1-8.

[158] R. Jones and P. Waite, "Optimised power converter for multi-MW direct drive permanent magnet wind turbines," in *Proc. 14th European Conference on Power Electronics and Applications*, 2011, pp. 1-10.

[159] M. Barcaro, N. Bianchi, and F. Magnussen, "Six-phase supply feasibility using a PM fractional-slot dual winding machine," in *Proc. IEEE Energy Conversion Congress and Exposition (ECCE)*, 2010, pp. 1058-1065.

[160] M. Barcaro, N. Bianchi, and F. Magnussen, "Six-phase supply feasibility using a PM fractional-slot dual winding machine," *IEEE Trans. Ind. Appl.,* vol. 47, no. 5, pp. 2042-2050, 2011.

[161] X. Jiang, W. Huang, R. Cao, Z. Hao, and W. Jiang, "Electric drive system of dual-winding fault-tolerant permanent magnet motor for aerospace applications," *IEEE Trans. Ind. Electron.,* vol. PP, no. 99, pp. 1-1, 2015.

[162] X. Jiang, W. Huang, R. Cao, Z. Hao, J. Li, and W. Jiang, "Analysis of a dual-winding fault-tolerant permanent magnet machine drive for aerospace applications," *IEEE Trans. Magn.,* vol. PP, no. 99, pp. 1-1, 2015.

[163] R. Bojoi, M. Lazzari, F. Profumo, and A. Tenconi, "Digital field-oriented control for dual three-phase induction motor drives," *IEEE Trans. Ind. Appl.,* vol. 39, no. 3, pp. 752-760, 2003.

[164] T. M. Jahns, "Improved reliability in solid-state AC drives by means of multiple independent phase drive units," *IEEE Trans. Ind. Appl.,* vol. IA-16, no. 3, pp. 321-331, 1980.

[165] G. K. Singh, K. Nam, and S. K. Lim, "A simple indirect field-oriented control scheme for multiphase induction machine," *IEEE Trans. Ind. Electron.,* vol. 52, no. 4, pp. 1177-1184, 2005.

[166] J. Karttunen, S. Kallio, P. Peltoniemi, P. Silventoinen, and O. Pyrhonen, "Dual three-phase permanent magnet synchronous machine supplied by two independent voltage source inverters," in *Proc. Int. Symp. Power Electron., Electr. Drives, Autom. and Motion*, 2012, pp. 741-747.

[167] E. Levi, R. Bojoi, F. Profumo, H. A. Toliyat, and S. Williamson, "Multiphase induction motor drives - A technology status review," *IET Electr. Power Appl.,* vol. 1, no. 4, pp. 489-516, 2007.

[168] W. Cao, B. C. Mecrow, G. J. Atkinson, J. W. Bennett, and D. J. Atkinson, "Overview of electric motor technologies used for more electric aircraft (MEA)," *IEEE Trans. Ind. Electron.,* vol. 59, no. 9, pp. 3523-3531, 2012.

[169] H. Amimeur, D. Aouzellag, R. Abdessemed, and K. Ghedamsi, "Sliding mode control of a dual-stator induction generator for wind energy conversion systems," *Int. J. Electr. Power Engery Syst.,* vol. 42, no. 1, pp. 60-70, 2012.

[170] K. Gopakumar, V. T. Ranganthan, and S. R. Bhat, "Split-phase induction motor operation from PWM voltage source inverter," *IEEE Trans. Ind. Appl.,* vol. 29, no. 5, pp. 927-932, 1993.

[171] R. Bojoi, F. Farina, G. Griva, F. Profumo, and A. Tenconi, "Direct torque control for dual three-phase induction motor drives," *IEEE Trans. Ind. Appl.,* vol. 41, no. 6, pp. 1627-1636, 2005.

[172] F. Barrero, M. R. Arahal, R. Gregor, S. Toral, and M. J. Duran, "One-step modulation predictive current control method for the asymmetrical dual three-phase induction machine," *IEEE Trans. Ind. Electron.,* vol. 56, no. 6, pp. 1974-1983, 2009.

[173] F. Barrero, M. R. Arahal, R. Gregor, S. Toral, and M. J. Duran, "A proof of concept study of predictive current control for vsi-driven asymmetrical dual three-phase ac machines," *IEEE Trans. Ind. Electron.,* vol. 56, no. 6, pp. 1937-1954, 2009.

[174] R. Gregor, F. Barrero, S. L. Toral, M. J. Duran, M. R. Arahal, J. Prieto, and J. L. Mora, "Predictive-space vector PWM current control method for asymmetrical dual three-phase induction motor drives," *IET Electr. Power Appl.,* vol. 4, no. 1, pp. 26-34, 2010.

[175] F. Barrero, J. Prieto, E. Levi, R. Gregor, S. Toral, M. J. Duran, and M. Jones, "An enhanced predictive current control method for asymmetrical six-phase motor drives," *IEEE Trans. Ind. Electron.,* vol. 58, no. 8, pp. 3242-3252, 2011.

[176] M. J. Duran, J. Prieto, F. Barrero, and S. Toral, "Predictive current control of dual three-phase drives using restrained search techniques," *IEEE Trans. Ind. Electron.,* vol. 58, no. 8, pp. 3253-3263, 2011.

[177] Y. Zhao and T. A. Lipo, "Space vector PWM control of dual three-phase induction machine using vector space decomposition," *IEEE Trans. Ind. Appl.,* vol. 31, no. 5, pp. 1100-1109, 1995.

[178] K. K. Mohapatra, R. S. Kanchan, M. R. Baiju, P. N. Tekwani, and K. Gopakumar, "Independent field-oriented control of two split-phase induction motors from a single six-phase inverter," *IEEE Trans. Ind. Electron.,* vol. 52, no. 5, pp. 1372-1382, 2005.

[179] D. Hadiouche, H. Razik, and A. Rezzoug, "On the modeling and design of dual-stator windings to minimize circulating harmonic currents for VSI fed AC machines," *IEEE Trans. Ind. Appl.,* vol. 40, no. 2, pp. 506-515, 2004.

[180] D. Yazdani, S. Ali Khajehoddin, A. Bakhshai, and G. Joos, "Full utilization of the inverter in split-phase drives by means of a dual three-phase space vector classification algorithm," *IEEE Trans. Ind. Electron.,* vol. 56, no. 1, pp. 120-129, 2009.

[181] A. R. Bakhshai, G. Joos, P. K. Jain, and J. Hua, "Incorporating the overmodulation range in space vector pattern generators using a classification algorithm," *IEEE Trans. Power Electron.,* vol. 15, no. 1, pp. 83-91, 2000.

[182] R. Bojoi, A. Tenconi, F. Profumo, G. Griva, and D. Martinello, "Complete analysis and comparative study of digital modulation techniques for dual three-phase AC motor drives," in *Proc. IEEE 33rd Annu. Power Electron. Spec. Conf.*, 2002, pp. 851-857 vol.2.

[183] K. Marouani, L. Baghli, D. Hadiouche, A. Kheloui, and A. Rezzoug, "A new PWM strategy based on a 24-sector vector space decomposition for a six-phase VSI-Fed dual stator induction motor," *IEEE Trans. Ind. Electron.,* vol. 55, no. 5, pp. 1910-1920, 2008.

[184] R. Bojoi, F. Farina, M. Lazzari, F. Profumo, and A. Tenconi, "Analysis of the asymmetrical operation of dual three-phase induction machines," in *Proc. IEEE Int. Electron. Mach. and Drives Conf.*, 2003, pp. 429-435 vol.1.

[185] R. Kianinezhad, B. Nahid, L. Baghli, F. Betin, and G. A. Capolino, "Aspects of current regulation in indirect field oriented control of dual three phase induction machines," in *Proc. IEEE Int. Conf. Ind. Technol.*, 2006, pp. 933-938.

[186] Y. He, Y. Wang, J. Wu, Y. Feng, and J. Liu, "A simple current sharing scheme for dual three-phase permanent-magnet synchronous motor drives," in *Proc. 25th Annu. IEEE Appl. Power Electron. Conf. and Expo.*, 2010, pp. 1093-1096.

[187] J. Karttunen, S. Kallio, P. Peltoniemi, P. Silventoinen, and O. Pyrhonen, "Decoupled vector control scheme for dual three-phase permanent magnet synchronous machines," *IEEE Trans. Ind. Electron.,* vol. PP, no. 99, pp. 1-1, 2013.

[188] R. Bojoi, F. Profumo, and A. Tenconi, "Digital synchronous frame current regulation for dual three-phase induction motor drives," in *Proc. IEEE 34th Annu. Power Electron. Spec. Conf.* , 2003, pp. 1475-1480 vol.3.

[189] R. Bojoi, E. Levi, F. Farina, A. Tenconi, and F. Profumo, "Dual three-phase induction motor drive with digital current control in the stationary reference frame," *IEE Proc. - Elect. Pow. Appl.,* vol. 153, no. 1, pp. 129-139, 2006.

[190] H. S. Che, W. P. Hew, N. A. Rahim, E. Levi, M. Jones, and M. J. Duran, "Current control of a six-phase induction generator for wind energy plants," in *Proc. 15th Int. Power Electron. and Motion Control Conf.*, 2012, pp. LS5b.2-1-LS5b.2-7.

[191] J. Liu, G. J. Yang, J. Y. Su, and J. B. Yang, "An improved vector control method for dual three phase PMSG," in *Proc. 7th Int. Power Electron. and Motion Control Conf.*, 2012, pp. 1252-1256.

[192] J. W. Choi and S. K. Sul, "Inverter output voltage synthesis using novel dead time compensation," *IEEE Trans. Power Electron.,* vol. 11, no. 2, pp. 221-227, 1996.

[193] H. S. Kim, K. H. Kim, and M.-J. Youn, "On-line dead-time compensation method based on time delay control," *IEEE Trans. Control Syst. Technol.,* vol. 11, no. 2, pp. 279-285, 2003.

[194] G. Escobar, A. M. Stankovic, and P. Mattavelli, "An adaptive controller in stationary reference frame for D-STATCOM in unbalanced operation," *IEEE Trans. Ind. Electron.,* vol. 51, no. 2, pp. 401-409, 2004.

[195] I. Etxeberria-Otadui, A. L. de Heredia, H. Gaztanaga, S. Bacha, and M. R. Reyero, "A single synchronous frame hybrid (SSFH) multifrequency controller for power active filters," *IEEE Trans. Ind. Electron.,* vol. 53, no. 5, pp. 1640-1648, 2006.

[196] M. Liserre, R. Teodorescu, and F. Blaabjerg, "Multiple harmonics control for three-phase grid converter systems with the use of PI-RES current controller in a rotating frame," *IEEE Trans. Power Electron.,* vol. 21, no. 3, pp. 836-841, 2006.

[197] L. L. Fan, R. Kavasseri, H. P. Yin, C. X. Zhu, and M. Q. Hu, "Control of DFIG for rotor current harmonics elimination," in *Proc. IEEE Power & Energy Soc.*, 2009, pp. 1-7.

[198] H. L. Xu, J. B. Hu, N. Heng, and Y. K. He, "Dynamic modeling and improved control of DFIG under unbalanced and distorted grid voltage conditions," in *Proc. IEEE Int. Symp. Ind. Electron.*, 2012, pp. 1579-1584.

[199] C. Liu, F. Blaabjerg, W. Chen, and D. Xu, "Stator current harmonic control with resonant controller for doubly fed induction generator," *IEEE Trans. Power Electron.,* vol. 27, no. 7, pp. 3207-3220, 2012.

Publications

Journal papers published or in press:

[J1] Y. Hu, Z. Q. Zhu, and K. Liu, "Current control for dual three-phase PM synchronous motors accounting for current unbalance and harmonics," Special Issue on Advanced Control of Electric Motor Drives in IEEE Journal of Emerging and Selected Topics in Power Electronics, vol.2, no.2, pp.272-284, 2014.

[J2] Y. Hu, M. Odavic, and Z. Q. Zhu, "DC bus voltage pulsation suppression of the permanent magnet synchronous generator with asymmetries accounting for torque ripple," IEEE Trans. Energy Convers., vol. PP, no. 99, pp. 1-1, 2016.

Submitted/To be submitted

[1] Y. Hu, Z. Q. Zhu, and M. Odavic, "Instantaneous power control for suppressing the second harmonic DC bus voltage under generic unbalanced operating conditions," *Submitted to IEEE Transactions on Power Electronics,* 2016.

[2] Y. Hu, Z. Q. Zhu, and M. Odavic, "An improved method of DC bus voltage pulsation suppression for asymmetric PMSG with compensation in parallel," *To be submitted,* 2016.

[3] Y. Hu, Z. Q. Zhu, and M. Odavic, "Compensation of unbalanced impedance of asymmetric PMSG compensated by external circuits in series," *To be submitted,* 2016.

[4] Y. Hu, Z. Q. Zhu, and M. Odavic, "Comparative study of current control methods of asymmetric PM synchronous machine," *Submitted to ICEM 2016.*.